William Cowley

The Nature of Dusty Star-Forming Galaxies

Springer

Springer Theses

Recognizing Outstanding Ph.D. Research

Aims and Scope

The series "Springer Theses" brings together a selection of the very best Ph.D. theses from around the world and across the physical sciences. Nominated and endorsed by two recognized specialists, each published volume has been selected for its scientific excellence and the high impact of its contents for the pertinent field of research. For greater accessibility to non-specialists, the published versions include an extended introduction, as well as a foreword by the student's supervisor explaining the special relevance of the work for the field. As a whole, the series will provide a valuable resource both for newcomers to the research fields described, and for other scientists seeking detailed background information on special questions. Finally, it provides an accredited documentation of the valuable contributions made by today's younger generation of scientists.

Theses are accepted into the series by invited nomination only and must fulfill all of the following criteria

- They must be written in good English.
- The topic should fall within the confines of Chemistry, Physics, Earth Sciences, Engineering and related interdisciplinary fields such as Materials, Nanoscience, Chemical Engineering, Complex Systems and Biophysics.
- The work reported in the thesis must represent a significant scientific advance.
- If the thesis includes previously published material, permission to reproduce this must be gained from the respective copyright holder.
- They must have been examined and passed during the 12 months prior to nomination.
- Each thesis should include a foreword by the supervisor outlining the significance of its content.
- The theses should have a clearly defined structure including an introduction accessible to scientists not expert in that particular field.

More information about this series at http://www.springer.com/series/8790

William Cowley

The Nature of Dusty Star-Forming Galaxies

Doctoral Thesis accepted by
Durham University, UK

Author
Dr. William Cowley
Kapteyn Astronomical Institute
Groningen
The Netherlands

Supervisors
Prof. Cedric Lacey
Department of Physics, Institute
    for Computational Cosmology
Durham University
Durham
UK

Prof. Carlton Baugh
Department of Physics, Institute
    for Computational Cosmology
Durham University
Durham
UK

Prof. Shaun Cole
Department of Physics, Institute
    for Computational Cosmology
Durham University
Durham
UK

When I heard the learn'd astronomer;
When the proofs, the figures, were ranged in
columns before me;
When I was shown the charts and diagrams,
to add, divide, and measure them;
When I, sitting, heard the astronomer where
they lectured with much applause in the
lecture-room,
How soon, unaccountable, I became tired
and sick;
Till rising and gliding out, I wander'd off by
myself,
In the mystical moist night-air, and from time
to time,
Look'd up in perfect silence at the stars.

Walt Whitman

To mum and dad, for everything

Supervisors' Foreword

Will Cowley's Ph.D. thesis focuses on understanding the evolution of galaxies at far-infrared and sub-millimetre wavelengths within the framework of theoretical models for structure formation in the Universe. The emission from galaxies at these wavelengths comes predominantly from interstellar dust grains that have been heated by absorbing light from stars. Observations by the first space-based infrared telescopes in the 1970s and 1980s showed that galaxies in the local Universe emit a significant fraction of their radiation in this way, but the full importance of the far-infrared emission from galaxies only became apparent with the discovery in the 1990s of the cosmic infrared background. Measurements of this background showed that, over the history of the Universe, roughly as much radiation has been emitted by galaxies at infrared wavelengths by dust grains as at optical and ultra-violet wavelengths, where we are mainly seeing the direct emission from stars, unobscured by dust. It was also realised that most of the starlight that is absorbed by dust and reprocessed into infrared radiation is from young stars, since these emit most of their radiation at shorter wavelengths that are more effectively absorbed by dust grains. The light from young stars is used as one of the main observational tracers of star formation activity in galaxies. Since most of this light is absorbed by dust and reprocessed into infrared radiation, understanding the far-infrared emission from galaxies over the history of the Universe is crucial for understanding the cosmic history of star formation, which describes how the stellar mass of galaxies has built up over cosmic time.

The significance of Cowley's work is that it seeks to understand observations of galaxy evolution at far-infrared and sub-millimetre wavelengths in terms of phys-ical models of galaxy formation that are implemented within hierarchical models for structure formation in the Universe. Galaxy formation is a complex process. Structure forms in the dark matter by gravitational growth of initially small density fluctuations, leading to gravitationally bound dark matter halos, and gas then falls into the gravitational potential wells of these halos. The gas in halos undergoes heating and cooling processes, with some of it cooling and collapsing to the centres of halos, where it can form stars and also supermassive black holes. However, the efficiency of converting baryons in halos into stars is strongly limited by energy

injection by both young stars and black holes, a process called feedback. However, the detailed operation of these feedback processes is still poorly understood, which is why galaxy formation remains only a partly-solved problem.

Cowley's work uses a semi-analytical model of galaxy formation, GALFORM, that has been developed over the past two decades by researchers at the Institute for Computational Cosmology, which is part of Durham University. The GALFORM model incorporates modelling of all of the processes mentioned above, starting from dark matter halos predicted by a cosmological dark matter simulation. It also includes the evolution of stellar populations, the production and ejection of heavy elements by stars, their conversion into interstellar dust, and the reprocessing of starlight by this interstellar dust. The treatment of feedback processes is a key element of the model, which introduces parameters that must be calibrated using observations of real galaxies. Cowley's work used a version of the GALFORM model that had previously been carefully calibrated on an extensive set of observational data, resulting in a fully predictive ab initio theoretical model of galaxy formation that is able to predict galaxy luminosities from both stars and dust.

In his thesis, Cowley used the GALFORM model to further our understanding of a number of important aspects of galaxy evolution at far-infrared and sub-millimetre wavelengths. First, he constructed simulated images of the sky at sub-millimetre wavelengths including the effects of galaxy clustering as well as the angular resolution of the telescope and instrumental noise, and extracted sources from these images in the same way as is done when analysing observational data. He found that for the relatively poor angular resolution of the single dish telescopes used for most surveys at these wavelengths up to now, blending of sources by the telescope beam has a significant effect on the measured number counts of sources, in agreement with observational results using interferometers.

Additionally, Cowley discovered a new and previously unsuspected effect in galaxy clustering called 'blending bias', whereby the blending of multiple galaxies into a single source by the telescope beam causes an artificial boost in the angular clustering of the observed sources compared to that of the real galaxies. Since the observed clustering of galaxies is used to infer the typical masses of the dark matter halos containing these galaxies, this blending bias could result in halo masses being greatly overestimated.

He then used the GALFORM model to predict the contribution to the far-infrared emission from galaxies in halos of different masses, finding that over a wide range of redshifts, the far-infrared emissivity should be dominated by halos of mass around $10^{12} \, M_\odot$, as a result of the competing effects of gas cooling and feedback on the efficiency with which baryons in halos are converted into stars. He shows that, as a consequence, the model predicts a power spectrum for angular fluctuations in the cosmic infrared background in remarkably good agreement with that measured by the *Herschel Space Telescope*. This agreement provides important support for current theoretical ideas about galaxy formation.

Finally, Cowley coupled GALFORM with a more detailed radiative transfer model for stellar and dust emission from galaxies to make predictions for what

high-redshift galaxies should be seen in future deep imaging surveys with the *James Webb Space Telescope*. This type of theoretical modelling will be crucial for interpreting observations from future telescopes in terms of physical processes in galaxy formation.

Durham, UK   Cedric Lacey
July 2017   Carlton Baugh
                                                                                           Shaun Cole

Abstract

The Cosmic Infra-red Background (CIB) has a similar energy density to that at UV/optical wavelengths, implying that a significant proportion of star formation over the history of the Universe has been obscured by dust. We investigate the dusty star-forming galaxies responsible for the CIB. For this, we use the latest version of the hierarchical galaxy formation model, GALFORM, which is embedded within the Λ cold dark matter cosmological paradigm. To compute far-IR (FIR) galaxy spectral energy distributions (SEDs), a simple model for the absorption and re-emission of radiation by interstellar dust is used. Recent interferometric observations have highlighted that the coarse angular resolution of single-dish telescopes used for FIR imaging surveys can blend the emission of multiple galaxies into a single source. Simulating single-dish imaging, we show that the model can reproduce the difference between the observed interferometric and single-dish derived sub-millimetre number counts. Additionally, we make the prediction that the blended galaxies are typically physically unassociated. The simulated imaging is also used to show that the clustering of single-dish sources is boosted with respect to the underlying galaxy population. We term this 'blending bias', and show that it can lead to the dark matter halo masses of FIR-bright galaxies being significantly overestimated. These galaxies are predicted to reside in halos of masses $10^{11.5} - 10^{12}\ h^{-1}\ \mathrm{M}_\odot$, and taking the blending bias into account yields a good level of agreement with halo masses inferred from observed clustering. This is also the halo mass range that produces the bulk of the CIB, as it represents the halos most conducive to star formation in the model. We show that the model can predict the observed average FIR SEDs of main sequence galaxies to a remarkable degree of accuracy over the redshift range $0.5 \lesssim z \lesssim 4$. However, a shortcoming of the simple dust model is that it cannot make accurate predictions for mid-IR emission. To address this, we couple GALFORM with the spectrophotometric code grasil to compute UV-to-mm SEDs, which we use to make predictions for future *James Webb Space Telescope* galaxy surveys.

Introductory Preface

This thesis is concerned with the theoretical study of galaxy formation, and in particular the titular dusty star-forming galaxies. We investigate this galaxy population using predictions from a physical model of galaxy formation, GALFORM. This model has been developed over the past couple of decades by researchers at Durham University's Institute for Computational Cosmology.

Throughout, the GALFORM model is embedded within the current standard cosmological paradigm, commonly referred to as ΛCDM. This assumes that the Universe is mostly composed of: (i) a somewhat mysterious cosmological constant, Λ, which is thought to be the driving force behind the observed accelerating expansion of the Universe, and (ii) cold dark matter (CDM), a somewhat mysterious fundamental particle, yet to be directly detected, that only interacts through the force of gravity. Some of the observational and theoretical threads underpinning the emergence of ΛCDM as the generally accepted paradigm are discussed in more detail in Sect. 1.1. In ΛCDM, minute density fluctuations that exist shortly after the Big Bang can grow over time due to the attractive force of gravity. These density fluctuations are observed as hot (overdense) or cold (underdense) spots in the cosmic microwave background (CMB) and are thought to be an artifact of quantum mechanical fluctuations following a period of exponential expansion in the very early Universe, commonly referred to as inflation. At some point in their evolution they become so massive that they will undergo gravitational collapse, forming an approximately ellipsoidal object referred to as a dark matter halo. In ΛCDM these halos grow hierarchically, small halos form first and grow larger through merging with others. It is within these dark matter halos that galaxies are thought to form and evolve.

Galaxy formation is an extremely complex phenomenon, which involves the interplay of many physical processes over a wide range of spatial and temporal scales. To directly simulate all of these in a cosmologically significant volume of the Universe and over a cosmologically significant period of time, is currently beyond the ability of the world's most powerful supercomputers. Additionally, our knowledge of the complicated physics involved in many of the processes at play is still significantly lacking. In order to make the problem more tractable, a technique

known as semi-analytical modelling has been developed over the last 30 years. In the semi-analytical framework, the multitude of physical processes important for galaxy formation (e.g. gas cooling, star formation, black hole growth) are described by simplified equations which are easily solvable with a modern computer. This allows these models to make testable predictions for the galaxy population, offering a physical interpretation for corresponding observations, whilst uncertainties introduced by the simplified descriptions of the physics involved are accounted for by calibrating the model against pre-determined observational data. GALFORM, which was one of the first fully realised semi-analytical models, and the semi-analytical technique are discussed in more detail in Chap. 2, and some further historical background to galaxy formation theory is given in Sect. 1.2.

The infrared portion of the electromagnetic spectrum comprises radiation with wavelengths in the range $1 - 1000$ μm. Observational infrared astronomy dates back to the 1800s and a famous set of experiments by the British scientist and composer, William Herschel. A brief history of this field is given in Sect. 1.3, however it wasn't until the late 1900s that its importance in the context of galaxy formation and evolution was fully realised. The extragalactic background light (EBL) is formed of the radiation emitted from all galaxies over the history of the Universe. Observations of the infrared portion of the EBL, the cosmic infrared background (CIB), taken in the 1990s found that it had a similar energy density to that at ultraviolet/optical wavelengths, where the EBL is composed of the emission of radiation directly from stars. This implied that a significant proportion of star formation over the history of the Universe has taken place in 'dusty' galaxies, in which the light from young, hot stars is absorbed by interstellar dust and then re-emitted at longer infrared wavelengths. Here, in order to account for the dust absorption and emission within these dusty star-forming galaxies, GALFORM is combined with a model that computes the radiative transfer of stellar light through the interstellar dust. Further details of this dust model are given in Sect. 2.9.

Shortly after the discovery of the CIB, a new population of galaxies, detected by their bright emission at 850 μm and thus commonly referred to as sub-millimetre galaxies (SMGs), was found. Whilst these bright galaxies are only responsible for a relatively small proportion of the CIB (the majority comes from galaxies too faint to be detected individually at these wavelengths) they are important to study in their own right as they appear to be amongst the most highly star-forming objects in the Universe. They also represent a significant challenge for galaxy formation models to reproduce. The GALFORM model used throughout this thesis can only do so by assuming that the distribution of the masses of stars forming in these galaxies is significantly different to that of stars forming in the Milky Way today. This assumption is discussed further in Sect. 2.10.

A significant difficulty associated with observing SMGs is the coarse angular resolution of the single-dish telescope used in these surveys. This is due to the fact that the angular resolution, the angular separation at which a lens can distinguish two separate objects, θ, of a telescope can be approximated by $\theta \approx \lambda/D$, where λ is the wavelength of the incident radiation and D is the diameter of the telescope. Thus for a telescope with a primary mirror of a given diameter (building larger

telescopes are complicated, expensive and time-consuming procedures) the longer the wavelength of the radiation under observation, the poorer the angular resolution. Interferometers can achieve a much greater angular resolution by combining the data from a number of small telescopes spread out over a certain area. This mimics the resolving power of a single-dish telescope that has an area equal to the configuration of the smaller telescopes used. However, a downside is that interferometers take much longer to survey a given portion of the sky, as such their use has been limited mostly to targeted follow-up of bright sources previously identified in single-dish imaging. Such survey strategies with these high-resolution interferometers have shown that single-dish telescopes had blended together the light from multiple fainter galaxies into what was previously considered to be a single SMG. This has implications for the observed abundances of these galaxies.

In Chap. 3, 'simulated observations' are made from the raw predictions of the GALFORM model. This procedure accounts for the coarse angular resolution of the single-dish telescope used to make many of the observations to which the predictions of the model are compared. The results here show good agreement with available observational data from both single-dish and interferometric surveys. Moreover, the model predicts that the emission from multiple galaxies is being blended together due to random line-of-sight projection, rather than a physical association between the galaxies involved.

The clustering of these SMGs, and the fainter galaxies responsible for the bulk of the EBL at infrared wavelengths, is investigated in Chap. 4. This measures how these objects group together, by comparing their spatial distribution to that of a randomly distributed set of points. Due to the way structures develop in ΛCDM, dark matter halos of different masses exhibit different clustering strengths. Thus, measuring the clustering of a galaxy population can give information regarding the masses of the dark matter halos the galaxies inhabit. This can in turn constrain potential evolutionary pathways for the population, based on how their host halos evolve in ΛCDM simulations, and can thus constrain the physical processes that shape the galaxy population in question. We find that the clustering of the sources identified in the simulated imaging developed in the previous Chapter is much stronger than that intrinsic to the underling galaxies in the model. This is a key result of this thesis, and is termed 'blending bias', a novel analytical derivation of this phenomenon is given in Appendix A. Blending bias implies that the dark matter halo masses inferred from single-dish imaging surveys of SMGs has previously been significantly overestimated (by roughly an order of magnitude), this has severe consequences for our understanding of this galaxy population. The GALFORM model predicts that SMGs inhabit halos in the mass range $\sim 10^{11.5} - 10^{12}$ $M_{\odot}$, though once the blending bias is taken into account this is consistent with observational studies which had placed them in halos ten times more massive. Halos in this $\sim 10^{11.5} - 10^{12}$ $M_{\odot}$ mass range also host the fainter galaxies responsible for producing the bulk of the predicted CIB. This feature arises as this mass range is the most conducive for star formation in the model, as a result of the interplay between the various physical prescriptions in the model.

We investigate the far-infrared spectral energy distributions (SEDs) predicted by our model for computing the absorption and emission of stellar radiation by dust in Chap. 5. These spectral energy distributions describe the emission from each galaxy at a range of wavelengths whereas in earlier chapters we only consider monochromatic predictions. For this we compare the predicted SEDs to some recent observations of the far-infrared SEDs of so-called 'main sequence' galaxies. The 'main sequence' of star-forming galaxies is an observed tight correlation between the stellar mass of a galaxy and its instantaneous star formation rate, on which the majority of galaxies are located and that appears to be in place over much of the history of the Universe. We find remarkable agreement between the observed SEDs and those predicted by the model. This allows us to interpret the measured decrease in the average temperature of the interstellar dust in these main sequence galaxies over the history of the Universe. We find that this is produced in the model by star formation on the main sequence being more 'bursty' at earlier times, which results in hotter dust.

A shortcoming of the dust model is that it does not accurately predict emission in the mid-infrared portion of the electromagnetic spectrum. We mitigate this in Chap. 6, where we couple GALFORM with a more sophisticated code for modelling dust absorption and emission, GRASIL, though the increased accuracy gained here comes with a significant increase in computation time. This coupling is used to make predictions for the *James Webb Space Telescope*, which is scheduled to be launched in October 2018 and is expected to significantly advance our understanding of the early Universe. These predictions mark an exciting opportunity to test the GALFORM model used throughout this thesis against observations of galaxies at an unprecedentedly early stage of the Universe's history.

This thesis forms the basis of a number of interesting avenues for further research, these are thoroughly discussed in Chap. 7.

Groningen, The Netherlands   Dr. William Cowley

Acknowledgements

Declaration

The work in presented in this thesis is based on research carried out between 2012 and 2016 at the Institute for Computational Cosmology, Durham University, whilst the author was a research student under the supervision of Prof. Cedric Lacey, Prof. Carlton Baugh and Prof. Shaun Cole. No part of this thesis has been submitted elsewhere for any other degree or qualification.

Chapter 3 has been published in the form of an article in the Monthly Notices of the Royal Astronomical Society:

Simulated observations of sub-millimetre galaxies: the impact of single-dish resolution and field variance Cowley, W.I., Lacey C.G., Baugh, C.M., Cole S., 2015, MNRAS, 446, 1784.

DOI: https://doi.org/10.1093/mnras/stu2179

Chapter 4 has been published in the form of an article in the Monthly Notices of the Royal Astronomical Society:

The clustering evolution of dusty star-forming galaxies Cowley, W.I., Lacey C.G., Baugh, C.M., Cole S., 2016, MNRAS, 461, 1621,

DOI: https://doi.org/10.1093/mnras/stw1069

with the exception of Sect. 4.4.4, which has been published as:

Blending bias impacts the host halo masses derived from a cross correlation analysis of bright sub-millimetre galaxies Cowley, W.I., Lacey C.G., Baugh, C.M., Cole S., Wilkinson A., 2017c, MNRAS, 469, 3396

DOI: https://doi.org/10.1093/mnras/stx928

Chapter 5 and Appendices B and C have been published in the form of an article in the Monthly Notices of the Royal Astronomical Society:

The far infra-red SEDs of main sequence and starburst galaxies Cowley, W.I., Béthermin M., Lagos C.d.P., Lacey C.G., Baugh, C.M., Cole S., 2017b, MNRAS, 467, 1231

Chapter 6 has been submitted as an article to the Monthly Notices of the Royal Astronomical Society:

Predictions for deep galaxy surveys with JWST from ΛCDM Cowley, W.I., Baugh, C.M., Cole S., Frenk C.S., Lacey C.G., 2017a, MNRAS (submitted), pre-print https://arxiv.org/abs/1702.02146.

Appendix D summarises the author's contribution to an article published in the Astrophysical Journal:

The SCUBA-2 Cosmology Legacy Survey: ALMA resolves the bright end of the sub-millimetre number counts Simpson, J.M., Smail I., Swinbank A.M., Chapman S.C., Geach J.E., Ivison R.J., Thomson A.P., and 16 additional co-authors, 2015, ApJ, 807, 128

All figures in this thesis have been created by the author, with the exception of Figs. 2.3 and 2.4 which are taken from Lacey et al. (2016), where they are Fig. 3 and Fig. C21 respectively. The author would like to thank Cedric Lacey for allowing them to be reproduced here.

A unified multiwavelength model of galaxy formation Lacey C.G., Baugh C.M., Frenk C.S., Benson A.J., Bower R.G., Cole S., Gonzalez-Perez V., Helly J.C., Lagos, C.d.P., Mitchell P.D., 2016, MNRAS, 462, 3854

Contents

Acronyms

AB	Absolute Bolometric (magnitude system)
ALESS	ALMA LESS
ALMA	Atacama Large Millimetre/sub-millimetre Array
APEX	Atacama Pathfinder EXperiment
ASTE	Atamaca Sub-millimetre Telescope Experiment
AZTEC	AZtronomical Thermal Emission Camera
BAO	Baryon Acoustic Oscillations
CDM	Cold Dark Matter
CIB	Cosmic Infra-red Background
COBE	COsmic Background Explorer
EBL	Extragalactic Background Light
ECDFS	Extended *Chandra* Deep Field - South
FIRAS	Far Infrared Absolute Spectrophotometer
FWHM	Full Width Half Maximum
HOD	Halo Occupation Distribution
IMF	Initial Mass Function
IRAC	Infrared Array Camera
IRAS	Infrared Astronomy Satellite
ISM	Interstellar Medium
ISO	Infrared Space Observatory
JCMT	James Clerk Maxwell Telescope
JWST	James Webb Space Telescope
LABOCA	Large Apex BOlometer Camera Array
LESS	LABOCA ECDFS Sub-millimetre Survey
MACHOs	Massive Astrophysical Compact Halo Objects
MBB	Modified Black Body
MS	Main Sequence
NFW	Navarro, Frenk & White
PAH	Polycyclic Aromatic Hydrocarbon
PdBI	Plateau de Bure Interferometer

S2CLS	SCUBA-2 Cosmology Legacy Survey
SB	Starburst
SCUBA	Super Common User Bolometer Array
SDSS	Sloan Digital Sky Survey
SED	Spectral Energy Distribution
SFR	Star Formation Rate
SHADES	SCUBA HAlf Degree Extragalactic Survey
SMBH	Supermassive Black Hole
SMG	Sub-millimetre Galaxy
SNe	Supernovae
SPT	South Pole Telescope
UKIDS-UDS	UKIRT Infra-red Deep Sky Survey—Ultra Deep Survey
UKIRT	United Kingdom Infrared Telescope
VISTA	Visible and Infrared Survey Telescope for Astronomy
WMAP	Wilkinson Microwave Anisotropy Probe

List of Figures

List of Tables

Chapter 1
Introduction

Galaxies were observed as early as the late 1700s when Messier compiled a list of
~100 bright nebulae (Messier 1781). However, it wasn't until the work of Hubble in
the 1920s who showed the extragalactic nature of the spiral nebulae (Hubble 1925),
that it was understood they were in fact galaxies in their own right. This thesis is
concerned with the study of galaxy formation theory, which is embedded within the
Λ cold dark matter (ΛCDM) cosmological paradigm. In particular, it is concerned
with predictions from galaxy formation models at infra-red wavelengths.

Here, a brief historical overview of the ΛCDM paradigm and galaxy formation
theory is given in Sects. 1.1 and 1.2 respectively. In Sect. 1.3 we offer a brief overview
of infra-red extragalactic astronomy. In doing so we introduce some of the issues that
form the main areas of research addressed in this thesis, the structure of which is
outlined in Sect. 1.4.

1.1 The ΛCDM Paradigm

The currently accepted cosmological paradigm, and the one assumed throughout this
thesis, is referred to as ΛCDM. The present matter energy density of the Universe is
dominated by a cosmological constant, or vacuum energy, (Λ) and cold dark matter
(CDM), which is non-baryonic matter with negligible thermal velocity at decoupling.
These two main components comprise approximately 70 and 26% respectively of the
present matter energy density. The remaining 4% is composed of baryons, 'ordinary'
matter from which the subject of the thesis, galaxies, have formed over the history
of the Universe. Radiation (i.e. photons) contribute a negligible proportion of the
matter energy density today.

There are many observational threads of evidence that support this cosmo-
logical model. These include cosmic microwave background (CMB) experiments
(e.g. Penzias and Wilson 1965; Smoot et al. 1992; Dunkley et al. 2009) combined
with independent measures of the expansion history of the Universe such as lumi-
nosity distances from observations of Type 1a Supernovae (e.g. Riess et al. 1998;

Perlmutter et al. 1999) and the angular-diameter distances obtained from baryon acoustic oscillations measured in the clustering of galaxies (e.g. Cole et al. 2005; Eisenstein et al. 2005). Complementary datasets such as the abundances of light elements produced in Big Bang nucleosynthesis (e.g. Alpher et al. 1948; Wagoner 1973; Cyburt et al. 2008), gravitational weak lensing (e.g. Massey et al. 2007) and the abundances of galaxy clusters (e.g. Vikhlinin et al. 2009; Rozo et al. 2010) also support this paradigm.

The idea of a dark matter component (i.e. undetected through electromagnetic absorption or emission) in the Universe can be traced back to the 1930s and the work of Oort (1932) and Zwicky (1933) who analysed the orbits of stars in the Milky Way and of galaxies in the Coma cluster respectively. They found that the mass inferred from the observed light was insufficient to explain the velocities of the bound orbits.

These measurements were complemented decades later by Vera Rubin and collaborators who, through measuring the rotation curves of galaxies, found that they were remarkably flat out to large radii (e.g. Rubin et al. 1980) i.e. $v_{circ} \approx$ constant. This is in stark contrast to the expectation for a mass distribution that traces the light i.e. $v_{circ} \propto r^{-1/2}$, hinting that there was a significant amount of unobserved mass surrounding galactic discs (such that $M \propto r$).

The consensus now is that this 'dark' matter is non-baryonic. This is supported by observations of the CMB (e.g. Smoot et al. 1992; Komatsu et al. 2011; Planck Collaboration et al. 2016), the abundances of light elements (e.g. Steigman 2007; Cyburt et al. 2008), and the lack of detections of micro-lensing signatures from Massive Astrophysical Compact Halo Objects (MACHOs), a potential baryonic explanation for non-luminous mass in which it is formed of compact baryonic objects such as black holes or white dwarf stars (e.g. Alcock et al. 2000).

The CMB was discovered by Penzias and Wilson (1965) and is a thermal relic of the early Universe from the epoch of recombination, which occurred $\sim 3.8 \times 10^5$ yr after a hot big bang, at which point the Universe had cooled sufficiently to allow protons and electrons to combine into neutral atoms allowing photons to propagate freely. Prior to this baryons and photons had been tightly coupled via Compton scattering. The CMB is generally isotropic and can be extremely well described by a blackbody with a temperature of $\sim$3 K. There are, however, small deviations $\pm 30\,\mu$K from this uniform temperature, thought to be seeded by quantum fluctuations in the pre-inflationary Universe (e.g. Guth 1981; Linde 1986). The angular distribution of these anisotropies provide strong constraints on the cosmological paradigm. On small scales (large wavenumber ℓ) baryon acoustic oscillations (BAO) of the pre-recombination baryon-photon fluid imprint oscillatory peaks onto the CMB power spectrum. The position and amplitude of these peaks give strong constraints on the cosmological paradigm. Baryonic perturbations can oscillate as acoustic waves in the coupled baryon-photon fluid once they are within the horizon and prior to decoupling. The position of the first peak ($\ell \approx 200$) corresponds to a perturbation that has undergone a single compression at decoupling (the position of this peak also gives a strong indication that the Universe is flat i.e. $\Omega = 1$), and the minima at $\ell \approx 400$ to a perturbation that has undergone a single compression-rarefaction episode. The relative amplitude of these peaks gives a strong constraint on the matter-energy

density of baryons at the epoch of recombination. Computations of the abundances of light elements (e.g. deuterium, ^{3}He) produced in big bang nucleosynthesis ($\sim$100 s after the big bang) show that they are sensitive to the baryon density (here expressed in units of the critical density), Ω_b, (e.g. Alpher et al. 1948; Wagoner 1973; Cyburt et al. 2008) with subsequent measurements of interstellar absorption lines (e.g. Linsky et al. 2006) providing lower bounds on the primordial abundances. These are consistent with the independent measurements of the baryon fraction from the CMB, which indicate $\Omega_b \ll \Omega_m$.

Though a particle candidate for non-baryonic dark matter remains currently undetected, N-body simulations (e.g. Davis et al. 1985; Frenk 1986) indicate that it should be 'cold' i.e. it has a negligible thermal velocity at decoupling (or equivalently a high $\gtrsim 1$ GeV rest mass if it is produced in thermal equilibrium). These simulations begin with particles arranged with Gaussian density fluctuations, or equivalently random phases in Fourier space, and according to a primordial power spectrum, $P(k) \propto k^{n_s}$. A spectral index of $n_s = 1$ results in a scale-free Universe (e.g. Harrison 1970; Zeldovich 1972). Recent measurements suggest $n_s \approx 0.95$ (e.g. Komatsu et al. 2011), consistent with simple inflationary models. The primordial power spectrum is first multiplied by a transfer function $T(k, t)$ (e.g. Bardeen et al. 1986), which describes the damping processes that can affect density perturbations on different scales once they fall within the horizon of the expanding Universe. These are primarily: (i) free-streaming damping, which produces an exponential cut-off in the power spectrum as collisionless particles with random motions can move from an overdensity to an underdensity (and vice-versa) damping the growth of perturbations below some scale related to the velocity of the particle, and thus its rest mass if produced in thermal equilibrium (this is generally unimportant for CDM which has a negligible velocity at decoupling but is important for hot dark matter cosmologies in which dark matter particles are still relativistic at decoupling) and; (ii) the Mézáros (1974) effect in which the growth of density perturbations is damped if the Universe is radiation dominated, this causes the spectral index to transition from $n = n_s$ on large scales to $n = n_s - 3$ on small scales, with the transition scale relating to the size of the horizon at matter-radiation equality. These early dark matter only simulations indicated that the observed two-point correlation function of galaxies [allowing for the possibility that galaxies could be 'biased' tracers of the mass (e.g. Kaiser 1986), meaning that they form in locations corresponding to high-density peaks in the initial Gaussian density field] could be better reproduced by cold dark matter. Hot dark matter simulations formed structures too late (i.e. after observed galaxies were thought to exist) and significantly overpredicted the resulting galaxy clustering. However, CDM simulations at this stage assumed $\Omega_m \approx 1$, and did not produce enough structure on large scales (e.g. Davis et al. 1992). An alternative which solved this problem through introducing a non-zero cosmological constant had been proposed (e.g. Efstathiou et al. 1990), before observational evidence became available confirming that this was the case (e.g. Riess et al. 1998; Perlmutter et al. 1999). This resulted in ΛCDM becoming accepted as the cosmological paradigm, a status which it retains today, and thus forms the starting point for simulations of galaxy formation.

1.2 Galaxy Formation Theory

The formation of galaxies is thought to be seeded by quantum fluctuations in the pre-inflationary Universe that ultimately appear as anisotropies in the CMB. The linear growth of these perturbations is theoretically well understood, however once their evolution becomes non-linear it is significantly more complicated to understand. However, empirical arguments (e.g. Sheth et al. 2001) complemented by N-body simulations (e.g. Springel et al. 2005) mean that the evolution of these primordial density perturbations to the present day is generally well understood. The final stage in the evolution of these perturbations is a dark matter halo, within which it is assumed that galaxies form. Once the density of a perturbation reaches some threshold such that it has sufficient mass for its self-gravity to overcome the expansion of the Universe, the dark matter will undergo dissipationless gravitational collapse (e.g. Gunn and Gott 1972). The result of this collapse is a dark matter halo, an approximately stable ellipsoidal object supported against further collapse due to its own self-gravity by the random motions of its constituent particles. In the ΛCDM paradigm structure formation proceeds hierarchically. Smaller halos form earlier and grow over time through further accretion of dark matter and mergers with other halos. Halos acquire angular momentum as they form due to tidal torques from the anisotropic distribution of structure. This angular momentum is then imparted to infalling gas, which is important for the formation of galactic discs as will be discussed later.

It is thought that the primordial baryon-photon fluid should trace the dark matter distribution. However, after recombination photons are decoupled so the baryons will fall into the potential wells provided by the dark matter perturbations. Prior to this the pressure support of the photons had prevented baryonic collapse. The resulting oscillations this produced are the BAO and their effect on the matter power spectrum can be observed in the CMB (e.g. Planck Collaboration et al. 2016) and the clustering of galaxies (e.g. Cole et al. 2005; Eisenstein et al. 2005). However, unlike the dark matter the baryon collapse is not collisionless. This means that the baryonic gas will become compressed as it falls into the potential well and is stopped by the baryonic structure that has already collapsed. This results in accretion shocks that will propagate outwards and heat the collapsing gas.

It is then thought that the gas will cool, radiating energy away through a variety of atomic and molecular processes. As it does so the gas will sink further into the potential well of the halo. Once the density of the cooled gas exceeds that of the dark matter halo it can become self-gravitating and collapse under its own self-gravity. This process forms a galactic disc, if the angular momentum of the gas is conserved during the collapse (e.g. Fall and Efstathiou 1980; Mo et al. 1998).

Once the gas has cooled and collapsed into a disc it is thought to be available for star formation. In the Milky-Way, and other nearby galaxies that can be observed with high spatial resolution, star formation is seen to take place within giant molecular clouds, which are thought to form from instabilities during the gravitational collapse of the gas. The exact process through which individual stars form is extremely complex (e.g. McKee and Ostriker 2007), so on galactic scales our understanding is

generally restricted to empirical laws such as the Kennicutt-Schmidt law (Schmidt 1959; Kennicutt 1998) that relates the surface density of star formation to the surface density of gas $\dot{\Sigma}_\star \propto \Sigma_{gas}^N$ where $N \sim 1 - 2$. More recent observations suggest that N is actually a function of the local molecular gas fraction within a galaxy, rather than a constant (e.g. Bigiel et al. 2008).

The idea of baryonic condensation as described above within the context of large-scale structure formation was first developed by White and Rees (1978), who combined the gravitational collapse framework of Press and Schechter (1974) with a simple prescription for gas cooling and star formation. However, this and other early galaxy formation models (e.g. White and Frenk 1991) suffered from the 'overcooling problem'. These models predicted many more faint galaxies than were observed. The halo mass function is an intrinsically different shape to the observed galaxy luminosity function, with a much steeper low mass slope. So models that result in an approximately constant mass-to-light ratio would struggle to reproduce both simultaneously.

The idea of an energy input from star formation has been around since the 1970s (e.g. Larson 1974). When stellar feedback is implemented into galaxy formation models such that this energy input inhibits further star formation it typically enables them to better reproduce the faint end of the observed galaxy luminosity function (e.g. Cole et al. 1994). The rationale is that the energy released from a solar mass of stars [formed with a solar neighbourhood stellar initial mass function (IMF)] is typically $\sim 10^{49}$ erg, if this energy can couple to the surrounding interstellar medium (ISM) then it is feasible that it could affect further star formation.

Benson et al. (2003) investigated various ways in which this could be done and concluded that at least two mechanisms were required to reproduce the observed galaxy luminosity function. A satisfactory fit to the faint end slope was produced through a 'disc reheating' method (Cole et al. 2000). This assumed that some of the energy available heated the surrounding gas, causing it to rise back out of the potential well and making it unavailable for star formation, as long as the energy input into some gas mass, M_{gas}, was comparable to the binding energy of the gas, $M_{gas} V_{disc}^2 / 2$. However, this came at the cost of exacerbating the overabundance of bright galaxies in the model. This was due to the reheating creating large reservoirs of hot gas which would cool later, when the energy available was insufficient to overcome the binding energy of the now more massive galaxy/halo. Benson et al. argued that this could be overcome by 'superwind' feedback, in which gas was ejected completely from the dark matter halo, however, the efficiency required was extremely high, indicating that the energy required was unlikely to come from star formation alone.

An alternative means of energy input to the ISM from the accretion of gas onto the supermassive black hole (SMBH) thought to reside at the centre of most galaxies was presented as means of feedback (e.g. Croton et al. 2006; Bower et al. 2006, though see also Silk and Rees 1998 for an earlier discussion). This came with the additional benefit of allowing these models to produce a 'red sequence' of bright galaxies, a locus on the galaxy colour-magnitude diagram that suggests the star formation in these galaxies has been 'quenched', and the black hole mass-bulge mass relation (e.g. Magorrian et al. 1998). Today it is generally accepted that the interplay of

these physical processes: gas cooling, star formation and feedback shape the key observables of the galaxy population.

Galaxies do not exist in isolation, and indeed processes such galaxy interactions/mergers and environmental effects such as ram-pressure stripping also play a role in shaping the rich diversity observed in galaxies. These will be discussed in more detail in Chap. 2, where we describe how the physical processes important for galaxy formation are implemented within the galaxy formation model used throughout this thesis.

1.3   Infra-red Extragalactic Astronomy

The infra-red radiation of the Sun was first discovered in 1800 by William Herschel, in a famous experiment in which he measured the temperature increase in mercury thermometers placed beyond the red end of an optical spectrum of the Sun (Herschel 1800a, b, c, d). Today's bolometers operate on the same principle. Incident radiation causes a temperature rise in some conducting material which can be measured through the resulting change in resistance.

Due to significant atmospheric absorption of radiation at far-IR wavelengths (due mainly to water vapour), many observations at these wavelengths have to performed from space. The first dedicated survey satellite at these wavelengths, the *Infra-Red Astronomy Satellite* (*IRAS*, Neugebauer et al. 1984) was launched in January 1983 and, over the proceeding 10 months, mapped $\sim$96% of the sky in bands centred on 12, 25, 60 and 100 μm, detecting $\sim$250, 000 sources. The resulting catalogue had an impact on many branches of astronomy, particularly in the study of star-forming regions and the realisation that galaxies can emit significant amounts of radiation in the infra-red. This infra-red emission represents the re-emission of stellar radiation following absorption by interstellar dust. The success of *IRAS* led to the launch of the *Infra-red Space Observatory* (*ISO*, Kessler et al. 1996) in November 1995 which was designed to follow up many of the sources identified by its predecessor with greater sensitivity and angular resolution. This mission was followed by the *Spitzer Space Telescope* (Werner et al. 2004) in August 2003, and the *Herschel Space Observatory* (Pilbratt et al. 2010) in May 2009. *Herschel* was designed to study longer wavelengths than the previous missions, with bands centred on 100, 170, 250, 350 and 500 μm, and thus probe the peak of the far-IR galaxy spectral energy distribution at high ($z \sim 2 - 3$ redshifts).

Complementing these space-based telescopes, observatories on the ground have probed the far-IR making using of various atmospheric transmission windows. The most notable of these perhaps is the 15 m diameter James Clerk Maxwell Telescope (JCMT) which was constructed on the summit of Mauna Kea, Hawaii in the mid 1990s. This coincided with improved bolometer technology which led to the Super Common-User Bolometer Array Camera (SCUBA), designed to operate within atmospheric windows at 450 and 850 μm. The SCUBA/JCMT configuration, assisted by one of the world's driest observing sites, allowed observations at these

wavelengths to be made ∼1000 times more rapidly than was previously possible. This led to the exciting discovery of the high-redshift galaxy population now commonly referred to as sub-millimetre galaxies (SMGs e.g. Smail et al. 1997; Barger et al. 1998; Hughes et al. 1998). More recently, ground-based advances have been made with interferometers such as the Atacama Large Millimetre/sub-millimetre Array (ALMA), which have approximately an order of magnitude greater resolution than offered by JCMT.

The emission from galaxies formed throughout cosmic history appears as a diffuse cosmological background. The infra-red (1 μm–1 mm) part of this background, the cosmic infra-red background (CIB), was first discovered in the 1990s by the Far Infra-Red Absolute Spectrophotometer (FIRAS) on board the *COsmic Background Explorer* (*COBE*) (e.g. Puget et al. 1996; Fixsen et al. 1998) and is mostly produced by the re-emission of stellar radiation by interstellar dust, with small ($\lesssim$5%) contributions from dust heated by UV/X-ray emission from AGN (e.g. Almaini et al. 1999; Silva et al. 2004) and stellar emission that has been redshifted into the mid-IR (see Chap. 6 for GALFORM predictions at mid-IR wavelengths). The CIB has a similar energy density to the background at UV/optical wavelengths (e.g. Hauser and Dwek 2001; Dole et al. 2006). This implies that most of the star formation over the history of the Universe has been obscured by interstellar dust, formed from metals produced by stellar nucleosynthesis which are then ejected by stellar winds and supernovae into the ISM, where a fraction (∼30–50%, e.g. Draine and Li 2007) condense into grains. Understanding the nature of the galaxies that contribute to the CIB is therefore critical to a full understanding of galaxy formation.

A key difficulty with observations at these long wavelengths is confusion noise, caused by the coarse angular resolution [∼20 arcsec full width at half maximum (FWHM)] of the telescopes and the high surface density of detectable objects. This means that only the brightest objects can be resolved above the confusion background of overlapping unresolved sources from imaging at these wavelengths (e.g. Hogg 2001; Nguyen et al. 2010).

Whilst these individually resolved galaxies (SMGs) do not form the dominant contribution to the CIB (e.g. Oliver et al. 2010), they are important to study in their own right as they appear to be amongst the most highly star-forming objects in the Universe. Their FIR/sub-mm emission is thought to be powered by star formation, leading to inferred star formation rates (SFRs) of $\gtrsim$ 100 $M_\odot$ yr^{-1} (e.g. Smail et al. 2002; Michałowski et al. 2010; Swinbank et al. 2014). They are typically characterised by their number counts i.e. the number per unit area on the sky at some apparent brightness/flux, the simplest measure of a galaxy population available from an imaging survey. However, it was found upon targeted follow-up of some sub-millimetre sources identified in single-dish imaging surveys with interferometers (e.g. Plateau de Bure Interferometer—PdBI, Atacama Large Millimetre/sub-millimetre Array—ALMA) that offer an order of magnitude greater angular resolution that these sources are actually composed of multiple fainter sources (e.g. Wang et al. 2011; Hodge et al. 2013), with the resulting effect on the 850 μm number counts being discussed in Karim et al. (2013) and Simpson et al. (2015). This is issue will be discussed in more detail in Chap. 3.

Characterising the multi-wavelength properties of these galaxies, necessary for a determination of their physical properties, is again challenging. This is in part due to the single-dish resolution spreading the sub-mm emission over a large solid angle making it difficult to pinpoint the precise origin to an accuracy of greater than $\pm 2''$. This means that it is not possible to assign counterparts at other wavelengths with complete certainty (e.g. Ivison et al. 2002; Biggs et al. 2011). Typically this was done by matching the sub-mm emission to radio 1.4 GHz, making use of the FIR-radio correlation. This is a well established relation (e.g. de Jong et al. 1985; Helou et al. 1985), thought to be produced as the star formation responsible for the UV emission which is absorbed by interstellar dust and re-emitted at FIR/sub-mm wavelengths also produces synchrotron emission when the some of the stars go supernova. However, this probabilistic counterpart matching can be avoided now to a certain extent with interferometers offering the resolution required for a more precise determination of the position of the sub-mm emission, without recourse to other wavelengths. Once this has been done however, many SMGs remain undetected at other wavelengths.

Sub-mm bands are subject to a negative k-correction (e.g. Oke and Sandage 1968) as the shape of a galaxy's spectral energy distribution (SED) at these wavelengths (the Rayleigh-Jeans tail of the dust emission) approximates a power law that decreases with increasing wavelength. This means that for a fixed bolometric luminosity and observer-frame wavelength, shifting the galaxy to higher redshifts means that the SED is sampled at a shorter rest-frame wavelength, where it is intrinsically brighter. This largely cancels out the effect of dimming due to the increasing luminosity distance, meaning that the observed flux of an SMG is roughly constant over $z \sim 1 - 10$ (e.g. Blain and Longair 1993; Blain et al. 2002). This is not the case at other positions on the SED, where the bands can be subject to a positive k-correction, which means the become increasingly fainter with increasing redshift. It also may be the case that the interstellar dust responsible for the observed emission at 850 µm absorbs much of the emission at shorter (UV/optical) wavelengths, further compounding the problem. However, despite these difficulties, over the last decade or so a picture has emerged, generally through fitting model SEDs to the available observed photometry, that these galaxies are a high-redshift population with a median redshift of $z_{50} \approx 2.5$ (e.g. Chapman et al. 2005; Simpson et al. 2014) of high stellar mass $M_\star \gtrsim 10^{11} \, h^{-1} \, \mathrm{M}_\odot$ (e.g. Michałowski et al. 2010; Hainline et al. 2011; Michałowski et al. 2012b) dust-rich galaxies (e.g. Swinbank et al. 2014) undergoing extreme star formation (e.g. Smail et al. 2002; Michałowski et al. 2010; Swinbank et al. 2014).

Despite the difficulties associated with deriving their physical properties, galaxies that emit at FIR/sub-mm wavelengths can provide an important observational probe of galaxy formation and evolution. Observations suggest that the majority of star formation over the history of the Universe has taken place on the so called 'main sequence' (MS) of star-forming galaxies, a tight correlation between star formation rate (SFR) and stellar mass ($M_\star$) that is observed out to $z \sim 4$, with a 1σ scatter of ~ 0.3 dex (e.g. Elbaz et al. 2007; Karim et al. 2011; Rodighiero et al. 2011; for theoretical predictions see Mitchell et al. 2014). This is thought to result from the regulation of star formation through the interplay of gas cooling and feedback processes. Galaxies that have elevated SFRs (typically by factors $\sim 4 - 10$) relative

to this main sequence are often referred to as starburst galaxies (SB) in observational studies. In contrast to the secular processes thought to drive star formation on the MS, the elevated SFRs in SB galaxies are thought to be triggered by some dynamical process such as a galaxy merger or disc instability.

The SFRs in these galaxies are usually inferred from a combination of UV and IR photometry. Observationally, an integrated FIR SED for the whole galaxy is required to give an indication of the luminosity from young stars that is absorbed and re-emitted by the dust. However, this can be complicated by the confusion issues discussed above. Stellar population evolutionary synthesis models (e.g. Bruzual and Charlot 2003; Maraston 2005) are then required to convert the infra-red luminosity derived from the observed photometry into a star formation rate (e.g. Kennicutt 1998). However, these must make assumptions about the star formation history of the galaxy and the IMF. Various models for dust emission and galaxy SEDs, that sometimes include evolutionary synthesis and make further assumptions about the composition and geometry of the dust, can be fitted to the observed FIR/sub-mm photometry (e.g. Silva et al. 1998; Draine and Li 2007; da Cunha et al. 2008) to give estimates for physical dust properties such as the dust temperature (T_d) and dust mass (M_{dust}).

At $z \sim 2$, MS galaxies have SFRs high enough to be resolved in *Herschel* imaging only if they have large stellar masses ($M_\star \gtrsim 10^{10.5} \, h^{-1} \, M_\odot$) whereas SB galaxies with stellar mass approximately an order of magnitude lower can still be resolved (e.g. Gruppioni et al. 2013). For less massive MS galaxies and galaxies at higher redshifts, as it is not possible to individually resolve a complete sample of galaxies, stacking techniques have been developed to overcome the source confusion and derive average FIR/sub-mm SEDs for different samples (e.g. Magdis et al. 2012; Magnelli et al. 2014; Santini et al. 2014; Béthermin et al. 2015). These studies typically begin with a stellar mass selected sample and stack available FIR/sub-mm imaging at the positions of these galaxies, in bins of stellar mass and redshift. Thus FIR/sub-mm emission can give an insight into star formation at high redshift. We discuss this in more detail, and compare the results of our theoretical model to observational results from such a stacking technique (Béthermin et al. 2015) in Chap. 5.

The use of gravitational lensing (e.g. Smail et al. 1997; Knudsen et al. 2008; Chen et al. 2013), stacking techniques (e.g. Béthermin et al. 2012; Geach et al. 2013) and interferometers (e.g. Hatsukade et al. 2013; Carniani et al. 2015) has to some extent circumvented the problem of confusion noise and allowed up to ~80% of the CIB to be statistically resolved into galaxies.

Placing these FIR/sub-mm galaxies into a consistent evolutionary context has proven challenging. In terms of resolved sub-mm galaxies (SMGs) it is still unclear what physical mechanisms trigger the prodigious SFRs inferred from observations. In the local Universe ($z \lesssim 0.3$), the majority of ultra-luminous galaxies ($L_{IR} > 10^{12} \, L_\odot$) are gas-rich major mergers (e.g. Sanders and Mirabel 1996), but whether this is the dominant triggering mechanism at the peak of the SMG redshift distribution ($z \sim 2.5$, e.g. Chapman et al. 2005; Simpson et al. 2014) remains unclear. Some dynamical studies using emission lines from the ^{12}CO molecule (e.g. Tacconi et al. 2008) and

H α (e.g. Menéndez-Delmestre et al. 2013) have concluded that they see evidence of merger activity, though the sample sizes are small ($\lesssim$ 10 objects). The merger scenario is also supported by some recent morphological studies (e.g. Chen et al. 2015). However, examples of rotationally supported discs have also been found (e.g. Swinbank et al. 2011) suggesting the star formation was triggered by secular disc instabilities. Simulations suggest that the contraction of gas towards the centre of a galaxy, fuelling the star formation which results in the enhanced FIR/sub-mm emission (e.g. Mihos and Hernquist 1996; Chakrabarti et al. 2008; Narayanan et al. 2010), could also cause accretion onto a supermassive black hole, with the resulting quasar phase quenching the star formation (e.g. Di Matteo et al. 2005), possibly resulting in compact quiescent galaxies (e.g. Toft et al. 2014). It has been speculated that SMGs could then evolve onto the scaling relations observed for massive local elliptical galaxies, based on simple arguments involving the timescale of the burst and the ageing of the stellar population (e.g. Lilly et al. 1999; Swinbank et al. 2006; Simpson et al. 2014), and assuming that most of the stellar mass at $z = 0$ is put in place during the 'SMG phase'. However, González et al. (2011) present an alternative scenario in which SMGs evolve into galaxies with stellar mass $\sim 10^{11}$ h^{-1} $M_\odot$ at $z = 0$, with the SMG phase accounting for little of this stellar mass.

A strong constraint on the evolution of a galaxy population can come from observational measurements of its clustering, which provides information regarding the masses of the dark matter halos the galaxies inhabit. Growth of structure arguments based on results from N-body simulations can then be used to infer the present day host halo mass of the galaxy's descendants (e.g. Fakhouri et al. 2010), which can then be compared to the halo masses inferred from the observed clustering of local galaxy populations. However, the spread in the host halo masses of SMG descendants could be significant ($\sim$2 dex, Sect. 4.3.3). For bright SMGs a further difficulty is their relatively sparse number density, meaning large area surveys are required to yield sufficient galaxy pairs for the correlation function to be estimated robustly. An observational study of the clustering of SMGs was performed by Hickox et al. (2012), who ameliorated the problem of small numbers of SMGs by using a cross-correlation (Blake et al. 2006) with a more abundant *Spitzer* Infra-Red Array Camera (IRAC)-selected galaxy population to find that $z = 1 - 3$ SMGs in the LESS[1] source catalogue (Weiß et al. 2009) have a correlation length of $r_0 = 7.7^{+1.8}_{-2.3}$ h^{-1} Mpc. This result was consistent with an earlier study by Blain et al. (2004) who used measured redshift separations of pairs of SMGs in a number of small SCUBA fields to estimate a correlation length of 6.9 ± 2.1 h^{-1} Mpc. Hickox et al. inferred a host halo mass of $M_{\mathrm{halo}} = 10^{12.8^{+0.3}_{-0.5}}$ h^{-1} $M_\odot$ from their observed clustering and used the median growth rate of haloes from Fakhouri et al. (2010) to suggest descendent halo masses consistent with those of local $\sim$2 − 3 $L_\star$ galaxies.

More recently, Wilkinson et al. (2017) performed a similar analysis. However, these authors were able to improve upon earlier work by making the first measurements of the clustering of SMGs as a function of redshift, owing to the greater number

---

[1]Large APEX (Atacama Pathfinder EXperiment) Bolometer Camera Array (LABOCA) Extended *Chandra* Deep Field South (ECDFS) Sub-millimetre Survey.

of SMGs detected as part of the SCUBA-2 (Super Common User Bolometer Array 2, Holland et al. 2013) Cosmology Legacy Survey (S2CLS, Geach et al. 2013) in the UKIDS-UDS[2] field. Cross-correlating their SMG sample with a more numerous K-band selected galaxy population, Wilkinson et al. estimated that the halo masses of SMGs ranged from $M_{\rm halo} \sim 10^{13} \, h^{-1} \, {\rm M_\odot}$ at $z \gtrsim 2$ to $M_{\rm halo} \sim 10^{11} \, h^{-1} \, {\rm M_\odot}$ for $1 < z < 2$. Wilkinson et al. concluded that the $z \gtrsim 2$ SMG population could evolve into local $\sim 2 - 3 \, L_\star$ galaxies.

However, the work of Blain et al., Hickox et al. and Wilkinson et al. is based on source catalogues derived from single-dish imaging surveys with a typical angular resolution of $\sim$20 arcsec FWHM. As mentioned earlier, targeted observations with interferometers have revealed that many sub-mm sources identified from single-dish imaging are in fact composed of multiple fainter galaxies. Until recently it has been unclear exactly what impact this has on measurements of the clustering of SMGs. This is discussed in more detail in Sect. 4.4.1.

Information about the clustering, and therefore host halo masses, of the unresolved FIR/sub-mm galaxies which contribute to the bulk of the CIB, can be obtained from the angular power spectrum of CIB anisotropies. The first attempts to measure this, by Peacock et al. (2000) for the Hubble Deep Field observed by SCUBA at 850 µm, and Lagache and Puget (2000) for a 0.25 deg² *ISO* field at 170 µm, found at best only a tentative signal above the shot noise. More recently studies have been able to measure a clear signal (e.g. Viero et al. 2009; Amblard et al. 2011; Viero et al. 2013; Planck Collaboration et al. 2014), though significant modelling is required in order to interpret these results in terms of halo masses. The Viero et al. (2013) and Plank Collaboration studies infer a typical halo mass for galaxies that dominate the CIB power spectrum of $10^{11.95\pm0.5} \, h^{-1} \, {\rm M_\odot}$ and $10^{12.43\pm0.1} \, h^{-1} \, {\rm M_\odot}$ respectively, making various assumptions such as the form of the relationship between galaxy luminosity and halo mass being independent of redshift, and that this relationship is the same for both central and satellite galaxies.

Historically, hierarchical models of galaxy formation have struggled to simultaneously match the number density of FIR/sub-mm galaxies at high redshift ($z \gtrsim 2$) and the present day ($z = 0$) luminosity function in optical and near-IR bands (e.g. Granato et al. 2000). It follows that theoretical predictions for the clustering, and host halo masses, of such galaxies are few. van Kampen et al. (2005) present a number of predictions for the angular clustering of SMGs under different scenarios. However, these models are phenomenological and do not attempt to predict the sub-mm flux of galaxies in a self-consistent manner. Baugh et al. (2005) presented a version of GALFORM, the Durham semi-analytic model of hierarchical galaxy formation (Cole et al. 2000), which successfully reproduced the observed number counts and redshift distribution of SMGs at 850 µm as well as the $z = 0$ luminosity function in optical and near infra-red bands. In order to do so these authors found it necessary to dramatically increase the importance of high redshift galaxy mergers relative to earlier versions of GALFORM (e.g. Cole et al. 2000; Benson et al. 2003) through the

---

[2]United Kingdom Infra-red Telescope (UKIRT) Infra-red Deep Sky Survey—Ultra Deep Survey.

introduction of a top-heavy IMF in starburst galaxies. In this instance sub-mm flux was calculated by combining GALFORM with the radiative transfer code GRASIL (Silva et al. 1998; Granato et al. 2000), see also Chap. 6 and Appendix C.

Predictions of the SMG clustering in this model were presented in Almeida et al. (2011), who found a correlation length of 5.6 ± 0.9 h^{-1} Mpc for galaxies with $S_{850\,\mu m} > 5$ mJy at $z = 2$, in good agreement with the subsequent observational measurement of Hickox et al. (2012). The angular power spectrum of CIB anisotropies predicted by this model was presented in Kim et al. (2012) and was within a factor of ~ 3 of the measurements of the Planck Collaboration (XVIII, 2011). The clustering evolution of FIR/sub-mm galaxies will be investigated further in Chap. 4.

1.4 Thesis Outline

In this thesis we use the Durham semi-analytical galaxy formation model, GALFORM, to explore a number of issues raised in the previous Section.

In Chap. 2 we describe the way the physical processes important for galaxy formation and evolution are implemented within the model. We also describe the model we assume for calculating the absorption and emission of stellar radiation by interstellar dust.

In Chap. 3 we investigate the effect of the coarse angular resolution of the single-dish beam used to make far-IR imaging surveys on the observed galaxy number counts, finding that the model can reproduce the difference between observed single-dish and interferometric number counts. We also make the prediction that the galaxies which have had their sub-mm emission blended together by the single-dish beam are physically unassociated.

In Chap. 4 we show the range of dark matter halos masses galaxies selected at FIR/sub-mm wavelengths occupy, and how this evolves, within the model. We find that in the model these occupy a relatively narrow range of halos masses, $10^{11.5} - 10^{12}$ h^{-1} $M_{\odot}$, over a broad range of redshifts ($0.5 \lesssim z \lesssim 5$), which represents the halo mass range most conducive to star formation due to the interplay of gas cooling, and supernova and AGN feedback processes. We also extend our investigation of the effect of the finite size of a single-dish beam on FIR/sub-mm observations and find that this induces a 'blending bias' in the angular clustering of sub-mm sources, implying that the host halo masses of sub-mm galaxies inferred from observations have been significantly overestimated.

In Chap. 5 we compare the entire dust emission SED computed by the model to observations of the stacked FIR/sub-mm SEDs of main sequence and starburst galaxies. We find remarkable agreement between observations and the model's predictions for galaxies on the star-forming main sequence and propose an explanation for the increase in the average dust temperature of galaxies on the star forming main sequence with redshift.

In Chap. 6 we integrate GALFORM with the more physically complete radiative transfer code GRASIL (Silva et al. 1998) allowing us to compute UV-to-mm galaxy

SEDs accounting for the absorption and emission of stellar radiation by interstellar dust. We use this to make predictions for future deep galaxy surveys with the *James Webb Space Telescope* (*JWST*) where at high-redshift the rest-frame UV/optical wavelengths will be redshifted into the mid-IR.

Finally, we summarise and discuss the main findings of this thesis as well as briefly presenting ideas for future work in Chap. 7.

Chapter 2
The Galaxy Formation Model

> *Right now, Will, you're 'tooling up', you're learning* FORTRAN
> *and* PYTHON*; it's like you're in the bike shop deciding if you*
> *want the blue shorts or the red shorts. Here,* GALFORM *is the*
> *bike, and once you get on it, it will take you places.*
>
> — Carlos S. Frenk, 2012

2.1 Introduction

The galaxy formation model used throughout this thesis is the Durham semi-analytical model GALFORM. It was first introduced in Cole et al. (2000), and builds on ideas outlined earlier by White and Rees (1978), White and Frenk (1991), Lacey and Silk (1991), Cole (1991) and Cole et al. (1994). There have been subsequent revisions since its initial inception (e.g. Benson et al. 2003; Baugh et al. 2005; Bower et al. 2006; Lagos et al. 2011; Gonzalez-Perez et al. 2014). However, this thesis is mostly concerned with the latest version presented in Lacey et al. (2016). This particular version is used as it can simultaneously reproduce optical luminosity functions at $z = 0$, rest-frame near-IR luminosity functions for $z < 3$, rest-frame UV luminosity functions for $z \sim 3 - 6$ and, importantly for this thesis, the number counts and redshift distributions of galaxies selected at sub-mm wavelengths (see Chap. 3). Some features of this version of GALFORM are discussed in more detail in Sect. 2.10.

In GALFORM, galaxy formation is modelled ab initio,[1] beginning with a specified cosmology and a linear power spectrum of density fluctuations, and ending with predicted galaxy properties at different redshifts. The process is treated in two stages. First the gravitational collapse of dark matter into halos is modelled, either through a Monte Carlo technique based on the extended Press-Schechter formalism

---

[1] In the sense that the calculation begins at high redshift ($z \gtrsim 20$).

(e.g. Parkinson et al. 2008), or through *N*-body simulation (e.g. Springel et al. 2005). Structure formation proceeds *hierarchically*. Smaller halos form earlier and coalesce, or merge, over time to create larger structures. Once the merging history of the halos is specified, baryonic physics is added as a set of equations which are designed to describe the complicated (and in many cases poorly understood) physical processes important for galaxy formation. In GALFORM these equations essentially track the exchange of mass and metals between different baryonic reservoirs: (i) hot halo gas, (ii) cold gas in galaxies, (iii) stars, (iv) ejected gas outside the virial radius and (v) supermassive black holes. The cold gas and stars can either be in a disc component formed through the cooling of hot gas, or in a bulge/spheroid, formed through a dynamical process, either a galaxy merger or a disc instability. Stellar luminosities are computed through combining the star formation and metal enrichment history of a galaxy predicted by the model with a stellar evolutionary population synthesis model (e.g. Tinsley 1972; Bruzual and Charlot 2003; Maraston 2005). The absorption and re-emission of stellar radiation by interstellar dust is computed assuming a simple geometry for the distribution of dust. The equations of radiative transfer are then solved for this geometry and global energy balance arguments are applied for the dust emission, assuming the dust emits as a modified blackbody.

The simplified nature of the equations used to describe the complex physical processes involved introduces a number of free parameters into the semi-analytical approach. These are calibrated by comparing the predictions of the model against a pre-determined set of observational data. This calibration is typically done manually [though see Bower et al. (2010), Henriques et al. (2013) and Rodrigues et al. (2017) for examples of statistical techniques being used to automate this procedure for semi-analytical models] and provides a strong constraint on the available parameter space, as discussed in Lacey et al. (2016). The GALFORM strategy is to calibrate the model against directly observed quantities (e.g. luminosities) rather than physical properties that have been inferred from observations (e.g. stellar mass). Inferring properties such as stellar mass from observed broadband photometry requires making assumptions about the star formation and chemical enrichment history of a galaxy, which may not be consistent with those predicted by GALFORM. In addition, as the model adopts multiple IMFs (see Sects. 2.8.2 and 2.10) the only consistent way to compare with observations is with directly observed properties, as inferred properties such as stellar mass are sensitive to the assumed IMF, which is no longer unique. For more details of the semi-analytical method, see the reviews by Baugh (2006) and Benson (2010).

The semi-analytical approach to galaxy formation on a cosmological scale is complementary to recent gas-dynamical cosmological simulations (e.g. Vogelsberger et al. 2014; Schaye et al. 2015) and the two methods can produce similar results when calibrated in a similar manner (e.g. Guo et al. 2016). Gas-dynamical simulations compute the distribution and dynamics of the gas with fewer approximations and can thus make detailed predictions regarding the internal structure of galaxies and their halos, rather than just global properties. However, they are still limited in terms of the volumes that can currently be simulated in this way. For example the reference EAGLE (Evolution and Assembly of GaLaxies and their Environments) simulation (e.g. Schaye et al. 2015; Crain et al. 2015) took ∼4.5 million CPU hours

to simulate a $\sim 100^3$ Mpc^3 volume to $z = 0$, whereas the GALFORM model used throughout this thesis takes only ~ 140 CPU hours to populate a $\sim 700^3$ Mpc^3 volume with galaxies.[2] Thus, semi-analytical models are more suited to interpreting large observational galaxy surveys, or populations of rare objects, and can be used to explore the parameter space relevant for reproducing various observational datasets. Gas-dynamical simulations are also forced to use 'sub-grid' models to describe many of the physical processes important for galaxy formation such as star formation and supernova feedback, that occur on scales currently below the resolution of the simulation. These are analogous to what is done in semi-analytical models, albeit on smaller spatial scales, and thus current cosmological simulations also require that free parameters in the sub-grid model are calibrated against observational data.

Just as advances in our understanding of how physical processes such as supernova and AGN feedback affect galaxy formation and evolution, gleaned from studies of semi-analytical models (e.g. Cole et al. 2000; Benson et al. 2003; Bower et al. 2006; Croton et al. 2006), have informed the current gas-dynamical simulations, it is expected that further study of the predictions that these simulations can make will inform future semi-analytical models.

2.2 Hierarchical Structure Formation

In GALFORM the baryonic processes are implemented within a halo merger tree, the merging history of a dark matter halo from its progenitors down to the redshift of interest. Once this is specified, various halo properties, and their evolution, can be incorporated into the galaxy formation calculation.

These halo merger trees can be constructed in two ways: (i) from a Monte Carlo technique following the extended Press-Schechter formalism (e.g. Bond et al. 1991; Lacey and Cole 1993; Cole et al. 2000; Parkinson et al. 2008) or; (ii) calculated directly from N-body dark matter only simulations (e.g. Helly et al. 2003; Springel et al. 2005; Bower et al. 2006; Guo et al. 2013; Jiang et al. 2014).

The former has the advantages that it is computationally cheap and straightforward to implement, and that it can give the desired halo mass resolution on the fly. However, throughout this thesis we utilise merger trees constructed from N-body simulations, as this allows the spatial distribution of galaxies, and hence their clustering, to be predicted directly (see Chap. 4). It also allows environmental effects to be studied. However, it comes with the drawback that, as the halo mass resolution of the simulation is fixed, a decreasing fraction of the mass in halos is followed with increasing redshift, which may have implications for predictions of integrated properties of the galaxy population e.g. the comoving cosmic star formation rate density,

---

[2]We note that the CPU time quoted for GALFORM does not include the time taken to run the initial dark matter only N-body simulation, which is typically much shorter that the time required to run a gas-dynamical simulation, and that both of these quoted times will have some dependence on various details of the codes, the machine used and the mass resolution of the simulations.

$\rho_{\mathrm{SFR}}(z)$. Here we briefly describe the construction of these merger trees, and how the halo properties relevant for galaxy formation are calculated. For more details see Merson et al. (2013), Jiang et al. (2014) and Lacey et al. (2016).

An N-body simulation is performed from high redshift (e.g. $z = 127$) to the present day with particle data being output at pre-specified 'snapshots' during the calculation. The initial conditions of the simulation are set by the desired cosmological parameters, halo mass resolution and cosmological volume. Groups of dark matter particles are identified in the simulation snapshots using the *Friends-of-Friends* algorithm (FOF; Davis et al. 1985). The SUBFIND algorithm (Springel et al. 2001) is then used to identify self-bound locally over-dense sub-groups within the FOF groups. Descendant sub-groups are then identified in subsequent snapshots as the sub-groups containing the largest fraction of the most bound particles from a sub-group in the previous snapshot.

It is possible for the SUBFIND algorithm to temporarily 'lose' a sub-group. This can happen if a small sub-group temporarily falls below the resolution limit (usually set to 20 dark matter particles) or if it passes close to the centre of its host halo. Whilst this is not necessarily a problem for the construction of halo merger trees, it is problematic for codes such as GALFORM that require the descendent of a sub-group to be present at the next snapshot, and mass conservation. To avoid this, if a sub-group is identified at some snapshot, i, but lost at snapshot $i + 1$, then 'orphaned' sub-groups (sub-groups with no immediate progenitors) are investigated at subsequent snapshots $(i + 2, i + 3\ldots)$. These orphans are then identified as the descendants of the 'lost' sub-group at snapshot i if they contain some fraction of its most bound particles and no other progenitors are identified. Once this is done, interpolated sub-groups are inserted at each snapshot for which a sub-group was missing.

The sub-groups are then organised into a hierarchy of halos within their FOF group i.e. halos, sub-halos, sub-sub-halos etc. depending on their mass and if they fall within the half-mass radius of a more massive sub-group. There is also a condition of mass loss such that when a halo falls within another, more massive halo, the two will only be considered to have merged (i.e. the less massive halo becomes a sub-halo) once the smaller halo has lost $\sim 25\%$ of its infall mass. For the GALFORM calculation it is also assumed that once a halo merges within another and becomes a sub-halo, it is subsequently always defined as a sub-halo even if its orbit puts it outside of the virial radius of its host at some later time. In GALFORM it is assumed that once a central galaxy becomes a satellite in a larger host halo, all of its hot gas is stripped away, which can only be done once. These halo fragmentation episodes are identified by searching for satellite sub-groups which split off from their host halo to become an independent halo at a subsequent snapshot. In this case the sub-halo is re-merged. Once these post-processing steps are carried out the merger tree is specified.

When halos form they are assumed to have a virial radius

$$r_{\mathrm{vir}} = [3M_{\mathrm{halo}}/4\pi\Delta_{\mathrm{vir}}\bar{\rho}]^{1/3}, \qquad (2.2.1)$$

where M_{halo} is the halo mass (the sum of the mass of all the sub-groups + diffuse mass), $\bar{\rho}$ is the mean cosmological density at that redshift and the overdensity Δ_{vir} is

calculated from the spherical top-hat collapse model (e.g. Eke et al. 1996). The dark matter halos are assumed to have a mass density profile of the Navarro, Frenk and White (NFW) form (Navarro et al. 1997)

$$\rho_{DM}(r) \propto \frac{1}{(r/r_s)(1 + r/r_s)^2}, \tag{2.2.2}$$

where r_s is the scale radius, related to the virial radius by the concentration parameter $c_{NFW} = r_{vir}/r_s$, which is calculated according to the prescription of Navarro et al. (1997). In the simulation halos can grow through merger events and accretion. A halo formation event is defined when a halo has grown by a factor of 2 since the previous such event. At this point, the density profiles are updated with a new value of c_{NFW}, and the virial velocity $V_{vir} = (G\,M_{vir}/r_{vir})^{1/2}$ is recalculated. These quantities are assumed to remain constant between each halo formation event.

Halos acquire angular momentum from tidal torques during their formation. At each halo formation event a value of the dimensionless spin parameter, λ_H, where

$$\lambda_H = \frac{J_{halo}|E_{halo}|^{1/2}}{G\,M_{halo}^{5/2}}, \tag{2.2.3}$$

is drawn from a lognormal distribution with a median $\lambda_{H,med} = 0.039$ and dispersion $\sigma_{\lambda_H} = 0.53$ in $\ln \lambda_H$ (e.g. Cole and Lacey 1996). Only the magnitude of the angular momentum is recorded.

2.3 Gas Cooling in Halos

In GALFORM, it is assumed that dark matter halos in the merger trees each accrete their 'fair' share of baryons i.e. $(\Omega_b/\Omega_M)M_{halo}$, where M_{halo} is the total (dark matter + baryonic) mass of the halo. Gas falling into halos is shock heated and subsequently must dissipate its energy through radiative cooling in order to condense into a galaxy and form stars. It is assumed that upon infall into the dark matter halo gas is shock heated to the virial temperature

$$T_{vir} = (\mu\,m_H/2\,k_B)V_{vir}^2, \tag{2.3.4}$$

where m_H is the mass of a hydrogen atom, μ is the mean molecular weight and $V_{vir} = (G\,M_{vir}/r_{vir})^{1/2}$ is the virial velocity i.e. circular velocity at the virial radius. The gas is then assumed to settle into a spherically symmetric density distribution given by

$$\rho_{hot}(r) \propto \frac{1}{r_c^2 + r^2}, \tag{2.3.5}$$

with a core radius $r_c = 0.1 r_{vir}$. The thermal energy per unit volume of the gas at radius, r, is given by

$$U_{hot}(r) = \frac{3}{2} \frac{k_B T_{vir}}{\mu \, m_H} \rho_{hot}(r). \tag{2.3.6}$$

This hot gas then loses its thermal energy through atomic processes, such that its cooling luminosity per unit volume is

$$\mathcal{L}_{cool}(r) = \rho_{hot}^2(r) \Lambda(T_{vir}, Z_{hot}), \tag{2.3.7}$$

where $\Lambda(T, Z)$ is the temperature and metallicity dependent cooling function tabulated by Sutherland and Dopita (1993). The local cooling rate, $\tau_{cool}(r)$, is simply the ratio of the two such that

$$\tau_{cool}(r) = \frac{3}{2} \frac{k_B}{\mu \, m_H} \frac{T_{vir}}{\rho_{hot}(r) \Lambda(T_{vir, Z_{hot}})}. \tag{2.3.8}$$

As the cooling time is inversely proportional to the density of the gas, denser gas at smaller radii will cool faster than that at larger radii. It is therefore possible to define a cooling radius r_{cool} as the radius at which the cooling time of the gas is equal to the age of the halo i.e. $\tau_{cool}(r_{cool}) = t - t_{form}$. This will propagate outwards with time and any gas at $r < r_{cool}$ is assumed to have cooled.

However, this in itself is not sufficient for the formation of a galactic disc as the cooled gas has to have had time to fall to the centre of the dark matter potential well. For a given mass distribution the free-fall time for a test particle to fall to the centre of the potential well, t_{ff}, is given by

$$t_{ff}(r) = \int_0^r \left[\int_r^{r''} -\frac{G \, M(r')}{r'^2} \mathrm{d}r' \right]^{-1/2} \mathrm{d}r''. \tag{2.3.9}$$

This can be inverted to find the free-fall radius, r_{ff}, such that $t_{ff}(r_{ff}) = t - t_{form}$, where a particle at $r < r_{ff}$ will have had sufficient time to fall to the centre of the potential well.

In GALFORM, the radius relevant for whether gas has become available to be accreted onto a galactic disc is defined by the minimum of these two radii i.e. $r_{acc} = \min[r_{ff}, r_{cool}]$. Gas needs to have had both sufficient time to cool and sufficient time to have fallen to the centre of the halo potential well for it to have been accreted onto the galactic disc. In a given time step in the calculation, r_{acc} is calculated at the beginning and end of the time step i.e. at t_{i-1} and t_i. The amount of gas that is said to have cooled, $\dot{M}_{acc} \Delta t$, is set to be equal to the mass of gas in the spherical shell defined by $\Delta r_{acc} = r_{acc}(t_i) - r_{acc}(t_{i-1})$. This defines the accretion rate of hot gas onto the cold gas disc, $\dot{M}_{acc}$ which is used later, and can be written as

$$\dot{M}_{acc} = 4\pi \, \rho_{hot}(r_{acc}) \, r_{acc}^2 \, \dot{r}_{acc}. \tag{2.3.10}$$

It is assumed that throughout the cooling process the angular momentum of the gas is conserved, such that it forms a disc. The rotational velocity of the hot gas, $V_{\rm rot}$, is assumed to be independent of radius and is given by

$$V_{\rm rot} = A(c_{\rm NFW})\lambda_{\rm H} V_{\rm vir}, \tag{2.3.11}$$

where $A(c_{\rm NFW})$ is a dimensionless coefficient with a weak dependence on the NFW concentration, determined such that the total specific angular momentum of the gas is in agreement with that of the dark matter, which is determined by the spin parameter $\lambda_{\rm H}$ (Cole et al. 2000). This results in a change in angular momentum of the cold gas due to accretion from the hot halo gas given by

$$\dot{j}_{\rm cold} = \pi^2 \, V_{\rm rot} \, \rho_{\rm hot}(r_{\rm acc}) \, r_{\rm acc}^3 \, \dot{r}_{\rm acc}. \tag{2.3.12}$$

It is assumed that the angular momentum of the disc is aligned with that of the halo.

2.4   Star Formation

Once the gas has cooled and been accreted onto the disc it becomes available for star formation. GALFORM has two modes of star formation, one that occurs in the galactic disc and one in a starburst, in a newly formed galactic bulge/spheroid.

2.4.1   Star Formation in the Disc

In the disc the SFR is calculated according to the empirical Blitz and Rosolowsky (2006) relation, based on the fraction of molecular gas in the disc, $f_{\rm mol}$, which depends on the midplane gas pressure, P, at each radius in the disc

$$R_{\rm mol} = \frac{\Sigma_{\rm mol}}{\Sigma_{\rm atom}} = \left(\frac{P}{P_0}\right)^{\alpha_{\rm P}}, \tag{2.4.13}$$

where $R_{\rm mol}$ is the ratio of molecular to atomic gas, $\alpha_{\rm P} = 0.8$ and $P_0/k_{\rm B} = 1.7 \times 10^4\,{\rm cm}^{-3}$ K based on the observations of Leroy et al. (2008). The SFR is then assumed to be proportional to the mass of molecular gas, integrated over the whole disc, such that

$$\psi_{\rm disc} = \nu_{\rm SF,quies}\, M_{\rm mol,disc} = \nu_{\rm SF,quies}\, f_{\rm mol}\, M_{\rm cold,disc}, \tag{2.4.14}$$

where $f_{\rm mol} = R_{\rm mol}/(1 + R_{\rm mol})$ and $\nu_{\rm SF,quies} = 0.74\ {\rm Gyr}^{-1}$ (Bigiel et al. 2011). This star formation prescription was first incorporated into GALFORM by Lagos et al. (2011).

2.4.2   Star Formation in Bursts

For star formation in bursts (which occur in a forming bulge/spheroid) it is assumed that $f_{mol} \approx 1$ and the SFR depends on the dynamical timescale of the bulge

$$\psi_{burst} = \nu_{SF,burst}\, M_{cold,burst}, \tag{2.4.15}$$

where $\nu_{SF,burst} = 1/\tau_{\star,burst}$ and

$$\tau_{\star,burst} = \max[f_{dyn}\tau_{dyn,bulge}, \tau_{burst,min}]. \tag{2.4.16}$$

Here $\tau_{dyn,bulge} = r_{bulge}/V_c(r_{bulge})$, where r_{bulge} is the half-mass radius of the bulge, and f_{dyn} and $\tau_{burst,min}$ are model parameters, such that for large dynamical times the SFR timescale scales with the dynamical timescale of the bulge ($f_{dyn} = 20$), but has a floor value ($\tau_{burst,min} = 100$ Myr) when the dynamical timescale of the bulge is short. These parameters are primarily constrained by the observed rest-frame far-UV (1500 Å) luminosity function.

2.5   Feedback Mechanisms

In GALFORM there are three channels of feedback, through which star formation is inhibited.

2.5.1   Supernova Feedback

Supernova explosions inject energy into the ISM and in doing so can remove gas from a galaxy. The energy injection is dominated by massive short-lived stars and so is approximately proportional to the SFR

$$\dot{M}_{eject} = \beta(V_c)\psi. \tag{2.5.17}$$

The 'mass loading' factor $\beta(V_c)$ is parametrised as

$$\beta(V_c) = (V_c/V_{SN})^{-\gamma_{SN}}, \tag{2.5.18}$$

where V_{SN} and γ_{SN} are adjustable parameters and V_c is the circular velocity of the disc (or of the bulge for starbursts) at the half-mass radius. The rationale behind this parametrisation is that for the same SFR (i.e. energy input) less mass should be ejected from deeper potential wells, for which V_c is a proxy. The removal of gas in this manner is assumed to not affect the specific angular momentum of the disc.

The ejected gas accumulates in the ejected mass reservoir of mass M_{res} beyond the virial radius, from which it is returned to the hot gas reservoir within the virial radius, according to

$$\dot{M}_{return} = \alpha_{ret} \frac{M_{res}}{\tau_{dyn,halo}}, \tag{2.5.19}$$

where $\tau_{dyn,halo} = r_{vir}/V_{vir}$ is the halo dynamical time, as first implemented into GALFORM in Bower et al. (2006). The parameters in this supernova feedback model are constrained primarily by requirement of the model to reproduce the faint end of the $z = 0$ galaxy luminosity function, values of $\gamma_{SN} = 3.2$, $V_{SN} = 320$ km s^{-1} and $\alpha_{ret} = 0.64$ are adopted in Lacey et al. (2016).

In Chap. 6 we discuss results from a variant supernova feedback model (Hou et al. 2016), in which a break is introduced into the parametrisation of the mass loading factor and its normalisation is allowed to evolve with redshift.

2.5.2 Photoionisation Heating of the IGM

The IGM is reionized and photo-heated by ionising photons produced by stars and AGN. This inhibits star formation in two ways: (i) the increased IGM pressure inhibits the collapse of gas into dark matter halos and (ii) continued photo-heating of gas inside halos by the ionizing UV background inhibits the cooling of gas. This was implemented into GALFORM by to Benson et al. (2003), assuming that reionization occurs instantaneously at z_{reion}. After this no cooling of gas occurs within halos with $V_c < V_{crit}$. A value of $z_{reion} = 10$ (e.g. Dunkley et al. 2009) is used and $V_{crit} = 30$ km s^{-1}, based on gas-dynamical simulations (e.g. Okamoto et al. 2008). Despite its simplicity this model has been shown to reproduce more detailed treatments quite well (Font et al. 2011).

2.5.3 Supermassive Black Hole Growth and AGN Feedback

The accretion of material onto supermassive black holes (SMBHs) causes huge amounts of energy to be released from the accreting material. In GALFORM SMBHs can grow via three different channels: (i) accretion of gas during a starbust, the cold gas mass accreted onto the black hole is some fraction f_{BH} of the mass of stars formed during the burst; (ii) accretion of gas from the hot halo; (iii) black hole mergers, in which the BH merger happens at the same time as the galaxy merger and mass loss through radiation of energy via gravitational waves is neglected. Black holes are not seeded in the model and are assumed to form after the first starburst event a galaxy experiences. This is a reasonable approximation as the seed mass of a black hole is expected to be a negligible contributor to its final mass (e.g. Malbon et al. 2007).

In GALFORM it is assumed that AGN feedback occurs in a *hot-halo mode*. The energy released by direct accretion of hot gas from the halo powers relativistic jets which deposit thermal energy into the hot gas. An equilibrium is reached such that this input of thermal energy balances the energy losses due to radiative cooling. This occurs as long as: (1) the gas is quasi-hydrostatic, that is that the cooling time is sufficiently long compared to the free-fall time at the cooling radius

$$\tau_{\text{cool}}(r_{\text{cool}})/\tau_{\text{ff}}(r_{\text{cool}}) > 1/\alpha_{\text{cool}}, \tag{2.5.20}$$

where $\alpha_{\text{cool}} \sim 1$ is an adjustable parameter; and (2) the AGN power required to balance the radiative cooling luminosity is below some fraction f_{Edd} of the Eddington luminosity of the SMBH that has mass M_{BH}

$$L_{\text{cool}} < f_{\text{Edd}} L_{\text{Edd}}(M_{\text{BH}}), \tag{2.5.21}$$

where the total cooling luminosity of the gas, L_{cool}, is given by

$$L_{\text{cool}} = \int_{r_{\text{cool}}}^{r_{\text{vir}}} \rho_{\text{hot}}^2(r) \Lambda(T_{\text{vir}}, Z_{\text{hot}}) 4\pi r^2 \mathrm{d}r. \tag{2.5.22}$$

When these criteria are met the black hole is assumed to grow at a rate such that the energy losses of the hot gas through radiative cooling are exactly balanced $\epsilon_{\text{heat}} \dot{M}_{\text{BH}} c^2 = L_{\text{cool}}$, where ϵ_{heat} is an adjustable parameter. This means the cooling rate has effectively been set to zero i.e. $\tau_{\text{cool}} \to \infty$. This prescription for AGN feedback was first implemented into GALFORM by Bower et al. (2006). Values of $f_{\text{Edd}} = 0.01$ and $\epsilon_{\text{heat}} = 0.02$ are adopted in Lacey et al. (2016), as determined by Fanidakis et al. (in preparation) who used observed X-ray luminosity functions and the black hole mass—bulge mass relation to calibrate these parameters.

2.6 Galaxy Mergers and Disc Instabilities

These dynamical processes are the channels of spheroid growth, and thus morphological transformation, in the model.

2.6.1 Galaxy Mergers

Galaxies are classified as *central* galaxies, which sit at the centre of the dark matter potential and *satellite* galaxies which orbit within the dark matter halo. When dark matter halos merge, the central galaxy of the most massive progenitor halo becomes the new central galaxy, while all other galaxies in the new halo are classed as satellites. Once a galaxy becomes a satellite it is instantaneously stripped of all its hot gas

(which is added to the hot gas reservoir of the central galaxy) through ram-pressure stripping and it is assumed that no further gas can cool onto it. Satellite galaxies are also subject to *dynamical friction* (e.g. Chandrasekhar 1943; Binney and Tremaine 1987), the timescale for which is an expression modified from the Chandrasekhar dynamical friction formula to account for the tidal stripping of dark matter from the satellite's halo, obtained through fitting to the results of N-body simulations (Jiang et al. 2008).

$$\tau_{\mathrm{merge}} = \frac{f(\epsilon)}{2C} \frac{M_{\mathrm{cen}}}{M_{\mathrm{sat}}} \frac{1}{\ln(1 + M_{\mathrm{cen}}/M_{\mathrm{sat}})} \left(\frac{r_{\mathrm{circ}}}{r_{\mathrm{vir}}}\right)^{1/2} \tau_{\mathrm{dyn,halo}}. \qquad (2.6.23)$$

Here M_{cen} and M_{sat} are the total dynamical mass, i.e. baryons + dark matter, of the central and satellite galaxies at infall, and ϵ is the circularity of the orbit at infall,[3] and r_{circ} is the radius of this equivalent circular orbit. The constant C, and parameters in the function $f(\epsilon) = a\epsilon^b + c$ are fit by Jiang et al. (2008). A random value for ϵ is drawn for each satellite from the probability distribution for infalling satellite halos as measured by Benson (2005) from cosmological N-body simulations.

The fate of the gas and stellar content following a galaxy merger depends on the ratio of the baryonic mass (cold gas + stars), $M_{\mathrm{b,sat}}$ of the satellite to that of the central $M_{\mathrm{b,cen}}$. Mergers with $M_{\mathrm{b,sat}}/M_{\mathrm{b,cen}} > f_{\mathrm{ellip}}$ are classed as major mergers. It is assumed that the stellar discs are destroyed and all of the stars in both galaxies form a new stellar spheroid, whilst all of the cold gas collapses into the spheroid. Other mergers are classed as minor. In minor mergers, stars from the satellite galaxy are added to the spheroid of the central galaxy, but cold gas is added to the gaseous disc of the central, without changing its specific angular momentum.

Additionally, mergers with $M_{\mathrm{b,sat}}/M_{\mathrm{b,cen}} > f_{\mathrm{burst}}$ trigger starbursts, in which all of the cold gas from the merging galaxies is transferred to the spheroid. The parameters f_{ellip} and f_{burst} satisfy $f_{\mathrm{burst}} \leq f_{\mathrm{ellip}} < 1$. Numerical simulations of isolated mergers suggest $f_{\mathrm{ellip}} \approx 0.3$ and $f_{\mathrm{burst}} \approx 0.1$ (e.g. Mihos and Hernquist 1994; Barnes 1998; Hopkins et al. 2009).

2.6.2 Disc Instabilities

If a disc becomes sufficiently massive that its self-gravity is dominant, then it would be unstable to small perturbations by minor satellites or dark matter substructures.

Analytical arguments based on idealized descriptions of rotating discs can show that perturbations to the surface density of the disc can generate a mode that leads

---

[3]This is defined as the ratio of the orbital angular momentum to that of a circular orbit of the same energy in the same potential.

to a rotating, elliptical deformation of the whole disc[4] (e.g. Kalnajs 1972; Binney and Tremaine 1987), referred to as the bar mode due to the similarity between this deformation and bars observed in disc galaxies. This can be thought of generally in terms of the ratio of kinetic energy in random motion (Π, which acts to stabilise the disc) to rotational kinetic energy, K. For example, Ostriker and Peebles (1973) find that their simulated discs were stable to bar formation if $\Pi/K \gtrsim 5$.

Based on the N-body simulations of Efstathiou et al. (1982), in GALFORM it is assumed that discs are dynamically unstable to bar formation (i.e. perturbations would result in the growth of a bar mode) if

$$F_{\text{disc}} \equiv \frac{V_{\text{c}}(r_{\text{disc}})}{(1.68G\,M_{\text{disc}}/r_{\text{disc}})^{1/2}} < F_{\text{stab}}, \qquad (2.6.24)$$

where M_{disc} is the total disc mass (stars + gas), r_{disc} is the disc half-mass radius and F_{stab} is a parameter approximately equal to unity. Efstathiou et al. derived $F_{\text{stab}} \approx 1.1$ for purely stellar discs embedded within a variety of dark matter halos,[5] whereas Christodoulou et al. (1995) found that the stability criterion for purely gaseous discs was a bit lower, $F_{\text{stab}} \approx 0.9$. If $F_{\text{disc}} < F_{\text{stab}}$ then it is assumed that the disc forms a bar which subsequently evolves into a spheroid (e.g. Combes 2000). This condition is tested at every timestep in the calculation, as cooled gas is continually being accreted (in the absence of AGN feedback) onto the disc from the hot halo component, and expelled by supernova feedback. It is assumed that the evolution from bar to spheroid occurs instantaneously (though in reality it is likely that this will take at least several disc dynamical times), and that a disc instability triggers a starburst.

2.7   Galaxy Sizes

The size of a disc is basically determined by the angular momentum of the halo gas from which it formed. In GALFORM, the size of the disc is solved for by assuming conservation of angular momentum and centrifugal equilibrium.

As the gas condenses to form a galaxy at the centre of a dark matter halo, it will exert a gravitational force on the dark matter halo, causing dark matter to contract. As long as this process occurs sufficiently slowly the adiabatic invariant, the pseudo-specific angular momentum of a particle in the halo, $r V_{\text{H}}(r)$, will be conserved. Applying this result to spherical shells of matter the final and initial radii of the shell, r, and, r_0, respectively can be related by

$$r_0 V_{\text{cH}}^0(r_0) = r\,V_{\text{cH}}(r), \qquad (2.7.25)$$

---

[4]Note that here we are concerned with the global stability of the disc i.e. perturbations with wavelengths comparable to the size of the disc, rather than local (in)stability where the wavelength of perturbation is much smaller than the disc and the Toomre (1964) criterion can be derived.

[5]This is important as the halo helps to stabilise the disc.

where $V_{cH}(r)$ and $V_{cH}^0(r_0)$ are the final and initial halo circular velocities. The circular velocity of the halo is then

$$V_{cH}^2(r) = G[M_H(r) + M_D(r) + M_B(r)]/r, \tag{2.7.26}$$

where $M_D(r)$ and $M_B(r)$ are the masses of the disc and the bulge within radius r respectively. Combining the above equations gives

$$r_0 M_H^0(r_0) = r[f_H M_H^0(r_0) + M_D(r) + M_B(r)], \tag{2.7.27}$$

where $1 - f_H$ is the fraction of the total halo mass that forms the central galaxy. This relates, for the relevant mass profiles, the final radius of a halo shell to its initial radius.

The disc is assumed to have an exponential surface density profile

$$\Sigma_D(r) = \frac{M_D}{2\pi h_D} \exp(-r/h_D), \tag{2.7.28}$$

where h_D is the radial scale length of the disc, related to the disc half-mass radius, r_D, by

$$2(r_D/h_D + 1)\exp(-r_D/h_D) = 1, \tag{2.7.29}$$

and M_D is the mass of the (gas + stars) in the disc. The specific angular momentum of the disc, j_D (see Eq. 2.3.12), is given by the integral

$$j_D = \int_0^\infty 2\pi\, r\, \Sigma_D(r) r\, V_{cD}\, dr / M_D = k_D r_D V_{cD}(r_D) \tag{2.7.30}$$

where

$$k_D = \int_0^\infty \frac{r^2}{h_D^2} \exp\left(-\frac{r}{h_D}\right) \frac{V_{cD}(r)}{1.68 V_{cD}(r_D)} \frac{dr}{h_D}, \tag{2.7.31}$$

and $V_{cD}(r)$ is the circular velocity of the disc. A flat rotation curve [i.e. $V_{cD}(r) = V_{cD}(r_D)$] gives a value of $k_D = 1.19$. Using the relation $V_{cD}^2(r_D) = G M(r_D)/r_D$ we can write

$$\begin{aligned} j_D^2 &= k_D^2 r_D^2 V_{cD}^2(r_D) \\ &= k_D^2 G r_D \left[f_H M_H^0(r_{D,0}) + \frac{1}{2} k_H M_D + M_B(r_D) \right], \end{aligned} \tag{2.7.32}$$

where the relation $M_H(r) = f_H M_H^0(r_0)$ has been used, and by definition $M_D(r_D) = M_D/2$. The constant k_H accounts for the fact that the disc is not spherically symmetric. For an exponential disc $k_H = 1.25$.

This can be equated to Eq. (2.7.27) at the half-disc radius to give

$$r_{D,0} M_H^0(r_{D,0}) = \left[f_H M_H^0(r_{D,0}) + \frac{1}{2} M_D + M_B(r_D) \right], \quad (2.7.33)$$

which can be solved to find r_D.

A similar procedure is followed to determine the size of the spheroid. Bulges are assumed to have an $r^{1/4}$ mass density profile in projection

$$\Sigma_B(r) = \Sigma_0 \exp\left[\beta_n \left\{ \left(\frac{r}{r_B}\right)^{1/n} - 1 \right\} \right], \quad (2.7.34)$$

for $n = 4$, where r_B is the half-mass radius of the bulge and β_n is well approximated by $\beta_n = 2n - 0.324$.

2.7.1 Spheroid Formation

GALFORM assumes that a spheroid is formed after a merger or disc instability (see Sect. 2.6). In the case of a merger galaxies are assumed to merge when their separation equals the sum of their half-mass radii. Assuming each galaxy is in equilibrium their gravitational self-binding energy is

$$E_{bind} = -\frac{c_{bind}}{2} \frac{G M^2}{r}, \quad (2.7.35)$$

where M is the total (dark matter + stars + gas) mass, r is the half-mass radius and c_{bind} is a constant that depends on the distribution of the mass. For an $r^{1/4}$-law $c_{bind} = 0.45$ whereas for an exponential disc $c_{bind} = 0.49$. For simplicity in GALFORM it is assumed that $c_{bind} = 0.5$. The orbital energy of two galaxies just prior to a merger is given by

$$E_{orbit} = -\frac{f_{orbit}}{2} \frac{G M_1 M_2}{r_1 + r_2}, \quad (2.7.36)$$

where M_1 and M_2 are the total (i.e. dark matter + baryons) masses of the galaxies and r_1 and r_2 are their half-mass radii. The parameter f_{orbit} depends on the orbital parameters of the galaxy pair. A value of $f_{orbit} = 1$ corresponds to point masses on circular orbits, however in Lacey et al. (2016) a value of $f_{orbit} = 0$, which corresponds to a marginally (un)bound orbit (or parabolic trajectory), is adopted. This has the effect of making the total binding energy of the new spheroid (see equation below) less negative, resulting in the spheroid sizes being slightly larger. This value for f_{orbit} is chosen to give an improved match to the observed size-luminosity relation for early-type galaxies. Conservation of energy then requires

$$E_{\text{bind,new}} = E_{\text{bind,1}} + E_{\text{bind,2}} + E_{\text{orbit}}, \qquad (2.7.37)$$

which can be solved to find the half-mass radius of the new spheroid, r_{new}. This can then be used to compute the angular momentum of the bulge/spheroid which in turn can be used to compute its size r_{B}. For a minor merger M_1 and r_1 are replaced by the mass and half-mass radius of the primary spheroid. A similar expression is used to compute r_{new} in the case of disc instabilities

$$\frac{c_{\text{B}}(M_{\text{disc}} + M_{\text{bulge}})^2}{r_{\text{new}}} = \frac{c_{\text{B}} M_{\text{bulge}}^2}{r_{\text{bulge}}} + \frac{c_{\text{D}} M_{\text{disc}}^2}{r_{\text{disc}}} + f_{\text{int}} \frac{M_{\text{bulge}} M_{\text{disc}}}{r_{\text{bulge}} + r_{\text{disc}}}, \qquad (2.7.38)$$

though here the mass refers only to the baryonic (i.e. stars + gas) mass of the galaxy. The final term on the right accounts for the gravitational interaction energy between the disc and the bulge, which is well approximated by $f_{\text{int}} = 2$.

2.8 Chemical Evolution

The interplay of the equations describing gas cooling, star formation and feedback discussed up until results in a set of coupled differential equations which track the exchange of mass and metals between the main baryonic reservoirs of a galaxy: hot halo gas (M_{hot}), cold disc gas (M_{cold}), stars ($M_\star$) and ejected gas (M_{res}). This is summarised in Fig. 2.1.

2.8.1 Evolution of Mass and Metals

The equations governing the exchange of mass between a galaxy's baryonic reservoirs are

Fig. 2.1 Schematic of the exchange of mass between a galaxy's baryonic reservoirs in GALFORM
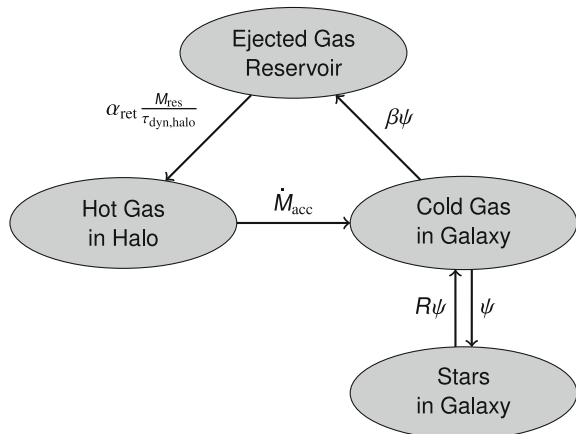
$$\dot{M}_{\text{hot}} = -\dot{M}_{\text{acc}} + \alpha_{\text{ret}} \frac{M_{\text{res}}}{\tau_{\text{dyn,halo}}}, \tag{2.8.39}$$

$$\dot{M}_{\text{cold}} = \dot{M}_{\text{acc}} - (1 - R + \beta)\psi, \tag{2.8.40}$$

$$\dot{M}_{\star} = (1 - R)\psi, \tag{2.8.41}$$

$$\dot{M}_{\text{res}} = \beta\psi - \alpha_{\text{ret}} \frac{M_{\text{res}}}{\tau_{\text{dyn,halo}}}, \tag{2.8.42}$$

and for metals

$$\dot{M}_{\text{hot}}^{Z} = -Z_{\text{hot}}\dot{M}_{\text{acc}} + \alpha_{\text{ret}} \frac{M_{\text{res}}^{Z}}{\tau_{\text{dyn,halo}}}, \tag{2.8.43}$$

$$\dot{M}_{\text{cold}}^{Z} = Z_{\text{hot}}\dot{M}_{\text{acc}} + [p - (1 - R + \beta)Z_{\text{cold}}]\psi, \tag{2.8.44}$$

$$\dot{M}_{\star}^{Z} = (1 - R)Z_{\text{cold}}\psi, \tag{2.8.45}$$

$$\dot{M}_{\text{res}}^{Z} = \beta Z_{\text{cold}}\psi - \alpha_{\text{ret}} \frac{M_{\text{res}}^{Z}}{\tau_{\text{dyn,halo}}}, \tag{2.8.46}$$

where the recycled fraction, R, is the fraction of the initial mass of a stellar population returned to the ISM by mass loss, and the yield, p, is the fraction of the initial mass of a stellar population synthesised into new metals and then ejected into the ISM. These quantities are determined by the choice of IMF, as described below.

2.8.2   The Initial Mass Function

The IMF describes the distribution in mass, m, of stars formed in a simple stellar population, normalized to unit solar mass

$$\int_{m_1}^{m_2} m\Phi(m)\, \mathrm{d}\ln m = 1, \tag{2.8.47}$$

such that $\Phi(m)\mathrm{d}\ln m$ is the number of stars formed between $[m, m + \mathrm{d}m]$ per unit mass of stars formed, where m_1 and m_2 are the mass limits of the IMF. The recycled fraction, R, and yield, p, described above are set by the IMF. The recycled fraction is the fraction of the initial mass of a stellar population that is returned to the ISM by mass loss from dying stars. In the instantaneous recycling approximation[6] it is given by the integral

$$R = \int_{1\text{M}_{\odot}}^{m_2} [m - m_{\text{rem}}(m)]\Phi(m)\, \mathrm{d}\ln m, \tag{2.8.48}$$

---

[6]Instantaneous recycling assumes that all stars with $m > 1$ M$_{\odot}$ die immediately, whilst all other stars live forever. This is a reasonable approximation as the lifetimes of massive stars are short compared to the timescales over which galaxies evolve. The effect of relaxing this approximation in GALFORM is discussed in e.g. Nagashima et al. (2005).

where $m_{\rm rem}(m)$ is the mass of the remnant (e.g. white dwarf, neutron star, black hole) left by a star of initial mass m, obtained from stellar evolution calculations (e.g. Marigo et al. 1996; Portinari et al. 1998). The yield, p, is the fraction of initial mass of a stellar population that is synthesised into new metals and then ejected. It is given by

$$p = \int_{1{\rm M}_\odot}^{m_2} p_Z(m)\Phi(m)\,{\rm d}\ln m, \qquad (2.8.49)$$

where $p_Z(m)$ is the fraction for a single star of initial mass m, also obtained from stellar evolution calculations. It is assumed that metals are instantaneously mixed into the cold gas component.

Due to the assumption of instantaneous recycling, time delays between the star formation event and enrichment of the ISM are ignored. We now briefly outline a example of when such time delays can be useful, in the context of Type I and Type II supernovae (SNe). Type II SNe are the result of the collapse of massive ($\gtrsim 8\,{\rm M}_\odot$) stars, and have lifetimes of $\lesssim 10^7$ years, whereas Type I SNe are the result of lower mass ($\sim 3 - 8\,{\rm M}_\odot$) stars and have longer lifetimes of 10^8 yr. Type I SNe occur if the star in question has a binary companion. Once the star has evolved into a $\sim 0.6\,{\rm M}_\odot$ white dwarf, subsequent accretion of matter from the companion leads to a supernova when the white dwarf reaches the Chandrasekhar mass limit of $\sim 1.4\,{\rm M}_\odot$ (such that the electron degeneracy pressure supporting the white dwarf is overcome), it is this constant mass limit that leads to the use of Type I SNe as a 'standard candle'.

Type I SNe are the the main producers of iron (producing $\sim 5 - 10\times$ more than a Type II), whereas both types can produce α elements (e.g. Ne, Mg, Si; those produced through the 'alpha' process which fuses Helium nuclei together). As the different supernovae occur on different timescales (there is a delay of $\sim 10^8$ yr between Type II and Type I) there is a corresponding delay between the enrichment of the ISM with Fe and α elements. Thus, the abundance ratio of $[\alpha/{\rm Fe}]$ can be used as a diagnostic of the star formation history of the galaxy, though $[\alpha/{\rm Fe}]$ is also affected by the assumed IMF.

In GALFORM, as Type I SNe make only a small contribution to the net production of heavy elements the metal yields are calculated assuming only Type II SNe, though see Nagashima et al. (2005) for an example of Type I SNe being included in GALFORM metal enrichment. The Portinari et al. yields used here incorporate the Type II SNe calculations of Woosley and Weaver (1995).

In GALFORM it is assumed that the IMF is a power law or piecewise power law

$$\Phi(m) = \frac{{\rm d}N}{{\rm d}\ln m} \propto m^{-x}, \qquad (2.8.50)$$

where, for example, $x = 1.35$ for a Salpeter (1955) IMF. In GALFORM, for quiescent/disc star formation, a Kennicutt (1983) IMF is assumed i.e. $x = 0.4$ for $m < {\rm M}_\odot$ and $x = 1.5$ for $m > {\rm M}_\odot$. For burst star formation x is treated as an adjustable parameter. This is discussed in more detail in Sect. 2.10.

2.9 The Spectral Energy Distribution of Galaxies

The star formation and metal enrichment history of a galaxy, $\Psi(t, Z)$, predicted by GALFORM is combined with models for stellar evolutionary population synthesis (e.g. Tinsley 1972; Bruzual and Charlot 2003; Maraston 2005) and a simple model for the absorption and re-emission of stellar radiation by interstellar dust to produce the spectral energy distributions of model galaxies. Importantly for the dust emission, the temperature of the interstellar dust is not a parameter in the model but is determined from the use of the equations of radiative transfer and global energy balance arguments.

The dust model presented here is motivated by the spectrophotometric code GRASIL (Silva et al. 1998). However, a number of simplifying approximations are made, such as each dust component being described by a single temperature and the dust being optically thin to its own emission. Despite its simplicity this model can reproduce the predictions of GRASIL to within a factor of ~ 2 for $\lambda_{\text{rest}} \gtrsim 70\,\mu\text{m}$ (see Appendix C).

2.9.1 Emission of Light

The unattenuated spectral energy distribution (SED) of a galaxy at time t is a convolution

$$L_\lambda^{\text{unatten}}(t) = \sum_i \int_0^t \mathrm{d}t' \int_0^\infty \mathrm{d}Z\, L_\lambda^{\text{SSP}}(t', Z; \Phi_i)\Psi_i(t - t', Z), \qquad (2.9.51)$$

where $\Psi_i(t, Z; \Phi_i)$ is the mass of stars formed with IMF Φ_i between $(t, t + \mathrm{d}t)$ in time and $(Z, Z + \mathrm{d}Z)$ in metallicity, summed over all the progenitors of the galaxy in question; and $L_\lambda^{\text{SSP}}(t, Z; \Phi_i)$ is the SED of a simple stellar population of unit solar mass, age t and metallicity Z, formed with IMF Φ_i. In turn, $L_\lambda^{\text{SSP}}(t, Z; \Phi_i)$ is related to the SED of its constituent stars by (e.g. Bruzual and Charlot 2003)

$$L_\lambda^{\text{SSP}}(t, Z; \Phi_i) = \int_{m_1}^{m_2} \mathrm{d}\ln m\, L_\lambda^{\text{star}}(t, Z, m)\Phi_i(m). \qquad (2.9.52)$$

The dust attenuated SED can be written as

$$L_\lambda^{\text{atten}}(t) = \sum_i A_\lambda^{\text{diff}} \int_0^t \mathrm{d}t' \int_0^\infty \mathrm{d}Z\, A_\lambda^{\text{MC}}(t')L_\lambda^{\text{SSP}}(t', Z; \Phi_i)\Psi_i(t - t', Z), \quad (2.9.53)$$

where A_λ^{diff} and $A_\lambda^{\text{MC}}(t')$ describe the attenuation at wavelength λ due to the diffuse and molecular cloud dust components respectively. These are described in more detail in the following Section.

2.9.2 Dust Absorption

It is assumed that dust exists in two components: (i) dense molecular clouds of fixed gas surface density in which stars form, escaping on some timescale (t_{esc}) and; (ii) a diffuse ISM which assumes the same radial and vertical scale lengths for the dust and gas as for the stellar disc i.e. $h_{z,\text{dust}}/h_{z,\text{stars}} = h_{R,\text{dust}}/h_{R,\text{stars}} = 1$. The fraction of gas mass in molecular clouds is determined by the parameter f_{cloud}. In GALFORM, the dust mass is calculated assuming a dust-to-gas ratio that scales linearly with cold gas metallicity, Z_{cold}, normalized to the local ISM value (Silva et al. 1998) such that

$$M_{\text{dust}} = \delta_{\text{dust}} M_{\text{cold}} Z_{\text{cold}}, \tag{2.9.54}$$

where $\delta_{\text{dust}} = 0.334$. This value for δ_{dust} is derived assuming a value of $1/110$ for the dust-to-hydrogen gas mass ratio at solar metallicity ($Z = 0.02$, e.g. Draine and Lee 1984) and a fixed hydrogen-to-total gas mass ratio of 0.735. However, in practise it is only the quantity $M_{\text{cold}} Z_{\text{cold}}$ that enters into the GALFORM calculation.

The dust is assumed to have the same extinction curve shape, k_λ, and albedo, a_λ, as for the Solar neighbourhood (Silva et al. 1998). The (extinction) optical depth of dust for light passing though gas with surface density Σ_{gas} is

$$\tau_{\lambda,\text{ext}} = 0.043 \left(\frac{k_\lambda}{k_V}\right) \left(\frac{\Sigma_{\text{gas}}}{\text{M}_\odot \, \text{pc}^{-2}}\right) \left(\frac{Z_{\text{cold}}}{0.02}\right), \tag{2.9.55}$$

where the normalisation is based on the local ratio of V-band extinction, A_V, to hydrogen column density, N_{H}, $A_V/N_{\text{H}} = 3.3 \times 10^{-22}$ mag cm^2 measured by Savage and Mathis (1979). For discs $\Sigma_{\text{gas}} = (1 - f_{\text{cloud}}) M_{\text{cold,disc}}/2\pi h_R^2$, where h_R is the radial scale length of the disc, for clouds $\Sigma_{\text{gas}} = 3m_{\text{cloud}}/4\pi r_{\text{cloud}}^2$ where $m_{\text{cloud}} = 10^6 \, \text{M}_\odot$ and $r_{\text{cloud}} = 16 \, \text{pc}$ are the assumed mass and radius of the clouds respectively. These values are motivated by those found by Silva et al. (1998, see their Table 2). These parameters enter into the calculation in the combination $m_{\text{cloud}}/r_{\text{cloud}}^2$ and only have a significant effect on results in the mid-IR (Vega et al. 2005), provided the clouds are still in the optically thick regime for UV/optical wavelengths.

In a cloud the effective absorption optical depth is approximated as

$$\tau_{\lambda,\text{eff}} = (1 - a_\lambda)^{1/2} \tau_{\lambda,\text{ext}}, \tag{2.9.56}$$

where a_λ is the albedo. The dust attenuation factor in a single cloud is $e^{-\tau_{\lambda,\text{eff}}}$ while the mean attenuation for stars of age t due to clouds is given by

$$A_\lambda^{\text{MC}}(t) = 1 - \eta(t)(e^{-\tau_{\lambda,\text{eff}}} - 1), \tag{2.9.57}$$

where $\eta(t)$ is the fraction of stars of age t still in their birth cloud. This is parametrised as

$$\eta(t) = \begin{cases} 1 & t < t_{\text{esc}} \\ 2 - t/t_{\text{esc}} & t_{\text{esc}} < t < 2t_{\text{esc}} \\ 0 & t > 2t_{\text{esc}} \end{cases} \tag{2.9.58}$$

such that stars begin to migrate out of their birth cloud at time t_{esc} and have completely left by time $2t_{\text{esc}}$. This parametrisation is meant to describe the destruction of a giant molecular cloud due to powerful stellar winds and outflows produced by massive stars over their lifetime. In Lacey et al. (2016) values of $t_{\text{esc}} = 1$ Myr and $f_{\text{cloud}} = 0.5$ are adopted, constrained primarily by requiring the model to reproduce the observed high-redshift ($z \gtrsim 3$) rest-frame far-UV (1500 Å) luminosity function. This is discussed in more detail in Sect. 5.3.4.

The dust-attenuated SED (see Eq. 2.9.53) can then be rewritten as

$$L_\lambda^{\text{atten}}(t) = A_\lambda^{\text{diff}} \langle A_\lambda^{\text{MC}}(t) \rangle L_\lambda^{\text{unatten}}(t), \tag{2.9.59}$$

where $\langle A_\lambda^{\text{MC}}(t) \rangle$ is the dust attenuation by clouds averaged over stellar age given by

$$\langle A_\lambda^{\text{MC}}(t) \rangle = 1 - \langle \eta(t) \rangle (e^{-\tau_{\lambda,\text{eff}}} - 1), \tag{2.9.60}$$

where $\langle \eta(t) \rangle$ is given by a luminosity-weighted average in each band

$$\langle \eta(t) \rangle = \frac{\sum_i \int_0^t dt' \int_0^\infty dZ \, \eta(t') L_\lambda^{\text{SSP}}(t', Z; \Phi_i) \Psi_i(t - t', Z)}{\sum_i \int_0^t dt' \int_0^\infty dZ \, L_\lambda^{\text{SSP}}(t', Z; \Phi_i) \Psi_i(t - t', Z)}. \tag{2.9.61}$$

This is calculated separately for quiescent and burst star formation. For burst star formation an exponentially decaying star formation history is assumed. The energy absorbed by the molecular cloud component is thus given by

$$L_{\text{abs}}^{\text{MC}} = \int_0^\infty (1 - \langle A_\lambda^{\text{MC}} \rangle) L_\lambda^{\text{unatten}} d\lambda. \tag{2.9.62}$$

For the diffuse component A_λ^{diff} is calculated from the tabulated radiative transfer results of Ferrara et al. (1999), which are derived from the code described in Bianchi et al. (1996). The central optical depth for the model galaxies are calculated according to Eq. (2.9.55) and the Ferrara et al. tables are interpolated to get the total attenuation as a function of wavelength. The energy absorbed by the diffuse dust medium is given by

$$L_{\text{abs}}^{\text{diff}} = \int_0^\infty (1 - A_\lambda^{\text{diff}}) \langle A_\lambda^{\text{MC}} \rangle L_\lambda^{\text{unatten}} d\lambda. \tag{2.9.63}$$

2.9.3 Dust Emission

The dust is assumed to be in thermal equilibrium and optically thin at the wavelengths at which the dust emits. We can therefore write the dust emission as

$$L_\lambda^{\text{dust}} = 4\pi \kappa_{\text{d}}(\lambda) B_\lambda(T_{\text{dust}}) M_{\text{gas}} Z_{\text{gas}}. \tag{2.9.64}$$

Here, T_{d} is the dust temperature (a major simplifying assumption made in this model is to assume that each dust component can be described by a single temperature), $B_\lambda(T_{\text{d}})$ is the Planck blackbody function and $\kappa_{\text{d}}(\lambda)$ is the dust opacity per unit mass of metals in the gaseous phase. This is parametrised as

$$\kappa_{\text{d}}(\lambda) = \begin{cases} \kappa_1 \left(\frac{\lambda}{\lambda_1}\right)^{-2} & \lambda < \lambda_{\text{b}} \\ \kappa_1 \left(\frac{\lambda_{\text{b}}}{\lambda_1}\right)^{-2} \left(\frac{\lambda}{\lambda_{\text{b}}}\right)^{-\beta_{\text{b}}} & \lambda > \lambda_{\text{b}}, \end{cases} \tag{2.9.65}$$

with $\kappa_1 = 140 \text{ cm}^2\text{g}^{-1}$ at a reference wavelength of $\lambda_1 = 30 \text{ }\mu\text{m}$ (Draine and Lee 1984). Blackbody spectra arise when a medium is in thermal equilibrium with its surroundings and are described by the Planck function

$$B_\lambda(T) = \frac{2 h_{\text{p}} c}{\lambda^5} \frac{1}{\exp(h_{\text{p}} c / \lambda k_{\text{B}} T) - 1}, \tag{2.9.66}$$

where h_{p} is the Planck constant, c is the speed of light and k_{B} is the Boltzmann constant (see, for example, the excellent Rybicki and Lightman 1979 text for a derivation). It can also be written equivalently in terms of frequency rather than wavelength,

$$B_\nu(T) = \frac{2 h_{\text{p}} \nu^3}{c^2} \frac{1}{\exp(h_{\text{p}} \nu / k_{\text{B}} T) - 1}, \tag{2.9.67}$$

note that $B_\nu \neq B_\lambda$, but $B_\nu \, \text{d}\nu = B_\lambda \, \text{d}\lambda$.

Blackbody spectra have a number of interesting properties which we will now discuss briefly. In the limits that $h_{\text{p}} \nu \ll k_{\text{B}} T$ and $h_{\text{p}} \nu \gg k_{\text{B}} T$ we regain respectively the Rayleigh-Jeans law,[7] $I_\nu^{\text{RJ}}(T) = 2(\nu^2/c^2)k_{\text{B}} T$, and the Wien law, $I_\nu^{\text{W}}(T) = 2(h_{\text{p}}\nu^3/c^2) \exp(-h\nu/k_{\text{B}} T)$. Throughout this thesis we are mostly concerned with the portion of the spectrum long-wards (in terms of wavelength) of the peak, which is often referred to as the Rayleigh-Jeans tail.

Another property of a blackbody is 'monotonicity of temperature', given two blackbody curves the one with the higher temperature will lie entirely above the other. This can be shown by the fact that the derivative with respect to temperature,

---

[7]Note that the integral of this law over all frequencies diverges, leading to the so-called *ultraviolet catastrophe*.

Fig. 2.2 Examples of blackbody spectra at different temperatures, as indicated in the legend
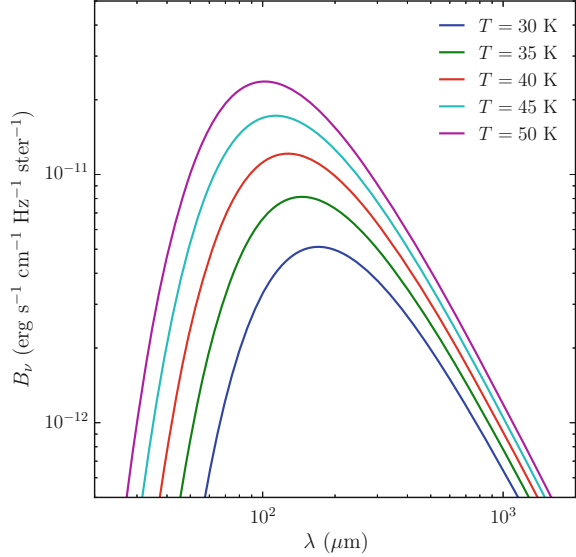
$$\frac{\partial\, B_\lambda(T)}{\partial\, T} \;=\; \frac{2\,h_{\mathrm p}^2\,c^3}{\lambda^6\,k_{\mathrm B}\,T^2}\,\frac{\exp(h_{\mathrm p}\,c/\lambda\,k_{\mathrm B}\,T)}{[\exp(h_{\mathrm p}\,c/\lambda\,k_{\mathrm B}\,T)-1]^2}, \qquad (2.9.68)$$

is always positive. We give a visual example of this in Fig. 2.2. What is also evident from this Figure is that as the temperature of increases so too does its integral (it can be shown that the bolometric luminosity $L = \int B_\lambda \, \mathrm{d}\lambda \propto T^4$) and the wavelength at which the function peaks shifts to shorter wavelengths. This latter point is referred to as the *Wein displacement law*, and it can be shown by solving $\partial B_\lambda/\partial\,\lambda|_{\lambda=\lambda_{\max}} = 0$, that $\lambda_{\max} T = \mathrm{const}$. Thus, as the temperature of the blackbody increases the wavelength at which its emission peaks must shift to shorter wavelengths to compensate. In the case of the 30 K spectrum it can be seen in Fig. 2.2 that the radiation peaks at $\lambda \sim 10^2\ \mu$m, which is roughly the wavelength at which the FIR SED of many dusty galaxies is observed to peak. This indicates that this is a good 'rule of thumb' for the dust temperature of such galaxies.

In practise, real-world materials rarely emit as a perfect blackbody and so they are often described by a 'modified' blackbody, the 'modification' in this case being described by the $\kappa_{\mathrm d}$ term in Eq. (2.9.64).

The assumption of thermal equilibrium with Eq. (2.9.64) is applied separately to dust in molecular clouds (Eq. 2.9.62) and the diffuse ISM (Eq. 2.9.63).

For galaxies undergoing a starburst a value of $\beta_{\mathrm b} = 1.5$ is used whereas for quiescently star forming galaxies an unbroken power law is assumed i.e. $\lambda_{\mathrm b} \to \infty$. This choice was originally motivated by Silva et al. (1998), who found that a lower value of $\beta_{\mathrm b}$ was necessary to reproduce the SED of Arp 220, a local starburst galaxy, and laboratory measurements of silicates suggest that values in the range $\beta_{\mathrm b} = 1.5 - 2$ are acceptable (e.g. Agladze et al. 1996). There is also some observational evidence that

suggests an anti-correlation between β and temperature, with hotter dust exhibiting lower values (e.g. Boudet et al. 2005). Note that in GALFORM, starburst galaxies have generally hotter dust temperatures than quiescently star-forming galaxies (Chap. 5).

2.9.4 Absorption by the IGM

Neutral hydrogen in the IGM along the line of sight can absorb ionizing photons. We compute this where relevant for the model galaxies according to the prescription of Meiksin (2005).

2.10 The Lacey et al. (2016) GALFORM Model

In this Section we briefly describe some features of the Lacey et al. (2016) version of GALFORM, the fiducial model throughout this thesis, that are pertinent to the work that follows.

This model incorporates a number of important physical processes from earlier iterations of GALFORM, and is thus thought of as a 'unifying' model for various ideas that have been developed throughout the GALFORM literature. Additionally, the cosmological parameters used are updated to those consistent with Wilkinson Microwave Anisotropy Probe 7 year (*WMAP7*) data (Komatsu et al. 2011).[8] The physical processes incorporated from earlier versions of GALFORM include the star formation treatment described in Sect. 2.4.1, which is based on an empirical relation between star formation rate and molecular gas (Blitz and Rosolowsky 2006) and was first implemented into GALFORM by Lagos et al. (2011), and a *hot-halo mode* AGN feedback prescription (Sect. 2.5.3) in which quasi-hydrostatic hot halo gas is prevented from cooling by energy input from relativistic jets (Bower et al. 2006).

Importantly for this thesis, the Lacey et al. (2016) model can simultaneously reproduce the optical and near-IR galaxy luminosity functions at $z = 0$ (see Fig. 2.3) and the observed 850 µm number counts and redshift distribution. As mentioned earlier, in order to do so it treats the slope of the IMF, x (Sect. 2.8.2), as a free parameter in starbursts, as was found to be necessary to reproduce the 850 µm number counts in the ΛCDM paradigm by Baugh et al. (2005). Following an extensive parameter search using GALFORM, Baugh et al. advocated a slope of $x = 0$ making the IMF 'top-heavy' relative to a solar neighbourhood IMF (e.g. a Salpeter 1955 IMF is described by a slope of $x = 1.35$). An earlier GALFORM model, Granato et al. (2000), was able to reproduce the b_J- and K-band luminosity functions at $z = 0$ but underpredicted the sub-mm number counts by a factor of $\sim$30. Attempts to increase

---

[8]$\Omega_0 = 0.272$, $\Lambda_0 = 0.728$, $h = 0.704$, $\Omega_b = 0.0455$, $\sigma_8 = 0.81$, $n_s = 0.967$. Though note that in Chap. 6 we us e cosmological parameters consistent with more recent *Planck* data (Planck Collaboration et al. 2016).
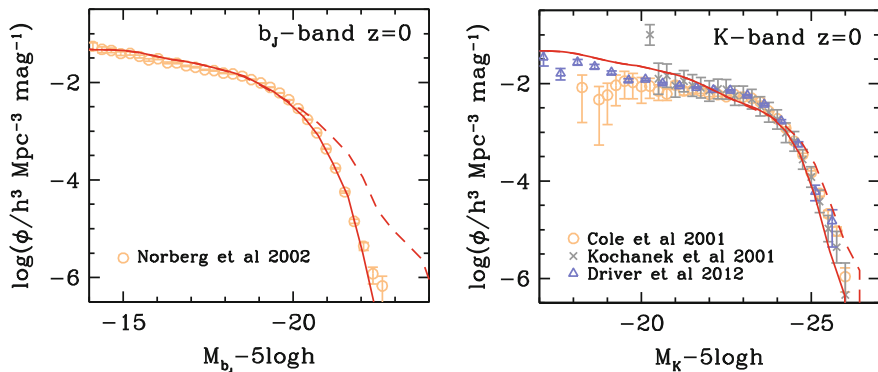
Fig. 2.3 Calibrated predictions of the fiducial Lacey et al. (2016) model for the b_J- and K-band luminosity functions (*left* and *right* panels respectively) at $z = 0$. The *solid* and *dashed lines* show the model predictions with and without dust extinction respectively. Observational data are from Norberg et al. (2002), Cole et al. (2001), Kochanek et al. (2001) and Driver et al. (2012). Figure taken from Lacey et al. (2016)

the star formation rate in the Granato et al. model (e.g. through reducing feedback strength) alleviated the discrepancy between the predicted and observed sub-mm number counts, but meant that galaxies were too massive by the present day and thus reduced the level of agreement between the predicted and observed $z = 0$ luminosity functions. A top-heavy IMF works here by boosting the sub-mm flux per unit star formation in a galaxy. This is through increasing the UV luminosity, as a greater number of massive stars are produced in a top-heavy IMF, and an increase in the dust mass of the galaxy through a larger yield as these stars go supernova and eject their metals into the ISM. This latter point allowed the dust to remain cool enough ($T_d \sim 30$ K) to re-emit the increased absorbed UV radiation effectively in sub-mm bands. It also has little impact on the $z = 0$ stellar mass of a galaxy, as most bursts occur at $z \gtrsim 2$ in the model, and the massive stars that form under the top-heavy IMF do not live long enough to persist to $z = 0$.

The assumption of a varying IMF is a somewhat contentious one. In a review of observational studies Bastian et al. (2010) argued against significant variations from a solar neighbourhood IMF in the nearby Universe. However, studies based on gravity-sensitive absorption features have found evidence for a bottom-heavy IMF in early-type galaxies (e.g. Conroy and van Dokkum 2012) whereas Gunawardhana et al. (2011) found a trend of flattening IMF slope (i.e. becoming increasingly 'top-heavy') with increasing SFR from studying integrated H α emission in the Sloan Digital Sky Survey (SDSS). There are also some theoretical arguments for a varying IMF. Larson (2005) argues that the characteristic mass in the ISM should scale with the Jeans mass of a star-forming cloud, and that this should be larger in actively star-forming galaxies due to radiation heating from massive stars, plausibly leading to a more top-heavy IMF than found locally. Thus it seems that IMF variation is still a somewhat open issue and is therefore worth investigating in models such as
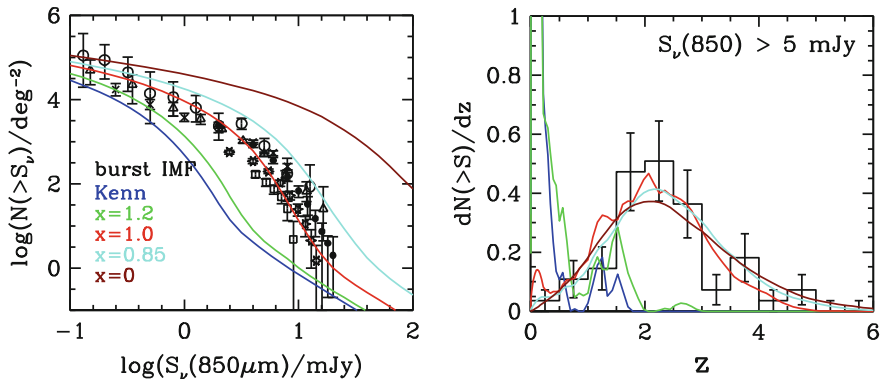
Fig. 2.4 Dependence of cumulative 850 μm number counts (*left panel*) and *redshift* distribution of galaxies with $S_{850\,\mu m} > 5$ mJy (*right panel*) on starburst IMF slope, x, in the Lacey et al. (2016) model. The different colour lines indicate the predictions from models with different values of x, as indicated in the legend. Observational number count data in the *left panel* are from Coppin et al. (2006, filled circles), Knudsen et al. (2008, open circles), Zemcov et al. (2010, crosses), Karim et al. (2013, open squares) and Chen et al. (2013, open triangles). The *right panel* shows the redshift probability distributions for galaxies with $S_{850\,\mu m} > 5$ mJy. Observational data is from Wardlow et al. (2011). Figure taken from Lacey et al. (2016)

GALFORM. Lacey et al. found a slope of $x = 1$ was better able to reproduce the observed sub-mm number counts, rather than the $x = 0$ used by Baugh et al. This is shown in Fig. 2.4.

The reason behind a steeper IMF slope than used by Baugh et al. is related to the inclusion of disc instabilities (Sect. 2.6.2) and AGN feedback (Sect. 2.5.3), which were not considered by Baugh et al. An additional consequence of this is that whereas in Baugh et al. sub-mm galaxies are undergoing merger-induced starbursts, in the Lacey et al. model they are predominantly disc instability-induced starbursts. Disc instabilities allow for more starbursts at early times so that the observed abundance of SMGs at $z \gtrsim 3$ can be reproduced, whilst also growing a galaxy's SMBH through accretion during a starburst (see Sect. 2.5.3) so that AGN feedback is efficient at later times ($z \lesssim 2$) resulting in further star formation being inhibited such that the model does not overproduce SMGs. This is summarised in Fig. 2.5. Turning off merger-induced starbursts has a negligible impact on the predicted sub-mm number counts. Indeed, we discuss that galaxy mergers are rather inefficient at boosting star formation in the model in Chap. 5, as they are responsible for a population of starburst galaxies that actually tend to lie below the main locus of star-forming quiescent galaxies on the specific star formation rate—stellar mass plane.

We end this Section by summarising the parameters in the Lacey et al. (2016) model in Table 2.1. It is worth noting that adjustable parameters form only a subset of those listed in Table 2.1. For example cosmological parameters are set by the adopted cosmology, similarly, the yield, p, and recycled fraction, R, are set by the choice of IMF, which is only treated as a parameter for burst star formation. Additionally,

Fig. 2.5 Dependence of the model redshift distribution for $S_{850\,\mu m} > 1$ mJy galaxies on AGN feedback and disc instabilities in the Lacey et al. (2016) model. The *red*, *blue* and *green lines* are, respectively, predictions from the fiducial model, a model in which AGN feedback has been turned off, and a model in which there are no disc instabilities
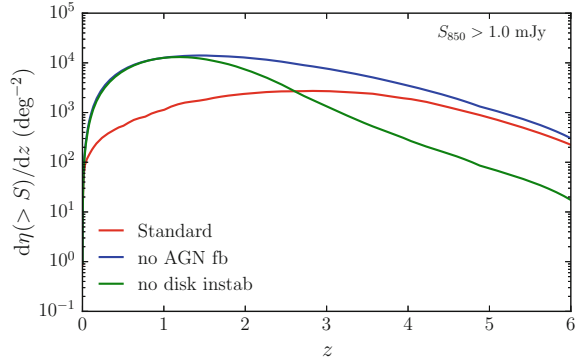
Table 2.1 Values of input parameters for the fiducial Lacey et al. (2016) GALFORM model. Adapted from Lacey et al. (2016)

Parameter	Value	Description	Reference
Cosmological parameters			Komatsu et al. (2011)
Ω_m	0.272	Matter density	
Ω_b	0.0455	Baryon density	
h	0.704	Hubble parameter	
σ_8	0.81	Fluctuation amplitude	
n_s	0.965	Scalar spectral index	
Stellar population			Maraston (2005)
IMF: Quiescent (Kennicutt 1983)			
p	0.021	Yield	(2.8.49)
R	0.44	Recycled fraction	(2.8.48)
IMF: Burst			
x	1	IMF slope	(2.8.50)
p	0.048	Yield	(2.8.49)
R	0.54	Recycled fraction	(2.8.48)
Star formation: Quiescent			Lagos et al. (2011)
ν_{SF}	0.74 Gyr^{-1}	Efficieny factor for molecular gas	(2.4.14)
P_0	1.7×10^4	Normalisation of pressure relation	(2.4.13)
α_P	0.8	Slope of pressure relation	(2.4.13)
Star formation: Burst			Baugh et al. (2005)
f_{dyn}	20	Multiplier for dynamical time	(2.4.16)
$\tau_{burst,min}$	0.1 Gyr	Minimum burst timescale	(2.4.16)

(continued)

Table 2.1 (continued)

Parameter	Value	Description	Reference
Supernova feedback			Cole et al. (2000)
V_{SN}	320 km s^{-1}	Normalisation of mass loading	(2.5.18)
γ_{SN}	3.2	Slope of mass loading	(2.5.18)
α_{ret}	0.64	Gas reincorporation timescale multiplier	(2.5.19)
AGN feedback and SMBH growth			Bower et al. (2006)
f_{BH}	0.005	Fraction of mass accreted onto SMBH in starburst	Malbon et al. (2007)
α_{cool}	0.8	Ratio of cooling/free-fall time	(2.5.20)
f_{Edd}	0.01	SMBH Eddington luminosity multiplier	(2.5.21)
ϵ_{heat}	0.02	SMBH heating efficiency	
Disc stability			
F_{stab}	0.9	Threshold for disc stability	(2.6.24)
Galaxy mergers			Jiang et al. (2008)
Size of merger remnants			Cole et al. (2000)
f_{orbit}	0	Orbital energy contribution	
Starburst triggering by mergers			Baugh et al. (2005)
f_{ellip}	0.3	Mass ratio threshold for major merger	
f_{burst}	0.05	Mass ratio threshold for starburst	
Dust model			Granato et al. (2000)
f_{cloud}	0.5	Fraction of dust mass in clouds	
t_{esc}	1 Myr	Escape time of stars from clouds	(2.9.58)
β_b	1.5	Dust emissivity slope in starbursts	(2.9.65)

Note P_0 is in units of k_B cm^{-3} K

parameters in the quiescent star formation law are set by observational results (e.g. Leroy et al. 2008; Bigiel et al. 2011). Once the parameter values are set the model is fully specified, this forms the starting point for the work presented in this thesis and unless explicitly stated they are not changed throughout.

Chapter 3
Simulated Observations of Sub-millimetre Galaxies: The Impact of Single-Dish Resolution and Field Variance

3.1 Introduction

[1]One of the main goals of the study of galaxy formation and evolution is to understand the star formation history of the Universe. A key advance in this area was the discovery of a cosmic extragalactic background light (EBL) in the infra-red by the *COsmic Background Explorer* (*COBE*) satellite (Puget et al. 1996; Fixsen et al. 1998) with an energy density similar to that of the UV/optical EBL, implying that a significant amount of star formation over the history of the Universe has been obscured and its light reprocessed by dust. Following this, the population of galaxies now generally referred to as sub-millimetre galaxies (SMGs) was first revealed using the Sub-millimetre Common User Bolometer Array (SCUBA) on the 15 m diameter James Clerk Maxwell Telescope (JCMT, e.g. Smail et al. 1997; Hughes et al. 1998). SMGs are relatively bright in sub-millimetre bands (the first surveys focussed on galaxies with $S_{850\mu m} > 5$ mJy) and some studies have now shown that the bulk of the EBL at 850 μm can be resolved by the $S_{850\mu m} > 0.1$ mJy galaxy population (e.g. Chen et al. 2013). SMGs are generally understood to be massive, dust enshrouded galaxies with extreme infrared luminosities ($L_{IR} \gtrsim 10^{12}$ L$_\odot$) implying prodigious star formation rates (SFRs, 10^2–10^3 M$_\odot$ yr^{-1}), though this is heavily dependent on the assumed IMF (e.g. Blain et al. 2002; Casey et al. 2014).

One difficulty for sub-millimetre observations is the coarse angular resolution ($\sim 20''$ FWHM) of the ground-based single-dish telescopes used for many blank-field surveys. Recently, follow-up surveys performed with greater angular resolution ($\sim 1.5''$ FWHM) interferometers (e.g. Atacama Large Millimetre Array—ALMA, Plateau de Bure Interferometer—PdBI, Sub-Millimetre Array—SMA) targeted at

---

[1]The content of this Chapter is based on the article Cowley et al. 'Simulated observations of sub-millimetre galaxies: the impact of single-dish resolution and field variance', Monthly Notices of the Royal Astronomical Society, Volume 446, Issue 2, p. 1784–1798, published 21 November 2014. Reproduced with permission. All rights reserved, https://doi.org/10.1093/mnras/stu2179.

single-dish detected sources have indicated that the resolution of single-dish tele-
scopes had, in some cases, blended the sub-mm emission of multiple galaxies into
one single-dish source (e.g. Wang et al. 2011; Smolčić et al. 2012; Hodge et al. 2013).
Karim et al. (2013) showed the effect this blending has on the observed sub-mm
number counts, with the single-dish counts derived from the Large APEX (Atacama
Pathfinder EXperiment) BOlometer CAmera (LABOCA) Extended *Chandra* Deep
Field-South (ECDFS) Sub-millimetre Survey (LESS, Weiß et al. 2009) exhibiting a
significant enhancement at the bright end relative to counts derived from the ALMA
follow-up (ALMA LESS, ALESS). Compounding this difficulty is the fact that, with
the exception of the South Pole Telescope (SPT) survey presented in Vieira et al.
(2010),[2] ground-based sub-mm surveys have to date been pencil beams ($<0.7 \, \mathrm{deg}^2$)[3]
leaving interpretation of the observed results subject to field-to-field variations. In
particular, Michałowski et al. (2012a) found evidence that photometric redshift dis-
tributions of radio-identified counterparts of 1100 and $850 \, \mu\mathrm{m}$ selected SMGs in the
two non-contiguous SCUBA Half-Degree Extragalactic Survey (SHADES) fields
are inconsistent with being drawn from the same parent distribution. This suggests
that the SMGs are tracing different large-scale structures in the two fields.

Larger surveys have been undertaken at 250, 350 and $500 \, \mu\mathrm{m}$ from space using the
Spectral and Photometric Imagine REceiver (SPIRE, Griffin et al. 2010) instrument
on board the *Herschel* Space Observatory (Pilbratt et al. 2010). These are also affected
by coarse angular resolution; the SPIRE beam has a FWHM of $\sim 18''$, $25''$ and $37''$
at 250, 350 and $500 \, \mu\mathrm{m}$ respectively. However, number counts at these wavelengths
have been derived from SPIRE maps through stacking analysis (Béthermin et al.
2012) using the positions and flux densities of sources detected at $24 \, \mu\mathrm{m}$ as a prior.

In this Chapter we investigate the effect of both the angular resolution of single-
dish telescopes and field-to-field variations on observations of the SMG population.
To do so we utilise 50 randomly orientated lightcones computed from the Lacey et al.
(2016) model to create mock sub-mm surveys taking into account the effects of the
single-dish beam.

This Chapter is structured as follows: in Sect. 3.2 we introduce our method for
creating our $850 \, \mu\mathrm{m}$ mock sub-mm surveys and imaging. In Sect. 3.3 we present
our main results concerning the effects of the single-dish beam and field-to-field
variance. In Sect. 3.4 we make a detailed comparison of the predictions of our model
with the ALESS survey and in Sect. 3.5 we present our predicted single-dish number
counts at 450 and $1100 \, \mu\mathrm{m}$. We summarise our findings and conclude in Sect. 3.6.

---

[2]These authors surveyed $87 \, \mathrm{deg}^2$ at 1.4 (2) mm to a depth of 11 (4.4) mJy with a $63''$ ($69''$) FWHM
beam. Due to the flux limits and wavelength of this survey, the millimetre detections are mostly
gravitationally lensed sources (Vieira et al. 2013).

[3]As of September 2014. Larger surveys have now been completed (e.g. Geach et al. 2017).

3.2   Creating Mock Surveys

In order to create mock catalogues of our sub-mm galaxies we utilise the lightcone treatment described in Merson et al. (2013). Briefly, as the initial simulation volume side-length ($L_{\text{box}} = 500 \, h^{-1}\text{Mpc}$) corresponds to the co-moving distance out to $z \sim 0.17$, the simulation is periodically replicated in order to fully cover the volume of a typical SMG survey, which extends to much higher redshift. This replication could result in structures appearing to be repeated within the final lightcone, which could produce unwanted projection-effect artefacts if their angular separation on the 'mock sky' is small (Blaizot et al. 2005). As our fields are small in solid angle (0.5 deg^2) and our box size is large, we expect this effect to be of negligible consequence and note that we have seen no evidence of projection-effect artefacts in our mock sub-mm maps. Once the simulation volume has been replicated, a geometry is determined by specifying an observer location and lightcone orientation. An angular cut defined by the desired solid angle of our survey is then applied, such that the mock survey area resembles a sector of a sphere. The redshift of a galaxy in the lightcone is calculated by first determining the redshift (z) at which its host dark matter halo enters the observer's past lightcone. The positions of galaxies are then interpolated from the simulation output snapshots (z_i, z_{i+1}, where $z_{i+1} < z < z_i$) such that the real-space correlation function of galaxies is preserved. A linear k-correction interpolation is applied to the luminosity of the galaxy to account for the shift in $\lambda_{\text{rest}} = \lambda_{\text{obs}}/(1+z)$ for a given λ_{obs}, based on its interpolated redshift.

To create the 850 µm mock catalogues we apply a further selection criterion so that our galaxies have $S_{850\,\mu\text{m}} > 0.035$ mJy. This is the limit brighter than which we recover $\sim$90% of the 850 µm EBL, as predicted by our model (Fig. 3.1). We have checked that our simulated SMG population is not affected by incompleteness at this low flux limit, due to the finite halo mass resolution of the N-body simulation. To allow us to test field-to-field variance we generate 50×0.5 deg^2 lightcone surveys[4] with random observer positions and lines of sight. In Fig. 3.2 we show that the lightcone accurately reproduces the SMG number counts of our model. We also show in Fig. 3.2 the predicted 850 µm number counts from starburst (dotted line) and quiescent (dash-dotted line) galaxies in the model. Starburst galaxies dominate the number counts in the range $\sim$0.2−20 mJy. Turning off merger-triggered starbursts in this model has a negligible effect on the predicted number counts (Lacey et al. 2016), from this we have inferred that these bursts are predominately triggered by disc instabilities.

---

[4]In practise our surveys are 0.55 deg^2. This allows for galaxies outside the 0.5 deg^2 area to contribute to sources detected inside this area after convolution with the single-dish beam.
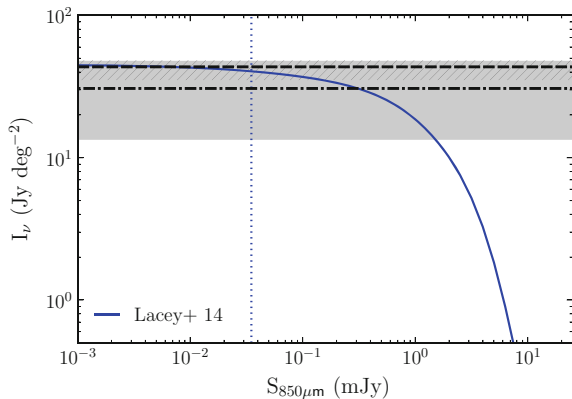
Fig. 3.1 Predicted cumulative extragalactic background light as a function of flux at 850 μm (*solid line*). The *horizontal dashed line* (Fixsen et al. 1998) and *dash-dotted line* (Puget et al. 1996) show the background light as measured by the *COBE* satellite. The *shaded* (Puget et al. 1996) and *hatched* (Fixsen et al. 1998) regions indicate the respective errors on the two measurements. The *vertical dotted line* indicates the flux limit above which 90% of the total predicted EBL is resolved. For historical reasons, the Lacey et al. (2016) model is referred to as 'Lacey+ 14' in this figure legend

3.2.1 Creating Sub-mm Maps

Here we describe the creation of mock sub-mm maps from our lightcone catalogues. First, we create an image by assigning the 850 μm flux of a galaxy to the pixel in which it is located, using a pixel size much smaller than the single-dish beam. This image is then convolved with a point spread function (PSF), modelled as a 2D Gaussian with a 15″ FWHM (∼SCUBA2/JCMT), and then re-binned into a coarser image with 2″ × 2″ pixels, to match observational pixel sizes. The resulting image is then scaled so that it is in units of mJy/beam. We refer to the output of this process as the astrophysical map (see Fig. 3.3a).

In order to model the noise properties of observational maps we add 'instrumental' Gaussian white noise to the astrophysical map. We tune the standard deviation of this noise such that after it has been matched-filtered (described below) the output is a noise map with $\sigma_{rms} \sim 1$ mJy/beam, comparable to jackknifed noise maps in 850 μm blank-field observational surveys (e.g. Coppin et al. 2006; Weiß et al. 2009; Chen et al. 2013).

It is a well known result in astronomy that the best way to find point-sources in the presence of noise is to convolve with the PSF (Stetson 1987). However, this is only optimal if the noise is Gaussian, and does not take into account 'confusion noise' from other point-sources. Chapin et al. (2011) show how one can optimise filtering for maps with significant confusion, through modelling this as a random (and thus un-clustered) superposition of point sources convolved with the PSF, normalised to the number counts inferred from $P(D)$ analysis of the maps. The PSF is then divided by the power spectrum of this confusion noise realisation. This results in a matched-
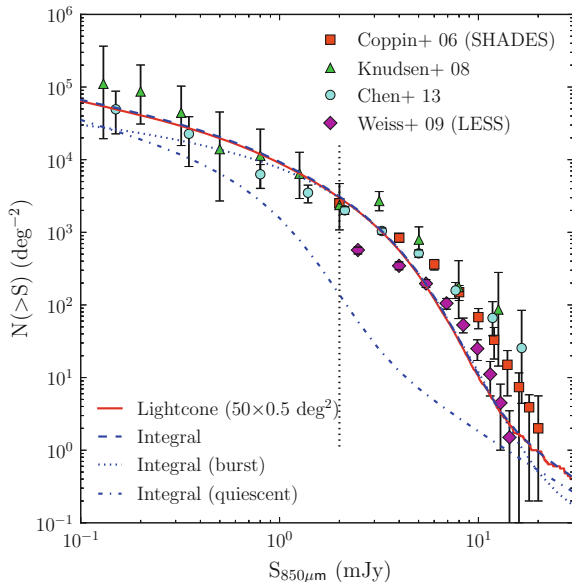
Fig. 3.2 Predicted cumulative number counts at 850 μm. Predictions from the lightcone catalogues (*red line*) and from integrating the luminosity function of the model (*dashed blue line*) are in excellent agreement. The *dotted* and *dash-dotted blue lines* show the contribution to the number counts from starburst and quiescent galaxies respectively. We compare the model predictions to single-dish observational data from Coppin et al. (2006; *orange squares*), Knudsen et al. (2008; *green triangles*), Weiß et al. (2009; *magenta diamonds*) and Chen et al. (2013; *cyan circles*). The *vertical dotted line* shows the approximate confusion limit (~2 mJy) of single-dish blank field surveys. Observational data fainter that this limit are derived from cluster-lensed surveys (see Sect. 3.3.1 for further discussion)

filter with properties similar to a 'Mexican-hat' kernel. An equivalent method is implemented in Laurent et al. (2005). Although our simulated maps contain a significant confusion background, for simplicity we do not implement such a method here, and have checked that the precise method of filtering does not significantly affect our source-extracted number counts.

Prior to source extraction, we constrain our astrophysical plus Gaussian noise map to have a mean of zero (Fig. 3.3b) and convolve with a matched-filter $g(x)$, given by

$$g(x) = \mathcal{F}^{-1} \left\{ \frac{s^*(q)}{\int |s(q)|^2 d^2q} \right\}, \tag{3.2.1}$$

where $\mathcal{F}^{-1}$ denotes an inverse Fourier transform, $s(q)$ is the Fourier transform of our PSF and the asterisk indicates complex conjugation. The denominator is the appropriate normalisation such that peak heights of PSF-shaped sources are preserved after filtering. Up to this normalisation factor, the matched-filtering is equivalent to convolving with the PSF. Point sources are therefore effectively convolved with the
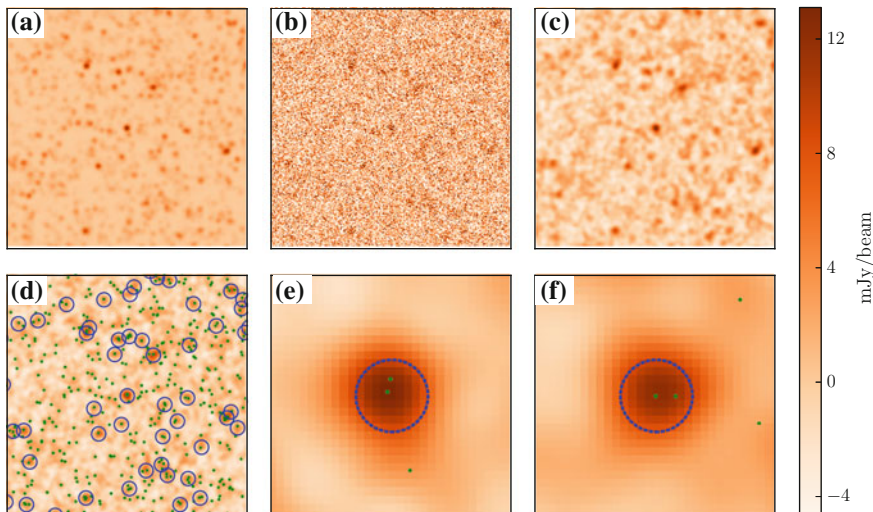
Fig. 3.3 Panels illustrating the mock map creation process at 850 μm. Panels **a**, **b**, **c** and **d** are 0.2×0.2 deg^2 and are centred on a 13.1 mJy source. **a** Astrophysical map including the effect of the telescope beam. **b** Astrophysical plus Gaussian white noise map, constrained to have zero mean. **c** Matched-filtered map. **d** Matched-filtered map with $S_{850\,\mu m} > 4$ mJy single-dish sources (*blue circles* centred on the source position) and $S_{850\,\mu m} > 1$ mJy galaxies (*green dots*) overlaid. **e** As for **d** but for a $0.5' \times 0.5'$ area, centered on the same 13.1 mJy source. The 2 galaxies within the $9''$ radius (*blue dotted circle*, $\sim$ALMA primary beam) of the source have fluxes of 1.2 and 11.2 mJy and redshifts of 1.0 and 2.0 respectively. **f** as for **e** but centred on a 12.2 mJy source. In this case the 2 galaxies within the central $9''$ radius have fluxes of 6.1 and 6.4 mJy and redshifts of 2.0 and 3.2 respectively

PSF twice, once by the telescope and once by the matched-filter. This gives our final matched-filtered map (Fig. 3.3c) a spatial resolution of $\sim 21.2''$ FWHM i.e. $\sqrt{2} \times 15''$.

For real surveys, observational maps often have large-scale filtering applied prior to the matched-filtering described above. This is to remove large-scale structure from the map, often an artefact of correlated noise of non-astrophysical origin. This is implemented by convolving the map with a Gaussian broader than the PSF and then subtracting this off the original, rescaling such that the flux of point sources is conserved (e.g. Weiß et al. 2009; Chen et al. 2013). As our noise is Gaussian, any excess in the power spectrum of the map on large-scales can only be attributed to our astrophysical clustering signal, so we choose not to implement any such high-pass filtering prior to our matched-filtering.

An example of one of our matched-filtered maps is shown in Fig. 3.4 and the associated pixel histogram in Fig. 3.5. The position of the peak of the pixel histogram is determined by the constraint that our maps have a zero mean after subtracting a uniform background. We attribute the broadening of the Gaussian fits from $\sigma = 1$ mJy/beam in our matched-filtered noise-only map to $\sigma = 1.2$ mJy/beam in our final

Fig. 3.4 An example of a matched-filtered map. Sources detected with $S_{850\,\mu m} > 4.5$ mJy by our source extraction algorithm are indicated by *blue circles*. The central 0.5 deg^2 region, from which we extract our sources, is indicated by the *black circle*
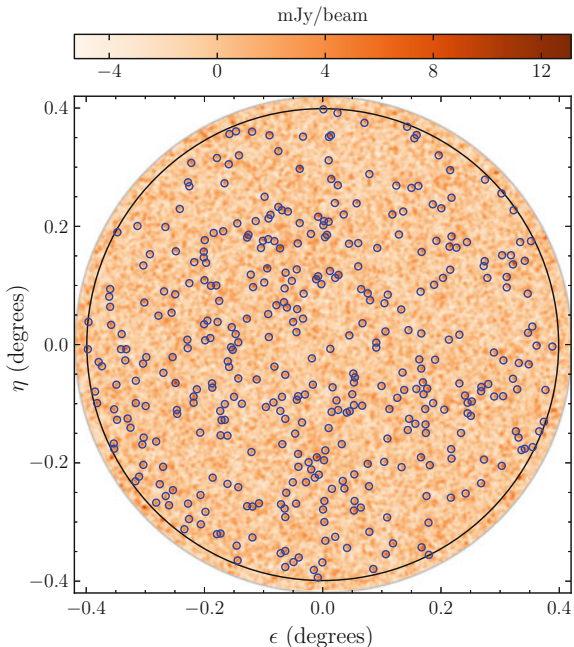
matched-filtered map to the realistic confusion background from unresolved sources in our maps.

For the source extraction we first identify the peak (i.e. brightest) pixel in the map. For simplicity we record the source position and flux to be the centre and value of this peak pixel. We then subtract the matched-filtered PSF, scaled and centred on the value and position of the peak pixel, from our map. This process is iterated down to an arbitrary threshold value of $S_{850\,\mu m} = 1$ mJy, resulting in our source-extracted catalogue.

3.3 Results

In this Section we present our main results: in Sect. 3.3.1 we show the effect the single-dish beam has on the predicted number counts through blending the sub-mm emission of galaxies into a single source. In Sect. 3.3.2 we quantify the multiplicity of blended sub-mm sources, in Sect. 3.3.3 we show that these blended galaxies are typically physically unassociated and in Sect. 3.3.4 we present the redshift distribution of SMGs in our model.
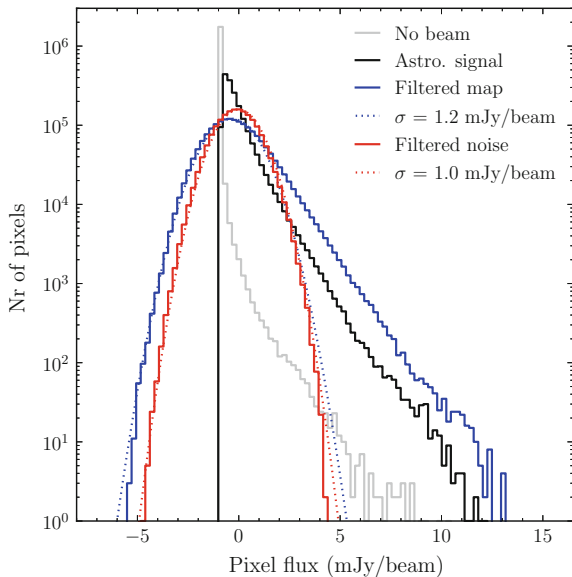
Fig. 3.5 Pixel flux histogram of the map shown in Fig. 3.4. The *grey* and *black lines* are the map before and after convolution with the single-dish beam respectively, with the same zero point subtraction applied as to our final matched-filtered map (*blue line*). The map is rescaled after convolution with the single-dish beam to convert to units of mJy/beam (*grey* to *black*), and during the matched-filtering due to the normalisation of the filter which conserves point source peaks (*black* to *blue*). *Dotted lines* show Gaussian fits to the matched-filtered noise-only (*red solid line*) and the negative tail of the final matched-filtered (*blue solid line*) map histograms respectively

3.3.1 Number Counts

The cumulative number counts derived from our lightcone and source-extracted catalogues are presented in Fig. 3.6. The shaded regions, which show the 10–90 percentiles of the distribution of number counts from the individual fields, give an indication of the field-to-field variation we predict for fields of 0.5 deg^2 area. This variation is comparable to or less than the quoted observational errors. Quantitatively, we find a field-to-field variation in the source-extracted number counts of 0.07 dex at 5 mJy and 0.34 dex at 10 mJy. A clear enhancement in the source-extracted number counts relative to those derived from our lightcone catalogues is evident at $S_{850\,\mu m} \gtrsim 1$ mJy. We attribute this to the finite angular resolution of the beam blending together the flux from multiple galaxies with projected on-sky separations comparable to or less than the size of the beam. Our source-extracted number counts show better agreement than our intrinsic lightcone counts with blank-field single-dish observational data above the confusion limit ($S_{lim} \approx 2$ mJy) of such surveys, which is indicated by the vertical dotted line in Fig. 3.6.
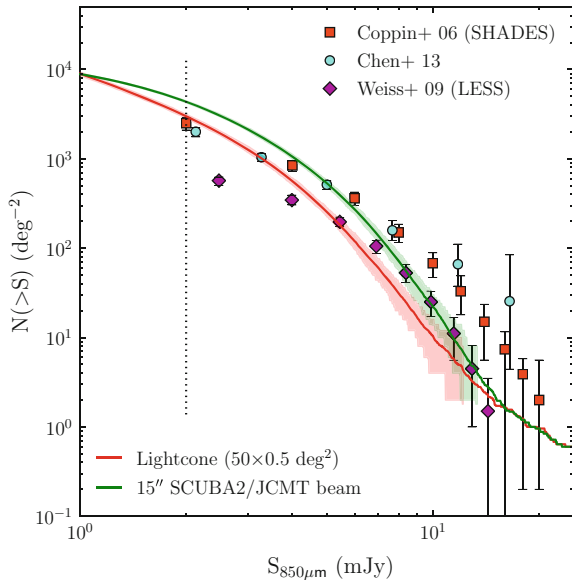
Fig. 3.6 The effect of single-dish beam size on cumulative 850 μm number counts. The *shaded regions* show 10–90 percentiles of the distribution of the number counts from the 50 individual fields, *solid lines* show counts from the combined 25 deg² field for the lightcone (*red*) and the 15″ FWHM beam source extracted (*green*) catalogues. The *vertical dotted line* at $S_{850\,\mu m} = 2$ mJy indicates the approximate confusion limit of single-dish surveys. The 15″ beam prediction is only to be compared at fluxes above this limit. Single-dish blank field observational data is taken from Coppin et al. (2006; *orange squares*) Weiß et al. (2009; *magenta diamonds*) and Chen et al. (2013; *cyan circles*)

Observational data fainter than this limit have been measured from gravitationally lensed cluster fields, where gravitational lensing due to a foreground galaxy cluster magnifies the survey area, typically by a factor of a few, but up to ∼20. The magnification increases the effective angular resolution of the beam, thus reducing the confusion limit of the survey and the instances of blended galaxies. The lensing also boosts the flux of the SMGs. These effects allow cluster-lensed surveys to probe much fainter fluxes than blank-field surveys performed with the same telescope. We show observational data in Fig. 3.2 at $S_{850\,\mu m} < 2$ mJy for comparison with our lightcone catalogue number counts, with which they agree well.

Figure 3.6 shows that at $S_{850\,\mu m} \gtrsim 5$ mJy our source-extracted counts agree best with the Weiß et al. (2009) data, taken from ECDFS. There is some discussion in the literature over whether this field is under-dense by a factor of ∼2 (see Sect. 4.1 of Chen et al. (2013) and references therein). Whilst the field-to-field variation in our model can account for a factor of ∼2 (at 10 mJy) it may be that our combined field source-extracted counts (and also those of Weiß et al.) are indeed underdense compared to number counts representative of the whole Universe.

At $2 \lesssim S_{850\,\mu m} \lesssim 5$ mJy our source-extracted number counts appear to follow a slightly steeper trend compared to the observed counts, this may be due to the underlying shape of our lightcone catalogue counts and the effect this has on our source-extracted counts. We stress here that the model was calibrated without regard to the precise effect the single-dish beam would have on the number counts. An extensive parameter search which shows the effect of varying certain parameters on the intrinsic number counts (and other predictions) of the model is presented in Lacey et al. (2016). We do not consider any variants of the model here, but it is possible that once the effects of the single dish beam have been taken into account some variant models will match other observational data better, and show different trends over the flux range of interest.

The observed number counts at faint fluxes, above the confusion limit, may also be affected by completeness issues. Whilst efforts are made to account for these in observational studies, they often rely on making assumptions about the number density and clustering of SMGs, so it is not clear that they are fully understood.

3.3.2   Multiplicity of Single-Dish Sources

Given that multiple SMGs can be blended into a single source, in this Section we quantify this multiplicity. For each galaxy within a 4σ radius[5] of a given $S_{850\,\mu m} > 2$ mJy source, we determine a flux contribution for that galaxy at the source position by modelling its flux distribution as the matched-filtered PSF with a peak value equal to that galaxy's flux. For example, a 5 mJy galaxy at a $\sim 10.6''$ ($\sigma \times \sqrt{2 \ln 2}$) radial distance from a given source will contribute 2.5 mJy at the source position. We do this for all galaxies within the 4σ search radius and label the sum of these contributions as the total galaxy flux of the source, $S_{\text{gal\_tot}}$. The fraction each galaxy contributes towards this total is the galaxy's flux weight. For each source we then interpolate the cumulative distribution of flux weights after sorting in order of decreasing flux weight, to determine how many galaxies are required to contribute a given percentage of the total.

We plot this as a function of source-extracted flux, which includes the effect of instrumental noise and the subtraction of a uniform background, in the top 4 panels of Fig. 3.7. Typically, 90% of the total galaxy flux of a 5 mJy source is contributed by $\sim 3-6$ galaxies and this multiplicity decreases slowly as source flux increases. This decrease follows intuitively from the steep decrease in number density with increasing flux in the number counts.

We note that this is not how source multiplicity is typically measured in observations. In Sect. 3.4.1 we discuss the multiplicity of ALESS sources in a way more comparable to observations, where we have considered the flux limit and primary

---

[5]We use the σ of our match-filtered PSF i.e. $\sqrt{2} \times$ FWHM$/2\sqrt{2 \ln 2} \approx 9''$, and choose 4σ so that the search radius is large enough for our results in this Section to have converged after our flux weighting scheme has been applied.

Fig. 3.7 *Top* 4 *panels*:
number of component
galaxies contributing the
percentage indicated in the
panel of the total galaxy flux
(see text) of a $S_{850\,\mu m} > 2$
mJy source. *Bottom panel*:
ratio of total galaxy flux to
source flux. *Black dashed
line* is a reference line drawn
at zero. *Solid line* shows
median and *errorbars*
indicate inter-quartile range
for a 2 mJy flux bin in all
panels. *Grey dots* show
individual sources, for clarity
only 10% of the sources have
been plotted
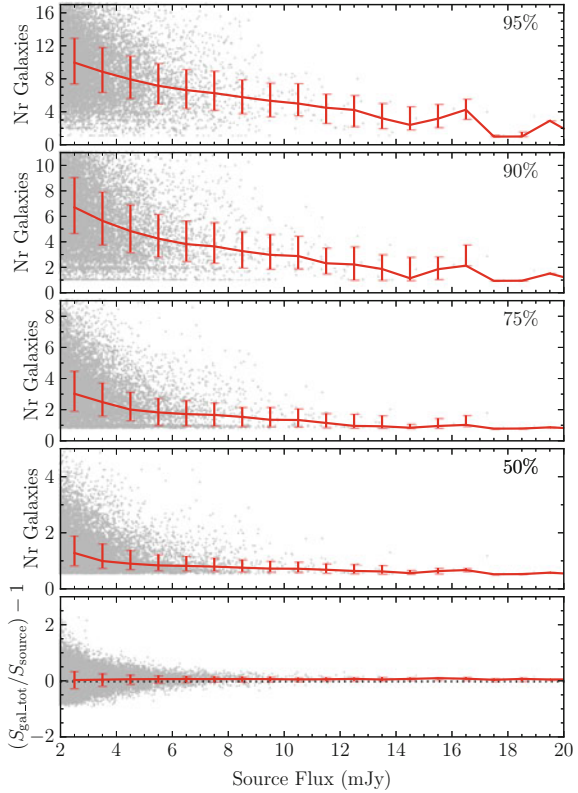
beam profile of ALMA, see also Table 3.1. Observational interferometric studies
which suggest that the multiplicity of single-dish sources may increase with increas-
ing source flux (e.g. Hodge et al. 2013) are likely to be affected by a combination
of the flux limit of the interferometer, meaning high multiplicity faint sources are
undetected, and small number statistics of bright sources.

We also show, in the bottom panel of Fig. 3.7, the ratio of the total galaxy flux to
source flux. The consistency with zero indicates that our source-extracted number
counts at 850 µm are not systematically biased. This is due to the competing effects
of subtracting a mean background in the map creation (which biases S_{source} low) and
the introduction of Gaussian noise (which biases S_{source} high due to Eddington bias
caused by the steeply declining nature of the number counts) effectively cancelling
each other out in this case. In Sect. 3.5 we find that our number counts at 450 µm
are strongly affected by Eddington bias, which we correct for in that case.

Fig. 3.8 Distribution of the logarithm of redshift separation (see text) of $S_{850\,\mu m} > 4$ mJy single-dish sources. The dominant peak at $\Delta z \approx 1$ implies that the majority of the blended galaxies are physically unassociated. The *hatched region* indicates the percentage ($\sim 36\%$) of sources for which $\Delta z = 0$ (see text in Sect. 3.3.3)
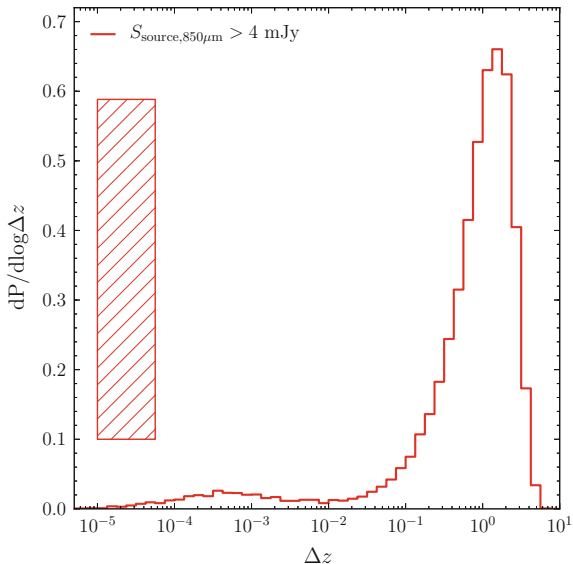
3.3.3 Physically Unassociated Galaxies

Given the multiplicity of our sources, we can further determine if the blended galaxies contributing to a source are physically associated, or if their blending has occurred due to a chance line of sight projection. For each source we define a redshift separation, Δz, as the inter-quartile range of the cumulative distribution of the flux weights (calculated as described above), where the galaxies have in this case first been sorted by ascending redshift. The distribution of Δz across our entire $S_{850\,\mu m} > 4$ mJy source population is shown in Fig. 3.8. The dominant peak at $\Delta z \approx 1$ is similar to the distribution derived from a set of maps which had galaxy positions randomised prior to convolution with the single-dish beam. This suggests that this peak is a result solely of a random sampling from the redshift distribution of our SMGs and thus that the majority of our sources are composed of physically unassociated galaxies with a small on-sky separation due to chance line of sight projection. This is unsurprising considering the large effective redshift range of sub-millimetre surveys, resulting from the negative k-corrections of SMGs. We attribute the secondary peak at $\Delta z \sim 5 \times 10^{-4}$ to clustering in our model. We also show as the hatched region the area ($\sim 36\%$) of sources for which $\Delta z = 0$. These are sources for which a single galaxy spans the inter-quartile range of the cumulative distribution described above, this can occur when the flux weight of that galaxy is >0.5 and must occur when the flux weight of that galaxy is >0.75. We understand that this is not how redshift separation would be defined observationally, and refer the reader to Sect. 3.4 and Fig. 3.12 for another definition of Δz. We note, however, that our conclusions in this Section are not sensitive to the precise definition of Δz.

Fig. 3.9 The predicted
redshift distribution for our
$50 \times 0.5 \ \text{deg}^2$ fields for the
flux limit indicated on each
panel. The *shaded region*
shows the 16–84 (1σ)
percentile of the distributions
from the 50 individual fields.
The *solid line* is the
distribution for the combined
25 deg^2 field. The *boxplots*
represent the distribution of
the median redshifts of the
50 fields, the *whiskers* show
the full range, with the *box*
and *central vertical line*
indicating the inter-quartile
range and median. The
errorbars show the expected
1σ variance due to Poisson
errors
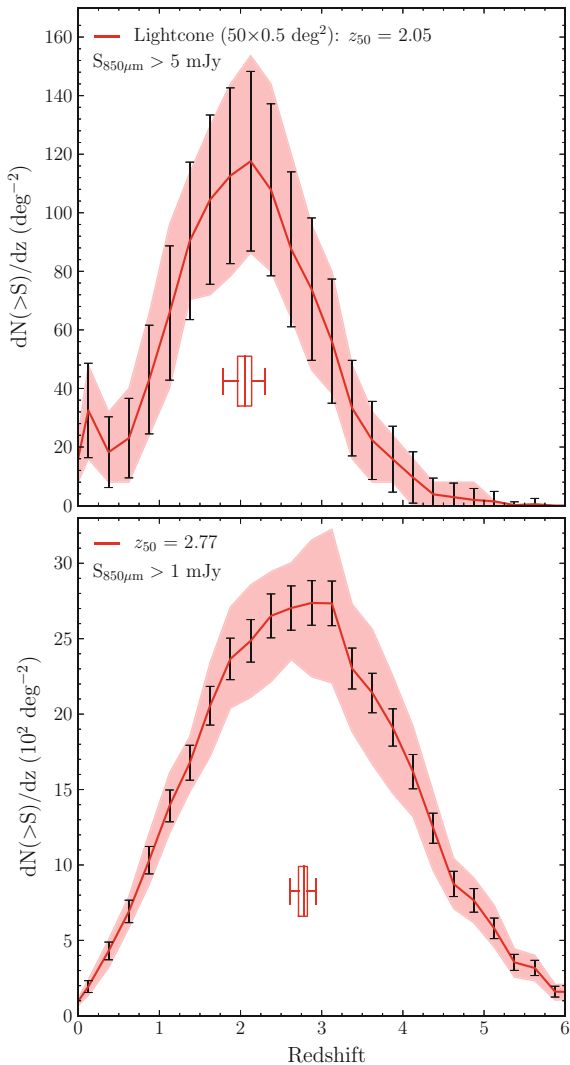
It is a feature of most current semi-analytical models that any star formation enhancement caused by gravitational interactions of physically associated galaxies prior to a merger event is not included. In principle this may affect our physically unassociated prediction, as in our model galaxy mergers would only become sub-mm bright post-merger, and would be classified as a single galaxy. However, as merger induced starbursts have a negligible effect on our sub-mm number counts, which are composed of starbursts triggered by disc instabilities (Lacey et al. 2016), we are confident our physically unassociated conclusion is not affected by this feature.

We note that this conclusion is in contrast to predictions made by Hayward et al. (2013). In this Hayward et al. model, halo merger trees from the *Bolshoi* simulation (Klypin et al. 2011) are populated with galaxies according to the abundance matching of Behroozi et al. (2013) and sub-mm fluxes are calculated according to the relation of Hayward et al. (2011), based on an empirically derived dust mass–gas mass–stellar mass relation. Hayward et al., in addition to physically unassociated blends, predict a more significant physically associated population than is presented here. However, we believe our work has a number of significant advantages over that of Hayward et al. (2013) in that: (i) galaxy formation is modelled here ab initio[6] with a model that can also successfully reproduce galaxy luminosity functions at $z = 0$; (ii) the treatment of blending presented here is more accurate through convolution with a beam, the inclusion of instrumental noise and matched-filtering prior to source-extraction, rather than a summation of sub-mm flux within some radius around a given SMG and; (iii) our $15''$ source-extracted number counts show better agreement with single-dish data for $S_{850\,\mu m} \gtrsim 5$ mJy, this is probably in part due to the exclusion of starbursts from the Hayward et al. model, though the effect including starbursts would have on the number counts in that model is not immediately clear.

3.3.4   Redshift Distribution

As we have shown that sub-mm sources are composed of multiple galaxies at different redshifts, for this Section we consider our lightcone catalogues *only*.

The redshift distributions for the 'bright' $S_{850\,\mu m} > 5$ mJy and 'faint' $S_{850\,\mu m} > 1$ mJy galaxy populations are shown in Fig. 3.9. The shaded region shows the 16–84 (1σ) percentiles of the distributions from the 50 individual fields, arising from field-to-field variations. The errorbars indicate the 1σ Poisson errors. The bright SMG population has a lower median redshift ($z_{50} = 2.05$) than the faint one ($z_{50} = 2.77$). We note that the median redshift appears to be a robust statistic with an inter-quartile range of 0.17 (0.11) for the bright (faint) population for the 0.5 deg^2 field size

---

[6]In the sense that it begins at high redshift ($z \gtrsim 20$).

assumed. The field-to-field variation seen in the bright population is comparable to the Poisson errors and thus random variations, whereas this field-to-field variation is greater compared to Poisson for the faint population. In order to further quantify this field-to-field variance, we have performed the Kolmogorov-Smirnoff (K-S) test between the 1225 combinations of our 50 fields, for the bright and faint populations. We find that for the bright population the distribution of p-values is similar to that obtained if we perform the same operation with 50 random samplings of the parent field, though with a slightly more significant low p-value tail. Approximately 10% of the field pairs exhibit $p < 0.05$, suggesting that it is not necessarily as uncommon as one would expect by chance to find that redshift distributions derived from non-contiguous pencil beams of sky fail the K-S test, as in Michałowski et al. (2012a). For the faint population, 92% of the field pairs have $p < 0.05$.

Thus, it appears that the bright population in the individual fields is more consistent with being a random sampling of the parent 25 deg^2 distribution. This is due to: (i) the number density of the faint population being $\sim$30 times greater than the bright population, which significantly reduces the Poisson errors; and (ii) the median halo mass of the two populations remaining similar, $7.6\,(5.5) \times 10^{11}\ h^{-1}M_{\odot}$ for our bright (faint) population implying that the two populations trace the underlying matter density with a similar bias. We consequently predict that as surveys probe the SMG population down to fainter fluxes, we expect that they become more sensitive to field-to-field variations induced by large-scale structure.

3.4 Comparison to ALESS

In this Section we make a detailed comparison of our model with observational data from the recent ALMA follow-up survey (Hodge et al. 2013) of LESS (Weiß et al. 2009), referred to as ALESS. LESS is an 870 μm LABOCA (19.2″ FWHM) survey of 0.35 deg^2 (covering the full area of the ECDFS) with a typical noise level of $\sigma \sim 1.2$ mJy/beam. Weiß et al. (2009) extracted 126 sources based on a S/N $> 3.7\sigma$ ($\simeq S_{870\,\mu m} > 4.5$ mJy) at which they were $\sim$70% complete. Of these 126 sources, 122 were targeted for cycle 0 observations with ALMA. From these 122 maps, 88 were selected as 'good' based on their rms noise and axial beam ratio, from which 99 sources were extracted down to $\sim$1.5 mJy. The catalogue containing these 99 sources is presented in Hodge et al. (2013), with the resulting number counts and photometric redshift distribution being presented in Karim et al. (2013) and Simpson et al. (2014) respectively. For the purposes of our comparison we randomly sample (without replacement) 70% ($\sim$88/126) of our $S_{850\,\mu m} > 4.5$ mJy sources from the central 0.35 deg^2 of our 50 mock maps.[7] Around all of these sources we place 18″ diameter masks ($\sim$ALMA primary beam). From these we extract 'follow-up' galaxies down to a minimum flux of $S_{850\,\mu m} = 1.5$ mJy from the relevant lightcone

---

[7]We re-calculate the 'effective' area of our follow-up surveys as $0.35\,\mathrm{deg}^2$ $\times N_{\mathrm{Good\ ALMA\ Maps}}/N_{\mathrm{LESS\ Sources}} \approx 0.25\,\mathrm{deg}^2$ as in Karim et al. (2013).

catalogue. We take into account the profile of the ALMA primary beam for this, modelling it as a Gaussian with an $18''$ FWHM, such that lightcone galaxies at a radius of $9''$ from a source are required to be > 3 mJy for them to be 'detected'. The result of this procedure is our 'follow-up' catalogue. We note that we do not attempt to simulate and extract sources from ALMA maps.

3.4.1 Number Counts and Source Multiplicity

We present the number counts from our simulated follow-up catalogues in Fig. 3.10 and observe a similar difference between our simulated single-dish and follow-up number counts as the (A)LESS survey found in their observed analogues (Weiß et al. (2009) and Karim et al. (2013) respectively). Also evident is the bias inherent in our simulated follow-up compared to our lightcone catalogues at fluxes fainter than the source extraction limit of the single-dish survey. This arises because follow-up galaxies are only selected due to their on-sky proximity to a single-dish source, so they are not representative of a blank-field population. For this reason Karim et al. (2013) do not present number counts fainter than the source extraction limit of LESS, despite the ability of ALMA to probe fainter fluxes. Whilst our model agrees well with both interferometric and single-dish data at bright fluxes, as discussed in Sect. 3.3.1, our single-dish predictions are in excess of the Weiß et al. (2009) data at fainter fluxes ($S_{850\,\mu m} \lesssim 7$ mJy). We also observe a minor excess in our 'follow-up' number counts when we compare to the Karim et al. (2013) data for $S_{850\,\mu m} \lesssim 5$ mJy.

We show the ratio of the brightest follow-up galaxy flux for each source to the source flux in Fig. 3.11 and our prediction is in excellent agreement with the observed sample, with the brightest of our follow-up galaxies being roughly 70% of the source flux on average. This fraction is approximately constant over the range of source fluxes probed by LESS. The scatter of our simulated data is also comparable to that seen observationally. Not plotted in Fig. 3.11 are sources for which the brightest

Table 3.1 A breakdown of the number of ALMA components from our simulated sample for comparison with the observed sample of Hodge et al. (2013). The columns are: (1) the number of ALMA components; (2) the percentage of our simulated sources with that number of ALMA components; (3) the percentage of observed LESS sources with 'good' ALMA maps that contain that number of ALESS components, errors are Poisson; and (4) the number of observed LESS sources with 'good' ALMA maps that contain that number of ALMA components

N	Sim. (%)	Obs. (%)	Obs. (/88)
0	10.6	22 ± 5	19
1	72.2	51 ± 8	45
2	16.5	22 ± 5	19
3	0.70	5 ± 3	4
4	0.01	1 ± 1	1
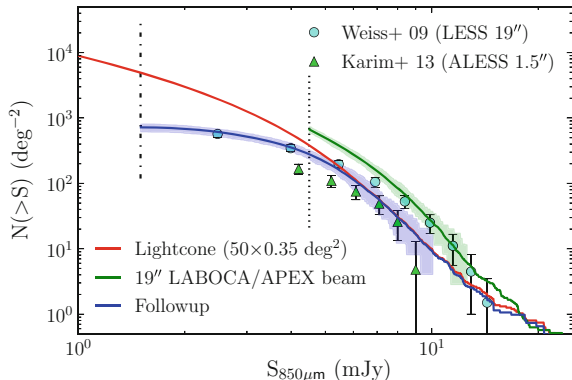
Fig. 3.10 Comparison with (A)LESS number counts. The *blue line* is our prediction for our com-bined (17.5 deg²) follow-up catalogues (described in text) and is to be compared to the ALESS number counts presented in Karim et al. (2013; *green triangles*). The *green line* is our 19″ source-extracted number counts for the combined (17.5 deg²) field and is to be compared to the number counts presented in Weiß (2009; *cyan circles*). The *shaded regions* indicate the 10–90 percentiles of the distribution of the individual (0.35 deg²) field number counts. The *red line* is the number counts for the combined field from our lightcone catalogues. The *vertical dotted* and *dash-dotted lines* indicate the 4.5 mJy single-dish source-extraction limit of LESS and the 1.5 mJy maximum sensitivity of ALMA respectively

galaxy is below the flux limit of ALMA. These account for ~10% of our sources. Hodge et al. (2013) found that ~21 ± 5% of the 88 ALMA 'Good Maps' yielded no ALMA counterpart. The greater fraction of blank maps in the observational study could be caused by extended/diffuse SMGs falling below the detection threshold of ALMA and/or a greater source multiplicity in the observed sample. We present a breakdown of the predicted ALMA multiplicity of our simulated LESS sources compared to the observed Hodge et al. (2013) sample in Table 3.1. Our simulated follow-up catalogue is consistent with the observed sample at ~2σ. However, we caution that it is difficult to draw strong conclusions from this comparison due to the relatively small number of observed sources. We also note that we observe a similar trend for increasing source multiplicity with flux to that suggested in Hodge et al. (2013). For example, at $S_{850\,\mu m} = 5$ mJy the fraction of simulated sources with 2 ALMA components is ~10% increasing to ~40% at $S_{850\,\mu m} = 10$ mJy with the fraction of simulated sources with 1 ALMA component decreasing from ~70% to ~60% over the same flux range. This is in contrast to conclusions drawn from Fig. 3.7 and shows that this observed trend is probably caused by the flux limit of the interferometer, meaning that faint components are undetected.

For comparison with future observations we calculate Δz for all of our sources with ≥2 ALMA components as the redshift separation of the brightest two. We show the resulting distribution in Fig. 3.12. It is of a similar bimodal shape to the distribution presented in Fig. 3.8 and supports the idea that, in our model, blended galaxies are predominantly chance line of sight projections with a minor peak at
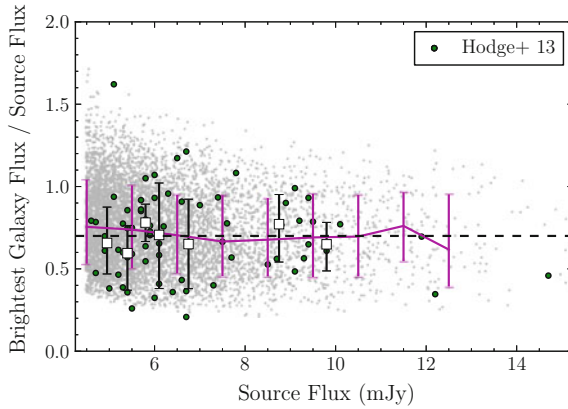
Fig. 3.11 Ratio of brightest galaxy component flux to single-dish source flux. *Grey scatter points* show the brightest galaxies from our targeted sources over the combined 17.5 deg^2 simulated field. The *solid line* shows the median in a given flux bin. Observational data is taken from the Hodge et al. (2013) ALESS catalogue. The *white squares* indicate the median observational flux ratio and source flux in a given bin, with the binning chosen such that there are roughly equal numbers of sources in each bin. *Error bars* indicate the 1σ percentiles of the ratio distribution in a given flux bin for both simulated and observed data. The *black dashed line* is a reference line drawn at 70%

Fig. 3.12 Distribution of the logarithm of redshift separation of the brightest two ALMA components of a $S_{850\,\mu m} > 4.5$ mJy single-dish source for our combined (17.5 deg^2) field
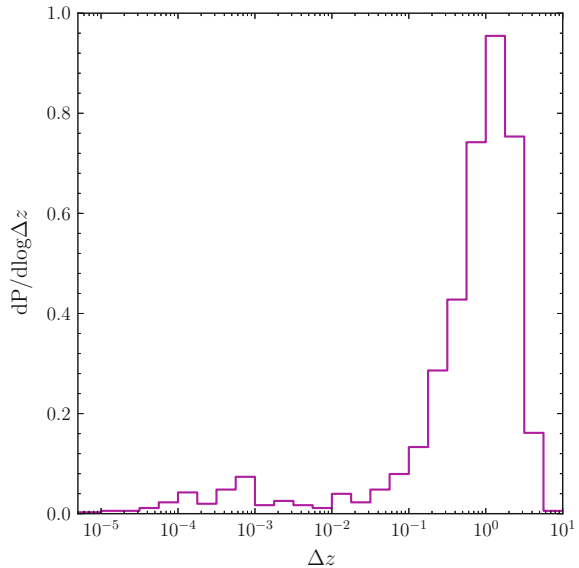
small Δz due to clustering. We leave this as a prediction for future spectroscopic redshift surveys of interferometer identified SMGs (e.g. Danielson et al. 2017).

3.4.2 Redshift Distribution

One of the main advantages of the 99 ALMA sources identified in Hodge et al. (2013) is that the greater positional accuracy ($\sim$0.2″) provided by ALMA allows accurate positions to be determined without introducing biases associated with selection at wavelengths other than sub-mm (e.g. radio). Simpson et al. (2014) derived photometric redshifts for 77 of 96 ALMA SMGs.[8] The remaining 19 were only detected in $\leq$ 3 bands and so reliable photometric redshifts could not be determined. Redshifts for these 'non-detections' were modelled in a statistical way based on assumptions regarding the H-band absolute magnitude (M_H) distribution of the 77 'detections' (see Simpson et al. 2014, for more details). We compare the redshift distribution presented in Simpson et al. (2014) to that of our simulated follow-up survey in Fig. 3.13. For the purposes of this comparison we have included the $P(z)$, the sum of the photometric redshift probability distributions for each galaxy, with (solid green line) and without (dotted green line) the H-band modelled redshifts.

Our model exhibits a high redshift ($z > 4$) tail when compared to the top panel of Fig. 3.9, due to the inclusion of fainter galaxies in this sample, and is in excellent agreement with the median redshift of the observed distribution. We performed the K-S test between each of our 50 follow-up redshift distributions and the ALESS distribution and find a low median p value of 0.16 with 18% of the K-S tests exhibiting $p < 0.05$. We do note, however, that the M_H band modelling of the 19 'non-detections' ($\sim$20% of the sample), and the sometimes significant photometric errors may affect the observed distribution.

We also investigate whether or not our model reproduces the same behaviour as seen in ALESS between redshift and $S_{850\,\mu m}$ in Fig. 3.14. Our model predicts that at lower redshift our simulated SMG population is generally brighter whilst in the observational data the opposite appears to be the case. However, Simpson et al. (2014) argue that this trend in their data is not significant and that their non-detections, 14/19 of which are at $S_{870\,\mu m} < 2$ mJy, would most likely render it flat if redshifts could be determined for these galaxies.

3.5 Multi-wavelength Surveys

Until now we have focussed on surveys performed at 850 μm, traditionally the wavelength at which most ground-based sub-mm surveys have been performed due to the atmospheric transmission window at this wavelength (e.g. Holland et al. 2013). However, there are now a number of observational blank-field surveys performed at other sub-mm wavelengths (e.g. Scott et al. 2012; Chen et al. 2013; Geach et al. 2013). In this Section we briefly investigate the effects of the finite single-dish beam-size at 450 μm ($\sim$8″ FWHM e.g. SCUBA2/JCMT) and 1100 μm ($\sim$28″ FWHM e.g.

---

[8]Three of the 99 SMGs presented in Hodge et al. (2013) lay on the edge of ECDFS with coverage in only two IRAC bands, and so were not considered further in Simpson et al. (2014).
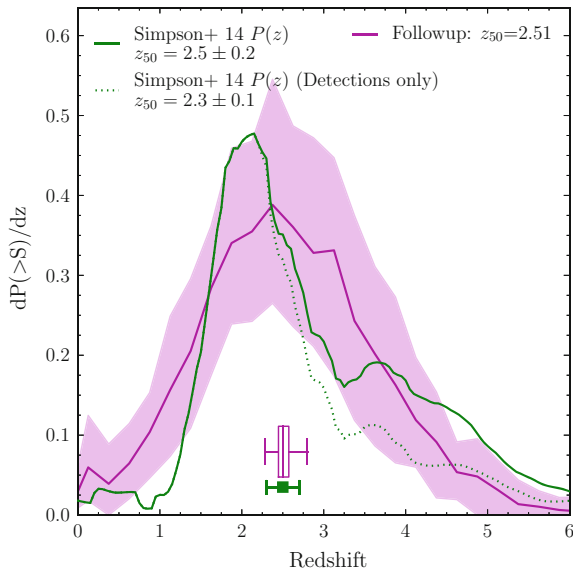
Fig. 3.13 Comparison of normalised redshift distributions for the simulated and observed ALESS surveys. We show the Simpson et al. (2014) $P(z)$, the sum of the photometric redshift probability distributions of each galaxy, both including redshifts derived from H-band absolute magnitude modelling for 'non-detections' (see Simpson et al. for details, *solid green line*) and for photometric detections only (*dotted green line*). The *square marker* indicates the observed median redshift (including H-band modelled redshifts), with associated errors. The *magenta solid line* is the distribution for the simulated, combined 17.5 deg^2 field with the *shaded region* showing the 10–90 percentiles of the distributions from the 50 individual fields. The *boxplot* shows the distribution of median redshifts for each of the 50 individual fields, the *whiskers* indicate the full range, with the *box* and *vertical line* indicating the inter-quartile range and median respectively

AZTEC/ASTE[9]). We add that due to our dust model the results presented in this Section are genuine multi-wavelength predictions and do not rely on applying an assumed fixed flux ratio.[10]

We create lightcones as described in Sect. 3.2, taking the lower flux limit at which we include galaxies in our lightcone catalogue as the limit above which 90% of the EBL is resolved at that wavelength, as predicted by our model. This is 0.125 (0.02) mJy at 450 (1100) μm. As at 850 μm, our EBL predictions are in excellent agreement with observational data from the *COBE* satellite. At 450 (1100) μm we predict a background of 140.1 (23.9) Jy deg^{-2} compared to $142.6^{+177.1}_{-102.4}$ ($24.8^{+26.5}_{-20.8}$) Jy deg^{-2} found observationally by Fixsen et al. (1998). We follow the same procedure

---

[9]Aztronomical Thermal Emission Camera/Atamaca Sub-millimetre Telescope Experiment.

[10]450 μm galaxies at high redshift ($z \gtrsim 5.5$) have $\lambda_{rest} < 70$ μm and therefore the sub-mm flux calculated by our dust model may be systematically incorrect when compared to GRASIL predictions (see Sect. 2.9 and Appendix C). We expect the contribution of such galaxies to our 450 μm population to be small.
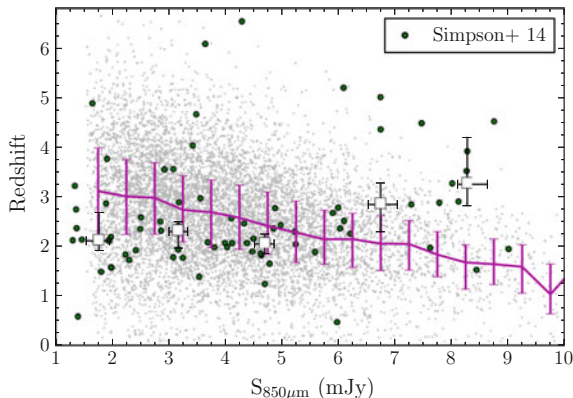
Fig. 3.14 Relation between $S_{850\,\mu m}$ and redshift for our simulated follow-up galaxies over our combined 17.5 deg^2 field. *Solid line* shows the median redshift in a given 1 mJy $S_{850\,\mu m}$ bin with *errorbars* indicating the inter-quartile range. Observational data from Simpson et al. (2014) has been binned in 2 mJy bins, with the median redshift plotted as the *white squares* with *errorbars* indicating 1σ bootstrap errors
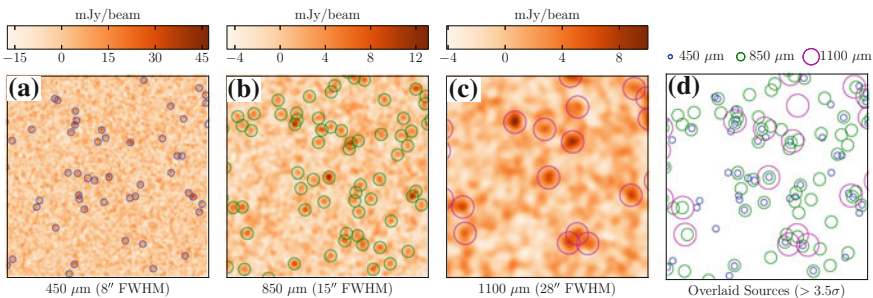
Fig. 3.15 Thumbnails of the same 0.2×0.2 deg^2 area as depicted in panels **a**, **b**, **c** and **d** of Fig. 3.3 but at **a** 450 μm, **b** 850 μm and **c** 1100 μm. Overlaid are the $>3.5\sigma$ sources, as *circles* centred on the source position with a radius of $\sqrt{2}\times$FWHM of the telescope beam at that wavelength. In **d** the $>3.5\sigma$ sources at each wavelength are overlaid, without background for clarity

as described in Sect. 3.2.1 for creating our mock maps. However, we change the standard deviation of our Gaussian white noise such that the match-filtered noise-only maps have a σ of $\sim$4(1) mJy/beam at 450 (1100) μm to be comparable to published blank-field surveys at that wavelength (e.g. Aretxaga et al. 2011; Casey et al. 2013).

Thumbnails of the same area, but for different wavelength maps, are shown for comparison in Fig. 3.15. The effect of the beam size increasing with wavelength is clearly evident, as is the resulting multiplicity of some of the sources. Drawing physical conclusions from this source multiplicity is not trivial. Selection at shorter wavelengths tends to select lower redshift and/or hotter dust temperature galaxies. For example, for an arbitrary flux limit of 1 mJy the median redshifts of the 450, 850
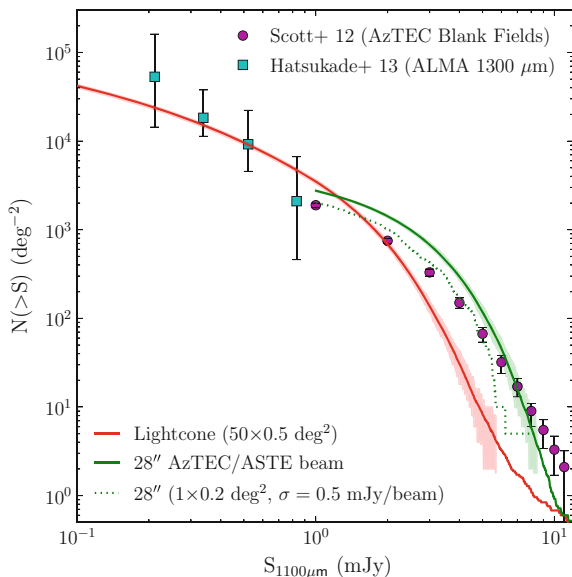
Fig. 3.16 Predictions for cumulative blank-field single-dish number counts at 1100 μm. Number counts from our lightcone (*red line*) and 28″ FWHM beam ($\sigma = 1$ mJy/beam) source-extracted (*green solid line*) catalogues are shown. The *shaded regions* are the 10–90 percentiles of our individual field number counts. We also show number counts derived from a smaller field with Gaussian white noise of $\sigma = 0.5$ mJy/beam (*green dotted line*). Blank field single-dish observational data is taken from Scott et al. (2012; *magenta circles*) and serendipitous ALMA 1300 μm number counts from Hatsukade et al. (2013; *cyan squares*) assuming $S_{1300\,\mu m}/S_{1100\,\mu m} = 0.71$

and 1100 μm populations in our model are 2.31, 2.77 and 2.93 respectively. This is complicated further by the fact that, as we have shown in this Chapter, at sub-mm wavelengths single-dish detected sources are likely to be composed of multiple individual galaxies, which may (or may not) also be bright at other wavelengths depending on the SED of the object, and that these galaxies are generally physically unassociated. If we restrict our analysis to galaxies only, thus avoiding complications caused by the single-dish beam, and consider flux limits of 12, 4 and 2 mJy at 450, 850 and 1100 μm respectively[11] we find median redshifts of 1.71, 2.26 and 2.55 for selection at each wavelength respectively. If we now consider a sample that satisfy these selection criteria at all wavelengths we find a median redshift of $z = 2.09$, and that this sample comprises 52, 80 and 66% of the single band selected samples at 450, 850 and 1100 μm respectively. It is unsurprising that the multi-wavelength selected sample overlaps most with the intermediate 850 μm band.

In Fig. 3.16 we present the 1100 μm number counts from our source-extracted and lightcone catalogues. The observational data from Scott et al. (2012) is a combined sample of previously published blank field single-dish number counts from

---

[11]These flux limits were motivated by the median flux ratios of our lightcone galaxies of $S_{1100\,\mu m}/S_{850\,\mu m} \approx 0.5$ and $S_{850\,\mu m}/S_{450\,\mu m} \approx 0.3$.

surveys of varying area and sensitivity with a total area of 1.6, 1.22 deg^2 of which were taken using using the AzTEC/ASTE configuration. As at 850 μm, considering the effects of the finite beam-size brings the model into better agreement with the single-dish observational data. We also plot, from Hatsukade et al. (2013), 1300 μm number counts derived from serendipitous detections found in targeted ALMA observations of star-forming galaxies at $z \sim 1.4$ (converted to 1100 μm counts assuming $S_{1300\,μm}/S_{1100\,μm} = 0.71$ as is done in Hatsukade et al.). These benefit from the improved angular resolution of the ALMA instrument $\sim$0.6-1.3″ FWHM and can thus probe to fainter fluxes than the single-dish data. Due to the higher angular resolution of these observations they are to be compared to the lightcone catalogue number counts (red line) and show good agreement with our model. However, we caution that due to the targeted nature of the Hatsukade et al. observations they may not be an unbiased measure of a blank field population. As the Scott et al. (2012) counts are derived from multiple fields of varying area and sensitivity, we also show in Fig. 3.16 number counts derived from a single 0.2 deg^2 field which has matched-filtered noise of 0.5 mJy/beam (green dotted line), similar to the 1100 μm counts from the SHADES fields (Hatsukade et al. 2011) used in the (Scott et al. 2012) sample. This shows better agreement with the Scott et al. data in the range $1 \lesssim S_{1100\,μm} \lesssim 5$ mJy (at brighter fluxes the smaller field will suffer from a lack of bright objects) which leads us to the conclusion that the discrepancy between our $\sigma = 1$ mJy/beam number counts (green solid line) and the Scott et al. (2012) data is due more to our assumed noise than of physical origin. As instrumental/atmospheric noise is unlikely to be Gaussian white noise in real observations, and various methods are used in filtering the observed maps to account for this, which we do not model here, we consider further investigation of the effect of such noise on observations beyond the scope of this work. At $\gtrsim 5$ mJy our $\sigma = 1$ mJy/beam, 0.5 deg^2 number counts (solid green line) agree well with the Scott et al. (2012) data, as the field size is more comparable to the largest field used in Scott et al. (0.7 deg^2), and instrumental noise will have less of an effect on both the simulated and observational data.

The number counts at 450 μm are presented in Fig. 3.17. We attribute the enhancement in our simulated source-extracted counts at $S_{450\,μm} \sim 8$ mJy to Eddington bias caused by the instrumental noise rather than an effect of the 8″ beam. In order to account for this we 'deboost' our $S_{450\,μm} > 5$ mJy sources following a method similar to one outlined in Casey et al. (2013). The total galaxy flux of each of our $S_{450\,μm} > 5$ mJy sources is calculated as described in Sect. 3.3.2 and we plot this as a ratio of source flux in Fig. 3.18. We multiply the flux of our 450 μm sources by the median of this ratio (red line) before re-calculating the number counts (green dotted line in Fig. 3.17). These corrected number counts show good agreement with observational data in the flux range $5 \lesssim S_{450\,μm} \lesssim 20$ but may slightly overestimate the counts for $S_{450\,μm} \gtrsim 20$.
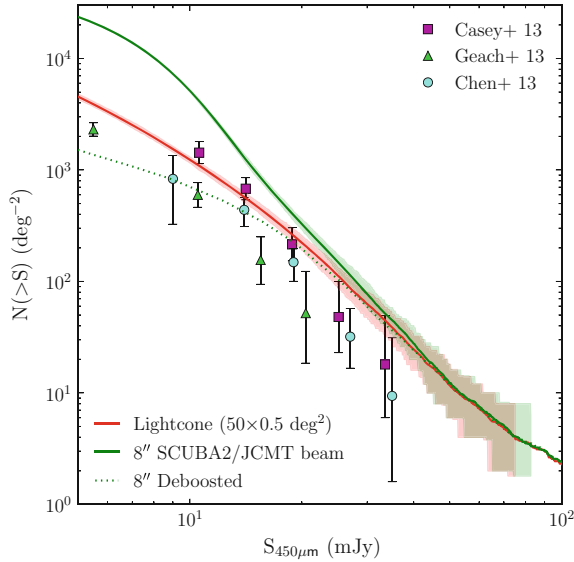
Fig. 3.17 Predictions for cumulative blank-field single-dish number counts at 450 µm. Number counts from our lightcone (*red*) and 8″ FWHM beam ($\sigma = 4$ mJy/beam) source-extracted (*green*) catalogues are shown for our combined 25 deg² field. The *dotted green line* shows the de-boosted source-extracted counts for the combined field (see text). The *shaded regions* show the 10–90 percentiles of our individual field number counts. Observational data is taken from Casey et al. (2013; *magenta squares*), Geach et al. (2013; *green triangles*) and Chen et al. (2013; *cyan circles*)

Fig. 3.18 Ratio of total galaxy flux (see Sect. 3.3.2) to source flux at 450 µm. *Solid line* and *errorbars* shows median and inter-quartile range in a given logarithmic flux bin respectively. For clarity, only 5% of sources have been plotted as *grey dots*
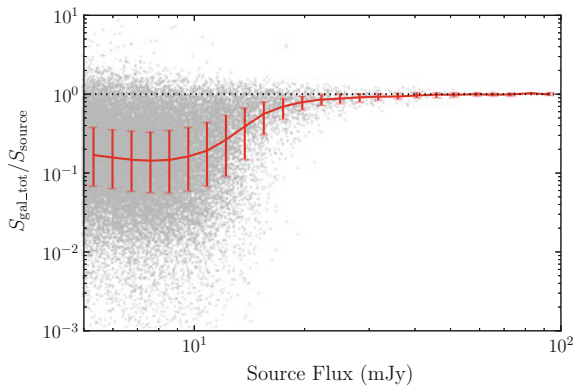
3.6 Conclusions

In this Chapter we presented predictions for the effect of the coarse angular-resolution of single-dish telescopes, and field-to-field variations, on observational surveys of SMGs. A new version of the GALFORM semi-analytic galaxy formation model is coupled with a simple model for computing the reprocessing of stellar radiation

by dust in order to predict the sub-mm emission from the simulated galaxies. We use a sophisticated lightcone method to generate mock catalogues of SMGs out to $z = 8.5$, from which we create mock sub-mm maps replicating observational techniques. Sources are extracted from these mock maps to generate our source-extracted catalogue and show the effects of the single-dish beam on the predicted number counts. To ensure a realistic background in our maps, we include model SMGs down to the limit above which 90% of our total predicted EBL is resolved. Our model shows excellent agreement with EBL observations from the *COBE* satellite at 450, 850 and 1100 µm. We generate 50×0.5 deg^2 randomly oriented surveys to investigate the effects of field-to-field variations.

The number counts from our 850 µm source-extracted catalogues display a significant enhancement over those from our lightcone catalogues at brighter fluxes ($S_{850\,\mu m} > 1$ mJy) due to the sub-mm emission from multiple SMGs being blended by the finite single-dish beam into a single source. The field-to-field variations predicted from both lightcone and source-extracted catalogues for the 850 µm number counts are comparable to or less than quoted observational errors, for simulated surveys of 0.5 deg^2 area with a 15″ FWHM beam ($\sim$SCUBA2/JCMT). Quantitatively we predict a field-to-field variation of 0.34 dex at $S_{850\mu m} = 10$ mJy in our source-catalogue number counts. Typically $\sim 3-6$ galaxies to contribute 90% of the galaxy flux of an $S_{850\,\mu m} = 5$ mJy source, and this multiplicity slowly decreases with increasing flux over the range of fluxes investigated by blank-field single-dish surveys at 850 µm. We find further that these blended galaxies are mostly physically unassociated, i.e. their redshift separation implies that they are chance projections along the line of sight of the survey.

Our redshift distributions predict a median redshift of $z_{50} = 2.0$ for our 'bright' ($S_{850\,\mu m} > 5$ mJy) galaxy population and $z_{50} = 2.8$ for our 'faint' ($S_{850\,\mu m} > 1$ mJy) galaxy population. We leave these as predictions for blank field interferometric surveys of comparable area. We also observe that the field-to-field variations we predict for our bright population are comparable to those expected for Poisson errors, whereas for our faint population the field-to-field variations are greater than Poisson.

A comparison between the ALESS survey and our model reveals that the model can reproduce the observed difference between observed single-dish and interferometer number counts, as well as estimates for the multiplicity of single-dish sources consistent (at $\sim 2\sigma$) with those derived observationally. It is in excellent agreement with observed relations between the flux of the brightest interferometric counterpart of a source and the source flux. The model also reproduces the median redshift of the observed photometric redshift distribution. In addition, we predict that the majority of the interferometric counterparts are physically unassociated, and leave this as a prediction for future spectroscopic redshift surveys of such objects.

We also present predictions for our lightcone and source-extracted catalogue number counts at 450 and 1100 µm, which show good agreement with the observational data. It is evident that the finite beam-size does not lead to a significant enhancement of the number counts at 450, as opposed to 850 and 1100 µm, as the beam-size at 450 µm is significantly smaller. At 1100 µm we show that the model agrees well with both interferometric and single-dish observational number counts. Due to our dust

model these are genuine multi-wavelength predictions and do not rely on applying an assumed fixed flux ratio.

Our results highlight the importance of considering effects such as the finite beam-size of single-dish telescopes and field-to-field variance when comparing sub-mm observations with theoretical models. In our model SMGs are predominantly a disc instability triggered starburst population, the sub-mm emission of which is often blended along the line of sight of observational single-dish surveys.

In the next Chapter we conduct a more thorough investigation of the properties and evolution of SMGs within the model presented in Lacey et al. (2016), including an analysis of their clustering with and without the effects of the single-dish beam. We hope that this, when compared with future observations aided by sub-mm inter-ferometry of increasing sample sizes, will lead to a greater understanding of this extreme and important galaxy population.

Chapter 4
The Clustering Evolution of Dusty Star-Forming Galaxies

4.1 Introduction

[1]The discovery that Cosmic Infra-red Background (CIB, e.g. Puget et al. (1996), Fixsen et al. 1998) had a similar energy density to the UV optical background (e.g. Hauser and Dwek 2001; Dole et al. 2006) implies that a significant proportion of the star formation over the history of the Universe has been obscured by dust. It is therefore critical for a complete theory of galaxy formation and evolution to understand the nature of the galaxies responsible for this background in an evolutionary context.

A key difficulty with observations at these long wavelengths is confusion noise, caused by the coarse angular resolution [$\sim$ 20 arcsec full width at half maximum (FWHM)] of the telescopes used and the high surface density of detectable objects. This means that only the brightest objects can be resolved above the confusion background from imaging at these wavelengths. Whilst these individually resolved galaxies do not form the dominant contribution to the CIB (e.g. Oliver et al. 2010), they are important to study in their own right as they appear to be amongst the most highly star-forming objects in the Universe. Their FIR/sub-mm emission is thought to be powered by star formation, leading to inferred star formation rates (SFRs) of $\gtrsim$ 100 $M_\odot$ yr^{-1} (e.g. Smail et al. 2002; Michałowski et al. 2010; Swinbank et al. 2014). It has been speculated that SMGs could evolve onto the scaling relations observed for massive local elliptical galaxies, based on simple arguments involving

---

[1]The content of this Chapter (with the exception of Sect. 4.4.4) is based on the article Cowley et al. 'The clustering evolution of dusty star-forming galaxies', Monthly Notices of the Royal Astronomical Society, Volume 461, Issue 2, p.1621–1641, published 6 May 2016. Reproduced with permission. All rights reserved, https://doi.org/10.1093/mnras/stw1069. The content of Sect. 4.4.4 is based on the article Cowley et al. 'Blending bias impacts the host halo masses derived from a cross correlation analysis of bright submillimetre galaxies', Monthly Notices of the Royal Astronomical Society, Volume 469, Issue 3, p.3396–3404, published 19 April 2017. Reproduced with permission. All rights reserved, https://doi.org/10.1093/mnras/stx928.

the timescale of the burst and the ageing of the stellar population (e.g. Lilly et al. 1999; Swinbank et al. 2006; Simpson et al. 2014), and assuming that most of the stellar mass at $z = 0$ is put in place during the 'SMG phase'. However, González et al. (2011) present an alternative scenario in which SMGs evolve into galaxies with stellar mass $\sim 10^{11} \, h^{-1} \, M_{\odot}$ at $z = 0$, with the SMG phase accounting for little of this stellar mass.

An important constraint on any evolutionary picture can come from observational measurements of the clustering of selected galaxies, which provides information regarding the masses of the dark matter halos in which they reside. At 850 µm Hickox et al. (2012) used a cross-correlation analysis (e.g. Blake et al. 2006) to find that SMGs selected from the LESS[2] source catalogue (Weiß et al. 2009) have a correlation length of $r_0 = 7.7^{+1.8}_{-2.3} \, h^{-1}$ Mpc. This result is consistent with an earlier study by Blain et al. (2004) who used measured redshift separations of SMG pairs to show that SMGs selected from a number of SCUBA fields have a correlation length of $6.9 \pm 2.1 \, h^{-1}$ Mpc. These correlation lengths are consistent with SMGs residing in halos of mass $10^{12} - 10^{13} \, h^{-1} \, M_{\odot}$. Both the Hickox et al. and Blain et al. studies were performed prior to interferometric observations, which showed that many single-dish sources are in fact composed of multiple, fainter galaxies (e.g. Wang et al. 2011; Hodge et al. 2013). It is currently unclear from previous work how this result affects the observed clustering of SMGs. We therefore present predictions for this in Sect. 4.4.

Information about the clustering, and therefore host halo masses, of the unresolved FIR/sub-mm galaxies which contribute to the bulk of the CIB, can be obtained from the angular power spectrum of CIB anisotropies. Recent studies have been able to measure this to a relatively high degree of accuracy (e.g. Viero et al. 2009; Amblard et al. 2011; Viero et al. 2013; Planck Collaboration XXX 2014), though significant modelling is required in order to interpret these results in terms of halo masses. The Viero et al. (2013) and Plank Collaboration studies infer the typical halo mass for galaxies that dominate the CIB power spectrum as $10^{11.95 \pm 0.5} \, h^{-1} \, M_{\odot}$ and $10^{12.43 \pm 0.1} \, h^{-1} \, M_{\odot}$ respectively, making various assumptions such as the form of the relationship between galaxy luminosity and halo mass being independent of redshift, and that this relationship is the same for both central and satellite galaxies.

In this Chapter we present model predictions for the evolution of the clustering, and host halo masses, of galaxies selected by total infra-red luminosity, and FIR/sub-mm emission. It is structured as follows: in Sect. 4.2 we briefly describe some of the physical nature of dusty star-forming galaxies in the galaxy formation model, in Sect. 4.3 we present predictions for the spatial clustering of galaxies selected by their total infra-red luminosity (L_{IR}), and by their 850 µm flux, in Sect. 4.4 we make predictions for the angular clustering of simulated galaxies selected by their 850 µm flux, taking into account the effect of the single-dish beam used to make such observations, and in Sect. 4.5 we present predictions for the angular power spectrum of CIB anisotropies at 250, 350, and 500 µm. We conclude in Sect. 4.6.

---

[2]Large APEX (Atacama Pathfinder EXperiment) Bolometer Camera Array (LABOCA) Extended *Chandra* Deep Field South (ECDFS) Sub-millimetre Survey.

4.2   **Dusty Star-Forming Galaxies in the Lacey et al. (2016) Model**

Here we give a brief description of the properties of the dusty star-forming galaxies which dominate the CIB and SMG population in the model, in order to aid the reader in understanding results presented later.

Dusty star-forming galaxies are predicted to be predominantly starburst galaxies (i.e. star formation occurs within a forming bulge), with the starburst phase being triggered by secular disc instabilities. The importance of disc instabilities in the model is twofold: (i) they result in faster gas consumption at higher redshifts by triggering starbursts, and (ii) they are the dominant channel in the model for the growth of supermassive black holes which allow AGN feedback to suppress star formation in massive halos ($M_{\mathrm{halo}} \gtrsim 10^{12} \, h^{-1} \, \mathrm{M}_\odot$) at late times. This means that the model displays the requisite star formation at early times to reproduce the redshift distribution of sub-millimetre galaxies at $z \gtrsim 1$ without overestimating it at lower redshifts.

Dusty star-forming galaxies are mostly central galaxies. In the model, instantaneous ram-pressure stripping of the hot gas halo is implemented when a galaxy becomes a satellite (its hot halo gas component is transferred to that of the parent halo) and it is assumed that no more gas will accrete onto the disc of the satellite galaxy. For this reason, the star formation in satellite galaxies is reduced due to their diminishing gas supply, and they form a minor proportion ($\lesssim 5\%$) of the dusty star-forming population.

Here we present some of the physical properties of the dusty star-forming galaxy population in the model, the illustrative values presented are the median values for the $L_{\mathrm{IR}} > 10^{12} \, h^{-2} \, \mathrm{L}_\odot$ population at $z = 2.6$. Dusty star-forming galaxies are amongst the most massive galaxies in the simulation at a given epoch with stellar masses $M_\star \sim 2 \times 10^{10} \, h^{-1} \, \mathrm{M}_\odot$, and they reside in the dark matter halos most conducive to star formation in the model ($M_{\mathrm{halo}} \sim 10^{11.8} \, h^{-1} \, \mathrm{M}_\odot$). They also have high star formation rates $\sim 140 \, h^{-1} \, \mathrm{M}_\odot \, \mathrm{yr}^{-1}$, translating to specific star formation rates of $\sim 8 \, \mathrm{Gyr}^{-1}$ (approximately $10\times$ the sSFR of the model's 'main sequence'), dust to stellar mass ratios, $M_{\mathrm{dust}}/M_\star \sim 0.03$ and molecular gas fractions $M_{\mathrm{cold,mol}}/(M_{\mathrm{cold,mol}} + M_\star) \sim 0.4$.

4.3   **The Spatial Clustering of Dusty Star-Forming Galaxies**

In this Section we present predictions for the spatial clustering of simulated galaxies selected by their total infra-red luminosity, L_{IR}, and their emission at 850 μm. We discuss how the clustering evolves with redshift, how this relates to the dark matter halos the selected objects occupy, and how the populations selected by L_{IR} and $S_{850\mu\mathrm{m}}$ are related. We also briefly discuss the stellar and host halo mass of the $z = 0$ descendants of the 850 μm selected galaxies.

We present the predictions of our model in this Section without considering any observational effects, such as the angular resolution of the telescopes used to identify galaxies at sub-mm wavelengths, redshift-space distortions, the accuracy of observed redshifts or any selection biases such effects can introduce. Some of these issues are dealt with in Sect. 4.4.

4.3.1 The Two-Point Spatial Correlation Function

We quantify the clustering of our selected galaxies by use of the two point spatial correlation function $\xi(r)$, which is defined as the excess probability of finding two galaxies at a given separation $r > 0$, compared to a random distribution:

$$\delta P_{12}(r) = n^2[1 + \xi(r)]\delta V_1 \delta V_2, \qquad (4.3.1)$$

(e.g. Peebles 1980) where n is the mean number density of the selected galaxies at a given redshift and δV_i is a volume element. The two-point correlation at $r = 0$ is described by a Dirac delta function $\delta^D(r)/n$ (referred to as the shot noise term) as the galaxies are treated as point objects.

On large scales the correlation function is shaped by the clustering of galaxies in distinct dark matter halos, referred to as the two-halo term (e.g. Cooray and Sheth 2002; Berlind and Weinberg 2002). On these scales the correlation functions of the dark matter and galaxies have a similar shape but differ in amplitude. This difference in amplitude, or bias, is defined as

$$b(r) = \left[\frac{\xi_{\text{gal}}(r)}{\xi_{\text{DM}}(r)}\right]^{1/2}. \qquad (4.3.2)$$

Although galaxy bias is scale dependent (e.g. Angulo et al. 2008) it is usually approximated as constant on large-scales, where it is governed by a weighted average of the bias values over the halos that are occupied. The effective bias of the selected galaxy population can then be written as

$$b_{\text{eff}} = \frac{\int b(M)n(M)\langle N_{\text{gal}}|M\rangle \mathrm{d}M}{\int n(M)\langle N_{\text{gal}}|M\rangle \mathrm{d}M}, \qquad (4.3.3)$$

where $b(M)$ is the bias of halos with mass M, $n(M)$ is the halo mass function such that $n(M)\mathrm{d}M$ describes the comoving number density of halos in the mass range $[M, M + \mathrm{d}M]$, and $\langle N_{\text{gal}}|M\rangle$ is the mean of the halo occupation distribution (HOD, the expected number of selected galaxies within a halo of mass M).

We measure the correlation function in the simulation volume using the standard estimator (e.g. Peebles 1980):

$$\xi(r) = \frac{DD(r)}{N_{\text{gal}}\, n\, \Delta V(r)/2} - 1, \tag{4.3.4}$$

where $DD(r)$ is the number of distinct galaxy pairs with separations between $r \pm \Delta r/2$, N_{gal} is the total number of selected galaxies, n is their mean number density and $\Delta V(r)$ is the volume of the spherical shell between $r \pm \Delta r/2$. We make use of the periodic nature of our simulation to calculate this volume analytically.

We calculate errors using the volume bootstrap method advocated in Norberg et al. (2009). We divide our simulation volume into $N_{\text{sub}} = 27$ subvolumes and for each bootstrap realisation draw $3N_{\text{sub}}$ subvolumes at random (with replacement). As our volume is no longer periodic due to the spatial sampling we calculate $\xi(r)$ for each bootstrap realisation using the estimator presented in Landy and Szalay (1993):

$$\xi(r) = \frac{DD(r) - 2DR(r) + RR(r)}{RR(r)}, \tag{4.3.5}$$

where $DD(r)$, $DR(r)$ and $RR(r)$ represent the number of data-data, data-random, and random-random pairs with separations between $r \pm \Delta r/2$. For each bootstrap realisation we generate a random catalogue with 10 times more points than there are galaxies in our initial sample, normalising the DR and RR terms in equation (4.3.5) to have the same total number of pairs as DD. We calculate 100 bootstrap realisations from which we derive the 16–84 (1σ) percentile variation for each bin of separation.

4.3.2 Spatial Clustering Evolution of Infra-red Luminous Galaxies

Here we present predictions for the clustering of galaxies selected by their total infra-red luminosity, L_{IR}, derived by calculating the energy of stellar radiation absorbed by dust through solving the equations of radiative transfer in our assumed dust geometry.

We show the model predicted spatial clustering for galaxies selected by their L_{IR} in Fig. 4.1 at a selection of redshifts, $z \sim 0 - 5$, and luminosities, $L_{\text{IR}} \sim 10^9 - 10^{12.5}\ h^{-2}\ \text{L}_\odot$. For clarity, we only show volume bootstrap errors for the most luminous (i.e. least numerous) population. We are confident that our selected galaxies are complete populations, at all redshifts considered here, and are not affected by the finite halo mass resolution of our simulation. We also plot the correlation function of the dark matter, calculated using a randomly chosen subset of 10^6 dark matter particles from the MR7 simulation, and can see that the selected galaxy populations represent biased tracers of the underlying matter distribution. Note that we do not show $\xi(r)$ of the most luminous population at $z < 1$ as the number of pairs of such objects in our simulation at these redshifts is not sufficient to provide a robust prediction.
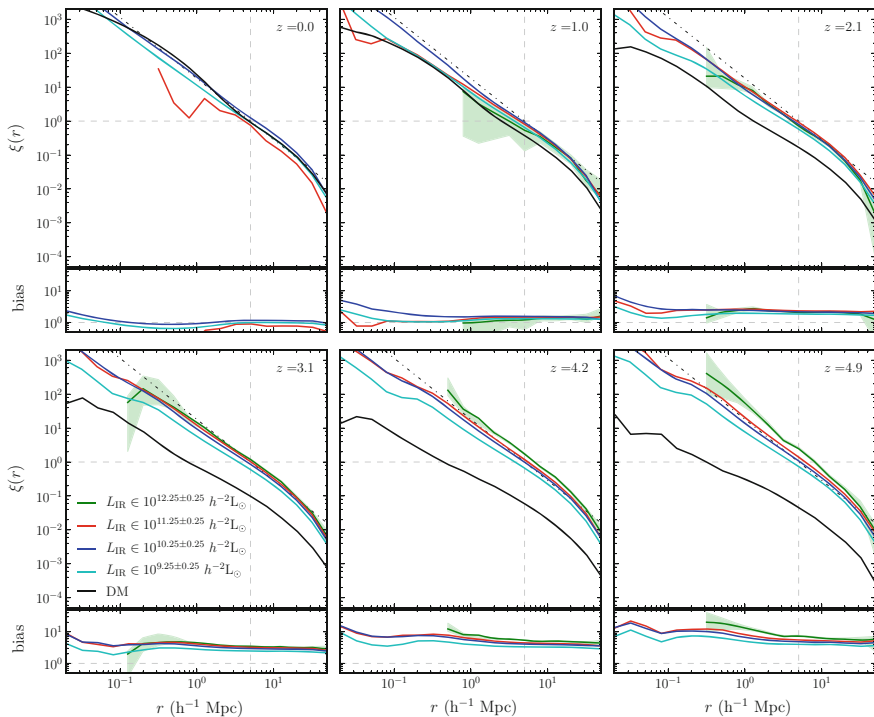
Fig. 4.1 *Main panels:* the predicted two-point spatial correlation function, $\xi(r)$, as a function of comoving separation, r, for galaxies selected by their total 8–1000 μm luminosity, L_{IR}, at the redshift indicated in each panel. The *cyan*, *blue*, *red* and *green* lines show galaxies with $L_{IR} = 10^9 - 10^{9.5}$, $10^{10} - 10^{10.5}$, $10^{11} - 10^{11.5}$ and $10^{12} - 10^{12.5}$ h^{-2} L$_\odot$ respectively. The green shaded region shows the 1σ volume bootstrap errors for the $L_{IR} = 10^{12} - 10^{12.5}$ h^{-2} L$_\odot$ population. The *black line* indicates the correlation function measured for dark matter particles in the MR7 simulation. The vertical and horizontal dashed *grey lines* are drawn for reference at $r = 5$ h^{-1} Mpc and $\xi = 1$ respectively. The diagonal *black dash-dotted line*, again for reference, indicates a $\gamma = -1.8$ power law with a correlation length of 5 h^{-1} Mpc. *Sub panels:* as for the main panels but indicating the bias, defined as $(\xi_{g}/\xi_{DM})^{1/2}$. A horizontal *grey dashed line* indicating a bias value of 1 is drawn for reference in each panel

It is notable that the clustering of the selected galaxies shows a dependence on the selection luminosity, and redshift. This is summarised in Fig. 4.2, which shows the redshift evolution of the comoving correlation length, r_0, defined such that $\xi(r_0) \equiv 1$, and the large-scale bias of the selected populations. In the right panel of Fig. 4.2 we show for reference the large-scale bias evolution of halos selected by their mass, calculated directly from the MR7 simulation.

At all redshifts shown the two fainter luminosity populations are predominantly composed of quiescently star-forming galaxies, they display a similar clustering evolution, though systematically offset such that the brighter of these two populations is more clustered at all redshifts. The brighter two populations are predominantly
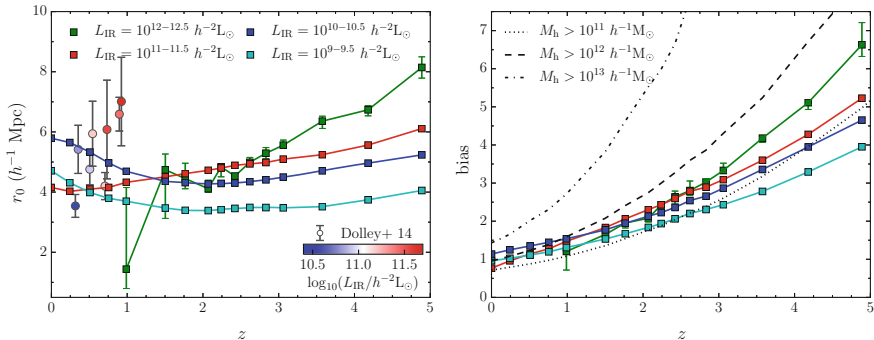
Fig. 4.2 *Left panel:* evolution of the comoving correlation length r_0 [defined such that $\xi(r_0) \equiv 1$]. The *cyan, blue, red* and *green lines* show galaxies with $L_{IR} = 10^9 - 10^{9.5}$, $10^{10} - 10^{10.5}$, $10^{11} - 10^{11.5}$ and $10^{12} - 10^{12.5}$ h^{-2} $L_\odot$ respectively. The errors indicate 1σ volume bootstrap errors for the $L_{IR} = 10^{12} - 10^{12.5}$ h^{-2} $L_\odot$ population. A selection of observational estimates from Dolley et al. (2014) are shown as circles, with the colour scale indicating the mean L_{IR} for each sample, as shown on the inset colour bar. *Right panel:* as for the left panel, but indicating the evolution of the large-scale bias. The *dotted, dashed* and *dash-dotted lines* indicate the bias evolution for halos of $M_h > 10^{11}$, 10^{12} and 10^{13} h^{-1} $M_\odot$ respectively, as measured directly from the MR7 simulation

composed of starburst galaxies[3] and display a different clustering evolution to the fainter two samples, with r_0 displaying a monotonic relationship with redshift.

Comparing with the large-scale bias evolution of mass-selected halos we can see that our most luminous population displays an evolution consistent with them residing in halos of mass $10^{11} - 10^{12}$ h^{-1} $M_\odot$ over the redshift range $z \sim 1 - 5$.

These results can be understood better in the context of the halo masses sampled by the infra-red luminosity selection. In Fig. 4.3 we show the distribution of galaxies in the star formation rate - halo mass plane for all galaxies (left panels) and for the infra-red luminosity selected populations (right panels). We can see that the distribution of SFRs is broad for halo masses $M_{halo} > 10^{11}$ h^{-1} $M_\odot$ and that the infra-red selections pick up a broad range of halo masses. We also see how this distribution evolves. At $z = 4.2$ the infra-red selection means that samples with increasing L_{IR} have increasing median halo masses, leading to them being more biased than samples selected by a lower infra-red luminosity. At $z = 1.5$ this is no longer the case, as the most luminous population has a slightly lower median halo mass than the next most luminous. This breaks the monotonic relation of increasing bias with increasing luminosity seen at higher redshifts.

In Fig. 4.2 we also compare our predictions to the observational estimates of Dolley et al. (2014), who used far infra-red luminosities derived from 24 μm fluxes. We show the r_0 values for their redshift bins that are complete in infra-red luminosity, for clarity showing only most and least luminous samples within each redshift bin.

---

[3]The luminosity at which the infra-red luminosity functions predicted by our model become dominated by starburst galaxies is dependent on redshift. For example, at $z = 0$ the luminosity function is dominated by starbursts for $L_{IR} \gtrsim 10^{11.3}$ h^{-2} $L_\odot$, at $z = 4.9$ this limit is $L_{IR} \gtrsim 10^{10.5}$ h^{-2} $L_\odot$.
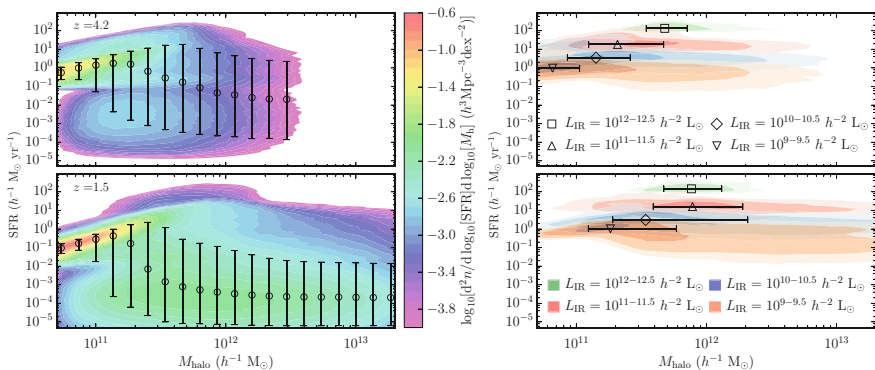
Fig. 4.3 Predicted distribution of galaxies in the star formation rate - halo mass plane at $z = 4.2$ (*top panels*) and $z = 1.5$ (*bottom panels*). *Left panels:* distribution of all galaxies with the shading representing the galaxy number density at that position on the plane, with red indicating the highest number densities and purple the lowest. Open circles show the median SFR in bins of halo mass, with the *errorbars* indicating the $16 - 84^{\text{th}}$ percentile scatter. *Right panels:* distribution of galaxies selected by their total infra-red luminosity for luminosities of $10^{12} - 10^{12.5}$ (*green*), $10^{11} - 10^{11.5}$ (*red*), $10^{10} - 10^{10.5}$ (*blue*) and $10^9 - 10^{9.5}$ h^{-2} L$_\odot$ (*orange contours*). The open symbols indicate the median halo mass and SFR in the corresponding luminosity bin, with the *errorbars* indicating the 16–84th percentile scatter in halo mass

The colour scale indicates the mean infra-red luminosities of their samples, the bins which have a width of 0.25 dex in L_{IR}. Whilst the overall agreement is generally favourable, Dolley et al. find, in contrast to our predictions, that for $z < 1$ at a fixed redshift r_0 increases with increasing luminosity. The model also appears to underpredict the clustering of $\sim 10^{11.5}$ h^{-2} L$_\odot$ galaxies at $z \sim 1$ and overpredict the clustering of $\sim 10^{10.5}$ h^{-2} L$_\odot$ galaxies at $z \sim 0.3$.

There could be a number of reasons for this discrepancy. Dolley et al. assumed a power-law slope of $\gamma = 1.9$ in order to derive a correlation length. If a lower value is used (as favoured by our model) they note that this increases their estimated correlation lengths (e.g. assuming $\gamma = 1.8$ gave correlation lengths ~ 0.5 h^{-1} Mpc larger). Our model shows a variation of power-law slope with redshift and infra-red luminosity, with lower luminosity samples having generally flatter slopes. It is also unclear whether the simulated galaxies follow the relation used by Dolley et al. to derive L_{IR} from the observed 24 μm photometry, which is based on templates derived from local galaxies (Rieke et al. 2009) and adjusted at higher redshifts according to Rujopakarn et al. (2013). Alternatively, further investigation into the physical processes which produce the distribution of galaxies on the SFR-M_{halo} plane as predicted by the model (Fig. 4.3) is required to understand how the predicted clustering could be brought into better agreement with the Dolley et al. results.

Our predictions for correlation length in this Section are lower than the observational estimates of Farrah et al. (2006), who infer correlation lengths of 9.4 ± 2.2 and 14.4 ± 2.0 h^{-1} Mpc for galaxies at $z \sim 1.7$ and 2.5 respectively, with $L_{\text{IR}} \gtrsim 5 \times 10^{11}$ h^{-2} L$_\odot$. However, we do not consider this a significant discrep-

ancy, due to the complicated selection criteria of the Farrah et al. sample, which we do not attempt to model here, and assumptions made by those authors regarding the redshift distribution of their sample, and their parametrisation of $\xi(r, z)$.

4.3.3   Spatial Clustering of SMGs

In this Section we present the spatial clustering of galaxies selected by their 850 μm flux. We focus on this wavelength as it is historically the wavelength at which the majority of ground-based observations of FIR/sub-mm galaxies have been performed, due to the atmospheric transmission window. The real space two-point correlation function and large-scale bias for our selected galaxies are presented in Fig. 4.4 over a range of redshifts which span the peak of the redshift distribution of the selected SMGs.

We consider three samples of galaxies selected by flux: (i) a bright population with $S_{850\mu m} > 4$ mJy (median $L_{IR} \sim 10^{12.2} \, h^{-2} \, L_\odot$ at $z = 2.6$, *green line*) as this is a typical limit at which single-dish surveys can detect SMGs (e.g. Weiß et al. 2009, though note we do not consider the effects of the single-dish beam in this Section), (ii) an intermediate population with $S_{850\mu m} > 1$ mJy (median $L_{IR} \sim 10^{11.8} \, h^{-2} \, L_\odot$ at $z = 2.6$, *red line*) as this is an approximate limit to which ALMA detected galaxies as part of Cycle 0 observations (e.g. Hodge et al. 2013) and (iii) a faint population
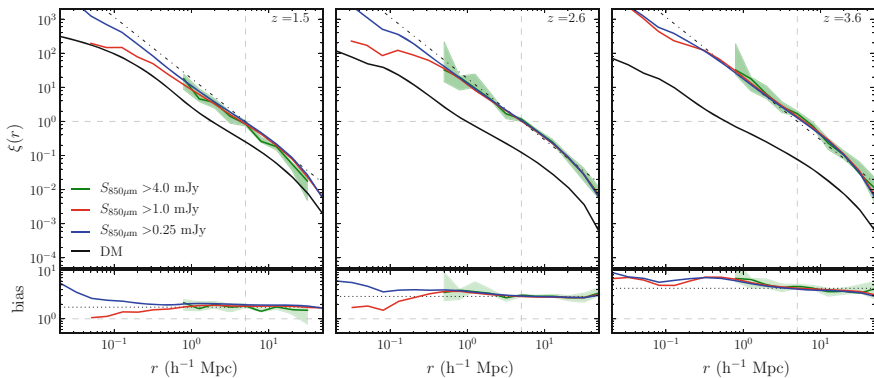
Fig. 4.4 *Top panels:* the spatial correlation function for 850 μm selected galaxies at redshifts of 1.5, 2.5 and 3.5 (left to right). The *blue, red and green lines* show the correlation function for $S_{850\mu m} >$ 0.25, 1.0 and 4.0 mJy respectively. The green shaded region shows the 1σ volume bootstrap errors for the $S_{850\mu m} > 4.0$ mJy population. The *black line* indicates the correlation function measured for dark matter particles in the MR7 simulation. The vertical and horizontal *dashed grey lines* are drawn for reference at $r = 5 \, h^{-1}$ Mpc and $\xi = 1$ respectively. The diagonal *black dash-dotted line*, again for reference, indicates a $\gamma = -1.8$ power law with a correlation length of $5 \, h^{-1}$ Mpc. *Bottom panels:* as for the top panel but indicating the bias, defined as $(\xi_g/\xi_{DM})^{1/2}$. A horizontal *grey dashed line*, drawn for reference in each panel, indicates a bias of 1. A horizontal *black dotted line*, again drawn for reference, indicates a bias of 1.7, 2.9 and 4.2 (left to right panels)

with $S_{850\mu m} > 0.25$ mJy (median $L_{IR} \sim 10^{11.2} \, h^{-2}$ L$_\odot$ at $z = 2.6$, *blue line*) which are in principle detectable by ALMA, though with longer integration times and more antennae than were used in Cycle 0. Our selected galaxies exhibit clustering with $r_0 \sim 5 \, h^{-1}$ Mpc, with little dependence on flux, for the fluxes considered here.

4.3.3.1 SMG Halo Occupation Distribution

We can gain further insight into the clustering of the selected SMGs from Fig. 4.5 which shows their halo mass probability distribution (i.e. the product of the halo mass function and the mean of the HOD - $n(m)\langle N_{gal}|M\rangle$ in Eq. 4.3.3, left panels) and the mean of the HOD ($\langle N_{gal}|M\rangle$ in Eq. 4.3.3, right panels) at redshifts $z = 3.1$
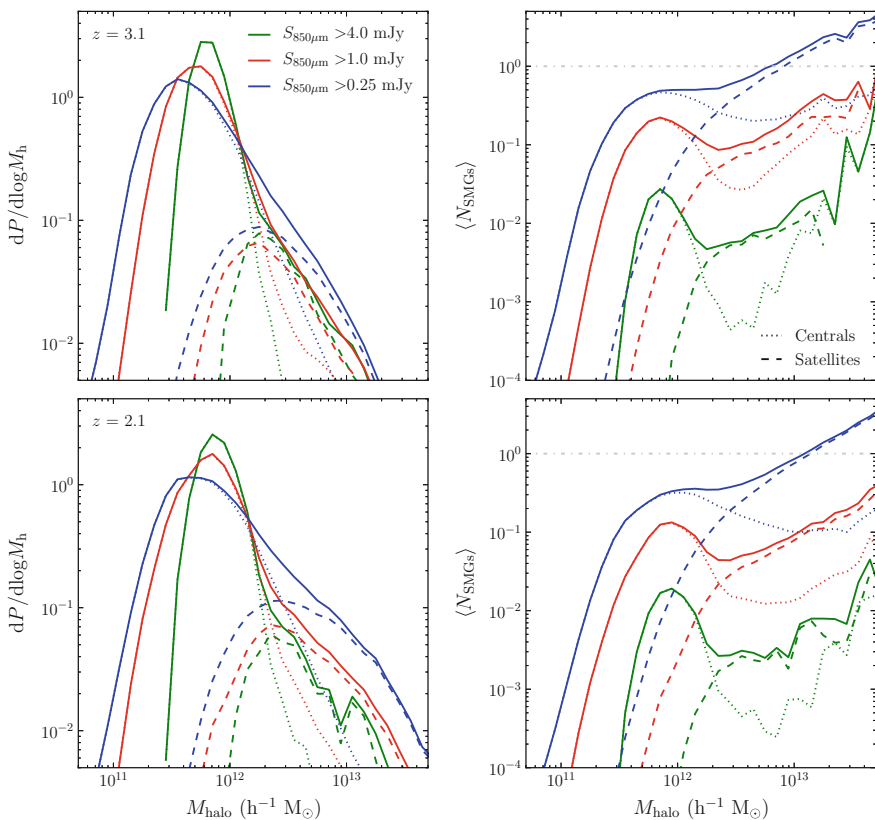
Fig. 4.5 Probability distribution of halo mass (*left*) and halo occupation distribution (*right*) for 850 μm selected SMGs at $z = 3.1$ (*top*) and 2.1 (*bottom*). The *blue, red* and *green lines* indicate the HOD for the $S_{850\mu m} > 0.25$, 1.0 and 4.0 mJy respectively, with the *dashed (dotted lines)* depicting satellite (central) galaxies. A horizontal *dash-dotted line* is drawn in both right panels at $\langle N_{SMGs}\rangle = 1$ for reference

and 2.1 (top and bottom panels respectively). It is evident from the left panels that SMGs reside predominantly in halos of mass $\sim 10^{11.5} - 10^{12} \ h^{-1} \ M_{\odot}$, the halo mass range most conducive for star formation in our model over a broad range of redshifts (see Fig. 4.27 of Lacey et al. 2016). For example, at $z = 3.1$: 87, 74 and 54% of galaxies in the $S_{850\mu m} > 4$, 1 and 0.25 mJy selected populations respectively reside in halos within this mass range. At $z = 2.1$ these percentages are 75, 69 and 53% respectively. The halo mass at which the probability distribution peaks seems insensitive to the 850 μm flux of the galaxies and their redshift, although fainter galaxies do occupy a broader range of halo masses, and the distribution for satellite galaxies (dashed lines) peaks at a higher halo mass ($\sim 2 \times 10^{12} \ h^{-1} \ M_{\odot}$).

In the right panels the HODs for central galaxies (dotted lines) peak below unity for all samples. The HODs only reach unity for satellites in fainter samples in massive halos ($M_{h} \gtrsim 10^{13} \ h^{-1} \ M_{\odot}$ at $z = 2.1$). Models which force $\langle N_{SMGs,c} \rangle = 1$ and adopt the same number density of SMGs would place them in more massive halos than predicted by our model. An $S_{850\mu m} > 1$ mJy galaxy is hosted in roughly 1 in every 10 halos of $\sim 10^{12} \ h^{-1} \ M_{\odot}$, showing the need for a large number of halo histories to be sampled (i.e. large cosmological volumes simulated) in order to make robust predictions for the SMG population as a whole (see also e.g. Almeida et al. 2011; Miller et al. 2015).

We attribute the minima in the HODs for the central galaxies to merger-induced SMGs. In our model AGN feedback becomes effective in massive haloes ($M_{halo} \gtrsim 10^{12} \ h^{-1} \ M_{\odot}$), which prevents hot halo gas from cooling, limiting the fuel for star formation and leading to the downturn in the HOD. Galaxy mergers bring in a fresh reservoir of cold gas to central galaxies, allowing further star formation in these high mass ($\gtrsim 10^{13} \ h^{-1} \ M_{\odot}$) halos without the need for in-situ gas cooling.

4.3.3.2 The Evolution of SMG Clustering

We show the evolution of the correlation length r_0 in the left panel of Fig. 4.6. This is approximately constant for $z \lesssim 2$ but increases with increasing redshift at higher redshifts. The errorbars shown are derived from the 1σ bootstrap errors described above.

In the right panel of Fig. 4.6 we show the evolution of the large-scale bias with redshift, in addition plotting for reference the evolution of the large-scale bias for halos selected by their mass. We can see that the bias evolution of our galaxies is of a similar form to that of the halos, indicating that SMGs typically reside in halos of $10^{11} - 10^{12} \ h^{-1} \ M_{\odot}$, over a large redshift range. This is in agreement with our previous findings in Fig. 4.5.

In Fig. 4.6 we compare to the observational results of Hickox et al. (2012) and Blain et al. (2004). Hickox et al. use sub-mm sources from the single-dish LESS source catalogue (Weiß et al. 2009), with $S_{850\mu m} \gtrsim 4.5$ mJy, at redshifts of $z \sim 2-4$, covering $0.35 \ deg^2$, and use the cross-correlation of these with IRAC selected galaxies over a similar redshift range, taking into account the photometric redshift probability distribution of their SMGs (Wardlow et al. 2011), to derive a large-scale bias of
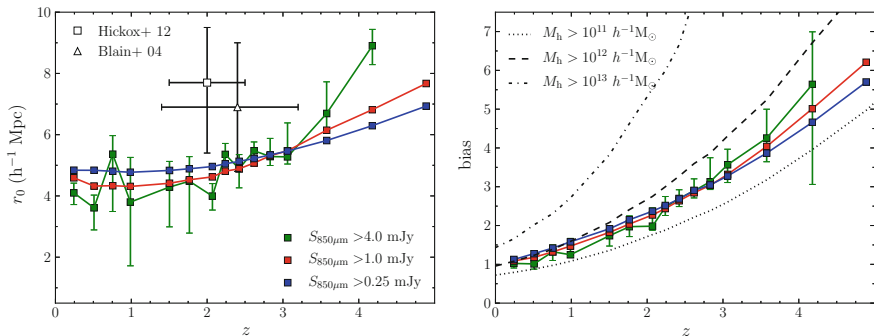
Fig. 4.6 *Left panel:* evolution of the comoving correlation length r_0 [defined such that $\xi(r_0) \equiv 1$] with redshift, for galaxies with $S_{850\mu m} > 0.25$, 1.0 and 4.0 mJy (*blue, red* and *green lines* respectively). The errors indicate 1σ volume bootstrap errors for the $S_{850\mu m} > 4.0$ mJy population. The observational data are taken from Hickox et al. (2012; *open square*) and Blain et al. (2004; *open triangle*). *Right panel:* symbols and coloured lines as for the left panel but indicating the evolution of the large-scale bias. The *dotted, dashed* and *dash-dotted lines* indicate the bias evolution for halos of $M_{halo} > 10^{11}$, 10^{12} and 10^{13} h^{-1} M$_\odot$ respectively, as measured directly from the MR7 simulation

3.4 ± 0.8 from which they find a correlation length of $r_0 = 7.7^{+1.8}_{-2.3}\,h^{-1}$ Mpc assuming a power-law correlation function $[\xi(r) = (r/r_0)^{-\gamma}]$ with $\gamma = 1.8$. Blain et al. also assume a power-law $\xi(r)$ with $\gamma = 1.8$, and a Gaussian redshift distribution (Chapman et al. 2005), whilst allowing r_0 to vary in order to match the number of SMG ($S_{850\mu m} \gtrsim 5$ mJy) pairs observed across a number of non-contiguous SCUBA fields with a combined area of ~ 0.16 deg^2. They obtain a correlation length of $r_0 = 6.9 \pm 2.1\,h^{-1}$ Mpc but note that if they exclude the most overdense field from their analysis, they derive $r_0 = 5.5 \pm 1.8\,h^{-1}$ Mpc, which is in better agreement with our predictions. However, due to the significant errors on the observational data and potential biases due to the single-dish beam used in these studies which we discuss in Sect. 4.4, it is difficult to draw any strong conclusions about the level of agreement between the model and data.

From comparing the left panel of Fig. 4.6 to that of Fig. 4.2, we can see that the clustering evolution of our SMG populations are remarkably similar to that of our most infra-red luminous galaxies ($L_{IR} = 10^{12} - 10^{12.5}\,h^{-2}$ L$_\odot$). We note that at $z = 2.6$ the median 850 μm flux for galaxies in our most luminous L_{IR} bin ($10^{12} - 10^{12.5}\,h^{-2}$ L$_\odot$) is $3.3^{+2.2}_{-1.5}$ mJy, where the errorbars represent the $10 - 90$ percentiles. Conversely, at the same redshift the $S_{850\mu m} > 4$ mJy population has a bolometric dust luminosity of $L_{IR} = 10^{12.04} - 10^{12.44}\,h^{-2}$ L$_\odot$ (10-90 percentiles). Thus in our model the 850 μm selection selects the most infra-red luminous starburst galaxies (our predicted galaxy number counts at 850 μm are dominated by starburst galaxies for $S_{850\mu m} \gtrsim 0.2$ mJy), hence the similarities in the model predicted clustering evolution of SMGs and the most infra-red luminous galaxies.

4.3.3.3 SMG Descendants and Environment

Arguments which assume that the majority of $z = 0$ stellar mass of an SMG descendant is formed during the sub-mm bright phase imply that by fading the stellar population, SMGs could evolve onto the $z = 0$ scaling relations of massive ellipticals (assuming a burst duration of typically ~ 100 Myr, e.g. Swinbank et al. 2006; Simpson et al. 2014). Here we investigate the stellar and halo masses of the $z = 0$ descendants, presenting our findings for the bright population ($S_{850\mu m} > 4$ mJy) in Fig. 4.7.

We find that across all redshifts shown in Fig. 4.7, which span the majority of the redshift distribution for this population, the selected galaxies evolve into galaxies with a stellar mass of $\sim 10^{11}$ h^{-1} $M_\odot$ at the present day. This is similar to the results presented from an analysis of an earlier version of the galaxy formation model used here (González et al. 2011).

The stellar masses of SMGs inferred from observations are the subject of much debate. They are typically inferred by SED fitting to broadband photometry, making a range of assumptions regarding the AGN contamination, dust obscuration, star formation history and IMF of the galaxies in question. Early estimates appeared to disagree by factors of $\sim 5 - 10$ for the *same* sample of SMGs. Hainline et al. (2011) quoted a median stellar mass for the Chapman et al. (2005) sample ($S_{850\mu m} > 5$ mJy)
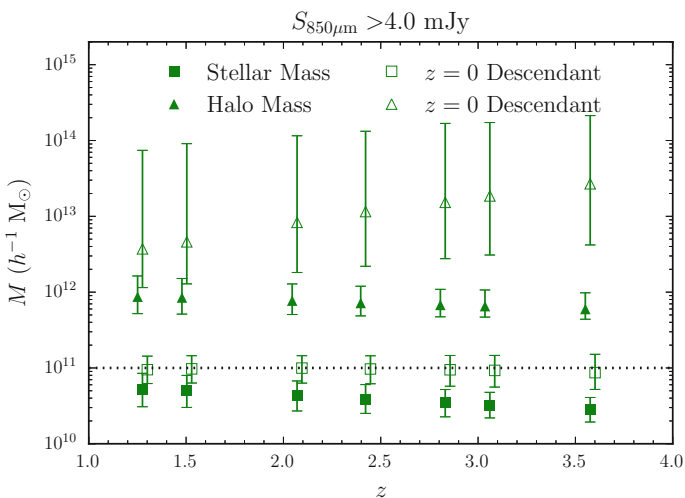
Fig. 4.7 The descendants of $S_{850\mu m} > 4.0$ mJy selected galaxies in our simulation. The *open squares* and *open triangles* indicate the median stellar and host halo mass of the selected galaxies respectively, with the filled symbols indicating this quantity at the redshift of interest and the open symbols indicating this quantity for the $z = 0$ descendant. The error bars indicate 10–90 percentile ranges. The *open squares* and *filled triangles* are offset in redshift by ± 0.025 for clarity. A dotted horizontal line is drawn at $M = 10^{11}$ h^{-1} $M_\odot$ for reference

of $\sim 5 \times 10^{10}~h^{-1}~\text{M}_\odot$ [assuming a Kroupa (2002) IMF] in contrast to the higher value of $\sim 2.6 \times 10^{11}~h^{-1}~\text{M}_\odot$ found by Michałowski et al. (2010) [assuming a Chabrier (2003) IMF], though subsequent work by Michałowski et al. (2012b) suggested that this discrepancy was mostly due to the assumed star formation histories used by the two studies, once differences due to the choice of IMF were taken into account. Michałowski et al. (2012b) also obtained a revised median stellar mass of $\sim 1.4 \times 10^{11}~h^{-1}~\text{M}_\odot$. More recently da Cunha et al. (2015) derived a median stellar mass of $\sim 6 \times 10^{10}~h^{-1}~\text{M}_\odot$ by applying the SED fitting code MAGPHYS [assuming a Chabrier (2003) IMF] to the ALESS (Hodge et al. 2013) SMG sample.

Our predicted stellar masses lie at the lower end of values quoted in the literature however, it is difficult to understand the significance of the (dis)agreement. The comparison is further complicated by the top-heavy IMF for starbursts assumed in the model. We therefore consider a proper comparison of the stellar masses of SMGs predicted by our model and those inferred from observations to be beyond the scope of this paper, and caution the reader against over-interpreting the values presented briefly here.

The predicted masses presented in Fig. 4.7 are qualitatively similar for the fainter populations, though they systematically shift to slightly lower masses, for example the $S_{850\mu\text{m}} > 0.25$ mJy population evolve into galaxies with stellar mass $\sim 5 \times 10^{10}~h^{-1}~\text{M}_\odot$. Note also that here we consider unique descendants, such that if two galaxies selected at a given redshift evolve into the same descendant at $z = 0$ it is only counted once.

In terms of halo mass, whilst sub-mm selected galaxies occupy a relatively narrow range of halo masses (~ 0.5 dex) at the redshift at which they are selected, the range of halo masses which host the $z = 0$ descendants is broad, spanning nearly two orders of magnitude $\sim 10^{12} - 10^{14}~h^{-1}~\text{M}_\odot$. In our model it appears then that bright SMGs do not necessarily trace the most massive $z = 0$ environments. As with stellar mass, here we consider unique halos, such that if a halo contains two galaxies selected at a given redshift, or the $z = 0$ descendant(s) of two galaxies selected at a given redshift, it is only counted once.

Our results for stellar and halo masses of bright SMGs and their descendants are a factor of ~ 5 lower than those found by Muñoz Arancibia et al. (2015), using the semi-anayltical model SAG (e.g. Lagos et al. 2008). However, their simulations do not self-consistently predict the sub-mm flux of galaxies as is done in this work, but instead rely on a 'count-matching' approach to link a galaxy's physical properties to its sub-mm flux. They infer median stellar and halo mass of $10^{11.2}$ and $10^{12.7}~h^{-1}~\text{M}_\odot$ respectively for SMGs; and $10^{11.7}$ and $10^{13.8}~h^{-1}~\text{M}_\odot$ respectively for the $z = 0$ descendants of SMGs.

4.4 Angular Clustering at 850 μm

The simplest measure of clustering from a galaxy imaging survey is the angular two-point correlation function $w(\theta)$. Analogously to equation (4.3.1), the probability of finding two objects separated by an angle $\theta > 0$[4] is defined as:

$$\delta P_{12}(\theta) = \eta^2[1 + w(\theta)]\delta\Omega_1\delta\Omega_2, \tag{4.4.6}$$

where η is the mean surface density of objects per unit solid angle and $\delta\Omega_i$ is a solid angle element, such that $w(\theta)$ represents the excess probability of finding objects at angular separation θ, compared to a random (Poisson) distribution.

In this Section we present the angular correlation function of galaxies, w_g, selected by their 850 μm emission. We compare this to the angular correlation function of sub-mm sources, w_s, extracted from simulated single-dish 850 μm imaging following the method presented in Chap. 3, and the angular correlation function of 850 μm intensity fluctuations, w_I.

4.4.1 The Angular Clustering of Galaxies

Angular clustering, $w(\theta)$, can be thought of as the on-sky projection of $\xi(r, z)$, weighted by the number density of selected objects at a given redshift. We therefore use the approximation of Limber (1953) to calculate $w_g(\theta)$ from $\xi(r, z)$, the spatial two-point correlation function. This assumes that the selection function (redshift distribution) of galaxies changes slowly over the comoving separations r for which $\xi(r, z)$ is appreciably non-zero. Assuming a flat cosmology (as we do throughout), this allows $w_g(\theta)$ to be related to $\xi(r, z)$ by

$$w_g(\theta) = \frac{\int N(z)^2 \frac{dz}{d\chi}dz \int du\, \xi(r, z)}{[\int N(z)dz]^2}, \tag{4.4.7}$$

where $N(z)$ is the predicted redshift distribution of the selected galaxies, $dz/d\chi = H_0 E(z)/c$ with $E(z) = [\Omega_m(1 + z)^3 + \Omega_\Lambda]^{1/2}$, χ corresponds to the comoving radial distance to redshift z. The comoving line of sight separation u is defined by $r = [u^2 + \chi^2\varpi^2]^{1/2}$ where $\varpi^2/2 = [1 - \cos(\theta)]$. We present w_g for our sub-mm selected galaxy populations, as defined in the previous Section, in Fig. 4.8.

---

[4] Analogously to the spatial case, at $\theta = 0$ the correlation function is described by a Dirac delta function, $\delta^D(\theta)/\eta$, which is referred to as the shot noise term.
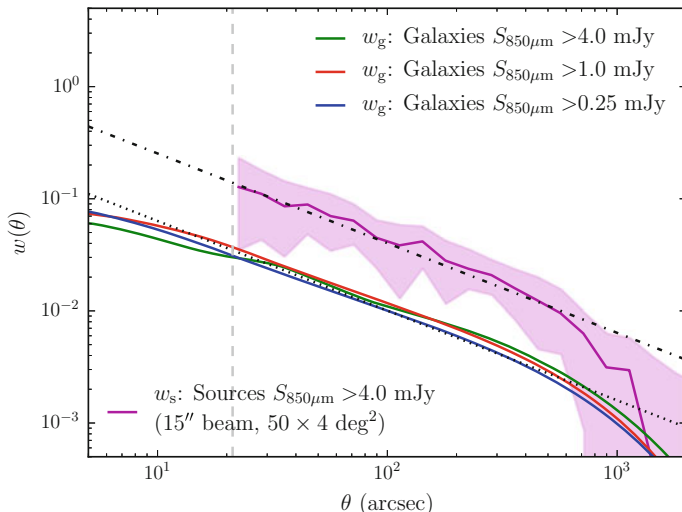
Fig. 4.8 The predicted angular correlation function for 850 μm selected galaxies (w_g) with $S_{850\mu m} > 0.25$, 1 and 4 mJy (*blue, red* and *green lines* respectively). Also shown is the angular correlation function for sources with $S_{850\mu m} > 4$ mJy extracted from simulated single-dish sub-mm imaging produced with a 15 arcsec FWHM Gaussian beam (*magenta line*) with the corresponding shaded region indicating the 1σ (16–84th percentile) field-to-field variation over 50 lightcone realisations of 4 deg^2 each. For reference, the diagonal dotted and *dash-dotted lines* show two $w \propto \theta^{1-\gamma}$ power laws, with $\gamma = 1.8$, offset from each other in amplitude by a factor of 4

4.4.2   The Angular Clustering of Single-Dish Sources

To make predictions for the angular clustering from sub-mm sources that would be observed in single-dish surveys we simulate such observations using the method presented in Chap. 3.

Briefly, we generate lightcone catalogues of simulated SMGs using the method described in Merson et al. (2013).[5] We include in our lightcone catalogue galaxies brighter than the flux at which 90% of the predicted CIB at 850 μm is recovered. The predicted value of the CIB is in good agreement with the observations of Fixsen et al. (1998), and thus gives our image a realistic background. The galaxies are then binned into pixels according to their on-sky position, with the flux value of a pixel being the sum of the fluxes of all the galaxies within it. The pixel scale is chosen such that the beam is well sampled. This image is then smoothed with a Gaussian with a FWHM chosen to be equal to that of the beam used in observational studies following which Gaussian white noise is added of a magnitude comparable to that found in observations. The image is constrained to have a mean of zero by the subtraction of a uniform background, and then matched-filtered prior to source extraction. Sources are found by iteratively identifying the maximal pixel in the map and subtracting

---

[5]This does not include any treatment of gravitational lensing.

off the matched-filtered PSF scaled to and centred on the value and position of the pixel. For simplicity the position of the source is recorded as being at the centre of the identifying pixel. The result of this source extraction is referred to hereafter as our source-extracted catalogue.

Here we choose to make predictions for the 850 μm SCUBA-2 Cosmology Legacy Survey (S2CLS, e.g. Geach et al. 2013), as measuring the clustering of SMGs is one of the main survey goals. For this reason we choose a Gaussian beam with a FWHM of 15 arcsec (similar to that of the SCUBA-2/JCMT configuration at 850 μm). In order to estimate field-to-field variation we generate $50 \times 4 \, \mathrm{deg}^2$ randomly oriented lightcones. We add instrumental Gaussian white noise with $\sigma_{\mathrm{inst}} = 1$ mJy/beam, which gives our maps a total noise of $\sigma_{\mathrm{tot}} \approx 1.2$ mJy/beam, calculated from a pixel histogram of our image. This broadening of the noise distribution is due to the confusion noise from faint unresolved galaxies in the image, as $\sigma_{\mathrm{tot}} \approx \sqrt{\sigma_{\mathrm{inst}}^2 + \sigma_{\mathrm{conf}}^2}$. We extract sources down to 4 mJy ($\sim 3.5\sigma$) as this is the typical limit at which sources are extracted out of single-dish surveys (e.g. Coppin et al. 2006; Weiß et al. 2009).

To calculate w_s for our source extracted catalogue we use the angular equivalent of equation (4.3.5). To ensure we are not affected by noise in the random catalogue, we generate random catalogues using the same selection function as for the data (i.e. same survey geometry) but with 250 times the number of points as there are sources for each of our simulated surveys.

In estimating $w_s(\theta)$ for each of the 50 lightcone realisations we used the actual number of sources in each field to calculate the mean surface density in order to match what is done observationally, rather than the true mean surface density. This causes the mean angular correlation function to be underestimated by an average amount

$$\sigma^2 = \frac{1}{\Omega^2} \int \int w_{\mathrm{true}}(\theta) \, \mathrm{d}\Omega_1 \mathrm{d}\Omega_2, \qquad (4.4.8)$$

(Groth and Peebles 1977) due to the integral constraint (that by construction the estimated angular correlation function will integrate to zero over the area of the field), where $w_{\mathrm{true}}(\theta)$ is the true angular correlation function of the sources and the angular integrations are over a field of area Ω. This quantity is related to the field-to-field variation in the number counts through

$$\sigma^2 = \frac{\langle (\eta - \langle \eta \rangle)^2 \rangle}{\langle \eta \rangle^2} - \frac{1}{\langle \eta \rangle}, \qquad (4.4.9)$$

(e.g. Efstathiou et al. 1991). We evaluate equation (4.4.9) for our $50 \times 4 \, \mathrm{deg}^2$ light-cones and find $\sigma^2 = 4.8 \times 10^{-5}$, which we add onto our computed angular correlation functions for sub-mm sources (w_s).

In Fig. 4.8 we show the mean $w_s(\theta)$ from the 50 lightcone realisations (*magenta line*), with the corresponding shaded region indicating the 1σ (16–84th percentile) field-to-field variation in $w_s(\theta)$ in each bin of angular separation. In Fig. 4.9 we compare $w_s(\theta)$ with observational estimates from the 0.35 deg² LESS source catalogue
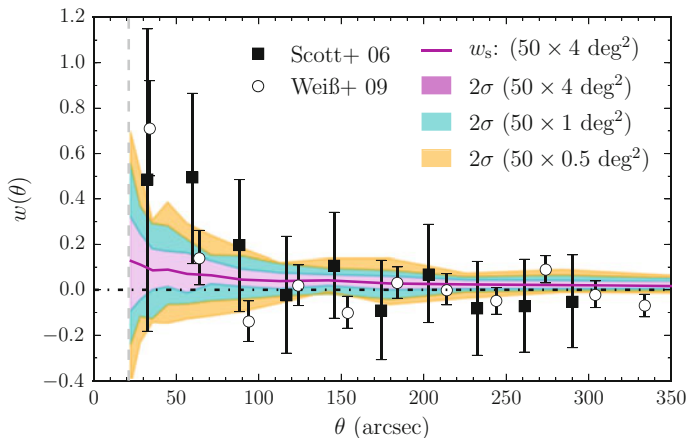
Fig. 4.9 Comparison of the predicted angular correlation function for our $S_{850\mu m} > 4$ mJy simulated single-dish source catalogue, w_s (*magenta line*), to observational estimates from Scott et al. (2006, *filled squares*) and Weiß et al. (2009, *open circles*). The shaded *magenta, cyan* and *orange* regions indicate the 2σ ($2.25 - 97.75$th percentile) range derived from the field-to-field variation over 50 lightcone realisations for fields of 4, 1 and 0.5 deg^2 respectively

(Weiß et al. 2009, 19 arcsec FWHM, $S_{850\mu m} \gtrsim 4.5$ mJy); and from sources identified from a compilation of non-contiguous SCUBA fields totalling ~ 0.13 deg^2 in area (Scott et al. 2006, 15 arcsec FWHM, $S_{850\mu m} \gtrsim 5$ mJy). The magenta, cyan and orange shaded regions indicate the 2σ ($2.25 - 97.75$th percentile) field-to-field variation in each bin of angular separation we predict for fields of 4, 1 and 0.5 deg^2 respectively, which must be considered when comparing theory and observations. For this we recalculate the angular correlation function for each field considering only sources within the central 1 or 0.5 deg^2. As in Fig. 4.6, the large error bars of the observational data make a detailed comparison difficult and highlight the need for larger sub-mm surveys. We note however, that our predictions are consistent with the data once field-to-field variations are taken into account.

4.4.3 Blending Bias in the Angular Clustering of Single-Dish Sources

One of the key results of this work, evident in Fig. 4.8, is that the angular correlation function of sources, w_s, is greater in amplitude by a factor of ~ 4 than the angular correlation function of galaxies, w_g, for the source flux limit used here (4 mJy). In this Section we investigate the dependence of this effect on a number of factors and conclude that it is due to confusion in the simulated survey caused by the 15 arcsec FWHM beam blending the emission of multiple, typically physically unassociated galaxies (Chap. 3), with an on-sky separation comparable to or less than the size of the

beam into an object recognised as a single source by the source extraction algorithm.[6] Thus the angular distribution of sources found in the simulated map is different from the angular distribution of the input galaxies. We label this effect 'blending bias,' b_b, where $b_b^2 \equiv [w_s(\theta)/w_g(\theta)]$, and note that a similar effect has been observed in low resolution X-ray surveys (e.g. Vikhlinin and Forman 1995; Basilakos et al. 2005).

In the upper panel of Fig. 4.10 we test how sensitive this bias is to the size of the beam and 'instrumental' noise. We repeat the calculation for deriving the angular correlation function of single-dish sources for images generated using Gaussian beams with FWHM of 30 and 7.5 arcsec. We kept the instrumental noise constant at $\sigma_{inst} = 1$ mJy/beam in each case and used the same flux limit of $S_{850\mu m} > 4$ mJy to select our sources, noting that varying the beam size will change the confusion in the image and thus the overall noise. We derived blending bias factors in w_s of $b_b^2 \sim 2$ and $b_b^2 \sim 8$ for the 7.5 and 30 arcsec beams respectively. We tested the effect of instrumental noise by creating a set of images with a 15 arcsec beam, but without the addition of instrumental noise. This can be seen in Fig. 4.10 to have a negligible effect on the angular correlation function of the sources, as one would expect given that our 'instrumental' noise is random and has no dependence on scale.

In the lower panel of Fig. 4.10 we repeat the calculation on images which had the positions of galaxies with $S_{850\mu m} < 2$ mJy and $z > 2.5$ randomised prior to being created and find that the blending bias is reduced to $b_b^2 \sim 2$. For maps which had the position of all galaxies with $S_{850\mu m} < 2$ mJy randomised the blending bias is approximately unity i.e. has been removed. Although not shown in Fig. 4.10, we also tested this effect on a set of images which had the positions of all galaxies randomised prior to their creation, and observed a result consistent with the selected sources being completely unclustered. We conclude that blending bias in the angular clustering of single-dish sources is due to the confusion noise or rather the clustering of faint unresolved galaxies and the way in which, when their emission is smoothed with a single-dish beam, this causes certain on-sky positions to be selected as sources. It thus depends on the combined effect of the finite beam size, the intrinsic clustering of the underlying galaxies, and their intrinsic number counts.

We also consider how calculating the angular correlation function using different redshift intervals can affect the blending bias. In order to assign a redshift to a single-dish source we first define a source-counterpart as the galaxy which is contributing the most sub-mm flux to a source, taking into account the profile of the beam. We can then select these counterparts within a given redshift interval and recalculate the angular correlation function, now using the on-sky position of the counterpart. For the underlying galaxies and dark matter we calculate the angular correlation function over a given redshift interval by appropriately changing the limits in the Limber (1953) equation (4.4.7). An example of this is shown in the upper panel of Fig. 4.11 for two redshift intervals centred on $z = 2.5$, $2.25 < z < 2.75$ (*solid lines*) and

---

[6]In Chap. 3 we showed that this confusion effect boosts the cumulative 850 μm number counts by a factor of ~ 2 at $S_{850\mu m} = 4$ mJy for a 15 arcsec FWHM beam. See also Hayward et al. (2013) and Muñoz Arancibia et al. (2015) who investigate the effect of coarse angular resolution on the observed sub-mm number counts.
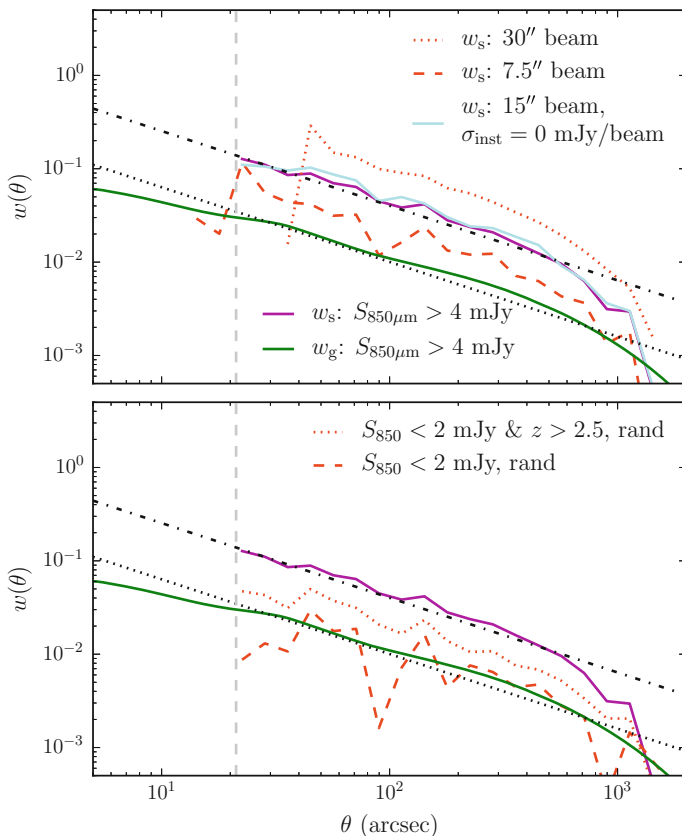
Fig. 4.10 The effect of beam-size, instrumental noise and the clustering of faint ($S_{850\mu m} < 2$ mJy) galaxies on the angular correlation function of brighter ($S_{850\mu m} > 4$ mJy) single-dish sources. The *green* and *magenta lines* show the angular correlation function for galaxies and sources (for a 15 arcsec beam) respectively, as shown in Fig. 4.8. The vertical *dashed*, and diagonal *dashed* and *dash-dotted lines*, shown for reference, are also as described in Fig. 4.8. *Upper panel:* the *dotted (dashed) orange line* indicates the correlation function for sources extracted from simulated images generated with a 30 (7.5) arcsec beam. The *light blue line* is the source correlation function derived from images created with no 'instrumental' noise added. *Lower panel:* the *dotted orange line* indicates the correlation function for sources extracted from images where the position of galaxies with $S_{850\mu m} < 2$ mJy and $z > 2.5$ were randomised prior to creation. The *orange dashed line* shows the same for images which had the position of all galaxies with $S_{850\mu m} < 2$ mJy randomised

$1.0 < z < 4.0$ (*dashed lines*). In this way we can derive a large-scale bias, defined as $[w(\theta)/w_{DM}(\theta)]^{1/2}$, for the galaxies and source-counterparts, as a function of redshift interval considered. This is shown in the bottom panel of Fig. 4.11 where we consider 8 redshift intervals of varying width centred on $z = 2.5$. We can see that the derived source-counterpart bias, which is affected by blending bias, increases monotonically as the width of the redshift interval increases whilst the bias derived from the angular correlation function of galaxies is approximately constant and consistent with the bias
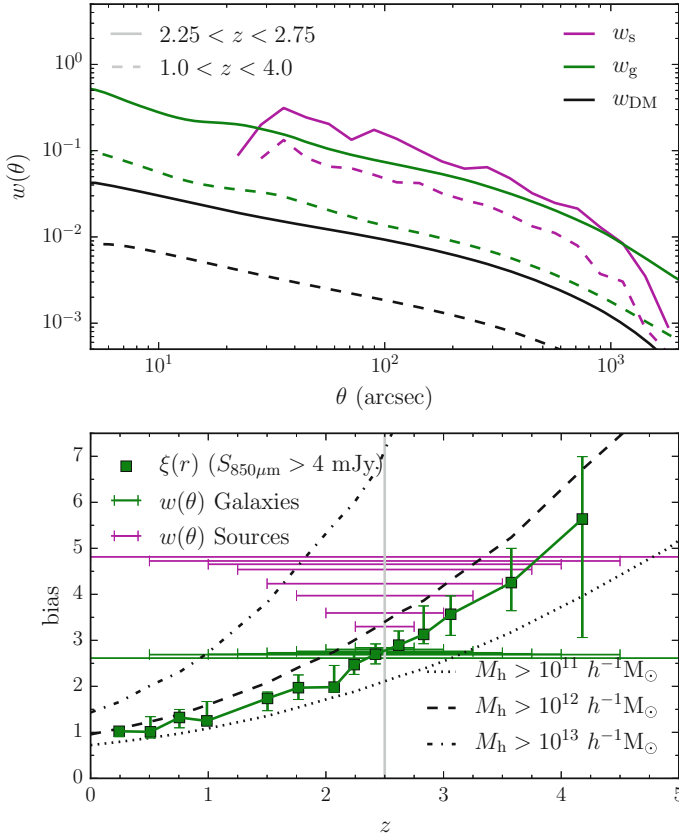
Fig. 4.11 The effect of the redshift interval considered on the angular correlation function of $S_{850\mu m} > 4$ mJy single-dish source counterparts (see text). *Upper panel:* angular correlation function of single-dish source counterparts (*magenta lines*), $S_{850\mu m} > 4$ mJy galaxies (*green lines*) and dark matter (*black lines*) for the redshift interval $2.25 < z < 2.75$ (*solid lines*) and $1.0 < z < 4.0$ (*dashed lines*). *Bottom panel:* evolution of large-scale bias with redshift. *Green squares* indicate the bias evolution of $S_{850\mu m} > 4$ mJy galaxies, derived from the spatial correlation function as in Fig. 4.6. The *dotted, dashed* and *dash-dotted lines* indicate the bias evolution of halos with $M_{halo} > 10^{11}$, 10^{12} and 10^{13} h^{-1} $M_{\odot}$ respectively. The green bars indicate the bias derived from the angular correlation functions of galaxies and dark matter, with the width of the bar indicating the redshift interval considered. The magenta bars show the same but for bias derived from the angular correlation functions of single-dish source counterparts. The vertical *grey line* indicates $z = 2.5$, on which all redshift intervals considered are centred

derived from the spatial correlation function (see Sect. 4.3.3) for all redshift intervals considered. Also evident in this panel is how the halo mass can be significantly overestimated as a result of this effect. As a further example of this, using equation (8) in Sheth et al. (2001) to infer halo mass from a measured bias, we find that doubling the bias (i.e. $b_b = 2$) of halos with mass 10^{12} h^{-1} $M_{\odot}$ yields an inferred halo mass of $10^{13.1}$ h^{-1} $M_{\odot}$ at a redshift of 2.5, an over-estimation of more than an order of magnitude.

To further illustrate the results in this Section we imagine a simplified scenario with two distinct redshift intervals A and B and two angular positions $\underline{\theta}_1$ and $\underline{\theta}_2$. Within each redshift interval the positions of galaxies will be correlated according to some $w(S_1, S_2, z \pm \Delta z, |\underline{\theta}_1 - \underline{\theta}_2|)$, and we define some flux limit S_{lim} brighter than which galaxies will be resolved as point sources in the beam-smoothed imaging and fainter than which they would require some boost to be counted in the single-dish catalogue.

If we now consider the effect of the beam, we have a beam-smoothed flux density field in each redshift interval, $\mathcal{S}(\Omega_{\text{beam}}, z \pm \Delta z, \underline{\theta})$, dominated by galaxies with $S < S_{\text{lim}}$, the distribution of which will be correlated with the positions of galaxies with $S > S_{\text{lim}}$ in that interval, according to w. It is also now possible for flux from B to boost objects (at the same on-sky position) in A into the selection (and vice-versa). This induces an artificial cross-correlation between the sources selected in A and B, as some objects in B required a flux boost from A to be considered and this flux is correlated with selected objects in A. Thus we make the prediction that the cross-correlation of single-dish source counterparts (for sources with $S_{850\mu\text{m}} > 4$ mJy) in distinct redshift intervals will be non-zero, even in the absence of effects such as gravitational lensing which are not considered here.

This is demonstrated in Fig. 4.12, where we show the angular cross correlation between source counterparts in two distinct redshift intervals $1.0 \le z < 2.4$, z_{A}, and $2.6 \le z < 4.0$, z_{B} (blue line). This is found to be non-zero whilst the equivalent calculation for bright galaxies (with $S_{850\mu\text{m}} > 2$ mJy[7]) is zero (cyan line). We also find that source counterparts in z_{A} are correlated with bright galaxies in z_{B}, in this case shown for galaxies with $S_{850\mu\text{m}} > 2$ mJy (green line). The physical correlation of the faint with the bright galaxies in z_{B} has caused the sources from z_{A}, many of which were selected as sources because of a flux contribution from faint galaxies in z_{B}, to be correlated with bright galaxies in z_{B}. This is an induced correlation introduced by the finite beam. When we repeat the source-galaxy cross-correlation using sources from maps which had the positions of galaxies with $S_{850\mu\text{m}} < 2$ mJy and $z > 2.5$ randomised prior to the image being created, the randomisation removes the physical correlation between faint and bright galaxies in z_{B}, thus we find that the induced cross-correlation between sources in z_{A} and bright galaxies in z_{B}, on scales larger than the beam, is now zero. This is despite the fact the positions of galaxies with $S_{850\mu\text{m}} > 2$ mJy in z_{B} were not changed.

We infer that it is these induced cross-correlations that cause the trend in blending bias with redshift interval width seen in the lower panel of Fig. 4.11, as increasing the redshift interval increases the number of induced cross-correlations considered. It also explains the trends seen in the lower panel of Fig. 4.10, as randomising the positions of faint galaxies reduces the correlation between the distribution of flux density, $\mathcal{S}$, and the distribution of galaxies with $S > S_{\text{lim}}$ at a given redshift, and thus the contribution of the induced cross-correlation terms. For the same S_{lim} increasing

---

[7]Here we use a limit of 2, rather than 4 mJy, so we have enough objects for a robust determination of w_{cross}. We do not expect the result to be sensitive to this given that the auto-correlation of galaxies is roughly independent of flux over this flux range.
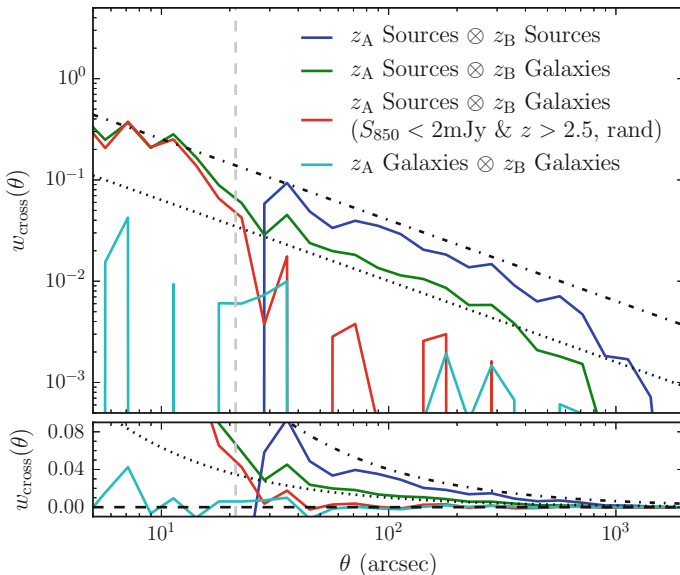
Fig. 4.12 Angular cross correlations between two separated redshift intervals, $z_A = [1.0, 2.4)$ and $z_B = [2.6, 4.0)$. In the legend 'Sources' refers to the counterparts of sources (see text) extracted from our simulated imaging with $S_{850\mu m} > 4$ mJy and 'Galaxies' refers to galaxies selected with $S_{850\mu m} > 2$ mJy. *Top panel*: We show the angular cross correlation of: (i) source counterparts in z_A with source counterparts in z_B (*blue line*); (ii) source counterparts in z_A with galaxies ($S_{850\mu m} > 2$ mJy) in z_B (*green line*); (iii) source counterparts in z_A with galaxies ($S_{850\mu m} > 2$ mJy) in z_B but with the sources extracted from images where the positions of galaxies with $S_{850\mu m} < 2$ mJy and $z > 2.5$ were randomised prior to creating the images (*red line*); and (iv) galaxies ($S_{850\mu m} > 2$ mJy) in z_A with galaxies ($S_{850\mu m} > 2$ mJy) in z_B (*cyan line*). The *vertical dashed*, and *diagonal dashed* and *dash-dotted lines*, shown for reference, are as described in Fig. 4.8. *Bottom panel*: as for top panel but with a linear y-axis. A *dashed line* at $w = 0$ has been added for reference

the beam-size will on average increase the multiplicity of sources. As the components of each source are, in our simulations, drawn from different redshift intervals (galaxies composing a single source are generally at different redshifts) this means that for each source more induced cross-correlation terms are considered, producing the trends seen in the upper panel of Fig. 4.10.

We therefore caution that significant modelling is needed to interpret the angular correlation function of sources identified in single-dish surveys, at flux limits at which the sources are confused (i.e. composed of multiple fainter galaxies). The implication is that the halo masses of the galaxies in question could be seriously overestimated if blending bias is not corrected for. It appears from Fig. 4.22 that $w_I(\theta)$, described in the Sect. 4.4.5, exhibits angular clustering more representative of the underlying galaxy population. We suggest then that information regarding the halo masses of SMGs should be inferred from $w_I(\theta)$. This comes with the important caveat that the effects of correlated noise in observed images, e.g. large-scale structure due to correlated atmospheric contamination and $1/f$ noise, need to be removed or accurately modelled.

Targeted follow-up of single-dish sources with interferometers could also be used to overcome blending bias, as the order of magnitude better resolution would allow the underlying galaxies from which the sources are composed to be identified, down to flux limits dependent on integration time. This would provide an approximately complete flux-limited catalogue of galaxies down to slightly above the source-extraction limit of the single-dish survey (some galaxies are de-boosted by instrumental noise to below the flux limit of the single dish survey and are therefore missed from the follow-up observations, e.g. Karim et al. 2013) which could then be used to derive the correlation function free from blending bias.

4.4.4 A Cross-Correlation Analysis of Sub-mm Sources

In this Section we extend our investigation of the blending bias to consider the case when the correlation function of sub-mm sources is derived via a cross-correlation analysis with a more abundant galaxy population, as was recently performed by Wilkinson et al. (2017). These authors used a K-band selected sample from the UKIDSS–UDS[8] to derive the clustering of SCUBA-2 sources identified in that field (Chen et al. 2016). This improved on the earlier work by Hickox et al. (2012) as it allowed the evolution of the clustering of the sub-mm sample to be investigated due to the greater number of sub-mm sources in the more recent SCUBA-2 catalogue. Wilkinson et al. estimated that the halo masses of SMGs ranged from $M_{halo} \sim 10^{13}\ h^1\ M_\odot$ at $z \gtrsim 2$ to $M_{halo} \sim 10^{11}\ h^1\ M_\odot$ for $1 < z < 2$ and concluded that the $z \gtrsim 2$ SMG population could evolve into local $\sim 2 - 3\ L_\star$ galaxies.

We present predictions for the blending bias when the correlation function of sub-mm sources is determined via a cross-correlation with a more abundant galaxy population. Also, in order to provide the best possible comparison of the observations of Wilkinson et al. and the galaxy formation model used throughout this thesis, we choose a K-band sample of similar depth and use the same redshift intervals considered in Wilkinson et al. We also mimic, to first order, the effect of broadening photometric redshift probability distributions with increasing redshift. In addition, the nature of our simulations allows us to make predictions for the field-to-field variation expected for such observations.

For the purposes of this study we use an Absolute Bolometric (AB) apparent magnitude of $m_K < 25$ to select our K-band population, similar to that used by Wilkinson et al. (2017). An example of the K-band absolute magnitude versus redshift for the resulting catalogue is shown in Fig. 4.13. The resulting redshift distributions are compared in Fig. 4.14. We can see that the source counterparts are more numerous than galaxies at this flux limit (see also Chap. 3), and that their distribution has a more prominent high-redshift tail. The surface number densities of the flux-limited K-band sample, the $S_{850\mu m} > 4$ mJy galaxies and the counterparts to $S_{850\mu m} > 4$ mJy sources are 4.02×10^5, 5.54×10^2 and 1.05×10^3 deg^{-2}, respectively.

---

[8]United Kingdom Infra-red Telescope (UKIRT) Infra-red Deep Sky Survey – Ultra Deep Survey.
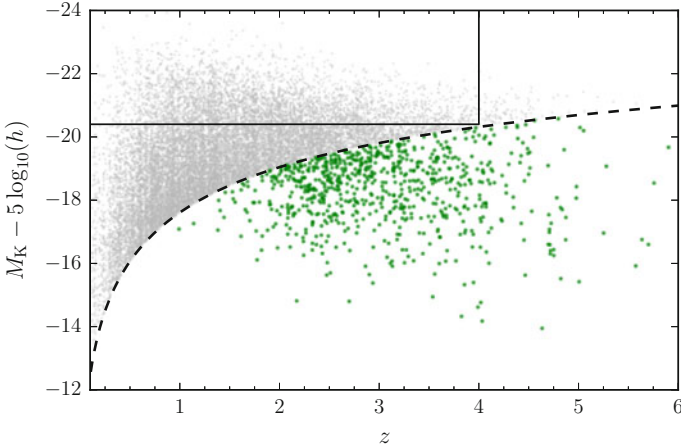
Fig. 4.13 The K-band absolute magnitude versus redshift for lightcone galaxies flux limited in the K-band at an apparent magnitude of 25 (*grey dots*) for one of the 50×4 deg^2 fields. For clarity, only 1 per cent of this sample is shown. The K-band flux limit is indicated by the *dashed black line*. The *green points* indicate galaxies with $S_{850\mu m} > 4$ mJy that are not selected in the K-band. The *black solid lines* indicate a volume-limited K-band sample for $z < 4$. All magnitudes are in the AB system
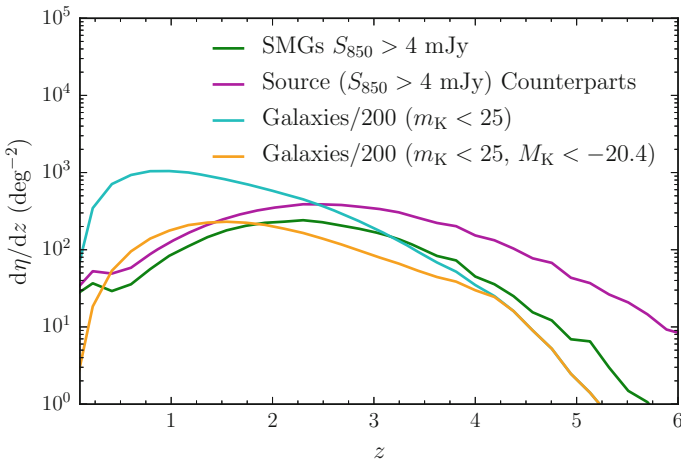
Fig. 4.14 Predicted average redshift distributions from our 50×4 deg^2 fields for $S_{850\mu m} > 4$ mJy galaxies (*green line*), the counterparts (see text) of sources with $S_{850\mu m} > 4$ mJy extracted from the simulated sub-mm imaging (*magenta line*), flux-limited sample of K-band selected galaxies (*cyan line*) and a volume-limited sample (for $z < 4$) of K-band selected galaxies (*orange line*). The latter two lines have both been divided by a factor of 200 for presentation purposes. All magnitudes are in the AB system

As we are comparing the predictions of our model to the analysis of Wilkinson et al. (2017), we begin with the source catalogue ($S_{850\,\mu m} > 4\,\text{mJy}$) derived from source extraction from the simulated images as described in Chap. 3. The SMG sample used by Wilkinson et al. has a slightly fainter flux limit ($\sim 3.5\,\text{mJy}$, Chen et al. 2016), however we do not expect this to have a significant impact on our science results. Earlier, we showed that the angular auto-correlation of the sub-mm sources, w_s, was boosted by a 'blending bias' factor, b_b, relative to that of the underlying galaxy population, w_g, such that $w_s = b_b^2 w_g$. Here we calculate w_s via a cross-correlation with a volume-limited K-band selected galaxy population ($m_K < 25$). Assuming linear theory, the large-scale bias of the sub-mm sources, b_s, can be determined using

$$b_s = b_{s \otimes K}^2 / b_K, \qquad (4.4.10)$$

where b_K represents the bias of the K-band selected galaxy population as measured from its auto-correlation function and $b_{s \otimes K}$ is the bias of the cross-correlation of the two populations. This means that $(b_{s \otimes K}/b_K)^2 w_{s \otimes K}$ is equivalent to w_s, provided that the blending bias effects both measurements in the same way.

To calculate the angular cross-correlation of the sub-mm sources and the K-band galaxy sample, $w_{s \otimes K}$, we use the Landy and Szalay (1993) estimator adapted for cross-correlations

$$w_{s \otimes K}(\theta) = \frac{DD_{sK} - DR_{sK} - DR_{Ks} + RR_{sK}}{RR_{sK}}, \qquad (4.4.11)$$

where DD, DR and RR represent data-data, data-random and random-random pairs respectively, and the subscripts s and K represent the sub-mm sources and K-band selected galaxies respectively. In calculating $w_{s \otimes K}$ we use the actual number of sources in each field to estimate the mean surface density, rather than the true surface density. This causes the angular correlation function to be underestimated by an average amount, σ^2, often referred to as the integral constraint (Groth and Peebles 1977). For the cross-correlation functions this quantity is related to the field-to-field variation in the number counts through

$$\sigma_{s \otimes K}^2 = \frac{\langle (\eta_s - \langle \eta_s \rangle)(\eta_K - \langle \eta_K \rangle) \rangle}{\langle \eta_s \rangle \langle \eta_K \rangle} - \frac{\langle \eta_{sK} \rangle}{\langle \eta_s \rangle \langle \eta_K \rangle}, \qquad (4.4.12)$$

where η_{sK} represents the surface density of objects that are in both populations. We evaluate this quantity for our 50 lightcone fields and add it onto our computed cross-correlation functions. We also make the corresponding correction to our auto-correlation functions. These corrections are typically on the order of $\sim 10^{-3}$. We note that equation (4.4.12) is not how this correction is usually calculated in observational studies, where the expression $\sigma^2 = \sum RR(\theta) w(\theta) / \sum RR(\theta)$ is more commonly used to evaluate the integral constraint, in the absence of multiple fields (Roche and Eales 1999). However we have checked that this expression gives essentially identical results to equation (4.4.12).
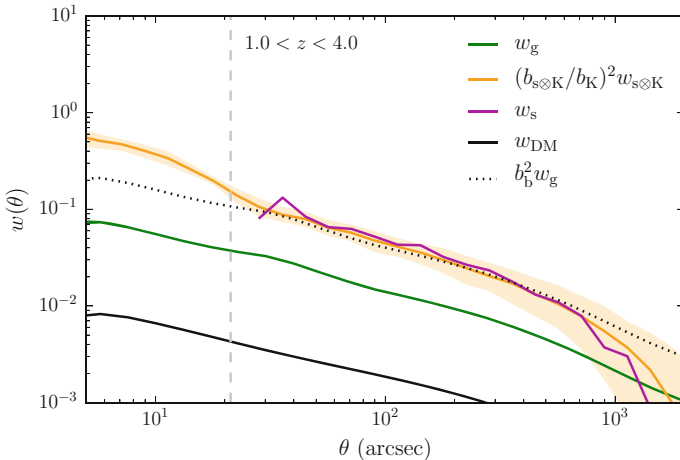
Fig. 4.15 Predicted angular correlation functions in the redshift range $1.0 < z < 4.0$. The angular correlation function of galaxies selected by $S_{850\mu m} > 4$ mJy is shown by the *green line*. The cross-correlation of counterparts to sources with $S_{850\mu m} > 4$ mJy with a volume-limited K-band selected sample, averaged over our 50×4 deg^2 fields and scaled to remove the bias of the K-band sample is shown by the *orange line*. The *shaded orange region* corresponds to the predicted 1σ (16–84 percentile) field-to-field variation for the 4 deg^2 field area used. The auto-correlation of the source counterparts (averaged over 50×4 deg^2) is shown by the *magenta line*, the correlation function of dark matter in the MR7 simulation is shown by the *black line*, and the correlation function of the galaxies scaled by the blending bias squared (here $b_b = 1.7$) is shown by the *black dotted line*. The vertical dashed line indicates the FWHM of the match-filtered point spread function used to create the simulated imaging ~ 21.2 arcsec

In Fig. 4.15 we show the angular cross-correlation function of sub-mm sources with the K-band galaxy population, and (for comparison) the auto-correlation of sub-mm sources, over the redshift range $1 < z < 4$. For our sub-mm sources we use the position and redshift of the galaxy that makes the largest contribution to the flux of the source. The angular correlation functions for the galaxies and dark matter are calculated from their spatial correlation functions using the Limber (1953) equation (computed using a method similar to that described in Gonzalez-Perez et al. 2011), appropriately changing the redshift limits, as is done in the previous Section.[9] We derive a blending bias factor of $b_b \sim 1.7$ comparing the clustering of sub-mm sources and galaxies. For reference we also show the galaxy correlation function scaled by b_b^2. For calculating the biases we restrict ourselves to the angular range over which the dark matter correlation function is approximately linear. We do this by excluding scales for which $w_{DM,non-linear} > 1.2 \times w_{DM,linear}$ from our computation of the bias. We also exclude angular scales larger than 10^3 arcsec to ensure that the bias measurements are not affected by the finite area of our mock surveys. We can see

---

[9]In principle these could be derived from lightcone catalogues giving essentially identical results, however we prefer using Limber's equation as it utilises all of the clustering information available in our simulation volume.

that the auto-correlation and the scaled cross-correlation functions are essentially the same. It therefore appears that blending bias behaves in a similar manner to a linear scale-independent bias. In this regime the ratio of the cross-correlation of the K-band sample with the sub-mm sources, to the cross-correlation of the K-band sample with sub-mm galaxies, should simply be equal to the blending bias i.e. $w_{s \otimes K} = b_b w_{g \otimes K}$. We show that this is the case in Fig. 4.16.

Thus, whilst the cross-correlation technique can provide smaller statistical errors than the auto-correlation due to the larger number of objects considered, it is still affected by blending bias in the same way.

4.4.4.1   Comparison with Wilkinson et al. (2017)

In order to compare the predictions of our model to the observations of Wilkinson et al. (2017) we repeat the above analysis using their quoted redshift intervals with $\Delta z = 0.5$. This is shown in Fig. 4.17. We also show the predicted $16 - 84$ percentile field-to-field variance, estimated from 50 lightcone fields. For calculating the predicted field-to-field variance we assume an area of 1 deg^2, comparable to that used in Wilkinson et al.

The agreement between the model and the observations appears to be generally favourable, with the majority of observed data points in each redshift bin (apart from the $1.5 < z < 2$ bin) lying within the predicted 1σ region, indicating that the model is broadly consistent with the observed data.
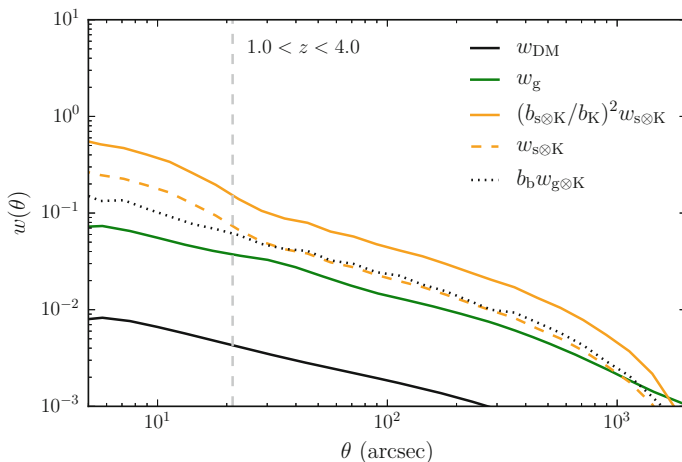
Fig. 4.16 Predicted angular correlation functions in the redshift range $1.0 < z < 4.0$. The *dashed orange line* shows the cross-correlation of counterparts to sources with $S_{850\mu m} > 4$ mJy with a volume-limited K-band selected sample, averaged over our 50×4 deg^2 fields. The *dotted black line* shows the cross-correlation of galaxies with $S_{850\mu m} > 4$ mJy with a volume-limited K-band selected sample, averaged over 50×4 deg^2 fields, and scaled by the blending bias. All other lines have the same meaning as in Fig. 4.15
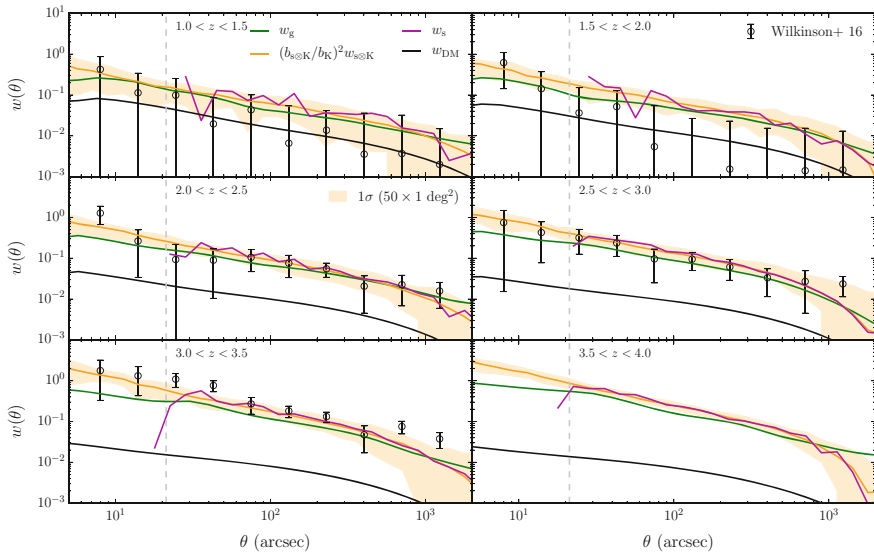
Fig. 4.17 Predicted angular correlation functions for different redshift intervals indicated in the panels for galaxies selected with $S_{850\mu m} > 4$ mJy (*green lines*), the cross-correlation of counterparts to sources with $S_{850\mu m} > 4$ mJy with a volume-limited K-band selected sample, averaged over 50×4 deg^2 fields and scaled so as to remove the bias of the K-band sample (*orange line*), and the auto-correlation of the source counterparts (averaged over the 50×4 deg^2 fields, *magenta line*). We show also observational data from Wilkinson et al. (2017), which are derived from a cross-correlation of sources with a K-band selected galaxy sample, and so should be compared with our orange line. The *shaded orange region* corresponds to the 1σ (16–84 percentile) scatter derived from field-to-field variations, calculated from the central 1 deg^2 region in each of our fields in order to match the area used in the observations of Wilkinson et al. The *vertical dashed line* indicates the FWHM of the match-filtered point spread function used to create the simulated imaging $\sim$21.2 arcsec

We can also see from Fig. 4.17 the blending bias factors have been reduced (to $b_b \sim 1.1 - 1.2$) due to the narrower redshift interval than considered previously. Again, they are essentially the same as those that would be derived from the auto-correlation of the sub-mm sources and are very similar to those derived in Wilkinson et al. (2017) for the auto-correlation case (see their Table 2).

In Fig. 4.18 we show the large-scale bias calculated from the cross-correlation derived function, compared to that of the actual underlying galaxies. We can see that blending bias still affects the inferred halo mass of the SMGs, although to a much lesser extent than it would for the broader $1 < z < 4$ redshift interval, where $b_b \sim 1.7$. Using the large-scale bias - halo mass relations of Sheth et al. (2001) we find that the blending bias ($b_b \sim 1.1 - 1.2$) results in the halo masses of SMGs being overestimated by a factor of $\sim$2. For the broader $1 < z < 4$ redshift interval this overestimate is a factor of $\sim$6. For this we have assumed that all galaxies occupy host dark matter halos of the same mass [i.e. the $\langle N_{gal}|M_h \rangle$ term in equation (4.3.3) is described by a Dirac delta function] and used the median redshift of the relevant

Table 4.1 Predicted large-scale bias of sub-mm galaxies (b_g), blending bias (b_b) and large-scale bias of sub-mm sources (b_s, note that $b_g b_b = b_s$) for the top-red redshift intervals indicated in columns (a) and (b). The large-scale bias observed by Wilkinson et al. is also shown

(a)	b_g	b_b	b_s	(b)	b_g	b_b	b_s	b_s (Wilkinson et al.)
$1.0 < z < 1.5$	1.7	1.1	2.0	$0.9 < z < 1.6$	1.7	1.1	1.9	1.34 ± 0.99
$1.5 < z < 2.0$	2.0	1.1	2.3	$1.3 < z < 2.2$	2.1	1.2	2.5	1.10 ± 1.09
$2.0 < z < 2.5$	2.7	1.1	2.9	$1.7 < z < 2.8$	2.6	1.3	3.3	4.26 ± 1.19
$2.5 < z < 3.0$	3.1	1.2	3.8	$2.1 < z < 3.3$	3.1	1.4	4.2	5.43 ± 1.32
$3.0 < z < 3.5$	3.8	1.2	4.5	$2.3 < z < 4.2$	3.4	1.5	5.0	9.51 ± 2.99

(a) Top-hat redshift interval used in Sect. 4.4.4.1 and quoted by Wilkinson et al.
(b) Top-hat redshift interval used in Sect. 4.4.4.2, chosen such that the normalisation of the dark matter correlation function is the same as used by Wilkinson et al.

population (sub-mm galaxies or sub-mm source counterparts) in the redshift interval considered. We also show in Fig. 4.18, for comparison, the large-scale bias values derived by Wilkinson et al. (2017), though recomputed assuming the same *WMAP7* cosmological parameters as assumed in this thesis.

Immediately apparent from Fig. 4.18 is that despite the general agreement between the predicted and observed correlation functions seen in Fig. 4.17 the inferred large-scale bias values do not agree. We attribute this to the photometric redshift probability distributions used for the observed galaxies, and discuss this in more detail in the next Section. We list our results from this section, the predicted large-scale sub-mm galaxy bias (b_g), blending bias (b_b) and large-scale sub-mm source bias (b_s) for each $\Delta z = 0.5$ redshift interval [listed in column (a)] in Table 4.1. The table also lists the results from Sect. 4.4.4.2, where we use the redshift intervals described in column (b), as discussed below. For reference we also list the large-scale bias values derived by Wilkinson et al. (2017).

4.4.4.2 The Effect of Photometric Redshifts

Given the apparent good agreement between the predicted and observed correlation functions in Fig. 4.17, the cause of the extreme differences in the derived bias values (and subsequent conclusions about the host halo masses) seen in Fig. 4.18 is worthy of further investigation. As mentioned earlier we attribute this to the width of the photometric redshift probability distributions used for each galaxy by Wilkinson et al. (2017), a necessary consequence of the available photometry. The redshifts
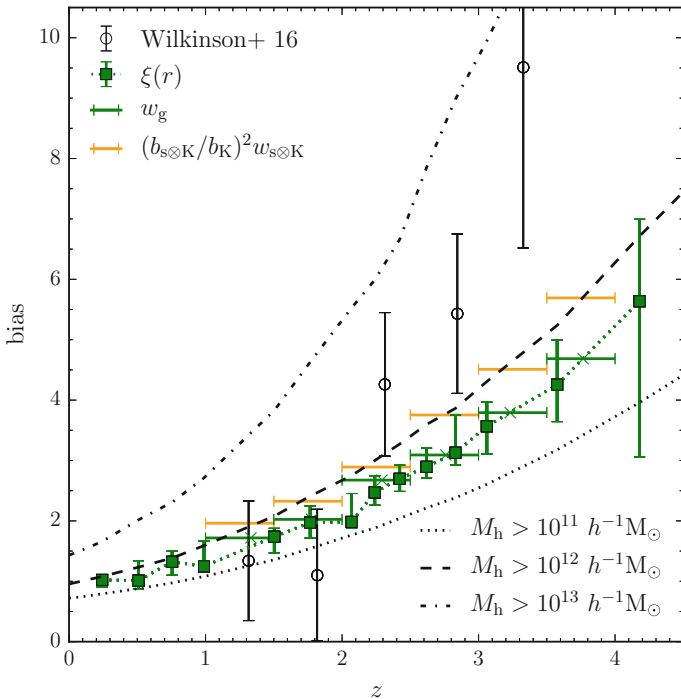
Fig. 4.18 Predicted evolution of large-scale bias with redshift. Green squares with errorbars represent the bias measured directly from the 3D spatial correlation function of SMGs with $S_{850\mu m} > 4$ mJy, as is done in Sect. 4.3. The 1σ errors are calculated using the volume bootstrap method advocated in Norberg et al. (2009). The *horizontal green bars* show the large-scale bias of the SMGs with $S_{850\mu m} > 4$ mJy derived from the angular correlation function over the redshift range indicated by the width of the bar. The *horizontal orange bars* show the same but for the angular correlation function of sub-mm sources calculated via a cross-correlation with a volume-limited K-band selected sample. The *dotted, dashed* and *dash-dotted black lines* show the evolution of the large-scale bias of halos with $M_{halo} > 10^{11}$, 10^{12} and 10^{13} h^{-1} $M_\odot$ respectively, measured directly from the MR7 simulation. Observational data (*open circles with errors*) are from Wilkinson et al. (2017)

in Wilkinson et al. were mostly obtained from the UDSz ESO Large Programme (ID:180.A-0776; PI: O. Almaini). The EAZY template-fitting pack (Brammer et al. 2008) was used to derive a photometric redshift probability distribution for each galaxy through a maximum likelihood analysis. SMG counterparts were assigned using the OIRTC method (Chen et al. 2016). A galaxy in the Wilkinson et al. analysis is able to appear in multiple redshift intervals, weighted by the integral of its probability distribution between the limits of the redshift interval.

A consequence of this is that the effective redshift distributions used for each bin are typically broader than the quoted limits of the bin would suggest, and become broader with increasing redshift as the quality of the photometric redshifts degrades.
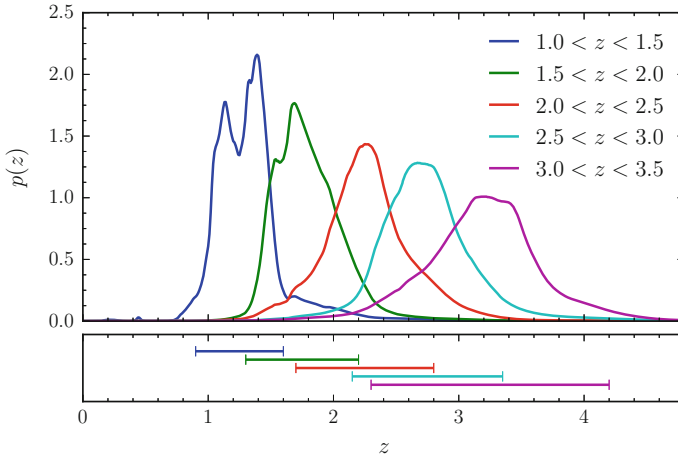
Fig. 4.19 *Top panel:* sub-millimetre galaxy photometric redshift distributions from Wilkinson et al. (2017). The distributions are shown for the redshift intervals indicated in the legend and are normalised to have unit area. *Bottom panel:* the width of the top-hat redshift interval required (with the same central redshift) so that the angular dark matter correlation functions computed using the predicted redshift distributions in Fig. 4.14 have the same normalisation as those computed using the redshift distributions in the top panel

We show the redshift distributions of each redshift interval from Wilkinson et al. (2017) in the top panel of Fig. 4.19.

Thus the angular correlation functions for dark matter used by Wilkinson et al. would typically have a lower normalisation than shown in Fig. 4.17 (where we used the true redshifts of the galaxies in the simulation and a top-hat redshift window of $\Delta z = 0.5$) as the spatial correlation function of the dark matter, $\xi_{DM}(r, z)$, has effectively been projected over a larger volume. This explains how the agreement between the angular correlation functions in Fig. 4.17 is consistent with the disagreement in the inferred large-scale bias in Fig. 4.18.

To mimic the effect of the width of photometric redshift distribution to first order, we increase the width of the redshift intervals we consider (symmetrically in redshift, maintaining the same central redshift) until our dark matter correlation functions have a similar normalisation to those calculated using the redshift distributions of Wilkinson et al. for each bin. These new redshift interval widths are shown in the bottom panel of Fig. 4.19 and listed in column (b) of Table 4.1.

We then repeat our analysis using these new top-hat redshift intervals. We show two examples of this, for the $2.0 < z < 2.5$ and $3.0 < z < 3.5$ bins (for which we now use redshift intervals of $1.7 < z < 2.8$ and $2.3 < z < 4.2$ respectively), in Fig. 4.20 and list the results for each interval in Table 4.1. Considering a broader redshift distribution brings the large-scale bias values we measure for the simulated sub-mm sources into broad agreement with the values quoted by Wilkinson et al.
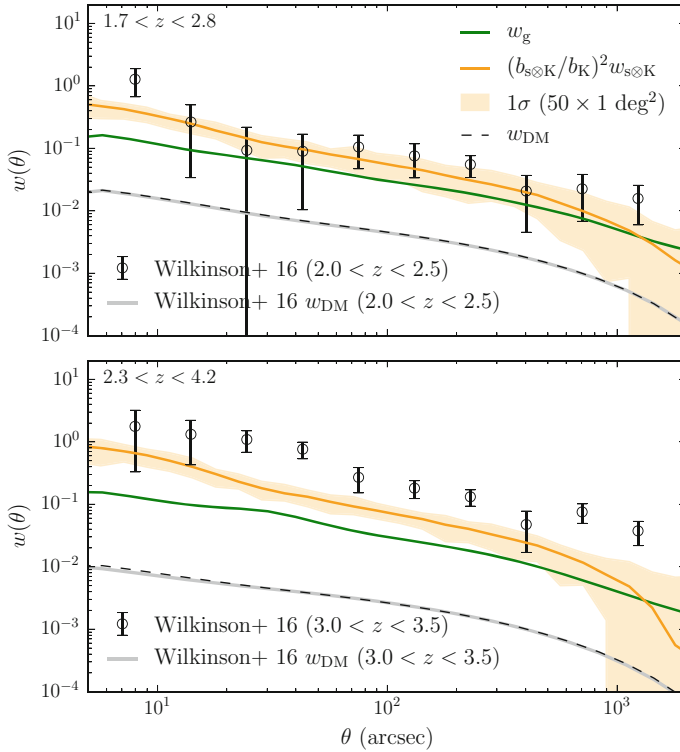
Fig. 4.20 Predicted angular correlation functions for the redshift intervals $1.7 < z < 2.8$ (*top panel*) and $2.3 < z < 4.2$ (*bottom panel*) that correspond to the $2.0 < z < 2.5$ and $3.0 < z < 3.5$ intervals in Fig. 4.17 respectively. These broader intervals are chosen such that the angular correlation function for dark matter (*dashed black line*) is in agreement with that used by Wilkinson et al. (*solid grey line*) for that redshift bin. All other lines and symbols have the same meaning as in Fig. 4.17

(2017), apart from the $1.0 < z < 1.5$ bin where the large-scale bias is overpredicted, and the $3.0 < z < 3.5$ bin where it is underpredicted.

Our reasoning for the agreement between the observed and predicted large-scale bias values for sub-mm sources found here is as follows. As the width of the redshift interval we consider increases, the blending bias also increases. This is due to the inclusion of more 'beam-induced' correlated pairs in the correlation function calculation as is discussed in Sect. 4.4.3. However, the intrinsic galaxy large-scale bias remains approximately constant. Therefore, the increase in blending bias means that the inferred large-scale bias for the sources becomes greater.

In Fig. 4.21 we show the effect this has on the inferred host halo masses as a function of redshift. We use the large-scale bias-to-halo mass relations of Sheth et al. (2001) and assume that the objects occupy halos of a single mass at the median redshift of the interval considered, which we calculate using the relevant redshift
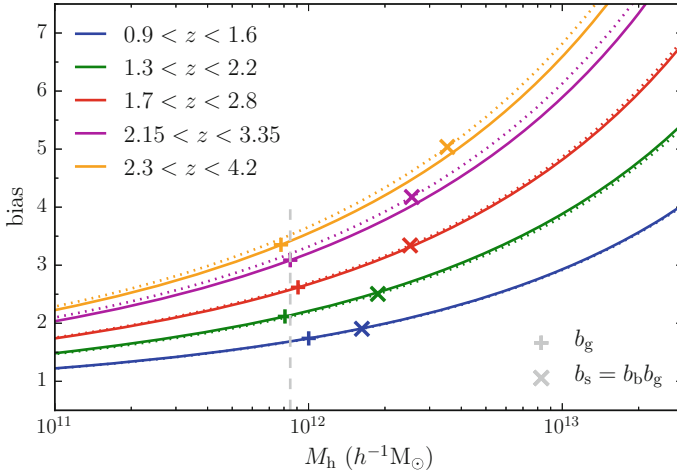
Fig. 4.21 Large-scale bias-to-dark matter halo mass relations of Sheth et al. (2001) calculated at the median redshift of the interval considered for galaxies (*solid lines*) and source counterparts (*dotted lines*). The different colours are for the redshift intervals indicated in the legend. Plus signs (crosses) indicate the position on this plane for galaxies (source counterparts) using the biases derived from the corresponding angular correlation functions. The vertical *dashed grey line* shows the median inferred halo mass for the galaxies

distributions from Fig. 4.14. For the galaxies we find this yields inferred halo masses consistent with those that the galaxies are known to occupy in the model (see Fig. 4.5) and with no significant redshift evolution over this range. For the sources however, we observe a mild evolution in halo mass from $\sim 4 \times 10^{12}\, h^{-1}\, M_{\odot}$ at $z \sim 3$ to $\sim 2 \times 10^{12}\, h^{-1}\, M_{\odot}$ at $z \sim 1$, due to the blending bias being larger at higher redshift as the redshift interval considered is broader. Whilst it appears unlikely from this analysis that this effect could account for all of the very strong halo mass 'downsizing' found by Wilkinson et al. it is possible that the apparent downsizing trend was amplified by this effect, as the broadening of the redshift intervals with increasing redshift was not considered by Wilkinson et al. when deriving their blending bias factors.

We conclude that measuring the correlation function for sub-mm sources via an auto- or cross-correlation is affected by blending bias in the same way. Measuring the cross-correlation using objects within a relatively narrow redshift range is the best way to perform such a measurement, due to the increased statistical significance from the cross-correlation with a more abundant sample and to the reduced blending bias due to the narrower redshift range being investigated. Such an analysis is performed by Wilkinson et al. (2017). However, this comes with the important caveat that accurate redshifts for the correct counterpart to the sub-mm source are required, and there are a sufficient number of objects in each redshift bin for the result to

be statistically significant. Alternatively, as is discussed in Sect. 4.4.3, a significant targeted follow-up campaign with interferometers such as ALMA would allow the blended sources in the single-dish catalogue to be identified and removed from the clustering analysis, providing a result free from blending bias. Investigation of the evolution of the SMG clustering with redshift will still require accurate redshifts (at the level that the typical redshift error is expected to be factors of a few smaller than the width of the redshift bin), but this is an issue separate from the blending bias.

Finally, we note that the blending bias values quoted here may be somewhat model dependent and caution that further work is required to fully understand the implications of this bias on measurements made from catalogues derived from single-dish imaging surveys at FIR/sub-mm wavelengths. An attempt towards an analytical derivation of blending bias is given in Appendix A.

4.4.5 The Angular Clustering of Intensity Fluctuations

In this Section[10] we calculate the angular clustering of intensity fluctuations in our simulated images, $w_I(\theta)$. We first introduce this quantity before describing how it is calculated in this paper. It can be defined as

$$\langle I(\underline{\theta}_1) I(\underline{\theta}_2) \rangle = \langle I \rangle^2 [1 + w_I(\theta)], \tag{4.4.13}$$

where $I(\underline{\theta}_1)$ represents the intensity in a given direction $\underline{\theta}_1$, $\theta = |\underline{\theta}_1 - \underline{\theta}_2|$ and $\langle I \rangle$ is the mean intensity, which can be calculated from the number counts of our model by

$$\langle I \rangle = \int S \frac{d\eta}{dS} dS. \tag{4.4.14}$$

The function $w_I(\theta)$ can be expressed as a flux-weighted integral of the angular correlation function of galaxies, w_g, such that

$$w_I(\theta) = \frac{1}{\langle I \rangle^2} \left[\int \int w_g(S_1, S_2, \theta) S_1 S_2 \frac{d\eta}{dS_1} \frac{d\eta}{dS_2} dS_1 dS_2 + \delta^D(\theta) \int S^2 \frac{d\eta}{dS} dS \right] \tag{4.4.15}$$

where $w_g(S_1, S_2, \theta)$ is the angular cross-correlation of galaxies with fluxes S_1 and S_2 and $d\eta/dS_i$ is the surface density per unit solid angle of galaxies with flux S_i. The angular cross-correlation of galaxies $w_g(S_1, S_2, \theta)$ derives from a more general form of equation (4.4.7) such that

---

[10]In this Section, for ease of reading, and as here we are only considering a single band (850 μm), we suppress the explicit frequency dependence in our notation. For example, we write the mean intensity at a given observed frequency ν, $\langle I_\nu \rangle$, as $\langle I \rangle$.

$$w_{\mathrm{g}}(S_1, S_2, \theta) = \frac{\int N_1(z)N_2(z)\frac{\mathrm{d}z}{\mathrm{d}\chi}\mathrm{d}z \int \mathrm{d}u\, \xi(S_1, S_2, r, z)}{\int N_1(z)\mathrm{d}z \int N_2(z)\mathrm{d}z}, \tag{4.4.16}$$

where $N_i(z)$ represents the redshift distribution of galaxies with flux S_i and $\xi(S_1, S_2, r, z)$ is the spatial cross-correlation of galaxies with S_1 and S_2, at redshift z. We can recover w_{g} for an individual galaxy population by integrating $w_{\mathrm{g}}(S_1, S_2, \theta)$ over the flux limits defining the selection of the population. The term containing the Dirac delta function $\delta^{\mathrm{D}}(\theta)$ on the right hand side of equation (4.4.15) is the shot noise, which arises from galaxies being treated as point sources.

We can calculate w_{I} for the clustered galaxy population directly from our simulated images using the estimator

$$w_{\mathrm{I}}(\theta) = \frac{\sum_{ij} \delta_i \delta_j \Theta_{ij}}{\sum_{ij} \Theta_{ij}}, \tag{4.4.17}$$

where δ_i is the fractional variation of flux in the ith pixel and is calculated using $\delta_i = (S_i/\langle S\rangle) - 1$ where S_i is the flux value of the ith pixel and $\langle S\rangle$ is the average flux value of a pixel, as all of our pixels are of equal area. The step function Θ_{ij} is 1 if pixels i and j are separated by a distance in the angular bin $\theta \pm \Delta\theta/2$ and zero otherwise. However, in practice it is more computationally efficient to make use of the fact that w_{I} can be obtained from the angular power spectrum of CIB anisotropies, $P_{\mathrm{I}}(k_\theta)$, using a Fourier transform such that

$$w_I(\theta) = \frac{2\pi}{\langle I\rangle^2} \int P_{\mathrm{I}}(k_\theta) J_0(2\pi k_\theta \theta) k_\theta \mathrm{d}k_\theta, \tag{4.4.18}$$

where J_0 is the zeroth order Bessel function of the first kind and the convention $k_\theta = 1/\lambda_\theta$ is used.[11] We therefore compute $P_{\mathrm{I}}(k_\theta)$ directly from our simulated images, prior to any matched-filtering, and make use of equation (4.4.18) to calculate w_{I}. This quantity is shown in Fig. 4.22 (gold line), with the corresponding shaded region indicating the 1σ percentile variation of our 50 lightcone realisations at a given θ. The Gaussian-like profile on small scales ($\theta < 30$ arcsec) is due to the beam used to convolve the simulated image and is mostly produced by the shot noise term in equation (4.4.15). It can be seen that on scales larger than the beam w_{I} is very similar to w_{g}, which is unsurprising given that $\sim 70\%$ of the total background light predicted by the model at 850 μm is in galaxies with $S_{850\mu\mathrm{m}} > 0.25$ mJy.

---

[11] We use this convention as it is the standard practice for angular power spectra of CIB anisotropies (e.g. Gautier et al. 1992; Viero et al. 2009). Under this convention the angular wavenumber is related to the multipole index, ℓ, by $\ell = 2\pi k_\theta$ (when angles are measured in radians).
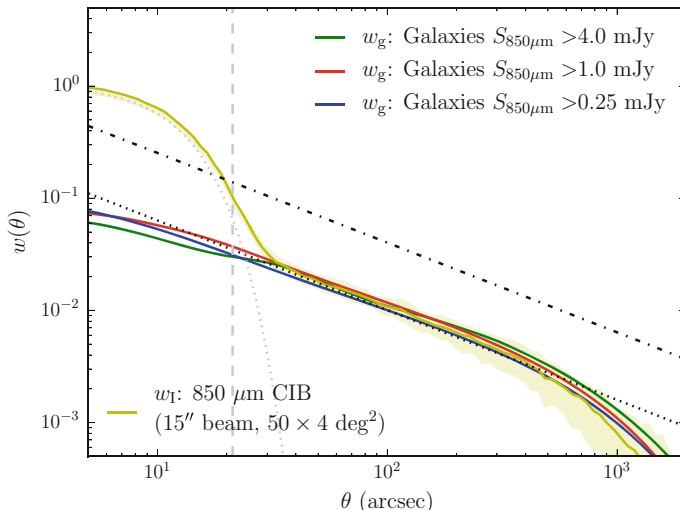
Fig. 4.22 Predicted angular auto-correlation functions. The angular correlation function of the 850 μm intensity fluctuations, derived from the angular power spectrum of the simulated single-dish imaging, prior to matched filtering is shown by the *gold line*. The *gold shaded region* indicates the 1σ ($16-84$th percentile) field-to-field variation over 50 lightcone realisations of $4\,\text{deg}^2$ each. The *grey dotted line* indicates the expectation for the angular correlation function of the CIB intensity fluctuations if the galaxies contributing to it were unclustered. All other lines are as described in Fig. 4.8

4.5   Angular Power Spectrum of CIB Anisotropies

The galaxies which contribute to the bulk of the CIB cannot be individually resolved with current instruments, and instead information regarding their clustering and hence the masses of the halos they occupy is derived from observations of the clustering of fluctuations in the background light. Therefore, in this Section we compare predictions with recent measurements of the angular power spectrum of CIB anisotropies $P_I^\nu(k_\theta)$. Here ν is a fixed observed frequency [related to the emitted frequency, ν_e, by $\nu = \nu_e(1+z)^{-1}$].

The angular power spectrum of CIB anisotropies was introduced in equation (4.4.18) and can be expressed as an integral over redshift of the 3D power spectrum of fractional emissivity fluctuations $\mathcal{P}_j^\nu(k, z)$, where spatial wavenumber k is related to spatial wavelength λ by the convention $k = 2\pi/\lambda$. Using the approximation of Limber (1953), the small-angle approximation ($k_\theta \gg 1$) and assuming a flat cosmology, we can write $P_I^\nu(k_\theta)$ (for k_θ in units of radians^{-1}) as

$$P_I^\nu(k_\theta) = \int dz \frac{d\chi}{dz} \left(\frac{a}{\chi}\right)^2 \langle j_\nu(z)\rangle^2 \mathcal{P}_j^\nu(k = 2\pi k_\theta/\chi, z) \qquad (4.5.19)$$

(e.g. Viero et al. 2009; Shang et al. 2012). Here χ is the radial comoving distance to redshift z, $a = (1 + z)^{-1}$ is the cosmological scale factor and $\langle j_\nu(z) \rangle$ describes the mean emissivity per unit solid angle at redshift z, which can be expressed as

$$\langle j_\nu(z) \rangle = \int \mathrm{d}L_\nu \frac{\mathrm{d}n}{\mathrm{d}L_\nu}(L_\nu, z) \left(\frac{L_\nu}{4\pi} \right), \tag{4.5.20}$$

and related to the mean intensity (see Eq. 4.4.14) by

$$\langle I_\nu \rangle = \int \mathrm{d}z \frac{\mathrm{d}\chi}{\mathrm{d}z} a \langle j_\nu(z) \rangle. \tag{4.5.21}$$

In our model, not all halos contribute equally to $\langle j_\nu(z) \rangle$. We can therefore define a differential emissivity $\mathrm{d}j_\nu/\mathrm{d}\log_{10} M_\mathrm{h}$ (e.g. Shang et al. 2012; Béthermin et al. 2013) such that equation (4.5.19) can be expressed as

$$P_\mathrm{I}^\nu(k_\theta) = \int \int \int \mathrm{d}z\, \mathrm{d}\log_{10} M_\mathrm{h}\, \mathrm{d}\log_{10} M_\mathrm{h}' \frac{\mathrm{d}\chi}{\mathrm{d}z} \left(\frac{a}{\chi} \right)^2$$
$$\times \frac{\mathrm{d}j_\nu}{\mathrm{d}\log_{10} M_\mathrm{h}} \frac{\mathrm{d}j_\nu}{\mathrm{d}\log_{10} M_\mathrm{h}'} \mathcal{P}_j^\nu(k, M_\mathrm{h}, M_\mathrm{h}', z), \tag{4.5.22}$$

where $\mathcal{P}_j^\nu(k, M_\mathrm{h}, M_\mathrm{h}', z)$ is the 3D cross-spectrum of fractional emissivity fluctuations, between halos of mass M_h and M_h'.

Whilst in principle it is possible to calculate $\langle j_\nu(z) \rangle$ and $\mathcal{P}_j^\nu(k, z)$ from the output of our model, for simplicity we compute $P_\mathrm{I}^\nu(k_\theta)$ from a simulated image of a lightcone catalogue at the wavelength of interest.

Here, as we compare $P_\mathrm{I}^\nu(k_\theta)$ predicted by the model to recent *Herschel*-SPIRE data (Viero et al. 2013), we use wavelengths of 250, 350 and 500 μm, and a Gaussian beam with a FWHM of 18, 25 and 36 arcsec respectively, to create our imaging. For simplicity we do not add any instrumental noise to these maps. Following the procedure outlined earlier we generate a lightcone catalogue including galaxies brighter than the flux at which we recover 90% of the predicted CIB at the wavelength of interest [this predicted CIB agrees well with the observations of Fixsen et al. (1998) at all wavelengths] and choose a pixel scale such that the beam is well sampled. We generate 3×20 deg^2 lightcones in order to have a similar total area to that used by Viero et al.

First, we show the differential emissivity of our model (described above) at 350 μm in Fig. 4.23, in terms of the contribution from central and satellite galaxies. The contribution from central galaxies peaks in the halo mass range $10^{11.5} - 10^{12}\ h^{-1}\ \mathrm{M}_\odot$ at all redshifts, with the peak evolving modestly from lower to higher
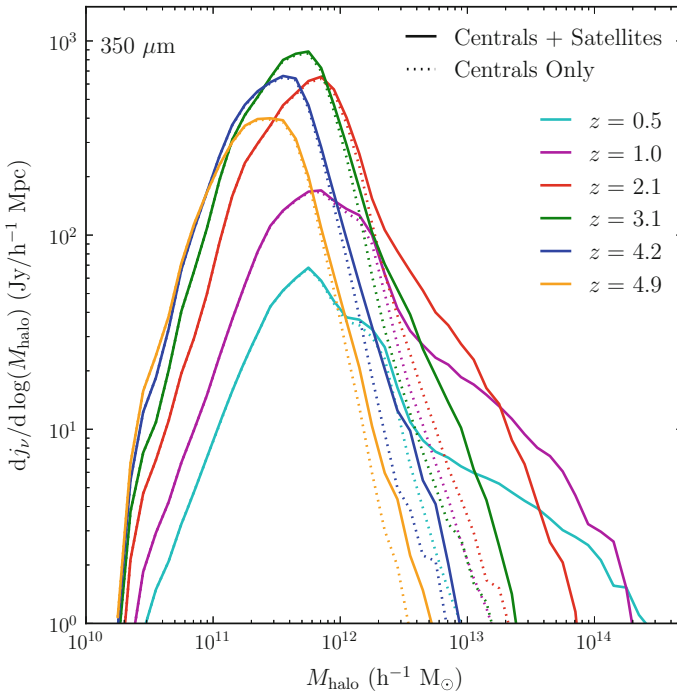
Fig. 4.23 Predicted differential emissivity of our model at 350 µm for a range of redshifts, as indicated in the legend. The contribution from central (central + satellite) galaxies is shown using *dotted* (*solid*) lines

halo masses from $z = 5$ to $z = 2$, and then being approximately constant for $z < 2$. The contribution from satellite galaxies spans a broader range of halo mass and peaks at higher halo mass, however, it is much smaller than that of the central galaxies, being only $\sim 6\%$ of the total 350 µm emissivity at $z = 3.1$ and only $\sim 14\%$ at $z = 0.5$.

In Fig. 4.24 we compare $P_1^\nu(k_\theta)$ predicted by our model to the observations of Viero et al. (2013). The horizontal dashed line in each panel represents the predicted shot noise. This is the power that would be expected if the background were composed of an un-clustered population of point sources and as such has no scale-dependence. It is related to the number counts of the model by

$$P_{\text{shot}}^\nu = \int_0^{S_{\text{cut}}} S_\nu^2 \frac{d\eta}{dS_\nu} dS_\nu, \tag{4.5.23}$$
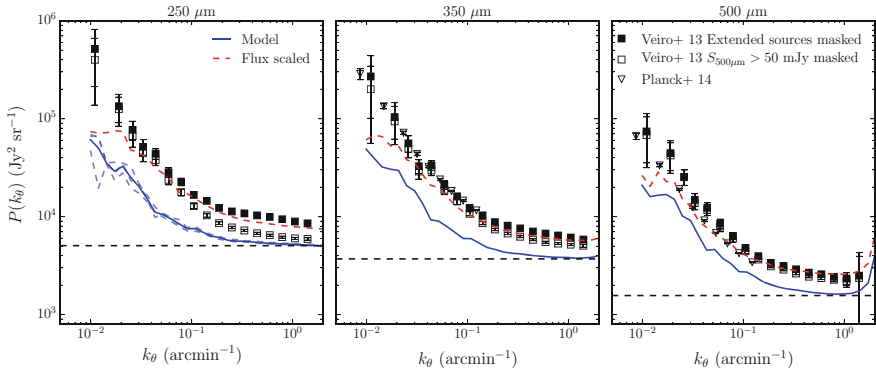
Fig. 4.24 Angular power spectra of CIB anisotropies predicted by our model at 250, 350 and 500 μm (*left* to *right* panels). The *blue solid line* indicates the power spectrum averaged over 3 randomly orientated lightcones, each with an area of 20 deg². The *dashed blue lines* in the *left panel* indicate the power spectra for each of these fields individually. The *horizontal dashed line* shows the predicted shot noise contribution to power spectra. The *dashed red line* shows the prediction of our model after the fluxes of our simulated galaxies have been rescaled (see text). We compare to the observational data of Veiro et al. (2013, *squares*) with the *filled* and *open squares* corresponding to different levels of masking, and to that of the Planck Collaboration et al. (2014, *triangles*)

(e.g. Tegmark and Efstathiou 1996), where S_{cut} is the limit above which sources can be resolved and are therefore removed/masked from further analysis in order to reduce the shot noise.[12] Note that this contribution to the power spectrum corresponds to the Dirac delta function term in equation (4.4.15).

We show the two extremes of masking schemes applied by Viero et al. to their data, in order to reduce the shot noise in their images. They identified sources by finding peaks > 3σ in the matched-filtered SPIRE images at each wavelength. Sources above a given flux limit (S_{cut}) were then masked by circles with a $1.1 \times$ FWHM diameter, before calculating the power spectra. Extended sources were removed by using the criterion $S_{cut} = 400$ mJy. We compare to the most extreme masking case $S_{cut} = 50$ mJy (open squares) and mimic the masking applied by Viero et al. (2013) by excluding galaxies with $S_\nu > 50$ mJy prior to the creation of our simulated images. We have tested that masking pixels in the full image produces near identical results.

At 350 and 500 μm we also compare our predictions to the observational data of the Planck Collaboration (XXX, 2014). These authors employ a slightly different masking scheme to that used by Viero et al. however this has a negligible effect on the scales covered by their data. Encouragingly, both observational datasets are in good agreement.

---

[12]Imposing the limit S_{cut} is necessary as for Euclidean number counts ($d\eta/dS \propto S^{-2.5}$) the integral in equation (4.5.23) does not converge.

We note that there is a discrepancy between the model predictions and the observational data of a factor ~ 2 over all wavelengths and angular scales. Whilst this represents much better agreement than for previous versions of our model (e.g. Kim et al. 2012) we investigate whether it is possible to further improve this by forcing a better agreement between our predicted number counts and those that are observed. By construction, this gives us the observed surface density of objects and should make the shot noise terms equal. This is merely an illustrative exercise to replicate one of the freedoms of empirical models which are constrained to match the observed counts e.g. HOD modelling. An example of this is shown in Fig. 4.25, where we scale the fluxes of our galaxies by the function shown in the bottom panel, chosen such that it brings our model number counts into better agreement with the observed data (top panel). We then apply this scaling relation to our galaxies prior to the creation of our simulated images and recalculate the power spectrum, resulting in the dashed red line in Fig. 4.24. This exercise produces power spectra in much better agreement with the observed data, even at low values of k_θ where clustering dominates over the shot noise. We recognise that this is an artificial adjustment to our model. However it is a relatively minor one as we do not adjust the flux of our galaxies by more than $\sim 40\%$ across all three bands. We do not draw strong conclusions from this, but simply note that good agreement with the observed number counts is required to reproduce the observed power spectra. In this case we have adjusted our number counts artificially but in future this could be achieved by developments to the treatment of physical processes in the model.

At 250 μm there remains a small ($\sim 25\%$) discrepancy between the observed shot noise and that predicted by our flux rescaling, despite the fact that the number counts are in close agreement ($\sim 14\%$). We attribute this to field-to-field variation between the fields used to measure the observed number counts and those used for measuring power spectra, and the uncertainties on both measurements.

As the FIR emissivity is dominated by a halo mass range of $10^{11.5} - 10^{12} \, h^{-1} \, M_\odot$ (e.g. at 350 μm and $z = 3.1$, 54% of the total emissivity comes from halos in this mass range) we investigate whether this mass range also contributes most to the angular power spectrum of CIB anisotropies. We retain the masking flux limit of $S_{\mathrm{cut}} = 50$ mJy from Viero et al. and divide our lightcone catalogue into three halo mass bins of 0.5 dex width, which span the peak of the differential emissivity distribution shown in Fig. 4.23. We then construct an image for each bin. The cross-power spectra for these images are shown in Fig. 4.26. We have ignored the contribution from halos outside the mass bins chosen for this plot, however, the bins chosen contribute $\sim 90\%$ of the total power spectrum (for $S_{350\mu m} < 50$ mJy). We can see that the same halo mass bin which dominates the emissivity dominates the contribution to the power spectrum, as one might expect if the fractional cross-power spectrum term, $\mathcal{P}_j^\nu (k, M_\mathrm{h}, M_\mathrm{h}', z)$, in equation (4.5.22) is a smoothly varying function of halo mass, given the peaked nature of the $\mathrm{d}j_\nu / \mathrm{d}\log_{10} M_\mathrm{h}$ term.
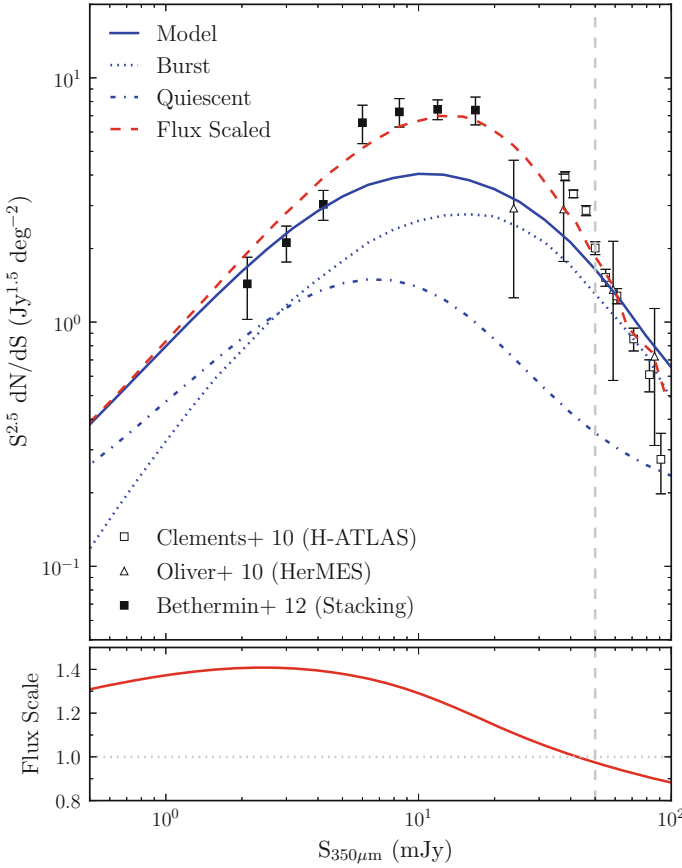
Fig. 4.25 An example of our flux re-scaling scheme at 350 μm. *Top panel:* predicted number counts (*blue line*) showing the contribution to the counts from starburst and quiescent galaxies (*dotted* and *dot-dashed lines* respectively). The *red dashed line* shows the number counts after the flux rescaling has been applied. Observational data are taken from Clements et al. (2010, *open squares*), Oliver et al. (2010, *open triangles*) and Bethermin et al. (2012, *filled squares*). *Bottom panel:* the flux rescaling applied to simulated galaxies as a function of original model flux. A *horizontal dotted line* is drawn at unity for reference. The *vertical dashed line* in both panels indicates a flux of 50 mJy, the limit brighter than which we do not include galaxies in our image in order to match the masking applied by Viero et al. (2013)

To investigate the fluxes of the galaxies which contribute most to the power spectrum, we divide our lightcone catalogue into four flux bins and construct an image for each. The cross-power spectra for these images shown for 350 μm in Fig. 4.27. We can see immediately that on larger angular scales ($k_\theta \lesssim 0.1$ arcmin^{-1}) the power is
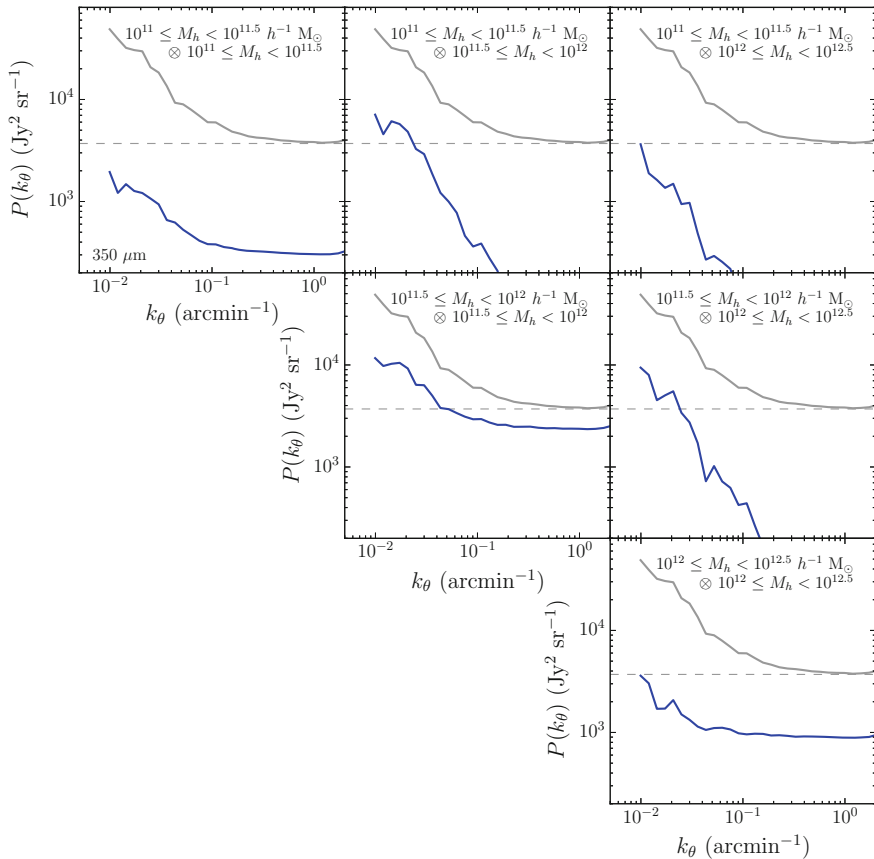
Fig. 4.26 Power spectrum of the CIB predicted by our model at 350 μm for $S_{350\mu m} < 50$ mJy (*solid grey line*) divided into the following halo mass bins $10^{11} M_h \leq 10^{11.5} h^{-1}$ M$_\odot$, $10^{11.5} \leq M_h < 10^{12} h^{-1}$ M$_\odot$ and $10^{12} \leq M_h < 10^{12.5} h^{-1}$ M$_\odot$. The diagonal panels indicate the auto-power spectrum of the halo mass bin indicated in the panel. The off-diagonal panels indicate the cross-power spectrum between different bins, as indicated in the panel. The *dashed grey horizontal line* indicating the total shot noise for the $S_{350\mu m} < 50$ mJy population

dominated by galaxies in the faintest bin $S_\nu < 5$ mJy (e.g. top left panel), whilst the shot noise is dominated by brighter galaxies (e.g. bottom right panel). In our model the dominant shot noise contribution at 350 μm (for galaxies with $S_{350\,\mu m} < 50$ mJy) comes from galaxies with $S_{350\mu m} \sim 20$ mJy.
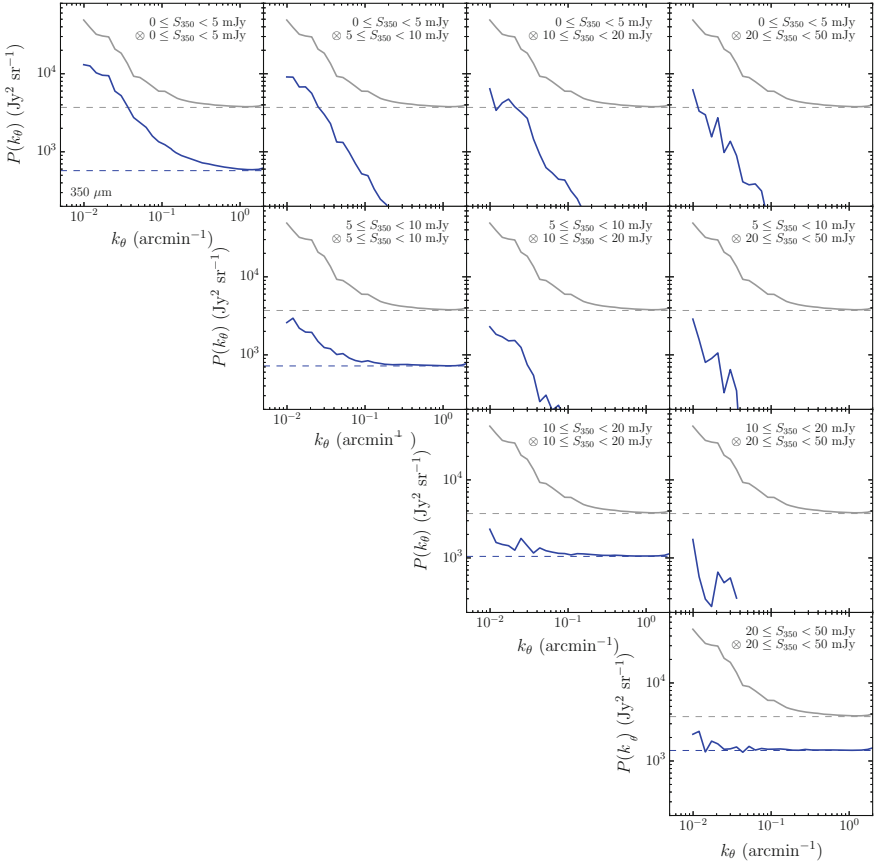
Fig. 4.27 Power spectrum of the CIB predicted by our model at 350 μm divided into the following flux bins $0 \leq S_{350\mu\mathrm{m}} < 5$ mJy, $5 \leq S_{350\mu\mathrm{m}} < 10$ mJy, $10 \leq S_{350\mu\mathrm{m}} < 20$ mJy and $20 \leq S_{350\mu\mathrm{m}} < 50$ mJy. The diagonal panels indicate the auto-power spectrum of the flux bin indicated in the panel and as such contains the shot noise term, indicated by the horizontal *dashed line*. The off-diagonal panels indicate the cross-power spectrum between different bins, as indicated in the panel. The *solid grey line* in each panel indicates the total power for $S_\nu < 50$ mJy, with the *dashed grey horizontal line* indicating the total shot noise

4.6   Conclusions

We present predictions for the clustering evolution of dusty star-forming galaxies selected by their total infra-red luminosity (L_{IR}), and their emission at far infra-red (FIR) and sub-millimetre (sub-mm) wavelengths. This includes the first predictions for potential biases on measurements of the angular clustering of these galaxies due to the coarse angular resolution of the single-dish telescopes used for imaging surveys at these wavelengths. Our model incorporates a state-of-the-art semi-analytic model of hierarchical galaxy formation, a dark matter only N-body simulation which

utilises the *WMAP7* cosmology and a simple model for calculating the emission from interstellar dust heated by stellar radiation, in which dust temperature is calculated self-consistently.

We present predictions for the spatial clustering of galaxies selected by the total infra-red luminosity for $L_{IR} \sim 10^9 - 10^{12} \, h^{-2} \, L_{\odot}$ for $z = 0 - 5$. We find that the clustering evolution in our model depends on the luminosity of the selected galaxies. The large-scale bias evolution of our most luminous galaxies ($10^{12} - 10^{12.5} \, h^{-2} \, L_{\odot}$) is consistent with them residing in halos of mass $10^{11.5} - 10^{12} \, h^{-1} \, M_{\odot}$ over this redshift range. In the model, this halo mass range is the one most conducive to star formation over these redshifts. For lower luminosity populations the range of halo masses selected changes with redshift, such that generally they move to higher mass halos with increasing redshift.

We find that 850 μm selected galaxies in our model represent a clustered population, with an $S_{850\mu m} > 4$ mJy selected sample having a correlation length of $r_0 = 5.5^{+0.3}_{-0.5} \, h^{-1}$ Mpc at $z = 2.6$, consistent with observations of Hickox et al. (2012) and Blain et al. (2004). The bias with which they trace the dark matter evolves with redshift in a way consistent with the SMGs residing in halos of $10^{11.5} - 10^{12} \, h^{-1} \, M_{\odot}$ up to a redshift of $z \sim 4$. This result is insensitive to the flux limit used to select the galaxies for $0.25 \lesssim S_{850\mu m} \lesssim 4$ mJy, and we note that even at the faintest fluxes investigated ($S_{850\mu m} \gtrsim 0.25$ mJy) the model predicted 850 μm number counts are dominated by starburst galaxies. Interestingly, the halo occupation distribution for 850 μm central galaxies peaks well below unity. Halo abundance matching models which force the HOD of central galaxies to equal unity would place galaxies in much more massive halos than our model, given the same galaxy number density. We find further that our brightest SMGs ($S_{850\mu m} > 4.0$ mJy) evolve into $z = 0$ galaxies with stellar mass $\sim 10^{11} \, h^{-1} \, M_{\odot}$, occupying a broad range of present day halo masses $10^{12} - 10^{14} \, h^{-1} \, M_{\odot}$. Thus, in our model, bright SMGs do not necessarily trace the progenitors of the most massive $z = 0$ environments. Our $S_{850\mu m}$ selected galaxy populations share significant overlap with the most infra-red luminous galaxy populations $L_{IR} \sim 10^{12} \, h^{-2} \, L_{\odot}$, and thus exhibit similar clustering evolution.

We make predictions for the angular clustering of sub-mm sources identified in the SCUBA-2 Cosmology Legacy Survey. We show that the angular clustering of 850 μm single-dish selected sources is biased with respect to that of the underlying galaxy population, in our model by a factor of ~4. We attribute this 'blending bias' to the coarse angular resolution of single dish telescopes blending the sub-mm emission of many (typically physically unassociated) galaxies into a single source. This induces cross-correlation terms between sources selected at different redshifts. The position of a galaxy at z_A boosted into the source selection by fainter galaxies at some other redshift z_B will thus be correlated with the positions of galaxies at z_B, some of which will already be included in the source selection. It is the addition of these induced cross-correlations that leads to the 'blending bias'. The value of this bias depends on the size of the beam, the intrinsic clustering of the underlying galaxy population, and their number counts.

We caution that this severely complicates the interpretation of measurements of the angular clustering of SMGs derived from single-dish survey source catalogues,

and if not considered could lead to the halo masses for SMGs being significantly overestimated. The angular clustering of galaxies selected at 850 μm in our model is insensitive to the flux limit used (as is the case for the spatial clustering), and agrees with the angular clustering of intensity fluctuations predicted by the model at that wavelength.

The FIR emissivity of our model is dominated by the emission from halos in the mass range $10^{11.5} - 10^{12}$ h^{-1} M$_\odot$ independent of redshift, and this halo mass range also dominates the angular power spectrum of CIB anisotropies. Our model agrees with the observed angular power spectrum of CIB anisotropies at *Herschel*-SPIRE wavelengths (250, 350 and 500 μm, Viero et al. 2013) to within a factor of ~ 2 over all scales, representing an improvement over previous versions of the model. This agreement can be further improved on by making minor ($\lesssim 40\%$) artificial adjustments to the fluxes of our galaxies which bring the predicted number counts into better agreement with those observed.

Galaxies selected by their FIR/sub-mm emission represent a large proportion of the cosmic star formation over the history of the Universe. As such, understanding the nature of these galaxies is critical to a full understanding of galaxy formation. In our model, the galaxies that contribute to the bulk of the CIB are predominantly disc instability triggered starbursts which reside in a relatively narrow range of halo masses $10^{11.5} - 10^{12}$ h^{-1} M$_\odot$ for $z \lesssim 5$.

Abundance matching arguments which combine the observed stellar mass function with the theoretically predicted halo mass function at $z = 0$ imply that this is also the mass range for present-day halos for which the conversion of baryons into stars has been most efficient (e.g. Guo et al. 2010). The stellar fraction in a halo depends on an integral over the past history of star formation in all of the progenitors of that halo. In our model, the fact that the conversion efficiency of baryons into stars peaks in present day halos of mass $\sim 10^{11.5} - 10^{12}$ h^{-1} M$_\odot$ is a simple consequence of most of the star formation occurring in such halos over a large range of redshifts ($z \lesssim 5$), combined with the growth of halos by hierarchical structure formation. This in turn is a consequence of the physical prescriptions on which our model for galaxy formation is based, in particular for gas cooling in halos and feedback from supernovae and AGN. Observationally, information regarding the host halo masses of selected galaxies can be derived from measurements of their clustering, however extracting significant results from observations at FIR/sub-mm wavelengths is a challenging exercise. This work presents predictions which we hope will inform the interpretation of future observations.

Chapter 5
The Far Infra-red SEDs of Main-Sequence and Starburst Galaxies

5.1 Introduction

[1]Interstellar dust plays an important role in observational probes of galaxy formation and evolution. It forms from metals produced by stellar nucleosynthesis which are then ejected by stellar winds and supernovae into the interstellar medium, where a fraction (∼30–50%, e.g. Draine and Li 2007) condense into grains. These grains then absorb stellar radiation and re-emit it at longer wavelengths. Studies of the extragalactic background light have found that the energy density of the cosmic infra-red background (CIB, ∼10–1000 μm) is similar to that found in the UV/optical/near infra-red (e.g. Hauser and Dwek 2001; Dole et al. 2006), suggesting that much of the star formation over the history of the Universe has been obscured by dust. Thus understanding the nature of dust and its processing of stellar radiation is crucial to achieve a more complete view of galaxy formation and evolution.

Observations suggest that the majority of star formation over the history of the Universe has taken place on the so-called main sequence (MS) of star-forming galaxies, a tight correlation between star formation rate (SFR) and stellar mass ($M_\star$) that is observed out to $z \sim 4$, with a 1σ scatter of ∼0.3 dex (e.g. Elbaz et al. 2007; Karim et al. 2011; Rodighiero et al. 2011; for theoretical predictions see also Mitchell et al. 2014). This is thought to result from the regulation of star formation through the interplay of gas cooling and feedback processes. Galaxies that have elevated SFRs (typically by factors ∼4–10) relative to this main sequence are often referred to as starburst galaxies (SB) in observational studies. In contrast to the secular processes thought to drive star formation on the MS, the elevated SFRs in SB galaxies are thought to be triggered by some dynamical process such as a galaxy merger or disc instability.

---

[1]The content of this Chapter is based on the article Cowley et al. 'The far-infrared SEDs of main sequence and starburst galaxies', Monthly Notices of the Royal Astronomical Society, Volume 467, Issue 1, p. 1231–1248, published 20 January 2017. Reproduced with permission. All rights reserved, https://doi.org/10.1093/mnras/stx165.

The SFRs in these galaxies are usually inferred from a combination of UV and IR photometry and thus a good understanding of the effects of dust in these galaxies is important. However, understanding the dust emission properties of these galaxies is challenging.

A significant difficulty with FIR/sub-mm imaging surveys of high-redshift galaxies is the coarse angular resolution of single-dish telescopes at these long wavelengths [$\sim$20 arcsec full width half maximum (FWHM)]. This, coupled with the high surface density of detectable objects, means that imaging is often confusion-limited and that only the brightest objects (with the highest SFRs) can be resolved as point sources above the confusion background (e.g. Nguyen et al. 2010). These resolved galaxies either form the massive end of the MS or have elevated SFRs relative to the MS and are thus defined as starburst galaxies (SB).

At $z \sim 2$, MS galaxies have SFRs high enough to be resolved in *Herschel* imaging only if they have large stellar masses ($M_\star \gtrsim 10^{10.5}\ h^{-1}\ \mathrm{M}_\odot$) whereas SB galaxies with stellar mass approximately an order of magnitude lower can still be resolved (e.g. Gruppioni et al. 2013). For less massive MS galaxies and galaxies at higher redshifts, as it is not possible to individually resolve a complete sample of galaxies, stacking techniques have been developed to overcome the source confusion and derive average FIR/sub-mm SEDs for different samples (e.g. Magdis et al. 2012; Magnelli et al. 2014; Santini et al. 2014; Béthermin et al. 2015). These studies typically begin with a stellar mass selected sample and stack available FIR/sub-mm imaging at the positions of these galaxies, in bins of stellar mass and redshift.

An early study using this stacking technique, Magdis et al. (2012), fitted the dust model of Draine and Li (2007) to stacked FIR/sub-mm SEDs of $M_\star \gtrsim 3.6 \times 10^9\ h^{-1}\ \mathrm{M}_\odot$ galaxies at $z \sim 1$ and $z \sim 2$. The Draine and Li model describes interstellar dust as a mixture of Polycyclic Aromatic Hydrocarbon molecules (PAHs), as well as carbonaceous and amorphous silicate grains, with the fraction of dust in PAHs determined by the parameter q_{PAH}. The size distributions of these species are chosen such that observed extinction laws in the Milky Way, Large Magellanic Cloud and the Small Magellanic Cloud are broadly reproduced. Dust is assumed to be heated by a radiation field with constant intensity, $U_{\min}$, with some fraction, γ, being exposed to a radiation field ranging in intensity from $U_{\min}$ to $U_{\max}$, representing dust enclosed in photodissociation regions. This model thus provides a best fitting value for the total dust mass, $U_{\min}$, γ and q_{PAH}. The resulting average radiation field $\langle U \rangle$ is strongly correlated with average dust temperature.

Magdis et al. found that the dust temperatures of MS galaxies increases with redshift. Béthermin et al. (2015) extended this analysis to $z \sim 4$ by stacking on a stellar mass-selected sample ($M_\star > 2.1 \times 10^{10}\ h^{-1}\ \mathrm{M}_\odot$) of galaxies derived from UltraVISTA data (Ilbert et al. 2013) in the COSMOS field. Béthermin et al. found, similarly to Magdis et al., that the dust temperatures of MS galaxies increases with redshift. From fitting the Draine and Li (2007) dust model to their stacked SEDs, Bethermin et al. found a strong increase in the mean intensity of the radiation field, $\langle U \rangle$, which is strongly correlated with T_{dust}, for MS galaxies at $z \gtrsim 2$. This led these authors to suggest a break to the fundamental metallicity relation (FMR, Mannucci et al. 2010), which connects gas metallicity to SFR and stellar mass, and is observed

to be redshift independent for $z \lesssim 2$. This break has the effect of reducing the gas metallicity (and hence dust mass) at a given stellar mass for $z \gtrsim 2$. This results in hotter dust temperatures than is implied by simply extrapolating the FMR from lower redshifts. Bethermin et al. also performed their stacking analysis on a sample of SB galaxies, finding no evidence for dust temperature evolution with redshift for these galaxies, and that they have a similar temperature to the $z \sim 2$ main sequence sample.

In this Chapter we compare predictions from the model to the observations presented in Béthermin et al. (2015). Béthermin et al. also compared their inferred dust-to-stellar mass ratios and gas fractions directly with those predicted by the GALFORM models of Lacey et al. (2016) and Gonzalez-Perez et al. (2014, hereafter GP14). Here, we extend this by comparing the FIR/sub-mm SEDs directly and inferring physical properties for both the observed and simulated galaxies in a consistent manner. An important feature of GALFORM is that it incorporates two modes of star formation, a quiescent mode which is fuelled by gas accretion onto a galactic disc and a burst mode in which a period of enhanced star formation is triggered by a dynamical process, either a galaxy merger or disc instability.

In order to avoid confusion with the definition of starburst arising from a galaxy's position on the sSFR-$M_\star$ plane relative to the main sequence, throughout this paper we will refer to populations of galaxies selected in this manner as MS, if they lie on the locus of the star-forming main sequence, or SB, if they are found at elevated SFRs relative to this locus. Additionally, we will refer to populations of galaxies selected according to the GALFORM star formation mode which is dominating their current total SFR as quiescent mode dominated and burst mode dominated populations respectively.

This Chapter is structured as follows: In Sect. 5.2 we briefly describe how we relate the true physical properties of galaxies in the model to what would be inferred from observations. In Sect. 5.3 we present our main results,[2] which include a detailed comparison with the observed stacked FIR/sub-mm SEDs of Béthermin et al. (2015). We conclude in Sect. 5.4. Throughout we assume a flat ΛCDM cosmology with cosmological parameters consistent with the 7 year *Wilkinson Microwave Anisotropy Probe* (*WMAP7*) results (Komatsu et al. 2011) i.e. $(\Omega_0, \Lambda_0, h, \Omega_b, \sigma_8, n_s) = (0.272, 0.728, 0.704, 0.0455, 0.81, 0.967)$.

5.2 Relation of Inferred to True Physical Properties

One consequence of a model that has multiple IMFs is that it complicates the comparison of physical properties predicted by the model with those inferred from observations assuming a universal IMF. Here, we scale the SFRs of the simulated galaxies to what would be inferred assuming a universal Kennicutt (1983) IMF. To do this we

---

[2]Some of the results presented here will be made available at http://icc.dur.ac.uk/data/. For other requests please contact the first author.

scale the burst mode SFR by a factor of 2.02, assuming that infra-red luminosity is used as a tracer of star formation, as derived by GP14. For stellar mass we use the SED fitting code presented in Mitchell et al. (2013) to investigate if the top-heavy IMF in the model would have a significant impact on the inferred mass in Appendix B, and conclude that changes in the inferred stellar mass due to the top-heavy IMF are small and so we make no explicit correction for this here. For the purposes of comparing to our model predictions we also convert physical properties derived from various observational data to what would have been inferred assuming a universal Kennicutt (1983) IMF, describing the conversion factors used in the text where relevant. Throughout we denote these *inferred* physical quantities by a prime symbol e.g. $M'_\star$, sSFR$'$.

5.3 Results

Here we present our main results. In Sect. 5.3.1 we show model predictions for the distribution of galaxies on the specific star formation rate (sSFR$'$)-$M'_\star$ plane [where the prime symbol indicates that these properties have been scaled to what would be inferred assuming a universal Kennicutt (1983) IMF as described in Sect. 5.2], describe our identification of a main sequence of star-forming galaxies, and how we define samples of galaxies selected based on their position relative to this main sequence. In Sect. 5.3.2 we then discuss the stacked SEDs of MS and SB galaxies selected in this way, and the trends we find in dust mass (M_{dust}) and total FIR luminosity (L_{IR}). In Sect. 5.3.3 we perform a detailed comparison to the observations presented in Béthermin et al. (2015), and we investigate if these can provide any further constraints on the parameters of our dust model in Sect. 5.3.4.

5.3.1 The Specific Star Formation Rate—Stellar Mass Plane

As we are concerned with galaxies selected by their location on the sSFR$'$-$M'_\star$ plane, we define a redshift-dependent sSFR$'_{\mathrm{split}}$, which separates star-forming and passive galaxies. To do this we fit a double Schechter function with a single value for the mass break (M_{bk})

$$\phi(M'_\star)\, \mathrm{d}M'_\star = e^{-M'_\star/M_{\mathrm{bk}}}\left[\phi_1\left(\frac{M'_\star}{M_{\mathrm{bk}}}\right)^{\alpha_1} + \phi_2\left(\frac{M'_\star}{M_{\mathrm{bk}}}\right)^{\alpha_2}\right]\frac{\mathrm{d}M'_\star}{M'_\star}, \qquad (5.3.1)$$

(e.g. Baldry et al. 2012) to the galaxy stellar mass function. This provides a best-fit characteristic stellar mass, M_{bk}, at each output redshift. We then investigate the sSFR$'$ distribution at this stellar mass (± 0.1 dex), identifying a well defined peak (at sSFR$'_{\mathrm{peak}}$) at high inferred sSFRs ($10^{-2} < \psi'/M'_\star < 10\,\mathrm{Gyr}^{-1}$). The value of sSFR$'_{\mathrm{split}}$, indicated by the vertical solid lines in Fig. 5.1, is then chosen so that by construction,
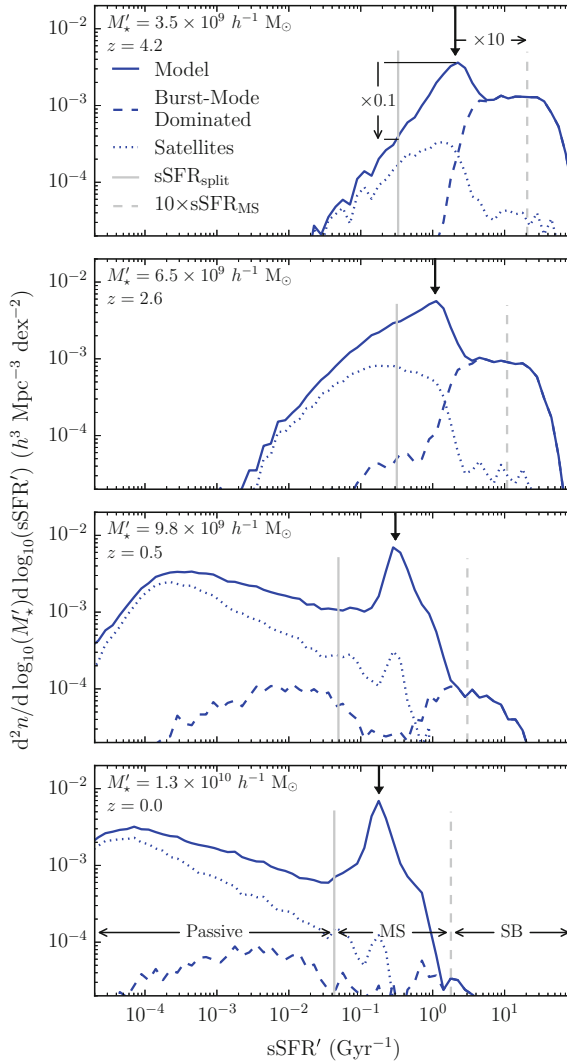
Fig. 5.1 Inferred specific star formation rate [sSFR′, where the prime indicates the value inferred assuming a universal Kennicutt (1983) IMF] distributions in various stellar mass mass bins (0.2 dex width) at redshifts $z = 4.2$, 2.6, 0.5 and 0.0 (*top* to *bottom panels* respectively). The centre of the stellar mass bin is the best fitting value for M_{bk} in Eq. (5.3.1) at the redshift indicated in the panel. The *dashed* and *dotted lines* show the contribution to the total inferred sSFR distribution for burst mode dominated galaxies and satellite galaxies respectively. The thick *black downward arrow* indicates the position of sSFR′$_{peak}$. By construction this is equal to sSFR′$_{MS}(M_\star, z)$ at this stellar mass and redshift (as $M'_\star = M_{bk}$). The *vertical grey solid line* indicates the split between star-forming and passive galaxies (sSFR′$_{split}$) and the *vertical grey dashed line* indicates the split between main sequence (MS) and starburst (SB) populations (i.e. $f_{SB} \times$ sSFR′$_{MS}$, here $f_{SB} = 10$)

at this characteristic mass, the median inferred sSFR for all galaxies with $\mathrm{sSFR}' > \mathrm{sSFR}'_{\mathrm{split}}$ is equal to $\mathrm{sSFR}'_{\mathrm{peak}}$. In cases where this is not well defined i.e. $\mathrm{sSFR}'_{\mathrm{peak}}$ is less than the median inferred sSFR for all galaxies at that redshift, we simply set $\mathrm{sSFR}'_{\mathrm{split}}$ to be the inferred sSFR at which the distribution, $\mathrm{d}n/\mathrm{d}\log_{10}\mathrm{sSFR}'$, is equal to a tenth of its maximum value (for $\mathrm{sSFRs}' < \mathrm{sSFR}'_{\mathrm{peak}}$, see the top panel of Fig. 5.1 for an example of this). In this manner we have a well defined method for choosing $\mathrm{sSFR}'_{\mathrm{split}}$ at each redshift that is not dependent on observations or on choosing $\mathrm{sSFR}'_{\mathrm{split}}$ by eye. We prefer this method to using rest-frame near-UV/optical colours to separate passive and star-forming galaxies, as this would be overly sensitive to assumptions made in the model about the details of the dust attenuation. We use a single $\mathrm{sSFR}'_{\mathrm{split}}$ at each redshift (i.e. independent of inferred stellar mass) for simplicity. We do not expect this to significantly affect our results as this assumption has a minor impact on the position of the main sequence.

The inferred sSFR of the main sequence of star-forming galaxies, which depends on stellar mass as well as redshift, $\mathrm{sSFR}'_{\mathrm{MS}}(M_\star, z)$, is then defined as the median inferred sSFR for all galaxies with $\mathrm{sSFRs}' > \mathrm{sSFR}'_{\mathrm{split}}$ at a given inferred stellar mass and redshift. We define galaxies as main sequence (MS) if they have $\mathrm{sSFR}'_{\mathrm{split}} < \mathrm{sSFR}' < f_{\mathrm{SB}} \times \mathrm{sSFR}'_{\mathrm{MS}}$, as starbursts (SB) if they have $\mathrm{sSFR}' > f_{\mathrm{SB}} \times \mathrm{sSFR}'_{\mathrm{MS}}$, and as passive if they have $\mathrm{sSFR}' < \mathrm{sSFR}'_{\mathrm{split}}$. This demarcation is shown in the bottom panel of Fig. 5.1. We use $f_{\mathrm{SB}} = 10$ throughout to distinguish SB and MS galaxies. This choice is somewhat arbitrary but motivated by the value used in observational studies (e.g. Béthermin et al. 2015).

We can see in Fig. 5.1 that the passive galaxy population is dominated by satellite galaxies. The star formation in these galaxies is inhibited by diminishing cold gas reservoirs. In our model a galaxy's hot gas halo is removed by instantaneous ram-pressure stripping upon becoming a satellite and it is assumed that no further gas will cool onto it [see Lagos et al. (2014) for an analysis of the effect this modelling has on the atomic and molecular gas content of galaxies].

Now that we have defined our galaxy populations, in Fig. 5.2 we show the predicted distribution of galaxies on the sSFR'-$M'_\star$ plane at a range of redshifts, and separated by the mode of star formation. We note that the definition of SB which uses a galaxy's position on the sSFR'-$M'_\star$ plane, is not the same as a model galaxy being dominated by burst mode star formation. In the middle panels of Fig. 5.2 we can see that these two definitions are somewhat different, and that many galaxies dominated by burst mode star formation would be classified as MS based on their position on the sSFR'-$M'_\star$ plane. We further emphasize this point in Fig. 5.3, where we show the contribution to the total comoving inferred SFR density predicted by the model for the MS and SB samples (red dotted and red dashed lines respectively) and for galaxies dominated by quiescent and burst mode star formation (blue dotted and blue dashed lines respectively). We can see here that whilst the MS sample dominates the inferred SFR density, contributing ∼65% at all redshifts, at higher redshifts ($z \gtrsim 1.5$) it is burst mode dominated galaxies that make the dominant contribution to the inferred SFR density. We note that the precise contribution of the MS to the inferred star formation rate density is somewhat sensitive to our definition of MS. If we reduce the value of f_{SB} to 4 then the MS contribution to the total drops to ∼50%.
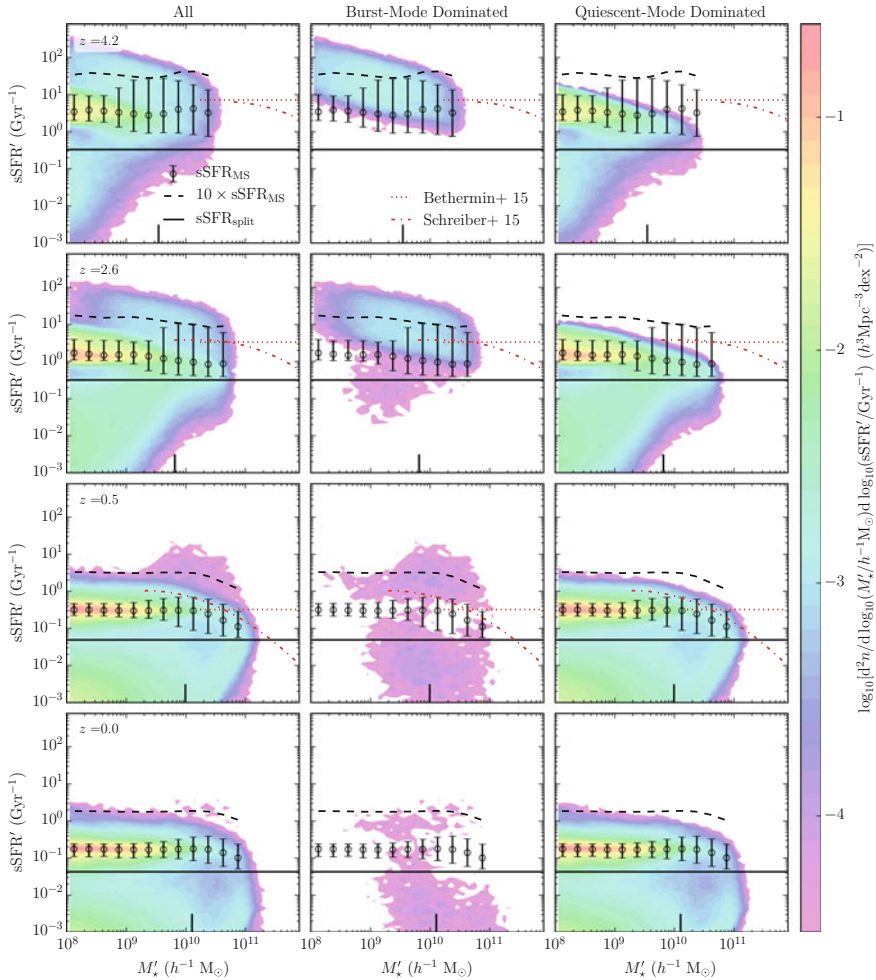
Fig. 5.2 The predicted galaxy number density in the sSFR$'$-$M'_\star$ plane at redshifts $z = 4.2$, 2.6, 0.5 and 0.0 (*top* to *bottom rows* respectively) for all galaxies (*left panels*), for burst mode dominated galaxies (*middle panels*) and for quiescent mode dominated galaxies (*right panels*). The *prime* indicates that the value for that property is what would be inferred assuming a universal Kennnicutt (1983) IMF. The *colour scale* indicates the predicted density of galaxies on this plane as shown in the key on the right. The *horizontal black line* indicates sSFR$'_{\rm split}$, above which galaxies are defined as star-forming. The *open circles* show the median sSFR of star-forming galaxies in logarithmic stellar mass bins i.e. sSFR$'_{\rm MS}(M_\star, z)$, whilst the *errorbars* show the 16–84 (1σ) percentile ranges of star-forming galaxies. The black dashed line is $f_{\rm SB} \times$ sSFR$'_{\rm MS}$, here $f_{\rm SB} = 10$. Galaxies that lie above this line are defined as SB galaxies. The heavy vertical *black tick mark* is the characteristic stellar mass ($M_{\rm bk}$) at that redshift, derived from fitting Eq. (5.3.1) to the predicted galaxy stellar mass function. The *red dotted* and *dash-dotted lines* are the observational estimates of the position of the star-forming main sequence from Schreiber et al. (2015) and Bethermin et al. (2015) respectively, scaled to a Kennicutt (1983) IMF as described in the text, over the ranges of redshift and inferred stellar mass for which these estimates are valid
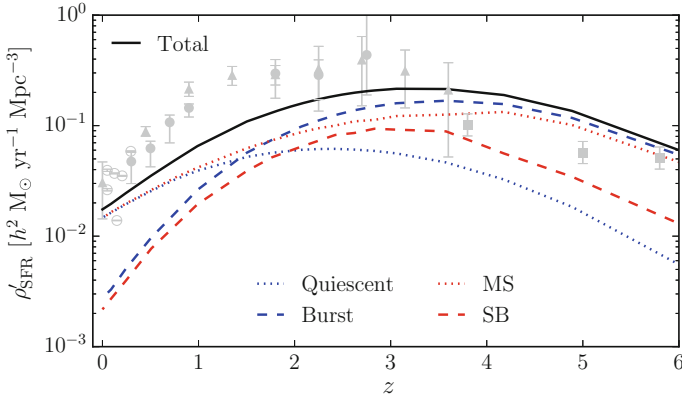
Fig. 5.3 The predicted comoving SFR density as a function of redshift [as inferred assuming a universal Kennicutt (1983) IMF, see Sect. 5.2]. The *black line* shows the total. The *blue dashed* and *dotted lines* show the contribution from galaxies which are respectively burst mode dominated and quiescent mode dominated in the model. The *red dashed* and *dotted lines* show the contribution from SB and MS galaxies respectively, classified according to their position on the sSFR$'$-$M'_\star$ plane. Observational data (*grey points* with *errorbars*) are from Burgarella et al. (2013, *triangles*), Gunawardhana et al. (2013, *open circles*), Oesch et al. (2012, *squares*) and Karim et al. (2011, *filled circles*). Observational data have been scaled to what would be inferred assuming a Kennicutt (1983) IMF using conversion factors derived by GP14 and Lacey et al. (2016)

We also note that the population of 'passive bursts' (i.e. burst mode dominated galaxies that lie below the MS) evident in the panels of the middle column of Fig. 5.2 comprises galaxies in which burst mode star formation was triggered by a galaxy merger. The main locus of burst mode dominated galaxies is populated by disc instability triggered bursts.

Our method of defining sSFR$'_{\rm MS}(M_\star, z)$ allows us to investigate the scatter around this relation. We can see from the errorbars shown in Fig. 5.2, which indicate the 16–84 percentile (1σ) scatter of star-forming galaxies around sSFR$'_{\rm MS}(M_\star, z)$, that the scatter tends to be smaller at lower stellar masses and at lower redshifts. We can understand this in terms of how a galaxy regulates its star formation. At low stellar masses ($M'_\star \lesssim 10^{10}\ h^{-1}\ {\rm M}_\odot$) and in quiescent mode a model galaxy's gas supply (and hence star formation) is self-regulated through the interplay of the accretion of matter onto the halo, and the prescriptions for gas cooling from the hot halo and stellar feedback in the model, which produces a tight relationship between the SFR and stellar mass of a galaxy (Lagos et al. 2011, see also Mitchell et al. 2014).

When this is not the case the relationship between SFR and stellar mass becomes weaker, resulting in a larger scatter. This can be due to a number of reasons which we now discuss in turn:

(i) *Burst mode star formation* in which star formation is enhanced due to some dynamical process. The sSFR distributions of burst mode dominated galaxies tend to be broader (Fig. 5.1), this has more of an effect at higher redshifts where the burst mode contributes more to the global star formation density.

(ii) *Environmental effects* such as ram-pressure stripping restricting a galaxy's gas supply. This affects satellite galaxies in our model and is the reason why they form the bulk of our passive galaxy population.

(iii) *AGN feedback* in massive ($M_{\rm h} \gtrsim 10^{12} \, h^{-1} \, {\rm M}_\odot$) halos, which generally affects galaxies with $M'_\star \gtrsim 10^{10} \, h^{-1} \, {\rm M}_\odot$. Whilst increasing the scatter, this physical process also inhibits star formation, giving rise to the negative slope seen in the sSFR$'_{\rm MS}$ at high stellar masses in the bottom two rows of Fig. 5.2. This negative slope at high stellar masses is also reflected in these galaxies being bulge dominated (e.g. Abramson et al. 2014; Schreiber et al. 2016). For example, in our model at $z = 0$ we find that MS galaxies with $M'_\star > 10^{10} \, h^{-1} \, {\rm M}_\odot$ have a median bulge-to-total ratio of stellar mass of $B/T = 0.5$, whereas galaxies with lower stellar masses ($10^9 < M'_\star < 10^{10} \, h^{-1} \, {\rm M}_\odot$) have a median ratio of $B/T = 0.002$. A galaxy's bulge and supermassive black hole are grown by the same processes in the model (disc instability or galaxy merger) and so it is not surprising that they are linked. This also evidenced in the anti-correlation between cold gas fraction and bulge mass found by Lagos et al. (2014). Galaxies with larger bulges are likely to have more massive SMBHs, and therefore more effective AGN feedback that inhibits gas cooling, leading to suppressed star formation rates.

As discussed earlier, we have scaled the observational estimates of the position of the main sequence from Schreiber et al. (2015) and Béthermin et al. (2015) that appear in Fig. 5.2 to what would be inferred assuming a universal Kennicutt (1983) IMF. We scale the Schreiber et al. (2015) SFRs, which were derived assuming a Salpeter (1955) IMF and using UV + IR as a tracer for star formation by a factor of 0.8. The Béthermin et al. (2015) SFRs, derived using $L_{\rm IR}$ as a tracer for star formation and assuming a Chabrier (2003) IMF are scaled by a factor of 1.29. These conversion factors were calculated by GP14, using the PEGASE.2 SPS model (Fioc and Rocca-Volmerange 1997). For stellar masses we scale the Schreiber et al. masses by a factor of 0.47 (Salpeter to Kennicutt IMF, Ilbert et al. 2010) and the Béthermin et al. masses by 0.81 (Chabrier to Kennicutt, Santini et al. 2012). The mass limit of the Béthermin et al. sample, quoted as $3 \times 10^{10} \, {\rm M}_\odot$, becomes $1.7 \times 10^{10} \, h^{-1} \, {\rm M}_\odot$, also accounting for the factor of $h = 0.7$ assumed by those authors.

Also evident in Fig. 5.2 is the global trend of increasing sSFR$'_{\rm MS}$ with redshift. We show the redshift evolution of sSFR$'_{\rm MS}$, and its 1σ percentile scatter, at a range of fixed stellar masses for both the Lacey et al. (2016) (blue line) and GP14 (red dashed line) models in Fig. 5.4. The models agree qualitatively with the observational data insofar as they both predict an increasing sSFR$'_{\rm MS}$ with increasing redshift. However, the predicted normalisation does not agree with the observed value at all stellar masses and redshifts. For example, the models appear to underpredict the sSFR$'_{\rm MS}$ for $0.5 \lesssim z \lesssim 4$ for $M'_\star \gtrsim 10^{10} \, h^{-1} \, {\rm M}_\odot$ by a factor of ~ 2. It is worth noting that both observational studies use the relation of Kennicutt (1998) to convert from observed $L_{\rm IR}$ to inferred SFR. This relation was derived initially for dusty circumnuclear starbursts (for a burst duration of $\lesssim 100$ Myr) in which the total bolometric luminosity of the stellar population is assumed to be re-radiated in the infra-red, an assumption that may not be wholly valid for the main sequence galaxies considered here. In addition, the evolution of the main sequence at low redshift ($z \lesssim 2$) is not as strong as implied by the observations. This is similar to what was found in a study performed
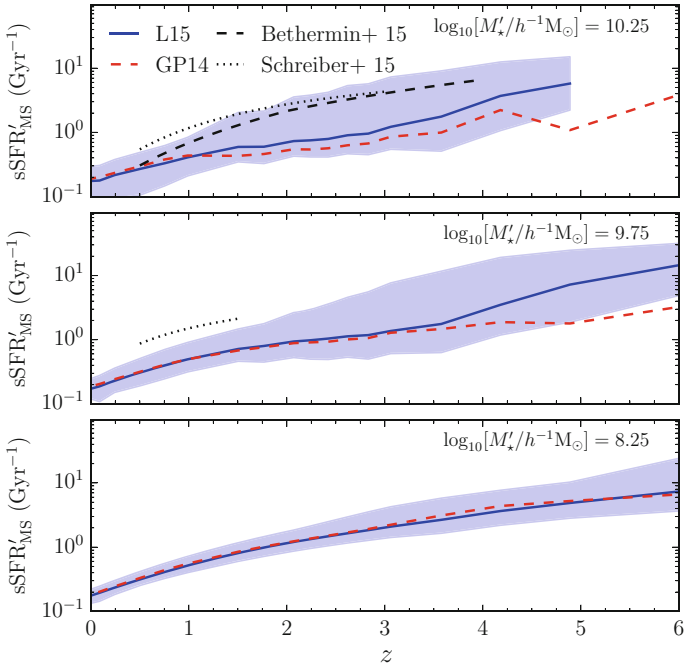
Fig. 5.4 Redshift evolution of sSFR$'_{MS}$ at fixed stellar masses indicated in the panels. In each panel the same stellar mass is used at all redshifts. Predictions are shown from the Lacey et al. (2016, *blue solid line*) and GP14 (*red dashed line*) models. The *blue shaded region* indicates the 16–84 (1σ) percentile scatter around sSFR$'_{MS}$ at that redshift and stellar mass for the Lacey et al. model. The *black dashed* and *dotted lines* show respectively observational estimates from Bethermin et al. (2015) and Schreiber et al. (2015), scaled to a Kennicutt (1983) IMF as described in the text, over the range in stellar mass and redshift for which these estimates are valid

using an earlier version of the GALFORM models used here by Mitchell et al. (2014), who used the model of Lagos et al. (2012) but with the continuous gas cooling model proposed by Benson and Bower (2010). Mitchell et al. attributed this discrepancy to the stellar mass assembly histories of the galaxies predicted by GALFORM being approximately flat for $z \lesssim 2$, driven primarily by the level of coevolution between stellar mass and dark matter assembly in the model, whereas the stellar mass assembly history inferred from observations decreases over the same epoch. Both GALFORM models shown here predict very similar evolution for sSFR$'_{MS}$, differing only at high masses and redshifts. This happens where the contribution to the MS from burst mode dominated galaxies is most significant, with the top-heavy IMF allowing the Lacey et al. (2016) model to have generally a higher sSFR$'_{MS}$ after adjusting to a universal Kennicutt (1983) IMF.

The 16–84 (1σ) percentile scatter around the main sequence for the Lacey et al. (2016) model is shown in Fig. 5.4 as the shaded blue region. At $z = 1$ this is 0.26, 0.5 and 0.6 dex respectively for $M'_\star = 10^{8.25}, 10^{9.25}$ and $10^{10.25}$ h^{-1} M$_\odot$, with the

scatter being smaller for lower stellar masses as this is where the main sequence is dominated by quiescent mode star formation. This scatter is approximately constant for $z \lesssim 1.5$ for the two higher stellar masses and for $z \lesssim 2$ for the lowest, increasing at higher redshift. These results are in qualitative agreement with the findings of Ilbert et al. (2015), who find that scatter around the MS increases with stellar mass and is independent of redshift up to at least $z \sim 1.4$.

5.3.2 Stacked Infra-red SEDs

Now we investigate the average spectral energy distributions (SEDs) at FIR wavelengths (8–1000 µm) predicted by the Lacey et al. (2016) model for MS and SB galaxies as defined above. In Fig. 5.5 we show the average SEDs for both populations at a range of stellar masses and redshifts. The broad trend of increasing bolometric luminosity with increasing redshift can be explained by the evolution of sSFR$'_{\mathrm{MS}}$ shown in Fig. 5.4, that in star-forming galaxies at a fixed stellar mass, the SFRs are generally higher at higher redshift, since the bolometric infra-red luminosity L_{IR} closely traces the star formation rate for systems with high dust extinction. The trend of bolometric luminosity increasing with mass, such that more massive galaxies on average have more star formation, is a simple consequence of the MS selection. The sSFR$'_{\mathrm{MS}}$ is approximately constant over the mass ranges shown, thus higher stellar masses correspond to selecting higher star formation rates (and thus higher L_{IR}). For this reason, at a given redshift and stellar mass, the bolometric luminosity of the SB SEDs are higher.

We can also see in Fig. 5.5 changes in the wavelength at which the average FIR SED peaks, due to variations in the average dust temperature of the selected sample. We show the evolution in the L_{IR} weighted average dust temperature of our samples in Fig. 5.6. We weight by L_{IR} to reflect the temperature that will dominate the stacked SEDs. In the top panel we see that for all samples the average dust temperature is predicted to increase with redshift. Dust temperature is driven by the ratio of infra-red luminosity to dust mass, as $L_{\mathrm{IR}}/M_{\mathrm{dust}} \propto T_{\mathrm{d}}^{\beta+4}$ (for single temperature dust in thermal equilibrium with a dust opacity that scales as $\kappa_{\mathrm{d}} \propto \lambda^{-\beta}$). At higher redshifts, galaxy SFRs (at a given stellar mass) are generally higher, resulting in a higher L_{IR}, whilst the distribution of dust masses evolves much less. This is probably due to a combination of competing effects such as the gas fractions of galaxies at a given stellar mass decreasing with redshift as cold gas is converted into stars and the metallicity of these galaxies increasing with time as stars return metals into the ISM, resulting in a dust mass (proportional to the product of cold gas mass and metallicity) that does not evolve strongly with time. This produces the hotter dust temperatures at higher redshift. This is shown in Fig. 5.7, where we plot the sSFR$'$-$M'_\star$ plane, but with the colourscale now indicating, from the top to bottom rows, the average dust temperature, dust mass and infra-red luminosity at that position on the plane. We also see from the top row of Fig. 5.7 that the range of temperatures $\sim$20–40 K and
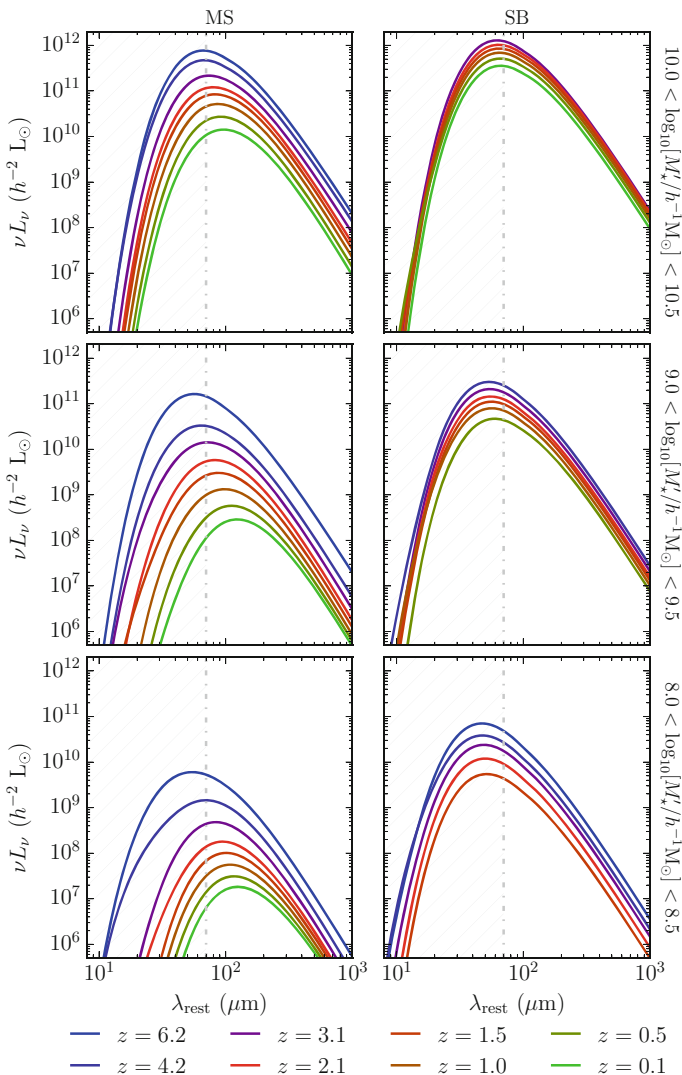
Fig. 5.5 Redshift evolution of stacked SEDs for main sequence (*left column*) and starburst galaxies (*right column*), for galaxies selected by their stellar mass at the redshift in question, for $10 < \log_{10}[M_\star/h^{-1} \, \mathrm{M}_\odot'] < 10.5$ (*top row*), $9 < \log_{10}[M_\star/h^{-1} \, \mathrm{M}_\odot'] < 9.5$ (*middle row*) and $8 < \log_{10}[M_\star/h^{-1} \, \mathrm{M}_\odot'] < 8.5$ (*bottom row*). Different colours indicate the redshift of the galaxies, as shown in the legend. The *vertical dash-dotted line* in each panel indicate $\lambda_{\mathrm{rest}} = 70 \, \mu\mathrm{m}$, the approximate rest-frame wavelength shorter than which our simple dust model breaks down (*hatched regions*)
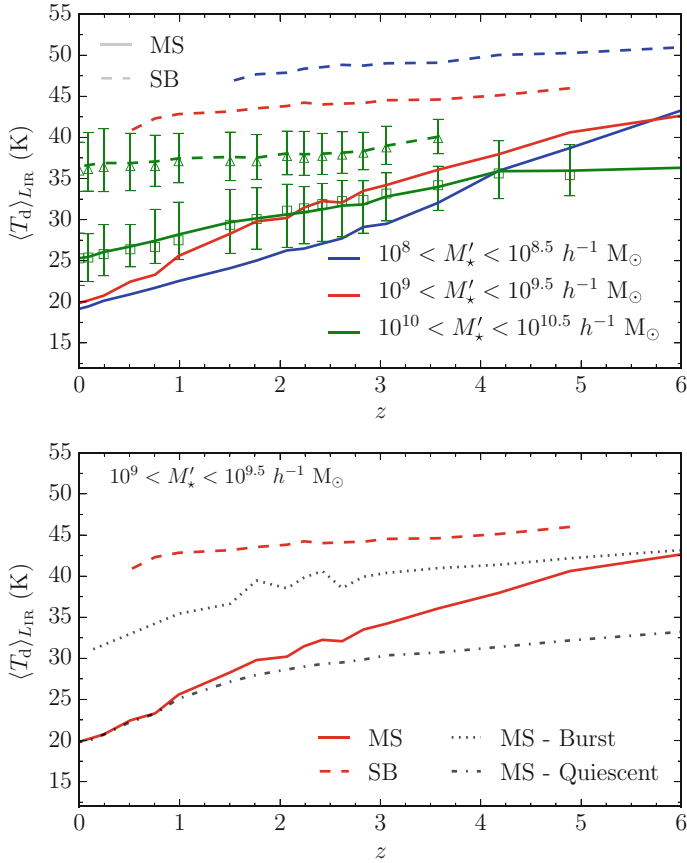
Fig. 5.6 Predicted evolution of infra-red luminosity weighted mean dust temperature. *Top panel:* for main sequence (MS, *solid lines*) and starburst (SB, *dashed lines*) galaxies. The *different colour lines* indicate different stellar mass selected samples as shown in the legend. The *symbols* indicate the median L_{IR} weighted dust temperature for the highest mass sample for MS (*open squares*) and SB (*open triangles*) galaxies with the *errorbars* indicating the 16–84 (1σ) L_{IR} weighted percentile scatter. *Bottom panel:* luminosity weighted dust temperature evolution for the $10^9 - 10^{9.5}$ h^{-1} $M_\odot$ MS sample (*red solid line*) and for this sample split by burst mode dominated and quiescent mode dominated galaxies (*grey dotted* and *dash-dotted lines* respectively). The SB temperature evolution for galaxies in this mass range is also shown for reference (*red dashed line*)

temperature gradient across the main sequence (hotter dust found above the main sequence) are extremely similar to those reported by Magnelli et al. (2014).

In the left panel of Fig. 5.6 we can see that the evolution of the average temperature is stronger for the MS samples. This is because they are composed of both burst and quiescent mode dominated galaxies in proportions that depend on stellar mass and redshift, whereas the SB samples are predominantly populated by burst mode dominated galaxies. In the right panel of Fig. 5.6 we illustrate this point by showing
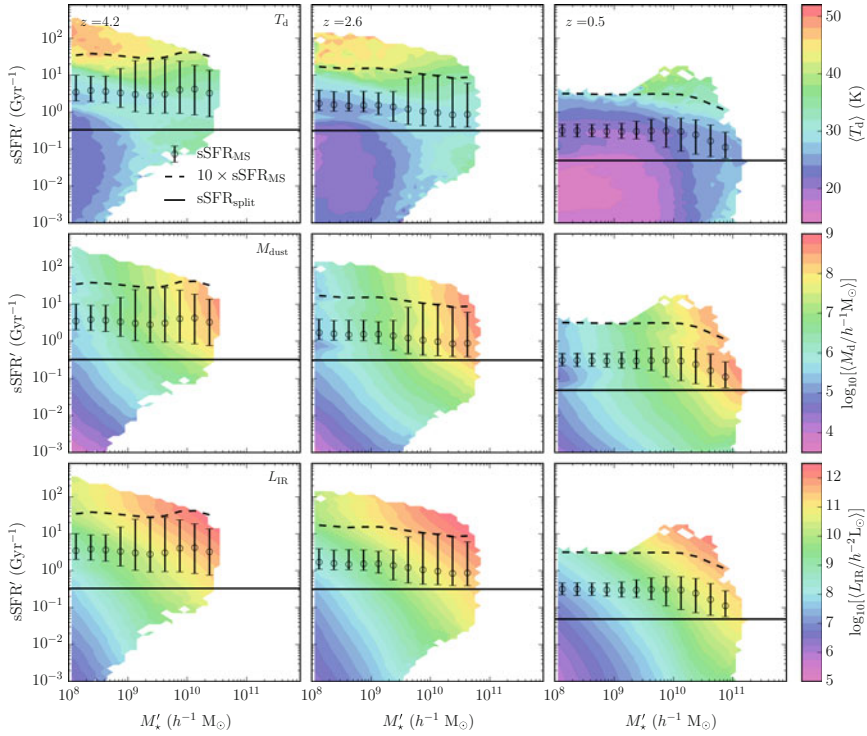
Fig. 5.7 The colour coding (see *right* hand side colourbar for scale) indicates the average dust temperature (*top row*), dust mass (*middle row*) and infra-red luminosity (*bottom row*) at different locations in the sSFR$'$-$M_\star'$ plane, at redshifts of 4.2 (*left column*), 2.6 (*middle column*) and 0.5 (*right column*). Lines and symbols have the same meaning as in Fig. 5.2

the temperature evolution for the MS (red line) and SB (red dashed line) populations for an intermediate stellar mass sample ($10^9 - 10^{9.5}\ h^{-1}\ M_\odot$) along with the evolution for the burst mode dominated and quiescent mode dominated galaxy populations in the MS sample (grey dotted and dash-dotted lines respectively). We can see that at high redshifts the average temperature is dominated by the burst mode dominated galaxies in the MS sample, transitioning to being dominated by quiescent galaxies at low redshift. This mixing of star formation modes on the MS could potentially be behind the sharp increase in the radiation field $\langle U \rangle$ (strongly correlated with dust temperature) found by Béthermin et al. (2015) for stacked MS galaxies at $z \gtrsim 2$.

The points with errorbars in the upper panel of Fig. 5.6 show the median and the 16–84 percentile scatter of dust temperatures for the high mass sample, ($10^{10} - 10^{10.5}\ h^{-1}\ M_\odot$). The scatter for MS galaxies ($\sim$10 K) is slightly larger than for the SB population ($\sim$5 K). This reflects the broader range of SFRs in, and the contribution from both modes of star formation to, the MS sample.

5.3.3 Comparison with Observations

We now perform a detailed comparison of the predictions of the model with the observational results of Béthermin et al. (2015). These authors stacked infra-red images of a stellar mass selected sample of galaxies taken from the COSMOS field, using a stellar mass limit of 3×10^{10} M$_\odot$ so that their sample was complete up to $z \sim 4$. They also removed X-ray detected active galactic nuclei (AGN) hosts, so we do not consider an AGN component in our simulated SEDs. We use the same mass limit as Bethermin et al. [scaled to a universal Kennicutt (1983) IMF as described earlier] and consider galaxies in the same redshift bins. In our simulation we stack galaxy SEDs over a redshift interval by weighting averaged SEDs at each output redshift by the comoving number density of selected galaxies, $n(z)$, and the comoving volume element dV/dz. The average SED for each redshift interval is therefore calculated using

$$S_{\lambda_o} = \frac{\int_{z_1}^{z_2} \frac{(1+z)\langle L_{\lambda_o/(1+z)}\rangle(z)}{4\pi D_L^2(z)} n(z) \frac{dV}{dz} dz}{\int_{z_1}^{z_2} n(z) \frac{dV}{dz} dz}. \tag{5.3.2}$$

Here, S_{λ_o} is the flux at some observer-frame wavelength λ_o which is related to the corresponding emitted (rest-frame) wavelength λ_e by $\lambda_e = \lambda_o/(1+z)$, $\langle L_{\lambda_o/(1+z)}\rangle$ is the average luminosity of the sample at this rest-frame wavelength, D_L is the luminosity distance to redshift z, and z_1 and z_2 represent the lower and upper limit respectively of the redshift bin considered.

We show the comparison to the data in Fig. 5.8. The agreement between the model predictions and the observations for MS galaxies is extremely good (for $z \gtrsim$ 0.5), which is remarkable given that the SEDs of galaxies were not considered in calibrating the model. For SB galaxies (bottom row) the agreement is generally good for $z \lesssim 2$.

To further investigate how our predictions compare to the observations, we compare their dust temperatures, dust masses and infra-red luminosities as a function of redshift in Fig. 5.9. To do this in a consistent way, we fit a modified black body (MBB),

$$L_\lambda = 4\pi M_{dust} \kappa_0 (\lambda/\lambda_0)^{-\beta} B_\lambda(T_d), \tag{5.3.3}$$

to both the observed and predicted photometry, noting that this form is not equivalent to the one assumed for the dust emission in GALFORM (Eq. 2.9.64) and has only a single dust temperature (whereas the GALFORM dust model assumes that there are two temperatures). We choose to assume a fixed $\beta = 2$ and only consider wavelengths from the available photometry (100, 160, 250, 350, 500, 850 and 1100 μm) for which $\lambda_{rest} > 70$ μm, so that we are confident that the approximations in our dust model (and in using the MBB) are valid. In order to derive a dust mass from the MBB fits we must assume an opacity for the dust. Here we use $\kappa_0 = 6.04$ cm^{-2} g^{-1} at
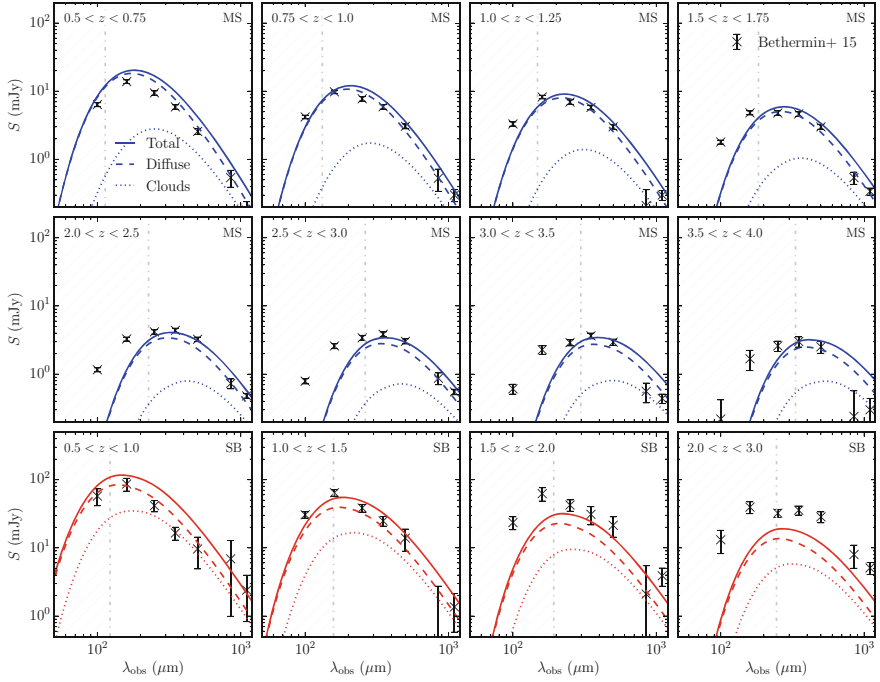
Fig. 5.8 Stacked FIR/sub-mm SEDs of main sequence galaxies (MS, *top* two rows) and starburst galaxies (SB, *bottom* row), at a range of redshift intervals indicated in each panel. *Dotted* and *dashed lines* indicate the stacked SED for the molecular cloud and diffuse ISM dust components respectively. Observational data (*crosses* with *errorbars*) are from Béthermin et al. (2015). The *vertical dash-dotted line* in each panel indicates $\lambda_{rest} = 70$ μm, the approximate wavelength shorter than which our simple dust model breaks down (*hatched regions*). For presentation purposes, a representative subset of the Bethermin et al. redshifts intervals are displayed here

$\lambda_0 = 250$ μm, such that the opacity per unit mass of metals in the gaseous phase of Draine and Lee (1984) is regained for our value of $\delta_{dust} = 0.334$.

For the observed photometry, we calculate the errors on the physical properties using the method of Magdis et al. (2012). Using the original flux measurements and measurement errors we generate 1000 simulated flux sets using a Gaussian distribution, and fit an MBB to these in the same way. The standard deviations in the derived values are then taken to represent the uncertainty in the values derived from the original observed photometry.

For MS galaxies the agreement in T_{dust} is generally good up to $z \sim 3$, at higher redshifts the observations appear to favour higher dust temperatures. This is a consequence of the higher dust masses predicted by the model, as the infra-red luminosities are in good agreement. This suggests that the model overproduces dust at these high redshifts. This is due, at least in part, to the top heavy IMF in burst star formation and the abundance of burst mode MS galaxies at these higher redshifts. When we repeat this calculation with the GP14 model, which has a universal IMF, we find MS
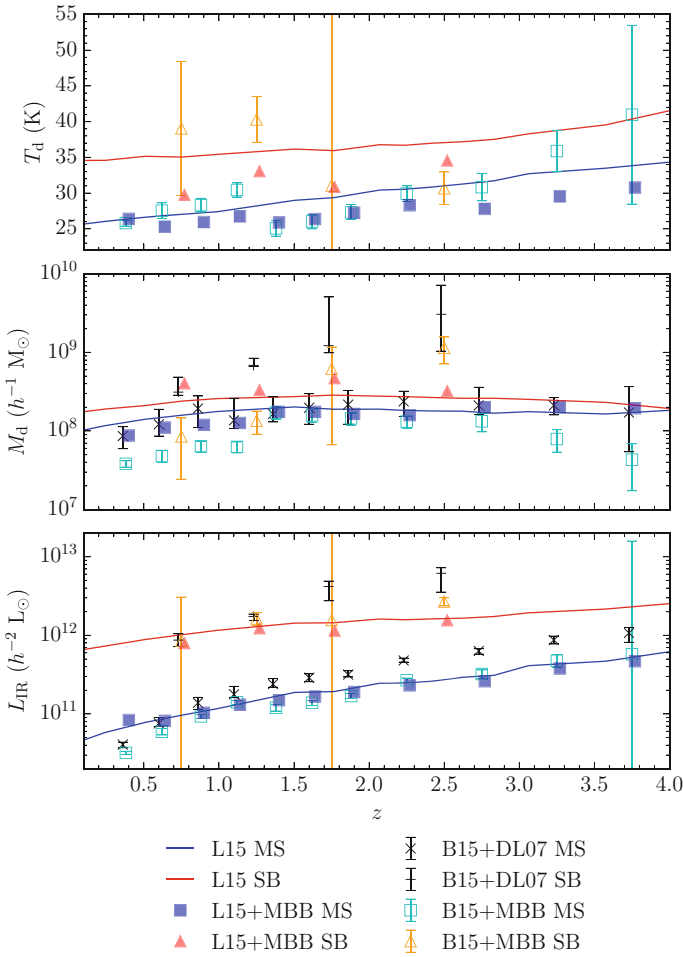
Fig. 5.9 Physical properties, dust temperature ($T_{\rm d}$, *top panel*), dust mass ($M_{\rm d}$, *middle panel*) and total infra-red dust luminosity ($L_{\rm IR}$, *bottom panel*) derived from a modified blackbody (Eq. 5.3.3) fit to both the simulated stacked photometry from the Lacey et al. model (*filled symbols*) and the observed stacked photometry from Bethermin et al. (2015, B15, *open symbols*), for main sequence (MS, *blue/cyan*) and starburst (SB, *red/orange*, model/observations) populations respectively. Also shown for reference are the average values for each population predicted directly by the Lacey et al. model (*solid lines*), and the values predicted by fitting the dust model of Draine and Li (2007) to the observed photometry, as was done in Béthermin et al. for MS (*crosses*) and SB (*bars*) populations

dust masses at $3.5 \lesssim z \lesssim 4$ that are a factor of ~ 2 lower. However, this model does not reproduce the observations as well over the whole redshift range considered.

It is also possible that systems at higher redshifts are composed of more hetero-geneous dust distributions than are accounted for in both GALFORM and the MBB fit, reflected in the larger errorbars for the fit to the observed photometry at higher redshifts, meaning that these physical properties are poorly constrained. However, the larger errors could also be due to our restriction of having $\lambda_{rest} > 70$ µm for the MBB fit, which means that our highest redshift bin has only 4 data points in the SED.

For SB galaxies, the model and the data are in good agreement for $z \lesssim 2$. At higher redshifts, the model's average infra-red luminosity appears too low to reproduce the observed photometry, as also seen in Fig. 5.8. Given the mass selected nature of the observed sample it is unlikely that this is caused by gravitational lensing, which is not included in the model, boosting the observed flux. One could imagine the dust geometry/composition of these extreme SB galaxies being more complicated than is modelled in GALFORM, however in the model these galaxies are in the regime where $\gtrsim 95\%$ of the stellar luminosity is being re-radiated by dust,[3] so it is unlikely that assuming a more complicated geometry could account for the difference in L_{IR} seen between the model and observations. It is therefore more likely to be a result of the inferred SFRs in the model being too low. The number of observed galaxies in the highest redshift SB bin is also relatively small ~ 5, so given that the observations could also be affected by sample variance, the significance of the discrepancy between the model predictions and the observations here is unclear. Performing a similar observational study over larger areas than the ~ 1 deg^2 used by Béthermin et al. (2015) (and/or using multiple fields) would help shed light onto the significance of these extremely IR luminous objects.

Of note also in Fig. 5.9 are instances where the value derived from the MBB fit to the simulated stacked photometry fails to reproduce the average value produced directly by the model (solid lines). We attribute these to the fact that the MBB makes different assumptions about the dust emission than are made in the model. The most striking example of this is in the dust temperatures of SB galaxies. SB galaxies are essentially all undergoing burst mode star formation, in the model this means a value of $\beta_b = 1.5$ is used, for rest-frame wavelengths longer than $\lambda_b = 100$ µm (see Eq. 2.9.65), to predict the dust SED. However, we assume a value of $\beta = 2$ in the MBB fit (see Eq. 5.3.3). This causes the MBB to return cooler dust temperatures.

There are also instances (predominantly at $z \lesssim 1.5$) where the MBB fit fails to reproduce the average dust mass predicted by the model. This we attribute to having two dust components in our model, whereas the MBB, by construction, assumes only one. Our model SEDs are dominated by the diffuse dust component, as this has a much greater luminosity than the molecular clouds (Fig. 5.8). However, as $f_{cloud} = 0.5$, in our model both components have the same dust mass. The MBB fit therefore 'misses' much of the less luminous dust in clouds. If we change the parameters of our dust model such that $\beta_b = 2$ and $f_{cloud} = 0$ then these discrepancies disappear.

---

[3]For a sample of SB galaxies at $z \sim 2$, for MS galaxies the percentage is ~ 65–95.

This highlights a drawback of using MBB fits to derive physical properties from dust SEDs. Even in the simplified case where a galaxy's dust SED is the sum of two modified blackbodies (as is the case in GALFORM) and the 'correct' dust opacity is used in the MBB fit, the MBB blackbody does not always return the correct values for the physical properties relating to the dust SED. In the worst case here the MBB underpredicts the actual average temperature by ∼5 K.

For reference we have also shown in Fig. 5.9 the values derived from fitting the dust model of Draine and Li 2007 to the observed photometry as is done in Béthermin et al. (2015). The MBB fits tend to produce slightly lower L_{IR} values, typically by small factors ∼1–2, compared to the Draine and Li model values. This is easily understood by the Draine and Li model allowing for emission in the mid- and near-infrared. We can also see that the MBB tends to predict lower dust masses than the Drain and Li model, as found by Magdis et al. (2012). These differences highlight the caution that is required when interpreting physical properties derived from modelling dust SEDs.

The results in this Section suggest that the model can accurately predict the average dust emission of MS galaxies, which contribute to the bulk of the SFR density, over a broad range of redshifts.

5.3.4 Constraints on Dust Model Parameters

In this Section we consider varying parameters in the dust model to investigate the robustness of our predictions, and whether the observed average SEDs can constrain the values of these parameters.

The parameters that we choose to vary are f_{cloud}, the fraction of dust mass in molecular clouds, and t_{esc}, the timescale over which stars migrate out of their birth clouds. The fiducial values for these parameters are $f_{cloud} = 0.5$ and $t_{esc} = 1$ Myr. Here we consider values of 0.1 and 0.9 for f_{cloud} and 0.5, 10 and 50 Myr for t_{esc}. We choose these values as we believe they describe a physically acceptable range for these parameters (see e.g. Table 2 in Silva et al. 1998) with the current fiducial values in the model being primarily constrained by the far-UV luminosity function of Lyman break galaxies (see below).

We choose not to explore variations in the gas mass ($m_{cloud} = 10^6$ M$_\odot$) and radius ($r_{cloud} = 16$ pc) of the clouds. These only enter into the calculation as the ratio m_{cloud}/r_{cloud}^2 which, along with the gas metallicity, determines the optical depth of the clouds. This is large at UV wavelengths, and so variations of m_{cloud} and r_{cloud} have a minor effect on the results of our simple dust model, provided the clouds are still in the optically thick regime for UV/optical light.[4] As shown in Vega et al. (2005) the main effect of changing these parameters is seen in the mid-IR dust emission, which we do not consider in this Chapter.

---

[4]We remind the reader that we have assumed that dust is optically thin to its own emission at FIR/sub-mm wavelengths.

We derive SEDs for the f_{cloud} and t_{esc} variants for comparison with the Béthermin et al. (2015) data as described above. These are shown for a selection of redshifts in the top two rows of Fig. 5.10, for MS galaxies (left panels), and for SB galaxies (right panels). We also compare the observations to predictions from the GP14 model (top row), which is similar to the Lacey et al. (2016) model used predominantly throughout this thesis but does not have a top-heavy IMF in burst mode star formation. We also test the sensitivity of our results to parameters used in defining our galaxy populations, $sSFR_{split}$, the specific star formation rate that separates passive and star-forming galaxies, and f_{SB}, the factor above the $sSFR_{MS}$ which separates MS and SB galaxies (Fig. 5.10, bottom row).

Varying the dust parameters f_{cloud} and t_{esc} results in only fairly modest changes to the predicted SEDs, for the stellar mass limit used here ($1.7 \times 10^{10}\ h^{-1}\ M_{\odot}$).
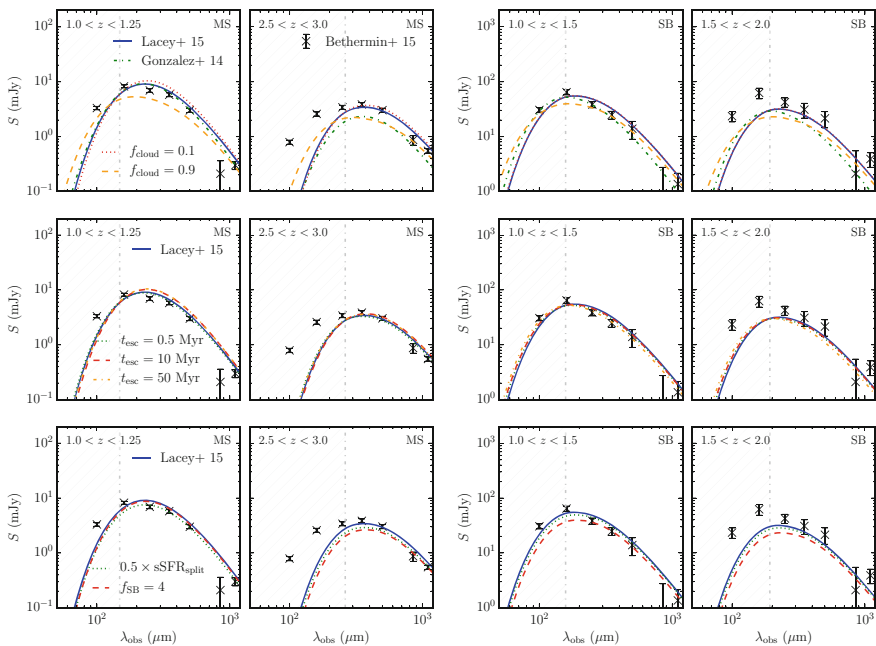
Fig. 5.10 The effect of varying model parameters and assumptions on the predicted stacked SEDs for MS (*left* two columns) and SB (*right* two columns) galaxies for the redshift intervals indicated in the panels. *Top row:* predictions for the fiducial Lacey et al. (2016) model (*blue solid line*), the GP14 model (*green dash-dotted line*) and the effect of varying the dust model parameter f_{cloud} on the Lacey et al. model predictions (the fiducial value of this parameter is 0.5). *Middle row:* effect of varying t_{esc} on the Lacey et al. model predictions (the fiducial value is 1 Myr). *Bottom row:* effect of varying the value of $sSFR_{split}$ and f_{SB}. The *vertical dashed-dotted line* in each panel indicates a rest-frame wavelength of 70 μm, shorter than which our simple dust model breaks down (*hatched region*s). The observational data are from Béthermin et al. (2015, *crosses* with *errorbars*). For historical, reasons the Lacey et al. (2016) model is referred to as 'Lacey+ 15' in this figure legend

Changing the parameter f_{cloud} does not change the energy absorbed by the cloud component as all clouds are assumed to have a fixed mass and radius, and thus a fixed optical depth as $\tau_{cloud} \propto Z_{cloud} m_{cloud}/r_{cloud}^2$, where Z_{cloud} is the gas metallicity of the molecular cloud. However, it does affect the cloud dust temperature as it changes the total mass of dust in the cloud component. Hence, increasing f_{cloud} will make the cloud dust temperature cooler. It also changes the mass of dust in, and thus the optical depth of, the diffuse component. Increasing f_{cloud} reduces the amount of diffuse dust, thus lowering its optical depth, and therefore the amount of energy it absorbs. How this changes the dust temperature of the diffuse component depends on the whether the reduction of energy absorbed (reducing the temperature) or reduction of dust mass (increasing the temperature) is the dominant effect.

Increasing the escape time of stars from their birth clouds allows more energy from stellar radiation to be deposited in the cloud component of our model, increasing the amount of energy absorbed by this component and thus its dust temperature. The diffuse component becomes cooler as less energy is then left to be absorbed by the same mass of diffuse dust.

However, as varying these parameters has such a modest impact on the model predictions, though it should be noted that high values of f_{cloud} appear unlikely for main sequence galaxies, we conclude that these observations do not provide a stronger constraint on the parameters in our dust model than previously available data, such as the 1500 Å luminosity function (see Fig. 5.11). The rest-frame far-UV (1500 Å) luminosity function probes star-forming galaxies typically selected at high redshifts by the Lyman-break technique, providing a strong constraint on the dust model at high redshift. Increasing the obscuration of young stars through either increasing t_{esc} such that stars spend longer in their birth cloud, or decreasing f_{cloud} which increases the amount of energy absorbed by the diffuse component (and thus the total amount of stellar radiation absorbed), reduces the number density of objects at the bright end of the luminosity function (see Lacey et al. 2011 and Gonzalez-Perez et al. 2013 for detailed studies of the effects of dust obscuration on UV-selected galaxies in GALFORM models).

The GP14 model makes similar predictions for the stacked SEDs to the Lacey et al. (2016) model, though it appears that it has generally lower L_{IR} for $z \gtrsim 1$ MS galaxies, a result of the lower sSFR$_{MS}$ predicted by the GP14 model for high mass galaxies (see Fig. 5.4). The SEDs predicted by the GP14 model also appear to have a slightly steeper Rayleigh-Jeans tail, which is due to the choice of a larger value for $\beta_b = 1.6$ in that model, compared with the value of $\beta_b = 1.5$ used in the Lacey et al. model (see Eq. 2.9.65).

Finally, in the bottom row of Fig. 5.10 we show predictions for the stacked SEDs predicted by the Lacey et al. model but where the value of sSFR$_{split}$ was halved prior to defining the position of the main sequence on the sSFR-M$_\star$ plane, and where the factor f_{SB}, which controls the divide between SB and MS galaxies was reduced from its fiducial value of 10 to 4. We note that neither of these changes makes a significant difference (which is reassuring as it means our results are not sensitive to choices we
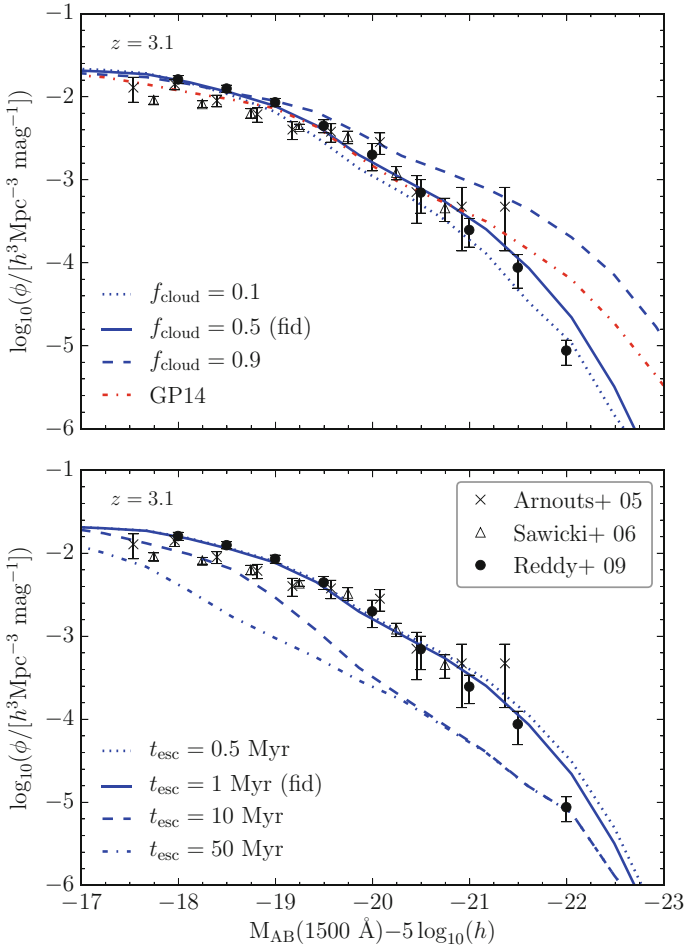
Fig. 5.11 Effect of varying parameters on the predicted rest-frame 1500 Å luminosity functions at $z = 3.1$. *Top panel:* we show the luminosity function for the fiducial model ($f_{cloud} = 0.5$, *solid line*), for $f_{cloud} = 0.1$ (*dotted line*) and for 0.9 (*dashed line*) as well as for the Gonzalez-Perez et al. (2014) model (*dash-dotted line*). *Bottom panel:* we show the luminosity function for the fiducial model ($t_{esc} = 1$ Myr, *solid line*) and for $t_{esc} = 0.5$ Myr (*dotted line*), $t_{esc} = 10$ Myr (*dashed line*) and $t_{esc} = 50$ Myr (*dash-dotted line*). Observational data shown in both panels are from Arnouts et al. (2005, *crosses*), Sawicki et al. (2006, *open triangles*) and Reddy et al. (2009, *filled circles*)

have made in defining the MS and SB populations) other than to slightly lower the normalisation of the SEDs and shift the peak to slightly longer wavelengths. This is because these changes will generally result in slightly lower SFRs and cooler dust temperatures (see Fig. 5.7) being selected in the MS and SB populations.

5.4 Conclusions

The re-emission of radiation by interstellar dust produces a large proportion of the extragalactic background light, implying that a significant fraction of the star formation over the history of the Universe has been obscured by dust. Understanding the nature of dust absorption and emission is therefore critical to understanding galaxy formation and evolution.

However, the poor angular resolution of most current telescopes at the FIR/sub-mm wavelengths at which dust emits (~ 20 arcsec FWHM) means that in the FIR/sub-mm imaging only the brightest galaxies (with the highest SFRs) can be resolved as point sources above the confusion background. These galaxies comprise either starburst galaxies which lie above the main sequence of star-forming galaxies on the sSFR-$M_\star$ plane, and do not make the dominant contribution to the global star formation budget, or the massive end (e.g. $M_\star \gtrsim 10^{10.5}\ h^{-1}\ \mathrm{M_\odot}$ at $z \approx 2$) of the main sequence galaxy population. For less massive galaxies, and at higher redshifts, where the galaxies cannot be resolved individually in the FIR/sub-mm imaging, their dust properties can be investigated through a stacking analysis, the outcome of which is an average FIR/sub-mm SED.

We present predictions for such a stacking analysis from a semi-analytical model of hierarchical galaxy formation. This is coupled with a simple model for the reprocessing of stellar radiation by dust in which the dust temperatures for molecular cloud and diffuse dust components are calculated self-consistently, based on the equations of radiative transfer and energy balance arguments, assuming the dust emits as a modified blackbody. This is implemented within a ΛCDM Millennium style N-body simulation which uses the *WMAP7* cosmology.

In a way consistent with observations, we define two populations of star-forming galaxies based on their location on the sSFR$'$-$M_\star'$ plane [where the prime symbol represents the value for this physical property that would be inferred assuming a universal Kennicutt 1983 IMF, see Sect. 5.2], namely main sequence (MS) if they lie close to the main locus of star-forming galaxies and starburst (SB) if they are elevated on that plane relative to the MS. We note that these definitions do not necessarily reflect the quiescent and burst modes of star formation as defined within the model based on physical criteria. Quiescent mode star formation takes place within the galaxy disc, and follows an empirical relation in which the star formation depends on the surface density of molecular gas in the disc. Burst mode star formation takes place in the bulge after gas is transferred to this from the disc by some dynamical process, either a merger or a disc instability. Burst mode dominated galaxies have generally hotter dust temperatures (driven by their enhanced SFRs) than quiescent mode dominated galaxies. Our model incorporates a top-heavy IMF, characterised by a slope of $x = 1$, for star formation in burst mode. However, when we make comparisons to physical properties we scale all quantities to what would be inferred assuming a universal Kennicutt (1983) IMF (see Sect. 5.2). Most conversion factors are taken from the literature and are described in the text. However, we do not apply a conversion factor to the true stellar masses predicted by our model, despite

the assumption of a top-heavy IMF for burst mode star formation. As discussed in Appendix B this has a relatively small effect on the stellar masses that would be inferred fitting the UV/optical/near-IR SED, a technique commonly used in observational studies, compared to the uncertainties and/or scatter associated with this technique.

The model exhibits a tight main sequence (sSFR$'$ = sSFR$'_{MS}$) on the sSFR$'$-$M'_\star$ plane when galaxies are able to self-regulate their SFR through the interplay of the prescriptions for gas cooling, quiescent mode star formation and supernovae feedback. In instances where this is not the case through either (i) dynamical processes triggering burst mode star formation, (ii) environmental processes such as ram-pressure stripping limiting gas supply or (iii) energy input from AGN inhibiting gas cooling, this causes the scatter around sSFR$'_{MS}$ to increase. We observe a negative high mass slope for sSFR$'_{MS}$ at low redshifts ($z \lesssim 1$) which we attribute to AGN feedback in high mass halos. This is also reflected in high bulge-to-total mass ratios in these galaxies. This negative slope exists at higher redshifts in quiescent mode dominated galaxies but is not seen for the total galaxy population, because at these redshifts the high mass end of the main sequence is populated predominantly by burst mode dominated galaxies. Additionally we find the model predicts that galaxies classified as being on the main sequence make the dominant contribution to the star formation rate density at all redshifts, as is seen in observations. For redshifts $z \gtrsim 2$ this contribution is predicted to be dominated by galaxies that lie on the main sequence but for which the current SFR is dominated by burst mode star formation.

We investigate the redshift evolution of the average temperature for main sequence galaxies and find that it is driven primarily by the transition from the main sequence being dominated by burst mode star formation (higher dust temperatures) at high redshifts, to quiescent mode star formation (lower dust temperatures) at low redshifts.

We compare the average (stacked) FIR SEDs for galaxies with $M'_\star > 1.7 \times 10^{10} \, h^{-1} \, M_\odot$ at a range of redshifts with observations from Béthermin et al. (2015). For main sequence galaxies the agreement is very good for $0.5 < z < 4$. The model predicts dust temperatures in agreement with those inferred from observations accurately up to $z \sim 3$, while at higher redshifts the observations appear to favour hotter dust temperatures than the model predicts. This appears to be due primarily to the model producing too much dust at these redshifts. It could also be that real galaxies are more heterogeneous at higher redshifts e.g. clumpier dust distributions resulting in a range of dust temperatures, which would not be well captured by our simple dust model.

For starburst galaxies, which lie elevated relative to the main sequence on the sSFR$'$-$M_\star$ plane, the agreement between the model and observations is also encouraging for $0.5 \lesssim z \lesssim 2$. For $z \gtrsim 2$ the model appears to underpredict the average L_{IR} inferred from the observations. This implies that the model does not allow enough star formation at higher redshifts ($z \gtrsim 2$) in extremely star-forming systems. However, the model *is* calibrated to reproduce the observed 850 μm number counts, which are composed predominantly of galaxies at $z \sim 1$–3 undergoing burst mode star formation. The apparent discrepancy here is most probably due to how these populations are defined. As we have shown, many of the model galaxies undergoing burst mode

star formation at $z \gtrsim 2$ would be classified as MS based on their position on the sSFR$'$-$M_\star'$ plane, and their SEDs not included in the SB stack. Thus the model can underpredict the average SEDs of objects with extreme sSFRs at high redshifts whilst still reproducing the abundance of galaxies selected by their emission at 850 μm at similar redshifts.

We investigate whether the predictions for the stacked SEDs are sensitive to choices made for the values of parameters in our dust model, mainly the fraction of dust in molecular clouds (f_{cloud}) and the escape time of stars from their molecular birth clouds (t_{esc}). We find that varying these parameters causes only fairly modest changes to the predicted stacked SED, thus these observational data do not provide a stronger constraint on these parameters than previously available data, e.g. the rest-frame 1500 Å luminosity function at $z \sim 3$.

In summary, the predictions made by our simple dust model, combined with our semi-analytic model of galaxy formation provide an explanation for the evolution of dust temperatures on the star-forming galaxy main sequence, and can reproduce the average FIR/sub-mm SEDs for such galaxies remarkably well over a broad range of redshifts. Main sequence galaxies make the dominant contribution to the star formation rate density at all epochs, and so this result adds confidence to the predictions of the model and the computation of the FIR SEDs of its galaxies.

Chapter 6
Predictions for Deep Galaxy Surveys with JWST

6.1 Introduction

[1]In this Chapter we couple GALFORM with the spectrophotometric radiative transfer code GRASIL (Silva et al. 1998). This is done in a manner similar to that presented in Granato et al. (2000), however, we have made a number of important improvements to the procedure. Coupling GALFORM and GRASIL allows us to calculate the full UV-to-mm SED of a galaxy, taking into account the absorption and re-emission of radiation by interstellar dust. This was not possible with the simple dust model described in Sect. 2.9, as dust emission in the rest-frame mid-IR is not computed accurately (see Appendix C). We use this new methodology to make predictions for the outcomes of future deep galaxy surveys with the *James Webb Space Telescope* (*JWST*).

The *James Webb Space Telescope* is scheduled for launch in October 2018 and is expected to significantly advance our understanding of the high-redshift ($z \gtrsim 7$) Universe (e.g. Gardner et al. 2006). Two of its on-board instruments, the Near InfraRed Camera (NIRCam) and the Mid InfraRed Instrument (MIRI), are dedicated to obtaining broadband photometry over the wavelength range 0.7–25.5 μm with unprecedented sensitivity and angular resolution. This wavelength coverage will enable *JWST* to probe the rest-frame UV/optical/near-IR spectral energy distributions (SEDs) of high-redshift ($z \gtrsim 7$) galaxies, opening up a hitherto unexplored regime of galaxy formation and evolution.

An early breakthrough in the study of galaxies in the high-redshift Universe came from the identification of galaxies at $z \sim 3$ using the Lyman-break technique (e.g. Steidel and Hamilton 1993; Steidel et al. 1996). This study took advantage of the break in galaxy SEDs produced at the Lyman limit (912 Å) to identify galaxies at $z \sim 3$ by searching for 'dropouts' in a set of broadband photometric filters.

---

[1]The content of this Chapter is based on the article Cowley et al. 'Predictions for deep galaxy surveys with *JWST* from ΛCDM', submitted to Monthly Notices of the Royal Astronomical Society. Preprint: https://arxiv.org/abs/1702.02146.

The significance of this development in the context of galaxy formation and evolution, in particular the implications for the cosmic star formation rate density and the formation of massive galaxies in the ΛCDM cosmological model, was discussed in Baugh et al. (1998, see also Mo and Fukugita 1996 and Mo et al. 1999). A further advance came with the installation of the Advanced Camera for Surveys (ACS) on the *Hubble Space Telescope* which, using the *z*-band, pushed the Lyman-break technique selection to $z \sim 6$ (e.g. Bouwens et al. 2003; Stanway et al. 2003). At these redshifts the Lyman-break technique makes use of the fact that neutral hydrogen in the intergalactic medium (IGM) effectively absorbs radiation with wavelengths shorter than the Lyman α transition (1216 Å), resulting in a strong break in the galaxy SED at the observer-frame wavelength of this transition. Installation of the Wide-Field Camera 3 (WFC3) with near-IR filters increased the number of galaxies that could be identified at $z \sim 7$ (e.g. Bouwens et al. 2010; Wilkins et al. 2010), pushing the samples of galaxies at these redshifts into the thousands, with a few examples at $z \sim 10$. These advances have been complemented by ground-based telescopes, such as the Visible and Infrared Survey Telescope for Astronomy (VISTA), that typically provide a larger field of view than their space-based counterparts; this has allowed the bright end of the rest-frame far-UV luminosity function to be probed robustly at $z \sim 7$ (e.g. Bowler et al. 2014).

As observations in the near-IR with *Hubble* have identified the highest-redshift galaxies to date, a wealth of further information regarding galaxy properties at intermediate redshifts ($z \sim 3$) has come from surveys with the *Spitzer* Space Telescope in the same wavelength range that will be probed by *JWST* (e.g. Labbé et al. 2005; Caputi et al. 2011, 2015), though *JWST* will have greater angular resolution and sensitivity than *Spitzer*. As a result, *JWST* is expected to greatly increase the number of observed galaxies at $z \gtrsim 7$, providing important information about their SEDs which can help characterise their physical properties, whilst also extending observations of the high-redshift Universe towards the first luminous objects at the end of the so-called cosmic dark ages.

In this Chapter we present theoretical predictions for deep galaxy surveys with *JWST* NIRCam and MIRI, in the form of luminosity functions, number counts and redshift distributions from a hierarchical model of galaxy formation within ΛCDM (Lacey et al. 2016). The model provides a physically-motivated computation of galaxy formation from $z \gtrsim 20$ to $z = 0$. For computing galaxy SEDs the model is coupled with the spectrophotometric code GRASIL (Silva et al. 1998), which takes into account the absorption and re-emission of stellar radiation by interstellar dust by solving the equations of radiative transfer in an assumed geometry. The Lacey et al. model is calibrated to reproduce a broad range of observational data at $z \lesssim 6$. A shortcoming of the fiducial Lacey et al. model, however, is that it does not reproduce the reionization redshift of $z = 8.8^{+1.7}_{-1.4}$ inferred from cosmic microwave background (CMB) data by Planck Collaboration et al. (2016). This is an important constraint for high-redshift predictions of the galaxy population. The model produces too few ionizing photons at early times, reionizing the Universe at $z = 6.3$ (Hou et al. 2016).

A simple and effective solution to this shortcoming was proposed by Hou et al. (2016) who, motivated by the dynamical supernova feedback model of Lagos et al.

(2013), allowed the strength of supernova feedback in the Lacey et al. (2016) model to vary as a function of redshift. Reducing the strength of supernova feedback at high redshift meant that the model could produce more ionizing photons at this epoch. The evolving feedback also enabled this model to reproduce the $z = 0$ luminosity function of the Milky Way satellites, as well as their metallicity–stellar mass relation. These further successes in matching observational data do not come at the expense of the agreement of the model with the data against which it was originally calibrated at $z \lesssim 6$, but it does introduce new parameters to describe the effects of supernova feedback.

Supernova feedback is an extremely important physical process in galaxy evolution (e.g. Larson 1974; White and Rees 1978; White and Frenk 1991; Cole 1991). However, its precise details, for example, exactly how energy input from supernovae should couple to the interstellar medium (ISM), are still poorly understood. This is mainly due to the difficulty of fully resolving individual star-forming regions in hydrodynamical simulations spanning a cosmologically significant time period and volume (e.g. Vogelsberger et al. 2014; Schaye et al. 2015). It is hoped that comparing the predictions of phenomenological models of supernova feedback, such as those presented here, with future observations from *JWST*, will lead to a greater understanding of this crucial process. This Chapter is structured as follows: In Sect. 6.2 we present some of the pertinent details of our galaxy formation model and the evolving feedback variant, the radiative transfer code used for the computation of UV-to-mm galaxy SEDs and some information regarding the coupling of these two codes. In Sect. 6.3 we present our main results[2]; these include galaxy luminosity functions, number counts and redshift distributions for varying exposures, and angular sizes in each of the NIRCam and MIRI broadband filters. We also present predictions for the evolution of some of the physical properties of the model galaxies (e.g. stellar masses, star formation rates) and compare some model predictions to available high-redshift ($z \gtrsim 7$) observational data. We conclude in Sect. 5.4. Throughout we assume a flat ΛCDM cosmology with cosmological parameters consistent with recent *Planck* satellite results (Planck Collaboration et al. 2016).[3] All magnitudes are presented in the absolute bolometric (AB) system (Oke 1974).

6.2 The Theoretical Model

We now briefly describe our galaxy formation model, which combines a dark matter only N-body simulation, a semi-analytical model of galaxy formation (GALFORM, see Chap. 2) and the spectrophotometric radiative transfer code GRASIL (Silva et al. 1998) for computing UV-to-mm galaxy SEDs.

---

[2]Some of the model data presented here will be made available at http://icc.dur.ac.uk/data/. For other requests please contact the author.

[3]$\Omega_m = 0.307$, $\Omega_\Lambda = 0.693$, $h = 0.678$, $\Omega_b = 0.0483$, $\sigma_8 = 0.829$.

6.2.1 GALFORM

The Durham semi-analytic model of hierarchical galaxy formation, GALFORM, was introduced in Cole et al. (2000), building on ideas outlined earlier by White and Rees (1978), White and Frenk (1991) and Cole et al. (1994). Galaxy formation is modelled ab initio, beginning with a specified cosmology and a linear power spectrum of density fluctuations, and ending with predicted galaxy properties at different redshifts.

Galaxies are assumed to form from baryonic condensation within the potential wells of dark matter halos, with their subsequent evolution being controlled in part by the merging history of the halo. Here, these halo merger trees are extracted directly from a dark matter only N-body simulation (e.g. Helly et al. 2003; Jiang et al. 2014) as this approach allows us to predict directly the spatial distribution of the galaxies. In this Chapter we use a new $(800 \text{ Mpc})^3$ Millennium-style simulation (Springel et al. 2005) with cosmological parameters consistent with recent *Planck* satellite results (Planck Collaboration et al. 2016), henceforth referred to as P–Millennium (Baugh et al. in preparation; McCullagh et al. 2017). The halo mass resolution of this simulation is $2.12 \times 10^9 \, h^{-1} \, \text{M}_\odot$, where a halo is required to have at least 20 dark matter particles and is defined according to the 'DHalo' algorithm (Jiang et al. 2014). This mass resolution is approximately an order of magnitude better than previous dark matter simulations that were used with this galaxy formation model. For example, the MR7 simulation (Springel et al. 2005; Guo et al. 2013) in which the Lacey et al. (2016) model was originally implemented had a halo mass resolution of $1.87 \times 10^{10} \, h^{-1} \, \text{M}_\odot$. This improved resolution is particularly important for predictions of the high-redshift Universe where, due to the hierarchical nature of structure formation in ΛCDM, galaxy formation takes place in lower mass halos. This halo mass resolution is in the regime where ignoring baryonic effects on the dark matter, a central assumption of the semi-analytical technique, is still a reasonable one, as the 'back-reaction' due to baryonic effects, such as feedback processes, on the dark matter is expected to reduce the mass of dark matter halos by only $\sim 30\%$ at the mass limit of the P-Millennium simulation (e.g. Sawala et al. 2013).

Baryonic physics in GALFORM are included as a set of coupled differential equations which track the exchange of mass and metals between between the stellar, cold disc gas and hot halo gas components in a given halo. These equations comprise simplified prescriptions for the physical processes (e.g. gas cooling, star formation and feedback) understood to be important for galaxy formation.

Given the change in cosmological parameters, and in the halo mass resolution, from the model presented in Lacey et al. (2016), it is necessary to adjust some of the galaxy formation parameters in the fiducial model such that it can still reproduce certain pre-specified observational datasets to the desired accuracy. Additionally, the model presented in this Chapter uses an improved prescription for the merger timescale of satellite galaxies from Simha and Cole (2016) that incorporates the effects of both dynamical friction and tidal disruption on a dark matter sub-halo. The adjustments will be discussed in more detail in Baugh et al. (in preparation);

however we briefly summarise the main ideas here. The changes caused the model to produce too few bright galaxies, so the gas reincorporation timescale multiplier, α_{ret}, was increased to return gas ejected by supernova feedback to the hot halo faster. The change in the halo mass resolution resulted in the number of faint galaxies being overpredicted, so it was necessary to increase the strength of the supernova feedback through increasing the value of the parameter γ_{SN}, to mitigate this.

We summarise these minor adjustments to the model presented in Lacey et al. (2016) in Table 6.1.

In GALFORM it is assumed that a disc with an exponential profile is formed from cold gas once it has had sufficient time to cool and fall to the centre of the dark matter halo potential well. The size of the disc is solved for by assuming conservation of angular momentum and centrifugal equilibrium (Cole et al. 2000). Galaxy bulges/spheroids are assumed to have a projected $r^{1/4}$ density profile and are formed through a dynamical process, either a disc instability or a galaxy merger. The size of the bulge is determined by the conservation of energy for the components involved i.e. baryons and dark matter in the disc and bulge of the galaxies (Cole et al. 2000). These dynamical processes can also trigger 'bursts' of enhanced star formation. When we refer to starburst galaxies throughout, we are referring to this dynamically triggered star formation rather than, for example, a galaxy's position on the specific star formation rate-stellar mass plane. This distinction is discussed in more detail in Chap. 5.

Table 6.1 Changes between parameter values presented in Lacey et al. (2016) and those used in this Chapter (and discussed further in Baugh et al. in preparation). The galaxy formation parameters are listed in the bottom part of the table

Parameter	Description	Lacey et al. (2016)	This work
Cosmological parameters		Komatsu et al. (2011)	*Planck* Collaboration (2016)
Ω_{m}	Matter density	0.272	0.307
Ω_{Λ}	Vacuum energy density	0.728	0.693
Ω_{b}	Baryon density	0.0455	0.0483
h	Hubble Parameter	0.704	0.678
σ_8	Fluctuation amplitude	0.810	0.829
N-body simulation parameters			
$M_{\mathrm{halo,min}}$	Minimum halo mass	$1.87 \times 10^{10}\ h^{-1}\ \mathrm{M}_{\odot}$	$2.12 \times 10^{9}\ h^{-1}\ \mathrm{M}_{\odot}$
Galaxy merger timescale		Jiang et al. (2008)	Simha and Cole (2016)
Galaxy formation parameters			
α_{ret}	Gas reincorporation timescale multiplier	0.64	1.0
γ_{SN}	Slope of SN feedback mass loading	3.2	3.4

6.2.2   Evolving Supernova Feedback and the Redshift of Reionization

As mentioned earlier, a shortcoming of the fiducial Lacey et al. (2016) model is that it does not reionize the Universe at a redshift as high as implied by recent *Planck* data, as it does not produce enough ionizing photons at early enough times. Here we discuss the variant feedback model of Hou et al. (2016) which provides a simple and effective solution to this shortcoming.

In the fiducial GALFORM model supernova feedback is implemented such that energy input into the interstellar medium (ISM) by supernovae causes gas to be ejected out of the disc. It is parametrised as

$$\dot{M}_{\mathrm{eject}} = \beta(V_{\mathrm{c}})\psi = (V_{\mathrm{c}}/V_{\mathrm{SN}})^{-\gamma_{\mathrm{SN}}}\psi. \tag{6.2.1}$$

Here $\dot{M}_{\mathrm{eject}}$ is the rate at which cold disc gas is ejected beyond the virial radius of the halo[4]; β is the mass loading factor; V_{c} is the circular velocity of the disc; ψ is the star formation rate; and V_{SN} and γ_{SN} are adjustable parameters. We assume $V_{\mathrm{SN}} = 320$ km s^{-1} (Lacey et al. 2016) and $\gamma_{\mathrm{SN}} = 3.4$ (Baugh et al. in preparation).

In order to produce more ionizing photons, and thus reionize the Universe earlier than the fiducial model, Hou et al., motivated by the dynamical supernova feedback model of Lagos et al. (2013), introduced a break into the power-law parametrisation of the mass loading factor and also a redshift dependence into its normalisation, such that

$$\beta(V_{\mathrm{c}}, z) = \begin{cases} [V_{\mathrm{c}}/V'_{\mathrm{SN}}(z)]^{-\gamma'_{\mathrm{SN}}} & V_{\mathrm{c}} \leq V_{\mathrm{thresh}} \\ [V_{\mathrm{c}}/V_{\mathrm{SN}}(z)]^{-\gamma_{\mathrm{SN}}} & V_{\mathrm{c}} > V_{\mathrm{thresh}}, \end{cases} \tag{6.2.2}$$

where V_{thresh} and γ'_{SN} are additional adjustable parameters [$V'_{\mathrm{SN}}(z)$ is set by the condition that β be a continuous function at $V_{\mathrm{c}} = V_{\mathrm{thresh}}$]. The redshift evolution of the normalisation is parametrised as

$$V_{\mathrm{SN}}(z) = \begin{cases} V_{\mathrm{SN2}} & z > z_{\mathrm{SN2}} \\ c_0 z + c_1 & z_{\mathrm{SN2}} \leq z \leq z_{\mathrm{SN1}} \\ V_{\mathrm{SN1}} & z < z_{\mathrm{SN1}}, \end{cases} \tag{6.2.3}$$

where V_{SN2}, z_{SN2} and z_{SN1} are additional adjustable parameters [the constants c_0 and c_1 are set by the condition that $V_{\mathrm{SN}}(z)$ be a continuous function]. Here we use the same values for these additional adjustable parameters as Hou et al.: $V_{\mathrm{thresh}} = 50$ km s^{-1}, $\gamma'_{\mathrm{SN}} = 1.0$, $V_{\mathrm{SN2}} = 180$ km s^{-1}, $z_{\mathrm{SN1}} = 4$ and $z_{\mathrm{SN2}} = 8$, without any further calibration, although we remind the reader that the value for γ_{SN} is different to the one used by Hou et al. Additionally, we adopt $V_{\mathrm{SN1}} = V_{\mathrm{SN}}$, as was done by Hou et al.

---

[4]This gas eventually falls back within the virial radius on a timescale which depends on the dynamical time of the halo.

We show the predicted redshift of reionization for both the fiducial model (lc16) and the evolving feedback variant (lc16.EvolFB) in Fig. 6.1. Following Hou et al. we calculate the ratio, $\mathcal{R}(z)$, of ionizing photons produced before redshift z, to the number density of hydrogen nuclei as

$$\mathcal{R}(z) = \frac{\int_z^\infty \epsilon(z')\,\mathrm{d}z'}{n_{\mathrm{H}}}, \qquad (6.2.4)$$

where $\epsilon(z')$ is the number of hydrogen-ionizing photons produced per unit comoving volume per unit redshift at redshift z' and n_{H} is the comoving number density of hydrogen nuclei. The Universe is assumed to be fully ionized at redshift $z_{\mathrm{re,\,full}}$, for which,

$$\mathcal{R}(z_{\mathrm{re,\,full}}) = \frac{1 + N_{\mathrm{rec}}}{f_{\mathrm{esc}}}, \qquad (6.2.5)$$

where N_{rec} is the mean number of recombinations per hydrogen atom up to reionization, and f_{esc} is the fraction of ionizing photons that can escape into the IGM from the galaxy producing them. Here we adopt $N_{\mathrm{rec}} = 0.25$ and $f_{\mathrm{esc}} = 0.2$ as was done by Hou et al. This gives a threshold for reionization of $\mathcal{R}(z_{\mathrm{re,full}}) = 6.25$.

Observations of the CMB (e.g. Planck Collaboration et al. 2016) directly constrain the electron scattering optical depth to recombination, which is then converted to a reionization redshift by assuming a simple model for the redshift dependence of reionization (e.g. Appendix B of Lewis et al. 2008). The redshift of reionization is commonly expressed in terms of the redshift, $z_{\mathrm{re,\,half}}$, at which half of the IGM is reionized. Here we assume $\mathcal{R}_{\mathrm{re,\,half}} = 0.5\,\mathcal{R}_{\mathrm{re,\,full}}$ as was done by Hou et al. The value of $\mathcal{R}_{\mathrm{re,\,half}}$ is shown as the horizontal dot-dashed line in Fig. 6.1. We can see
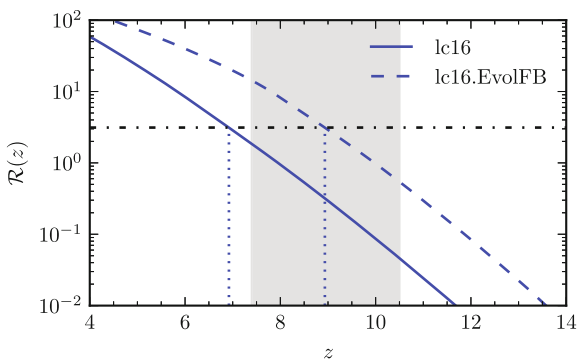
Fig. 6.1 Predicted ratio, $\mathcal{R}(z)$, of the total number of ionizing photons produced before redshift z to the total number of hydrogen nuclei, for the fiducial model (*solid line*) and the evolving feedback variant (*dashed line*). The *horizontal dot-dashed line* indicates the ratio at which the IGM is half ionized, $\mathcal{R}_{\mathrm{re,\,half}}$. The *grey shaded region* indicates the observational estimate of the redshift at which this happens, $z_{\mathrm{re,\,half}} = 8.8^{+1.7}_{-1.4}$, the 68% confidence limit from the *Planck* Collaboration (2016). *Dotted vertical lines* indicate the values of $z_{\mathrm{re,\,half}}$ predicted by the models

that the evolving feedback model predicts $z_{\text{re, half}} = 8.9$, in good agreement with the 68% confidence interval inferred from *Planck* satellite data (Planck Collaboration et al. 2016), $z_{\text{re, half}} = 8.8^{+1.7}_{-1.4}$. For the fiducial model the reionization redshift turns out to be lower, $z_{\text{re, half}} = 6.9$, which is discrepant by $\sim 1.5\sigma$ with the *Planck* data.

6.2.3 The Dust Model

We use the spectrophotometric radiative transfer code GRASIL (Silva et al. 1998) to compute model galaxy SEDs. Using the star formation and metal enrichment histories, gas masses and geometrical parameters predicted by GALFORM, and assuming a composition and geometry for interstellar dust, GRASIL computes the SEDs of the model galaxies, accounting for dust extinction (absorption and scattering) of radiation and its subsequent re-emission. In this Section we briefly describe the GRASIL model. For further details we refer the reader to Silva et al. (1998) and Granato et al. (2000).

Here GRASIL assumes that stars exists in a disc + bulge system, as is the case in GALFORM. The disc has a radial and vertical exponential profile with scale lengths, h_R and h_z, and the bulge is described by an analytic King model profile, $\rho \propto (r^2 + r_c^2)^{-3/2}$ out to a truncation radius, r_{trunc}. The half-mass radii, r_{disc} and r_{bulge}, are predicted by GALFORM. By definition, given the assumed profiles, the bulge core radius is related to the half-mass radius by $r_c = r_{\text{bulge}}/14.6$ whilst the radial disc scale-length, h_R, is related to the half-mass disc radius by $h_R = r_{\text{disc}}/1.68$. Star formation histories are calculated separately for the disc and bulge by GALFORM. For galaxies undergoing a starburst, the burst star formation, as well as the associated gas and dust, are assumed to also be in an exponential disc but with a half-mass radius, $r_{\text{burst}} = \eta r_{\text{bulge}}$, rather than r_{disc}, where η is an adjustable parameter. The disc axial ratio, h_z/h_R, is a parameter of the GRASIL model; for starburst galaxies the axial ratio of the burst is allowed to be different from that of discs in quiescent galaxies.

The gas and dust exist in an exponential disc, with the same radial scale-length as the disc stars but in general with a different scale-height, so $h_z(\text{dust})/h_z(\text{stars})$ is an adjustable parameter. The gas and dust are assumed to exist in two components: (i) giant molecular clouds in which stars form, escaping on some time scale, t_{esc}, and (ii) a diffuse cirrus ISM. The total gas mass, M_{cold}, and metallicity, Z_{cold}, are calculated by GALFORM. The fraction of gas in molecular clouds is determined by the parameter f_{cloud}. The cloud mass, m_{cloud}, and radius, r_{cloud}, are also parameters, though the results of the model depend only on the ratio, $m_{\text{cloud}}/r_{\text{cloud}}^2$, which determines (together with the gas metallicity) the optical depth of the clouds.

The dust is assumed to consist of a mixture of graphite and silicate grains and polycyclic aromatic hydrocarbons (PAHs), each with a distribution of grain sizes. The grain mix and size distribution were determined by Silva et al. so that the extinction and emissivity properties of the local ISM are reproduced using the optical properties of the dust grains tabulated by Draine and Lee (1984). At long wavelengths ($\lambda > 30\ \mu$m) this results in a dust opacity that approximates $\kappa_d \propto \lambda^{-2}$.

However, in galaxies undergoing a starburst this is modified (for $\lambda > 100\,\mu$m) such that $\kappa_d \propto \lambda^{-\beta_b}$, where β_b is treated as an adjustable parameter. Laboratory measurements suggest that values in the range $\beta_b = 1.5-2$ are acceptable (Agladze et al. 1996). Here a value of $\beta_b = 1.5$ is adopted (Lacey et al. 2016). The total dust mass in a galaxy is proportional to the cold gas mass and metallicity, which are predicted by GALFORM.

The adopted values of adjustable GRASIL parameters are summarised in Table 6.2. For the parameters which are analogous to those in the dust model used by Lacey et al. (2016): $f_{\rm cloud}$, $m_{\rm cloud}/r_{\rm cloud}^2$, $t_{\rm esc}$ and β_b, we use the values chosen by Lacey et al. For other parameters specific to the GRASIL model, we use the values chosen by by Baugh et al. (2005, see also Lacey et al. 2008, Swinbank et al. 2008 and Lacey et al. 2011), which was the last time a published version of GALFORM was coupled with GRASIL in the manner presented here.

The luminosities of the stellar components are calculated assuming the Maraston (2005) evolutionary population synthesis model, as is done in Lacey et al. (2016). GRASIL then calculates the radiative transfer of the stellar radiation through the interstellar dust. For molecular clouds a full radiative transfer calculation is performed. For the diffuse cirrus the effects of scattering are included approximately by using an effective optical depth for the absorption $\tau_{\rm abs,eff} = [\tau_{\rm abs}(\tau_{\rm abs} + \tau_{\rm scat})]^{1/2}$. The dust-attenuated stellar radiation field can be calculated at any point inside or outside the galaxy. GRASIL then computes the final galaxy SED by calculating the absorption of stellar radiation, thermal balance and the re-emission of radiation for each grain species and size at every point in the galaxy.

Examples of predicted star formation histories and the resulting galaxy UV-to-mm SEDs computed by GRASIL are shown in Fig. 6.2. One can see that the star formation histories are extremely 'bursty' at early times, when the Universe is a few Gyr old. Significant dust extinction and re-emission is evident for each of the galaxy SEDs shown. There are also a number of interesting features in the galaxy SEDs. These include: (i) Lyman-continuum breaks in the galaxy SEDs at 912 Å; (ii) a prominent 4000 Å break for the $z = 0$ galaxy, indicative of an old stellar population (which would be expected from the smoothly declining star formation history of this galaxy);

Table 6.2 Adopted values for adjustable parameters in GRASIL. See the text in Sect. 6.2.3 for their definitions

Parameter	Value
h_z/h_R (disc)	0.1
h_z/h_R (burst)	0.5
$h_z({\rm dust})/h_z({\rm stars})$	1
η	1.0
$f_{\rm cloud}$	0.5
$m_{\rm cloud}/r_{\rm cloud}^2$	$10^6\,{\rm M}_\odot/(16\,{\rm pc})^2$
$t_{\rm esc}$	1 Myr
β_b	1.5
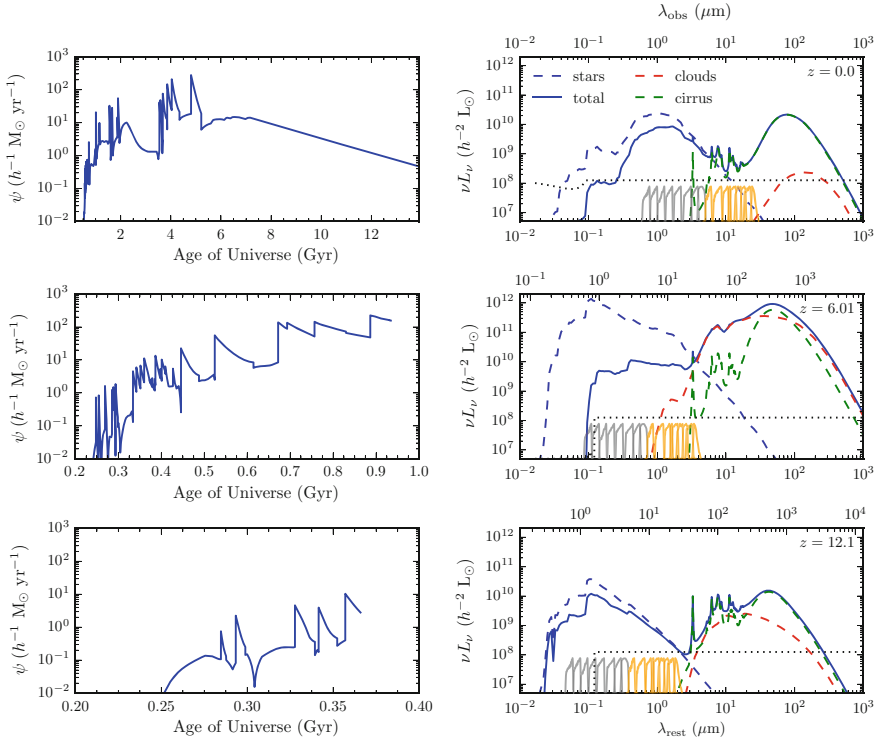
Fig. 6.2 Example galaxy star formation histories and GRASIL SEDs. Each row shows a galaxy selected at a different redshift, as indicated in the *right* panels. *Left panels*: star formation histories of three galaxies (in each case summed over all of the galaxy's progenitors) predicted by GALFORM. Note that the range of the abscissa is different in each panel. *Right panels*: corresponding galaxy SEDs predicted by GRASIL (Silva et al. 1998), plotted against rest-frame wavelength on the *bottom* axis and observed wavelength on the *top* axis. The *dashed blue line* is the intrinsic stellar SED. The *solid blue line* is the total galaxy SED including dust absorption and emission. The *dashed red* and *green lines* are the dust emission for the molecular cloud and diffuse cirrus components respectively. The *JWST* filter transmission function for NIRCam (MIRI) bands are shown in *grey* (*orange*), in arbitrary units. The intergalactic medium (IGM) transmission function of Meiksin (2005) is shown by the *dotted black line* (also in arbitrary units)

(iii) dust emission approximating a modified blackbody that peaks at $\lambda_{rest} \approx 100\,\mu m$, indicative of cold ($\sim 30$ K) dust, though the peak of the emission shifts to shorter wavelengths with increasing redshift suggesting hotter dust, and (iv) PAH emission lines in the cirrus dust at $\lambda_{rest} = 3.3, 6.2, 7.7, 8.6$, and $11.3\,\mu m$.

Once an SED has been computed, luminosities in specified bands are calculated by convolving the SED (redshifted into the observer frame) with the filter transmission of interest. We use the Meiksin (2005) prescription for the attenuation of radiation in the intergalactic medium (IGM) due to neutral hydrogen, also shown in Fig. 6.2.

6.2.4   Coupling GALFORM *and* GRASIL

Here we briefly describe how the GALFORM and GRASIL models are used in conjunction. For further details we refer the reader to Granato et al. (2000).

Due to the computational expense of running GRASIL ($\sim$5 CPU mins per galaxy) it is not feasible to compute an SED for each galaxy in the simulation volume, as has been discussed in previous studies (e.g. Granato et al. 2000; Almeida et al. 2010; Lacey et al. 2011). However, for the purposes of constructing luminosity functions it is possible to circumvent this by running GRASIL on a sample of galaxies, from which the luminosity function can be constructed if the galaxies in question are weighted appropriately. We choose to sample galaxies according to their stellar mass such that $\sim 10^3$ galaxies per dex of stellar mass are sampled. We use a lower mass limit of $10^6 \ h^{-1} \ M_\odot$, which we choose so that any artificial features it introduces into our predicted luminosity functions (see Sect. 6.3.2) are at fainter luminosities than are investigated here. This represents a factor of $\sim$10 increase over the number of galaxies sampled by Granato et al. (2000).

The procedure that we use to construct luminosity functions in a given band at each output redshift is as follows: (i) run GALFORM to the redshift of interest; (ii) create a sample of galaxies; (iii) re-run GALFORM to output the star formation and metal enrichment history for each of the sampled galaxies; (iv) run GRASIL on each of the sampled galaxies to produce a predicted SED; (v) convolve the output SED with the relevant broadband filter response and IGM attenuation curve (Meiksin 2005) and (vi) construct the galaxy luminosity function using the weights from the initial sampling and luminosities from the previous step.

We have made a number of improvements to this procedure for the purposes of generating the samples used in this Chapter, mainly to improve (or mitigate against) the I/O in steps (iii) and (iv) above. Previously, GALFORM, when used to output the star formation histories, would have to be run independently for each halo merger history and would output a separate file containing the star formation history for each galaxy. We have adjusted this so that GALFORM can output the star formation histories of galaxies from multiple merger histories into a single file when run only once. This improvement decreased the CPU duration of this step by approximately an order of magnitude. Additionally, we have mitigated the I/O of the GRASIL calculation by running it on disks local to each processor of the COSMA4 machine in Durham.

These improvements allow us to run GRASIL for samples of $\sim 10^5$ galaxies for each model, spread over 25 output redshifts from $z = 16$ to $z = 0$. For each model, this takes $\sim 7 \times 10^3$ CPU hours, approximately 95% of which is spent by GRASIL, with the remaining time being taken by GALFORM to calculate the necessary star formation histories.

6.3 Results

In this Section we present our main results. In Sect. 6.3.1 we present predictions
for the evolution of physical properties of the galaxy population as well as a com-
parison of our predictions with available high-redshift ($z \gtrsim 7$) observational data.
In Sect. 6.3.2 we present the predicted evolution of the galaxy luminosity function
for the NIRCam–F200W and MIRI–F560W filters. We make such predictions for
each NIRCam and MIRI broadband filter but only show these two in this Chapter for
brevity; results for other filters will be made available online. In Sect. 6.3.3 we present
predictions for galaxy number counts and redshift distributions (for a 10^4 s exposure)
observable by *JWST* in each NIRCam and MIRI band; we also show predictions for
the redshift distributions of galaxies observable with longer (10^5 and 10^6 s) expo-
sures. Finally, in Sect. 6.3.4 we present predictions for the angular sizes of galaxies
for the NIRCam–F200W and MIRI–F560W filters, again we make such predictions
for all NIRCam filters but show only these two here for brevity. Throughout we
show predictions for our fiducial model 'lc16' and the variant 'lc16.EvolFB' that
adopts the evolving feedback model presented in Hou et al. (2016) and is discussed
in Sect. 6.2.2.

6.3.1 *The Lacey et al. (2016) Model at High Redshift*

In this Section we present model predictions for the evolution of the physical prop-
erties of the galaxy population and compare our predictions at $z \gtrsim 7$ to available
observational data. In Fig. 6.3 we show predictions of the fiducial and evolving feed-
back variant models for the evolution of: (a) the galaxy stellar mass function; (b) the
galaxy star formation rate function (for $M_\star > 10^6 \, h^{-1} \, M_\odot$ galaxies); and (c) the frac-
tion of bulge-dominated (i.e. with bulge-to-total stellar mass ratios of $B/T > 0.5$)
galaxies as a function of stellar mass, from $z = 15.1$ to $z = 0$.

   The stellar mass function (Fig. 6.3a) evolves strongly until $z \sim 2$ for both models.
At lower redshifts further evolution is predominantly at the high-mass end. It is easily
seen that (for $z \gtrsim 2$) the evolving feedback model results in both more massive
galaxies and a greater abundance of galaxies at a given stellar mass (for $M_\star \gtrsim$
$10^6 \, h^{-1} \, M_\odot$, as galaxies with a lower stellar mass are not included in our GRASIL
sampling) by factors of up to $\sim$10. For $z < 4$, the normalisation of the supernova
feedback strength is the same in both models and the differences between their stellar
mass functions begin to disappear. At the low mass end ($M_\star \lesssim 10^8 \, h^{-1} \, M_\odot$), however,
the break in the power law for the mass-loading factor (at $V_{thresh} = 50 \, \mathrm{km \, s^{-1}}$) in the
evolving feedback model results in a greater abundance of galaxies at these stellar
masses than in the fiducial model. At the high mass end ($M_\star \gtrsim 10^{11} \, h^{-1} \, M_\odot$), an
increase in stellar mass at low redshift due to the reduced feedback strength at higher
redshift is apparent.

   The distributions of star formation rates (Fig. 6.3b) tell a similar story. For $z < 4$
the distributions predicted by both models are essentially identical, except at low
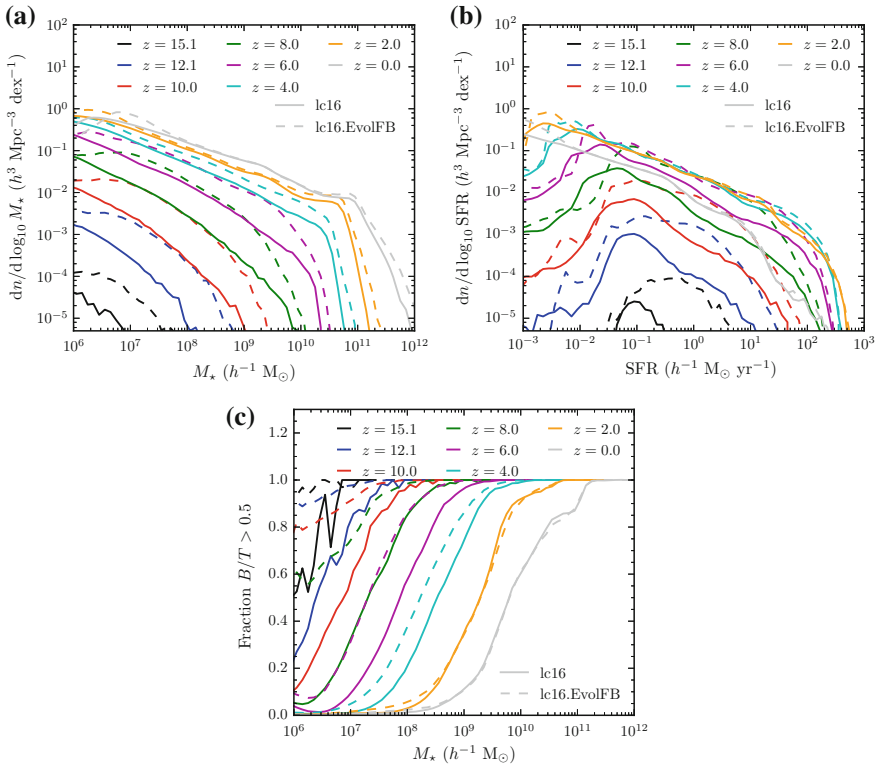
Fig. 6.3 Predicted evolution of physical galaxy properties from $z = 15.1$ to $z = 0$. *Panel a*: the galaxy stellar mass function. *Panel b*: the star formation rate function for galaxies with $M_\star > 10^6 \, h^{-1} \, M_\odot$. *Panel c*: the fraction of bulge-dominated (bulge-to-total stellar mass ratios, $B/T > 0.5$) galaxies as a function of stellar mass. In each panel the colour of the line indicates the redshift as shown in the legend. The *solid lines* are predictions from the fiducial model whereas the *dashed lines* are predictions from the evolving feedback variant

star formation rates (SFRs $\lesssim 10^{-2} \, h^{-1} \, M_\odot \, yr^{-1}$) where the break in the evolving feedback model results in this model having a greater abundance of galaxies. At higher redshifts $z > 4$ the differences in the star formation rate distributions are greater due to the different normalisations of feedback, with the evolving feedback variant having significantly more galaxies with SFRs $\gtrsim 3 \times 10^{-2} \, h^{-1} \, M_\odot \, yr^{-1}$. The apparent peak seen in each SFR distribution is mostly due to the imposed stellar mass limit of $10^6 \, h^{-1} \, M_\odot$, if lower stellar mass galaxies were included it would shift to lower star formation rates according to the (approximately) constant relation between specific star formation rate and stellar mass predicted by the model (e.g. Fig. 5.2, see also Mitchell et al. 2014).

Figure 6.3c shows the evolution in the fraction of galaxies with a bulge-to-total stellar mass ratio of $B/T > 0.5$, as a function of total stellar mass. In GALFORM, bulges are created by a dynamical process, either a galaxy merger or a disc instability.

The transition from a disc-dominated to a bulge-dominated galaxy population is relatively sharp, occurring over roughly one dex in stellar mass in most cases. In the evolving feedback model this transition generally occurs at lower stellar masses. At higher redshifts (and thus lower stellar masses), the shape of the relation is different for the evolving feedback variant, which predicts a much smoother transition. We caution against over interpreting the predicted B/T as a proxy for morphological type. The instabilities that create bulges in GALFORM do not necessarily create slowly rotating bulges, and so defining bulges as slow rotators would give different results to those presented here.

Having established some predicted physical properties of galaxies in the two models, we now compare predictions of the models to observational data at $z \gtrsim 7$. We note that none of the observational data considered in this Section were used to calibrate model parameters [Lacey et al. (2016) only considered rest-frame far-UV luminosity functions at $z \lesssim 6$ in their model calibration].

We compare the predictions of the models for the evolution of the rest-frame far-UV luminosity function to observational data over the redshift interval $7 \lesssim z \lesssim 10$ in Fig. 6.4. We can see that both models provide reasonable agreement with the observed data, and appear to 'bracket' the data for $M_{AB}(1500 \text{ Å}) - 5 \log_{10} h \gtrsim -18$. However, at brighter magnitudes the predictions of the two models converge. This is due to dust extinction becoming the limiting factor in a galaxy's brightness at far-UV wavelengths. To illustrate this, we show the predictions of the two models, without dust attenuation, in the $z = 10$ panel. These predictions resemble the star formation rate distributions in Fig. 6.3b, as the star formation rate of a galaxy is essentially traced by the rest-frame far-UV.

Finally, we compare predictions for the angular sizes of galaxies to observational data in the redshift range $7 \lesssim z \lesssim 9$ in Fig. 6.5. The stellar component of the model galaxies is assumed to be a composite system, consisting of an exponential disc and a bulge with a projected $r^{1/4}$ density profile (Cole et al. 2000). We compute the half-light radii for our model galaxies by weighting the density profile of each component by their predicted rest-frame far-UV (1500 Å) luminosity, dividing the half-light radii of the disc by a factor of 1.34 to account for inclination effects (Lacey et al. 2016), and interpolating to find the half-light radius of the composite system. We then bin the galaxies according to their flux, S_ν. The symbols in Fig. 6.5 show the median size in each flux bin, with the errorbars representing the 16–84 percentile scatter in each bin. We show this for the whole galaxy population, and also split into starburst and quiescent galaxies. The differences between the predictions of the two models are small and they both show reasonable agreement with data from Ono et al. (2013) and Shibuya et al. (2015), who use GALFIT (Peng et al. 2002) to derive sizes from *Hubble Space Telescope* imaging. For the Ono et al. data we present their stacked image results. For the Shibuya et al. data we bin their sizes for individual galaxies into bins of one mag width and present the median size in each bin. The errorbars presented represent the 16–84 percentile scatter of sizes within these bins. For reference, we also show the diffraction limit of *JWST*. The models predict that *JWST* should be able to resolve most galaxies in the rest-frame far-UV at these redshifts.

Fig. 6.4 The predicted
rest-frame far-UV (1500 Å)
luminosity functions for
$z = 7-10$ for the fiducial
model (*solid blue line*) and
the evolving feedback
variant (*dashed blue line*).
The redshift is indicated in
each panel. Observational
data are from Bouwens et al.
(2015, *open circles*),
Finkelstein et al. (2015, *filled
circles*), Bowler et al. (2014,
filled squares), Schenker et
al. (2013, *open squares*) and
Oesch et al. (2014, *open
triangles*) as indicated in the
legend. In the *bottom panel*
the *red lines* show the model
predictions without dust
extinction
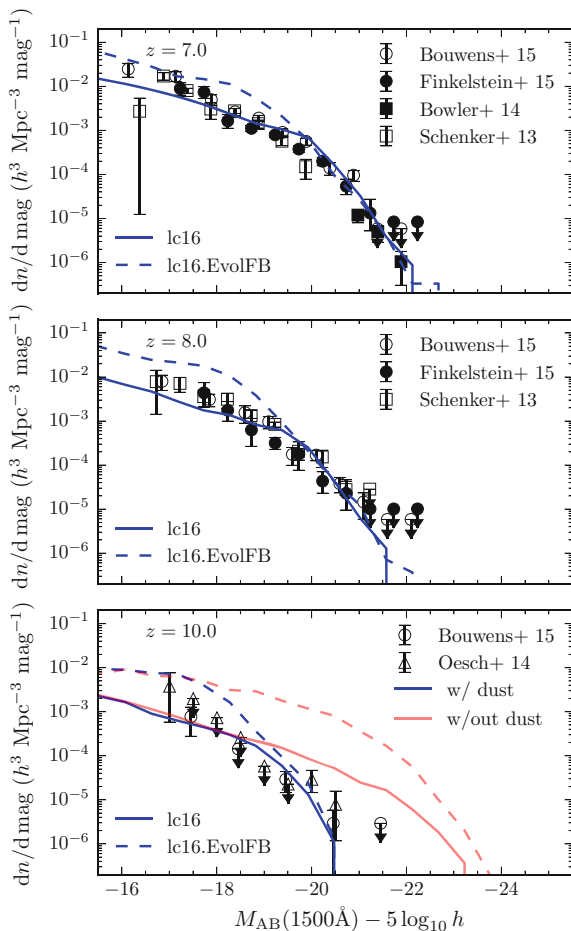
In summary, the predictions of both models show good agreement with the evolution of the rest-frame far-UV (1500 Å) luminosity function and observed galaxy sizes at high redshift ($z \gtrsim 7$). We re-iterate that these high-redshift data were not considered when calibrating the model.

6.3.2 Luminosity Functions Observable with JWST

In this Section we present predictions for the evolution of the galaxy luminosity function in the *JWST* NIRCam and MIRI bands. These are listed in Table 6.3, with their sensitivities (for a 10^4 s exposure), and the field of view (FoV) for each instrument is shown in Table 6.4. In Fig. 6.6 we show the predicted luminosity functions
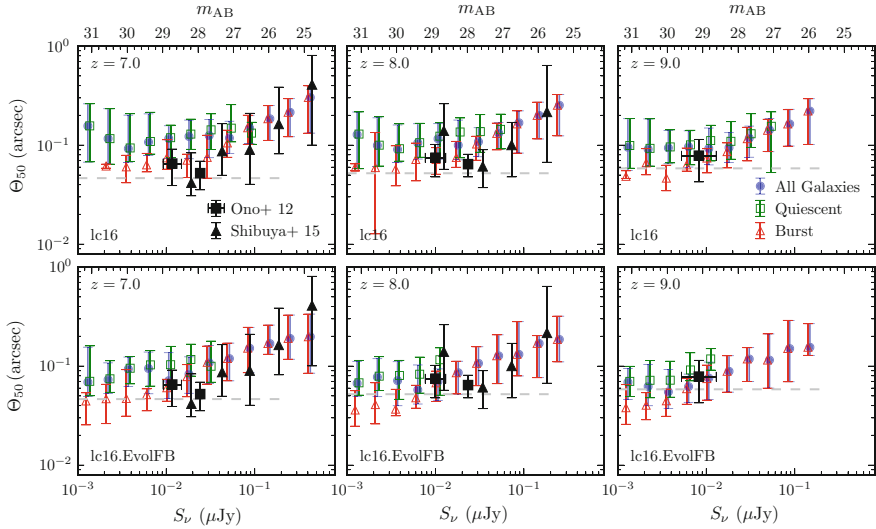
Fig. 6.5 Predicted rest-frame far-UV (1500 Å) galaxy projected half-light radii for $z = 7-9$. The redshift is indicated in each panel. The *top row* shows predictions from the fiducial model, whereas the *bottom row* shows predictions from the evolving feedback variant. *Blue filled circles* indicate the median size for all galaxies at a given flux, with the *errorbars* indicating the $16-84$ percentile range. The *open green squares* and *red triangles* indicate this for quiescent and starburst galaxies respectively. Observational data are from Ono et al. (2013, *black filled squares*) and Shibuya et al. (2015, *black filled triangles*). For reference, the *horizontal dashed line* in each panel indicates the diffraction limit for *JWST* for a fixed rest-frame wavelength of 1500 Å, assuming a 6.5 m diameter mirror

for the NIRCam–F200W and MIRI–F560W bands. We make such predictions for all broadband NIRCam and MIRI filters, but show only these two here for brevity. The predictions for other filters will be made available online.

In the top panels of Fig. 6.6 we can see that at high redshifts the difference between the two models is similar to that seen in Fig. 6.4, and that the models predict similar luminosity functions for $z < 4$, when the normalisation of the feedback strength is the same in both models.

In the bottom panels we show the predicted luminosity function at $z = 11$ for NIRCam–F200W (bottom left panel), and at $z = 6$ for MIRI–F560W (bottom right panel). We choose these values as they are the redshifts at which we predict *JWST* will see ∼1 object per field of view (FoV) for a 10^4 s exposure, as is discussed below. Here we show the contribution to the luminosity function predicted by the fiducial model from quiescent and starburst galaxies. We can see that the bright end of the luminosity function is dominated by galaxies undergoing a burst of star formation. As mentioned earlier, the definition of starburst here refers to a dynamical process, either a galaxy merger or disc instability, triggering a period of enhanced star formation. We also show predictions of the fiducial model without dust, and can see that the bright end of the luminosity functions at these redshifts is composed of

Table 6.3 Adopted sensitivities for *JWST* filters based on 10σ point source and 10^4 s exposure

Instrument	Filter	λ_{eff} (µm)	Sensitivity (µJy)
NIRCam	F070W	0.70	20.9×10^{-3}
	F090W	0.90	13.1×10^{-3}
	F115W	1.15	11.8×10^{-3}
	F150W	1.50	9.6×10^{-3}
	F200W	2.00	7.9×10^{-3}
	F277W	2.77	11.5×10^{-3}
	F356W	3.56	11.1×10^{-3}
	F444W	4.44	17.6×10^{-3}
MIRI	F560W	5.6	0.2
	F770W	7.7	0.28
	F1000W	10.0	0.7
	F1130W	11.3	1.7
	F1280W	12.8	1.4
	F1500W	15.0	1.8
	F1800W	18.0	4.3
	F2100W	21.0	8.6
	F2550W	25.5	28.0

Note Adapted from https://jwst.stsci.edu/files/live/sites/jwst/files/home/science%20planning/Technical%20documents/JWST-PocketBooklet_January17.pdf

Table 6.4 Adopted *JWST* instrument fields of view (FoV)

Instrument	FoV (arcmin^2)
NIRCam	$2 \times 2.2 \times 2.2$
MIRI	1.23×1.88

Note From https://jwst.stsci.edu/files/live/sites/jwst/files/home/science%20planning/Technical%20documents/JWST-PocketBooklet_January17.pdf

heavily dust-attenuated objects. We therefore expect such observations to provide a further constraint on the way dust absorption is accounted for in galaxy formation models.

For reference we have also shown the sensitivity limits of the filters based on 10^4 and 10^5 s exposures as the vertical dashed and dotted lines respectively. Our adopted sensitivities for a 10^4 s exposure are summarised in Table 6.3. We derive sensitivities for other exposures assuming they scale as $t^{-1/2}$.

In conjunction we also show the abundance at which the instrument will see one object per FoV per unit redshift at this redshift. Our adopted fields of view are summarised in Table 6.4. Objects that are in the upper right quadrant of each plot would be observable with a 10^4 s exposure in a single FoV. Therefore, the fiducial model predicts that ~ 1 object will be observable at $z = 11$ by NIRCam–F200W, and ~ 2 will be observable at $z = 6$ by MIRI–F560W. We recognise that single FoV observations will be sensitive to field-to-field variance. We hope to make direct
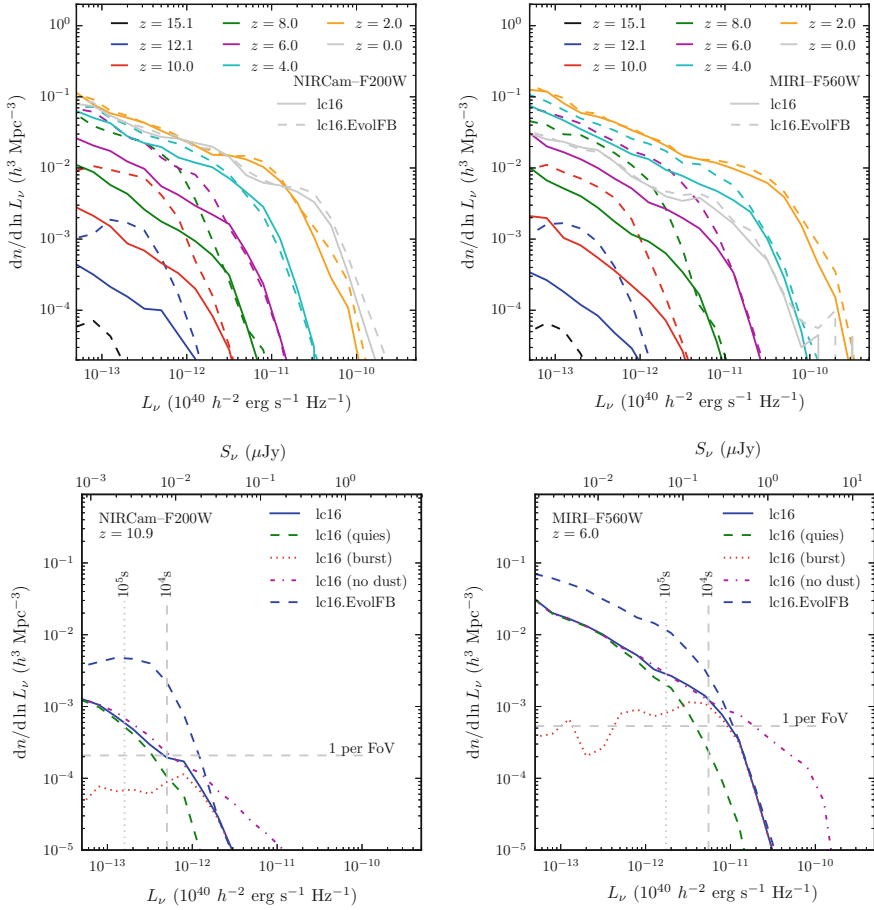
Fig. 6.6 *Top panels*: predicted evolution from $z = 15.1$ to $z = 0.0$ of the luminosity function in the NIRCam–F200W (*left panel*) and MIRI–F560W (*right panel*) bands (in the observer-frame). The colour indicates the redshift as shown in the legend. The *solid lines* show predictions from the fiducial model, whereas the *dashed lines* show predictions for the evolving feedback variant. *Bottom panels*: a breakdown of the predicted luminosity functions for NIRCam–F200W at $z = 10.9$ (*left panel*) and MIRI–F560W at $z = 6.0$ (*right panel*). The *solid blue lines* show the predictions for the fiducial model, and the *dashed green* and *dotted red lines* show the contribution to this from quiescent and starburst galaxies respectively. The predictions for the fiducial model excluding dust absorption are shown by the *dash-dotted magenta lines*. The *dashed blue line* is the prediction from the evolving feedback model. For reference, the *horizontal dashed lines* indicate the number density at which there is one object per *JWST* field of view at that redshift and the *vertical dashed* and *dotted lines* indicate the *JWST* sensitivity limits for that filter for a 10^4 and 10^5 s exposure, as labelled

predictions for the field-to-field variance by creating lightcone catalogues from our simulation in a future work.

6.3.3 Galaxy Number Counts and Redshift Distributions Observable with JWST

The simplest statistic of a galaxy population that can be derived from an imaging survey is their number counts. Here we present the predictions for the cumulative number counts observable with NIRCam (Fig. 6.7) and MIRI (Fig. 6.8). We also show the corresponding redshift distributions (for a 10^4 s exposure) in Figs. 6.9 (NIRCam) and 6.10 (MIRI). We obtain the number counts and redshift distributions by integrating the predicted luminosity functions according to

$$\frac{\mathrm{d}^3 \eta}{\mathrm{d} \ln S_\nu \, \mathrm{d}z \, \mathrm{d}\Omega} = \frac{\mathrm{d}n}{\mathrm{d} \ln L_\nu} \frac{\mathrm{d}^2 V}{\mathrm{d}z \, \mathrm{d}\Omega}, \tag{6.3.1}$$

where η is the surface density of galaxies projected on the sky, n is the number density of galaxies and $\mathrm{d}^2 V / \mathrm{d}z \, \mathrm{d}\Omega$ is the comoving volume element per unit solid angle. We show the contribution to the predicted number counts and redshift distributions from quiescent and starburst galaxies. For the NIRCam filters the counts are dominated by quiescent galaxies. This is because they are dominated by galaxies at low redshift, for which starbursts are not a significant population at these wavelengths. This is also why the predicted number counts from the fiducial and evolving feedback variant models are so similar, as at low redshifts the feedback normalisations are equal, though the lc16.EvolFB model does predict slightly more galaxies at faint fluxes. For the MIRI number counts we see the burst population becoming important at brighter fluxes in bands $\lambda_{\mathrm{obs}} \gtrsim 10$ µm. These wavelengths also correspond to a shift from the number counts being dominated by dust-attenuated stellar light to dust emission. Again, these number counts are dominated by relatively low-redshift galaxies, for which the MIRI filters probe the dust emission from the rest-frame mid-IR.

The redshift distributions in Figs. 6.9 and 6.10 exhibit a more discernible difference between the two models, particularly in the NIRCam bands at high redshift. For instance, in the NIRCam–F200W filter, the redshift at which one object per FoV per unit redshift is observable with a 10^4 s exposure is predicted to be $z \sim 11$. For the evolving feedback variant $\sim$5 times more galaxies are predicted to be observable at this redshift. From our predictions it appears that very few galaxies will be observable at $z \gtrsim 10$ with NIRCam and at $z \gtrsim 6$ with MIRI, although we stress that this is the case for a single FoV and a 10^4 s exposure. Additionally, we note that we have not considered effects such as gravitational lensing, which would allow surveys to probe fainter galaxies at higher redshifts (e.g. Infante et al. 2015).
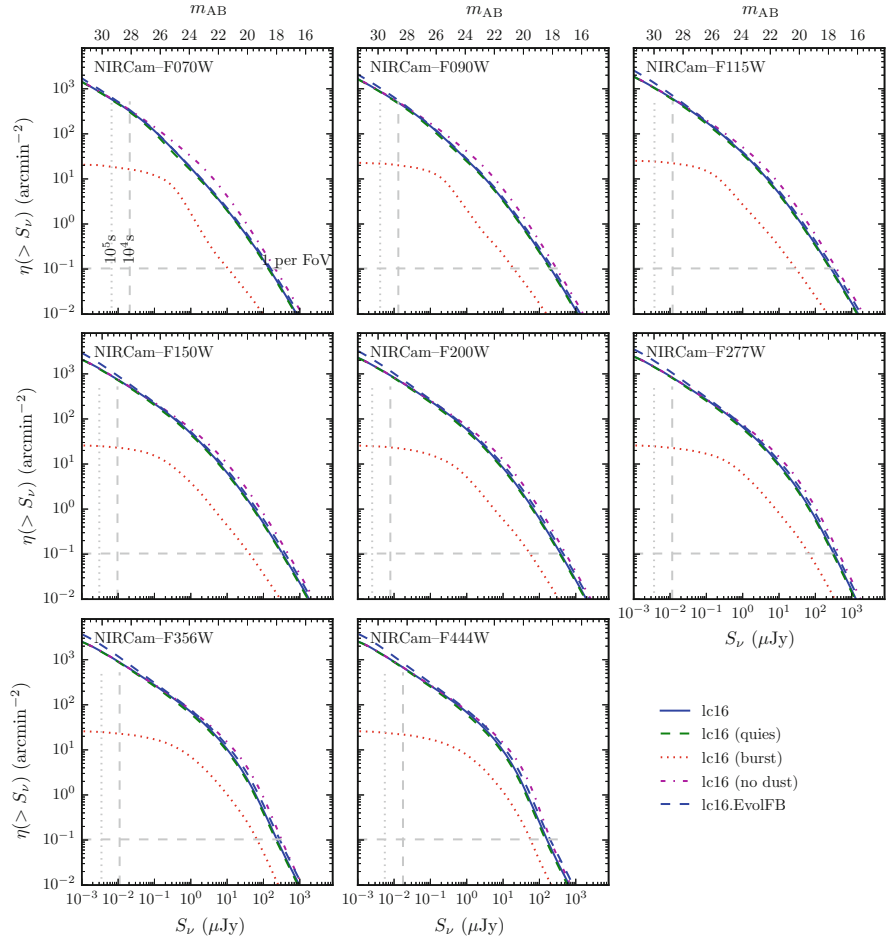
Fig. 6.7 Predicted cumulative galaxy number counts in the NIRCam bands. The name of the band is indicated in each panel. The *solid blue lines* show the predictions of the fiducial model and the *dashed green* and *dotted red lines* show the contribution to this from quiescent and starburst galaxies respectively. The predictions of the fiducial model excluding dust absorption are shown by the *dash-dotted magenta lines*. The *dashed blue lines* show the predictions from the evolving feedback variant. For reference, the *horizontal dashed lines* indicate the number density at which there is one object per field of view and the *vertical dashed* and *dotted lines* indicate the sensitivity limits for that filter for a 10^4 and 10^5 s exposure respectively

Various features in the predicted MIRI redshift distributions can be related to PAH emission. For example, the peaks at $z \sim 2.5$ in the MIRI–F1130W distribution and at $z \sim 3.6$ in the MIRI-F1500W distribution correspond to the 3.3 μm PAH feature.

We briefly consider the possibility that nebular emission lines may affect our predicted broadband photometry (e.g. Smit et al. 2015), as they are not included in our galaxy SEDs. For this we focus on the MIRI–F560W filter at $z \sim 7$ as the H α emission line is redshifted across the filter. The luminosity of the H α
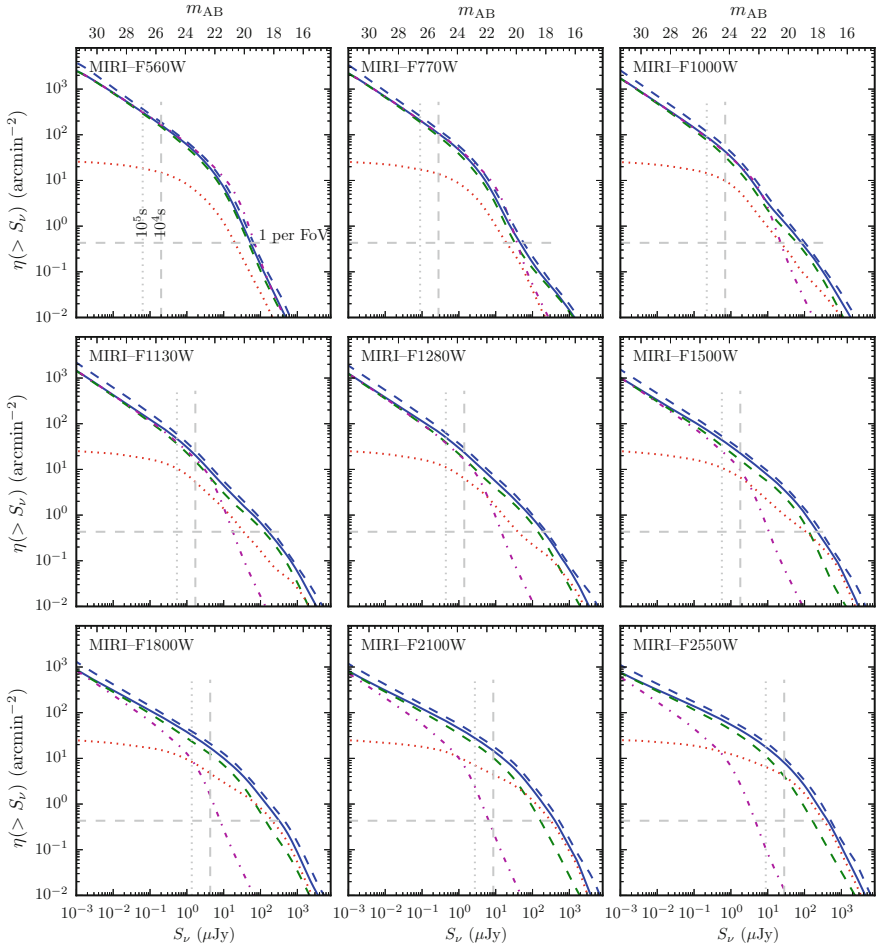
Fig. 6.8 Predicted cumulative galaxy number counts in the MIRI bands. The name of the band is indicated each panel. All lines have the same meaning as in Fig. 6.7

line is calculated assuming that all photons emitted with wavelengths shorter than 912 Å will ionize a hydrogen atom in the gas surrounding the star. We then assume
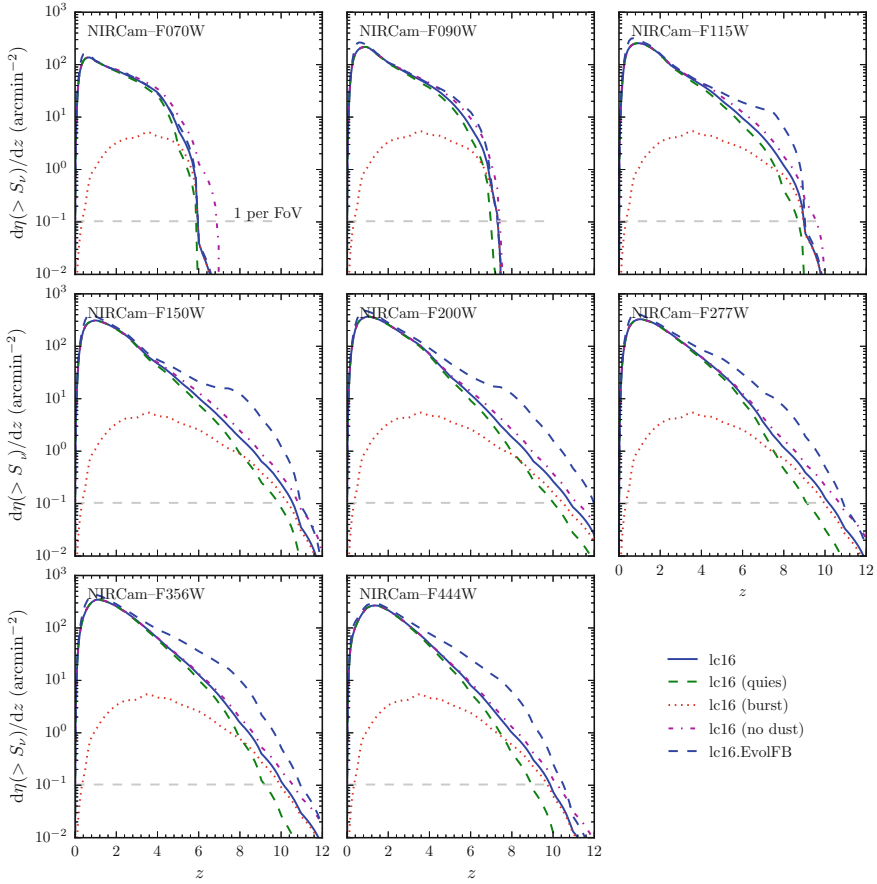
Fig. 6.9 Predicted redshift distributions for objects detectable in a 10^4 s exposure in NIRCam bands. The name of the band is indicated in each panel. The *solid blue lines* show the predictions of the fiducial model, and the *dashed green* and *dotted red lines* show the contribution to this from quiescent and starburst galaxies respectively. The predictions of the fiducial model excluding dust absorption are shown by the *dash-dotted magenta lines*. The *dashed blue lines* show the predictions from the evolving feedback variant. For reference, the *horizontal dashed line* indicates the number density at which there is one object per field of view per unit redshift

'Case B' recombination i.e. we ignore recombinations directly to the ground state ($n = 1$), as these just produce another ionizing photon. Thus only recombinations to $n > 1$ are counted. The fraction of such recombinations that produce an H α photon ($n = 2 \rightarrow 1$) is taken from Osterbrock (1974). We apply the dust extinction factor predicted by GRASIL at the wavelength of the line to the line luminosity. We find that the predicted equivalent widths (EWs) of the line are ∼400 Å, significantly
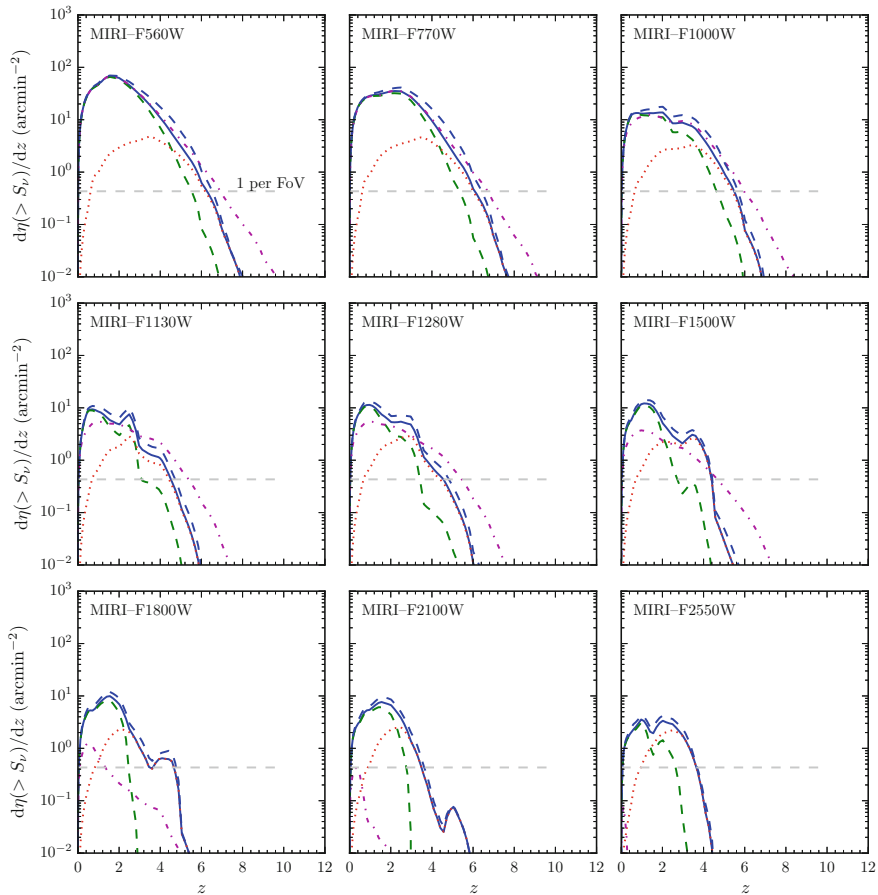
Fig. 6.10 Predicted redshift distributions for galaxies observable with a 10^4 s exposure in MIRI bands. The name of the band is indicated in each panel. All lines have the same meaning as in Fig. 6.9

narrower than the width of the MIRI–F560W filter $\sim$1.2 μm. As a result, the line luminosity has a minor effect on the broadband photometry. For example, at $z = 7.5$ in both models 95% of the sampled galaxies have their MIRI–F560W luminosity increased by less than $\sim$10%, and 90% by less than $\sim$7%. This results in a negligible difference in the luminosity functions if H α emission is included. Thus we conclude that a more detailed inclusion of nebular emission lines (e.g. Panuzzo et al. 2003) is unlikely to affect the results presented here (see also Bisigello et al. 2017 for an investigation of the effect of nebular emission lines on MIRI photometry).

We now consider the predicted redshift distributions of galaxies that would be observable with longer exposures than considered in Figs. 6.9 and 6.10. In Fig. 6.11 we show predictions for 10^4, 10^5 and 10^6 s exposures, for the NIRCam–F200W
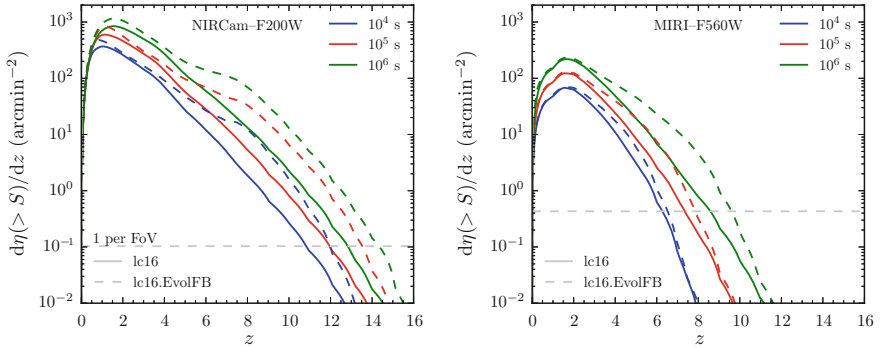
Fig. 6.11 Predicted redshift distributions for the NIRCam–F200W (*left panel*) and MIRI–F560W (*right panel*) bands for galaxies observable with a range of exposures. The *blue*, *red* and *green lines* show predictions for exposures of 10^4, 10^5 and 10^6 s respectively. The *solid* and *dashed lines* are the predictions for the fiducial and evolving feedback variant models respectively. For reference, the *horizontal dashed lines* show the number surface density at which there is one object per field of view

and MIRI–F560W filters. For the fiducial model a 10^6 s exposure will increase the number of observable objects in the NIRCam–F200W filter at $z \sim 11$ from 1 per FoV to $\sim$10 per Fov, and will increase the highest redshift at which an object is observable in a single FoV from $z \sim 11$ to $z \sim 13$. For the evolving feedback model the highest redshift will be $z \sim 14.5$. Thus, we expect that long ($>10^4$ s) exposures with *JWST* will provide better constraints on the effectiveness of supernova feedback in galaxies at high redshift.

6.3.4   *Sizes of Galaxies in* JWST *bands*

Finally, we present predictions for the angular sizes of galaxies for the NIRCam–F200W and MIRI-F560W filters in Fig. 6.12. We make such preditions for all NIR-Cam and MIRI filters but show only these two here for brevity, the predictions for other filters will be made available online. The sizes in each band are calculated as described in Sect. 6.3.1.

We can see that the predicted sizes are $\sim$0.1 arcsec, with the evolving feedback variant generally predicting slightly smaller sizes. By comparison to the diffraction limits for *JWST*, shown here as dashed horizontal lines, it is evident that NIRCam will be able to resolve the majority of detected galaxies whereas this will not be the case for MIRI (for $z \gtrsim 2$).
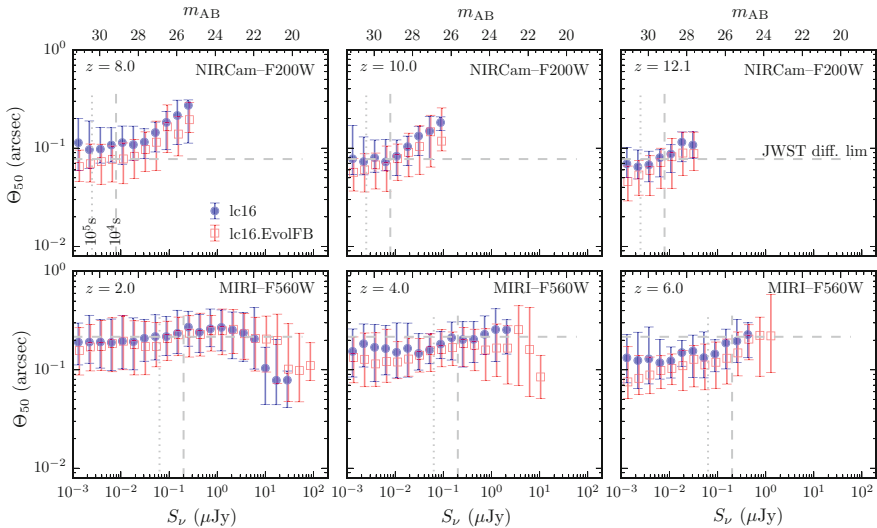
Fig. 6.12 Predicted projected half-light radii at a range of redshifts, as a function of galaxy flux, S_ν. The redshift is indicated in each panel. The *top row* shows predictions for the NIRCam–F200W filter, the *bottom row* shows predictions for the MIRI–F560W filter. The *filled circles* and open *squares* respectively indicate the median size for the fiducial and evolving feedback variant models at a given flux, with the *errorbars* indicating the 16–84 percentile ranges in a given flux bin. For reference, the *vertical dashed* and *dotted lines* respectively indicate the sensitivity limit for a 10^4 and 10^5 s exposure for that filter. The *horizontal dashed line* indicates the diffraction limit of *JWST* for that filter, assuming a 6.5 m diameter mirror

6.4 Summary

The *James Webb Space Telescope* (*JWST*) is scheduled for launch in October 2018 and is expected to significantly advance our understanding of the high-redshift ($z \gtrsim 7$) Universe.

Here we present predictions for deep galaxy surveys with *JWST*. To do so we couple the hierarchical galaxy formation model GALFORM (Lacey et al. 2016), with the spectrophotometric code GRASIL (Silva et al. 1998) for computing galaxy SEDs. GRASIL calculates the absorption and re-emission of stellar radiation by interstellar dust by solving the equations of radiative transfer in an assumed geometry. The galaxy formation model is implemented within a dark matter only N-body simulation using *Planck* cosmological parameters (Planck Collaboration et al. 2016). Adjustable parameters in the model are calibrated against a broad range of observational data such as optical and near-IR luminosity functions at $z = 0$, the evolution of the rest-frame near-IR luminosity functions for $z = 0-3$, far-IR galaxy number counts and redshift distributions, and the evolution of the rest-frame far-UV luminosity function for $z = 3-6$ (Lacey et al. 2016; Baugh et al. in preparation). Here we have shown

that the model predicts evolution of the rest-frame far-UV luminosity function for $7 \lesssim z \lesssim 10$, and galaxy sizes for $7 \lesssim z \lesssim 9$, in good agreement with observations.

We also present predictions for an evolving feedback variant model, in which the strength of supernova feedback is allowed to vary as a function of redshift (Hou et al. 2016). This adjustment allows the model to reproduce the reionization redshift inferred from *Planck* data (Planck Collaboration et al. 2016), as well as the luminosity function of the Milky Way satellites and their metallicity–stellar mass relation.

We present predictions for *JWST* in the form of luminosity functions, number counts, redshift distributions and angular sizes for each of the broadband filters on NIRCam and MIRI on *JWST*, for both the fiducial model 'lc16' and the evolving feedback variant 'lc16.EvolFB'.

We find that for a 10^4 s exposure the fiducial model predicts that *JWST* will be able to observe a single galaxy per field of view at $z \sim 11$ in the NIRCam–F200W filter; though the evolving feedback model predicts number surface densities factors of $\sim$5 greater. The model predicts that similar exposures with MIRI will not detect any galaxies at $z \gtrsim 6$ (in a single FoV). Longer integration times will increase the number of galaxies that are observable, for example, a 10^6 s integration will increase the number of galaxies predicted by the fiducial model to be observable in a single FoV by a factor of $\sim$10. A similar effect may be achieved by utilising strong gravitational lenses; however, we do not consider such an effect here. We consider a simple model for calculating H α emission and conclude that nebular emission lines will have a negligible effect on these results.

The predicted sizes of high-redshift galaxies observable with *JWST* are $\sim$0.1 arcsec, and as such we expect NIRCam to be capable of resolving the majority of detected galaxies.

We hope that the predictions presented here will help inform galaxy survey strategies for *JWST*. In the future we plan to make our results public for such a purpose, and to further develop our methodology to produce realistic mock galaxy catalogues for NIRCam and MIRI. This will allow us to make direct predictions for field-to-field variance. We envisage that observations with *JWST* will provide a wealth of information on physical processes important for galaxy formation, such as the effectiveness of supernova feedback in galaxies at high redshift.

Chapter 7
Overall Conclusions and Future Work

In this section we summarise the main conclusions of this thesis and outline some potential avenues for future investigation.

This thesis is concerned with the study of dusty star-forming galaxies that contribute to the cosmic infra-red extragalactic background light (CIB e.g. Puget et al. 1996; Fixsen et al. 1998), produced by the absorption and re-emission of radiation by interstellar dust. Observationally, it has been found that the energy density of this background is similar to that seen at UV/optical wavelengths (e.g. Hauser and Dwek 2001; Dole et al. 2006), implying that a significant proportion of star formation over the history of the Universe has been obscured by dust. An understanding of the galaxies that produce the CIB is therefore critical to our understanding of galaxy formation and evolution.

To investigate these galaxies within a theoretical framework we use the GAL-FORM semi-analytical model of hierarchical galaxy formation (e.g. Cole et al. 2000, Chap. 2) coupled with a simple model for the reprocessing of radiation by interstellar dust. This provides us with a physically motivated model for galaxy formation, embedded within the ΛCDM cosmological paradigm. In particular, we use the version of GALFORM presented in Lacey et al. (2016), which has been calibrated against a broad range of observational data at $z \lesssim 6$. Importantly for this thesis, this includes the observed galaxy number counts and redshift distributions at far-IR wavelengths, as well as the $z = 0$ optical and near-IR galaxy luminosity functions. This model makes the prediction that the galaxies responsible for producing the bulk of the infra-red background are undergoing a period of extreme star formation (in which stars form according to an IMF that is top heavy relative to that inferred in the Solar neighbourhood) triggered by a disc instability, as discussed in Sect. 2.10.

A key difficulty with observations at these wavelengths is the coarse angular resolution ($\sim$20 arcsec FWHM) of single-dish telescopes commonly used for imaging surveys at these wavelengths. It was recently discovered, through targeted interferometric follow up, that this can blend the emission from multiple galaxies along the line of sight into an object interpreted as a single source in the resulting image

(e.g. Wang et al. 2011; Hodge et al. 2013). This has a noticeable effect on the number counts derived from such observations (e.g. Karim et al. 2013). In Chap. 3 we investigated the impact that considering the finite beam size has on the predictions of the model. To do this we introduced a method for creating simulated single-dish imaging, following observational techniques, that accounts for the beam solid angle and instrument noise. We find that the model can reproduce the difference between interferometric and single-dish derived number counts. Additionally, we predict that the blended galaxies are physically unassociated, in agreement with recent observations (e.g. Wang et al. 2011; Zavala et al. 2015, though see also Simpson et al. 2015 who suggest otherwise). This implies that the degree of blending is determined primarily by the number counts of the galaxies, with their intrinsic clustering having a relatively minor effect.

However, it is a feature of the model (and most other current semi-analytical models) that any star formation enhancement caused by gravitational interactions of the galaxies involved prior to coalescence (e.g. first-passage bursts, Moreno et al. 2015), when the sub-mm emission from the galaxies in question would be blended together by a single-dish beam but they could still be resolved as separate galaxies by interferometers such as ALMA, is not included. This could affect the prediction that the blended galaxies are physically unassociated. In the model, galaxy mergers only become sub-mm bright after coalescence, and would therefore be classified as a single galaxy in the analysis presented in Sect. 3.3.3. Implementing such star formation enhancements prior to a merger in the model thus forms a potential avenue for future study. This could be achieved through investigating both suites of idealised galaxy merger simulations (e.g. Hopkins et al. 2013; Moreno et al. 2015) and galaxy mergers within cosmological gas-dynamical simulations (e.g. Vogelsberger et al. 2014; Schaye et al. 2015) to derive simplified prescriptions for this effect which can then be incorporated into the semi-analytical framework of the GALFORM model. This could potentially yield a sub-mm population of physically associated blended galaxies (early-stage mergers e.g. Hayward et al. 2011; 2013). However, as the Lacey et al. (2016) model currently predicts that sub-mm galaxies are predominantly disc instability (rather than galaxy merger) triggered starbursts, it is unclear to what extent this would be the case.

In Chap. 4 we made predictions for how the blending affects the clustering of sources derived from single-dish imaging surveys. In doing so we derived one of the key results of this thesis, namely *blending bias*. We found that the angular clustering of sources identified in single-dish imaging was boosted over all angular scales with respect to the actual clustering of the underlying galaxies. We explored some of the basic phenomenology of the blending bias and concluded that it is caused by confusion introduced by the beam which leads to induced correlations between galaxies at disparate redshifts. Fully understanding the blending bias forms a key avenue for future investigation. An attempt at an analytic derivation is presented in Appendix A, however this appears to give an incomplete description, as we observe larger blending bias factors in our simulated imaging than the derivation predicts.

Host halo masses for a population of galaxies are inferred from observations by determining the large-scale bias with which they trace the dark matter. If this has

been overestimated due to blending bias then the consequences for the inferred host halo masses can be severe. For example, the blending bias factors of $b_b \sim 2$ found in Sect. 4.4.1 could lead to the host halo masses being overestimated by an order of magnitude. This has additional consequences for understanding the evolution of the population to $z = 0$ [which can be inferred from their host halo masses using growth-of-structure arguments based on N-body simulations (e.g. Fakhouri et al. 2010)], and thus their place within the context of galaxy formation and evolution.

Observationally, targeted high-resolution interferometric follow-up of single-dish sub-mm sources allows the underlying galaxies from which they are composed to be identified, down to flux limits dependent on integration time. This would provide an approximately complete flux-limited catalogue of galaxies down to slightly above the source-extraction limit of the single-dish survey (below this limit the catalogue would become severely incomplete, and some galaxies would be de-boosted by instrumental noise to below the flux limit of the single dish survey and would therefore be missed from the follow-up observations, e.g. Appendix D). This could then be used to derive the clustering of galaxies free from blending bias, though this comes with the caveat that a large enough area is probed so that there are sufficient objects for a robust determination of the correlation function.

The model predicts that sub-mm bright galaxies reside in host halos in the relatively narrow mass range $10^{11.5}$–10^{12} h^{-1} $M_\odot$, over a broad range of redshifts ($0.2 \lesssim z \lesssim 4$). This is also the halo mass range that produces the bulk of the CIB in the model, as it represents the halo masses most conducive to star formation, due to the interplay of physical processes such as gas cooling, and supernova and AGN feedback. The model predicts clustering that is in reasonable agreement with observations when the blending bias is taken in account.

We have not included the effect of gravitational lensing (strong or weak) when generating the simulated single-dish imaging used in Chaps. 3 and 4. It may be possible to do so in a future work through using the mass distribution predicted by the N-body simulation along the line of sight used to generate the imaging, and assuming an NFW density profile for the inner regions of dark matter halos. Gravitational lensing is known to affect the sub-mm number counts (e.g. Negrello et al. 2010; Vieira et al. 2013), so it is important to include in model predictions, and it may induce an effect analogous to the blending bias discussed above. A mass overdensity along the line of sight may boost background (higher redshift) galaxies into the source catalogue selection, and the position of this mass overdensity will be correlated with other selected galaxies at its redshift. This could lead to induced correlations in the same way that the blending bias does. It may also be important to include gravitational lensing effects for predictions of high redshift galaxy surveys such as those presented in Chap. 6, as the probability of an object being lensed will increase with redshift due to hierarchical structure formation.

In Chap. 5 we investigated whether the simple dust model described in Sect. 2.9 produces realistic far-IR galaxy SEDs, as in the previous Chapters we had considered only monochromatic results. To do so we compared the observed average SEDs of galaxies presented by Béthermin et al. (2015) to the model predictions. We found remarkable agreement for galaxies on the so-called main sequence of star-forming

galaxies over a broad range of redshifts ($0.5 \lesssim z \lesssim 4$). These galaxies are responsible for the majority of the star formation in the model, so this result adds confidence to how the far-IR SEDs are computed. We also proposed that the observed evolution of dust temperatures for main sequence galaxies is due to main sequence star formation becoming more burst dominated with increasing redshift (here 'burst' refers to a period of enhanced star formation triggered by either a galaxy merger or disc instability).

A shortcoming of the simple dust model however, is that it does not compute emission in the mid-IR accurately (see Appendix C). In Chap. 6 we addressed this by using the spectrophotometric radiative transfer code GRASIL Silva et al. 1998 to compute UV-to-mm galaxy SEDs. We used GRASIL to make predictions for future *James Webb Space Telescope* galaxy surveys, which will probe the wavelength range 0.7–25.5 µm (observer-frame). We did this in the form of presenting predicted luminosity functions, number counts and redshift distributions in the *JWST* NIRCam and MIRI bands. We hope that these results will inform future survey strategies. In future, we hope to develop this methodology to produce mock galaxy catalogues. However, a significant obstacle to this is the time it takes GRASIL to compute a single galaxy SED ($\sim$5 CPU min). In Chap. 6 we have mitigated this by sampling galaxies from the simulation volume following the method presented in Granato et al. (2000). However, in order to produce mock catalogues it is necessary to compute SEDs for each galaxy in the simulation volume, and use a finer grid of output times than was used in Chap. 6 (e.g. Merson et al. 2013). Therefore, we propose to use machine-learning techniques (e.g. artificial neural networks) to reduce the time taken by the GRASIL calculation, as has been done in earlier works (e.g. Almeida et al. 2010, 2011; Silva et al. 2011, 2012), perhaps using the output spectra of the simple dust model described in Sect. 2.9 as the input to the machine-learning algorithm. Additionally, throughout this thesis we have have considered only stellar radiation and its processing by interstellar dust. However, dust emission from a hot AGN torus could emit significantly in the mid-IR, which could be important for the future *JWST* surveys that were the subject of Chap. 6. In a future work it may be possible to incorporate existing radiative transfer codes for AGN dust emission (e.g. Granato and Danese 1994; Granato et al. 1997) within the existing GALFORM framework. These studies will also open up further research opportunities investigating multi-wavelength infra-red predictions across a wavelength range not achievable before.

Appendix A
Towards a Derivation of the Blending Bias

In this Appendix we present a derivation of an approximate model for the blending bias discussed in Sect. 4.4.1.

Consider redshift intervals A and B and angular positions 1 and 2. For shorthand we write $\eta_1^A(>S_{\lim})$, the number density of galaxies at position 1 in interval A with a flux greater than some $S_{\lim}$ as η_1^A. We assume that all galaxies in a slice have the same correlation function, w_{12}^A, i.e.

$$\langle \eta_1^A \eta_2^A \rangle = \bar{\eta}^{A^2}(1 + w_{12}^A), \tag{A.0.1}$$

and that the positions of galaxies between the two intervals are uncorrelated. Now we consider the combined redshift interval A and B, for which the projected correlation function is

$$\begin{aligned}
\langle (\eta_1^A + \eta_1^B)(\eta_2^A + \eta_2^B) \rangle &\equiv (\bar{\eta}^A + \bar{\eta}^B)^2(1 + w_{12}^{\mathrm{tot}}) \\
&= \langle (\eta_1^A \eta_2^A + \eta_1^A \eta_2^B + \eta_1^B \eta_2^A + \eta_1^B \eta_2^B \rangle \\
&= \bar{\eta}^{A^2}(1 + w_{12}^A) + \bar{\eta}^{B^2}(1 + w_{12}^B) + 2\bar{\eta}^A \bar{\eta}^B, \tag{A.0.2}
\end{aligned}$$

which reduces to

$$(\bar{\eta}^A + \bar{\eta}^B)^2 w_{12}^{\mathrm{tot}} = \bar{\eta}^{A^2} w_{12}^A + \bar{\eta}^{B^2} w_{12}^B. \tag{A.0.3}$$

If we say $\bar{\eta}^A = \bar{\eta}^B = \bar{\eta}$ and $w_{12}^A = w_{12}^B = w_{12}$ we then have

$$w_{12}^{\mathrm{tot}} = w_{12}/2. \tag{A.0.4}$$

In the absence of any blending the two intervals add incoherently and their combined angular correlation function is reduced by a factor of 2 compared to their original functions.

Now we consider $\mathcal{S}_1^A$, the value of the PSF convolved flux field of all undetected galaxies fainter than some flux limit $S_{\mathrm{split}} < S_{\lim}$, (throughout we are concerned only with clustering on scales larger than the beam), at position 1. This field has a mean

value of $\bar{\mathcal{S}}^{\mathrm{A}} = \Omega_{\mathrm{beam}} \int_0^{s_{\mathrm{split}}} s\eta^{\mathrm{A}}(s)\,\mathrm{d}s$, where Ω_{beam} is the solid angle of the beam. Analogously to Eq. (A.0.1) we have

$$\langle \mathcal{S}_1^{\mathrm{A}} \mathcal{S}_2^{\mathrm{A}} \rangle = \bar{\mathcal{S}}^{\mathrm{A}^2}(1 + w_{12}^{\mathrm{A}}), \tag{A.0.5}$$

and

$$\langle \mathcal{S}_1^{\mathrm{A}} \eta_2^{\mathrm{A}} \rangle = \bar{\mathcal{S}}^{\mathrm{A}} \bar{\eta}^{\mathrm{A}}(1 + w_{12}^{\mathrm{A}}), \tag{A.0.6}$$

and similar equations for $\mathcal{S}^{\mathrm{B}}$, the convolved flux field for the undetected sources in interval B. Now $\mathcal{S}^{\mathrm{B}}$ will perturb the selection of galaxies in A (and vice-versa), such that,

$$\begin{aligned}
\tilde{\eta}_1^{\mathrm{A}}(> s_{\mathrm{lim}}) &= \eta_1^{\mathrm{A}}(> s_{\mathrm{lim}} - \mathcal{S}_1^{\mathrm{B}}) \\
&\approx \eta_1^{\mathrm{A}}(> s_{\mathrm{lim}}) - \frac{\mathrm{d}\eta^{\mathrm{A}}}{\mathrm{d}s} \mathcal{S}_1^{\mathrm{B}} \\
&= \eta_1^{\mathrm{A}} \left[1 - \frac{\mathrm{d}\eta^{\mathrm{A}}}{\mathrm{d}s} \frac{s}{\eta_1^{\mathrm{A}}} \frac{\mathcal{S}_1^{\mathrm{B}}}{s} \right] \\
&= \eta_1^{\mathrm{A}} \left[1 + \alpha^{\mathrm{A}} \frac{\mathcal{S}_1^{\mathrm{B}}}{s} \right],
\end{aligned} \tag{A.0.7}$$

where, for ease of notation, we have defined the logarithmic slope of the galaxy counts, $\alpha^{\mathrm{A}} \equiv -\mathrm{d}\ln\eta^{\mathrm{A}}/\mathrm{d}\ln S$. Now we want to find

$$\langle (\tilde{\eta}_1^{\mathrm{A}} + \tilde{\eta}_1^{\mathrm{B}})(\tilde{\eta}_2^{\mathrm{A}} + \tilde{\eta}_2^{\mathrm{B}}) \rangle = (\bar{\bar{\eta}}^{\mathrm{A}} + \bar{\bar{\eta}}^{\mathrm{B}})^2 (1 + \tilde{w}_{12}^{\mathrm{tot}}), \tag{A.0.8}$$

in terms of w_{12}^{tot}. We first expand as

$$\langle (\tilde{\eta}_1^{\mathrm{A}} + \tilde{\eta}_1^{\mathrm{B}})(\tilde{\eta}_2^{\mathrm{A}} + \tilde{\eta}_2^{\mathrm{B}}) \rangle = \langle \tilde{\eta}_1^{\mathrm{A}}\tilde{\eta}_2^{\mathrm{A}} + \tilde{\eta}_1^{\mathrm{A}}\tilde{\eta}_2^{\mathrm{B}} + \tilde{\eta}_1^{\mathrm{B}}\tilde{\eta}_2^{\mathrm{A}} + \tilde{\eta}_1^{\mathrm{B}}\tilde{\eta}_2^{\mathrm{B}} \rangle. \tag{A.0.9}$$

In the following it is useful to use the notation where $\eta_1^{\mathrm{A}} = \bar{\eta}^{\mathrm{A}} + \Delta\eta_1^{\mathrm{A}}$ and $\mathcal{S}_1^{\mathrm{A}} = \bar{\mathcal{S}}^{\mathrm{A}} + \Delta\mathcal{S}_1^{\mathrm{A}}$, where $\langle \Delta\mathcal{S}_1^{\mathrm{A}} \rangle = 0$, and $\langle \Delta\mathcal{S}_1^{\mathrm{A}} \Delta\mathcal{S}_2^{\mathrm{A}} \rangle = \bar{\mathcal{S}}^{\mathrm{A}^2} w_{12}^{\mathrm{A}}$, such that

$$\begin{aligned}
\eta_1^{\mathrm{A}} \left[1 + \frac{\alpha^{\mathrm{A}}}{s} \mathcal{S}_1^{\mathrm{B}} \right] &= (\bar{\eta}^{\mathrm{A}} + \Delta\eta_1^{\mathrm{A}}) \left[1 + \frac{\alpha^{\mathrm{A}}}{s} \bar{\mathcal{S}}^{\mathrm{B}} + \frac{\alpha^{\mathrm{A}}}{s} \Delta\mathcal{S}_1^{\mathrm{B}} \right] \\
&= \bar{\eta}^{\mathrm{A}}(1 + \delta_{\mathrm{beam}}^{\mathrm{AB}}) + \bar{\eta}^{\mathrm{A}} \Delta\mathcal{S}_1^{\mathrm{B}} \frac{\alpha^{\mathrm{A}}}{s} + \Delta\eta_1^{\mathrm{A}}(1 + \delta_{\mathrm{beam}}^{\mathrm{AB}}) + \Delta\eta_1^{\mathrm{A}} \Delta\mathcal{S}_1^{\mathrm{B}} \frac{\alpha^{\mathrm{A}}}{s},
\end{aligned} \tag{A.0.10}$$

where, for ease of notation, we have defined $\delta_{\mathrm{beam}}^{\mathrm{AB}} \equiv \alpha^{\mathrm{A}} \bar{\mathcal{S}}^{\mathrm{B}}/s$.

Now we consider the first auto-term on the RHS of Eq. (A.0.9), $\langle \tilde{\eta}_1^{\mathrm{A}}\tilde{\eta}_2^{\mathrm{A}} \rangle$. Using Eq. (A.0.10) we write this term out as

$$\left\langle \left(\bar{\eta}^{A}(1 + \delta_{\text{beam}}^{\text{AB}}) + \Delta \eta_1^{A}(1 + \delta_{\text{beam}}^{\text{AB}}) + \bar{\eta}^{A}\frac{\alpha^{A}}{s}\Delta \mathcal{S}_1^{B} + \frac{\alpha^{A}}{s}\Delta \eta_1^{A}\Delta \mathcal{S}_1^{B} \right) \times \left(1 \leftrightarrow 2 \right) \right\rangle. \tag{A.0.11}$$

We expand this out, terms which are on order $\Delta \eta$ or $\Delta \mathcal{S}$ will average to zero, as will terms involving the products of uncorrelated fluctuations in A and B. We assume the fourth-order term $\Delta \eta_1^{A}\Delta \eta_2^{B}\Delta \mathcal{S}_2^{A}\Delta \mathcal{S}_1^{B}$ is negligible. This means we are left with

$$\langle \tilde{\eta}_1^{A}\tilde{\eta}_2^{A} \rangle = \bar{\eta}^{A^2}(1 + \delta_{\text{beam}}^{\text{AB}})^2(1 + w_{12}^{A}) + \bar{\eta}^{A^2}\delta_{\text{beam}}^{\text{AB}^2}w_{12}^{B}. \tag{A.0.12}$$

Similarly for the other auto-term we have

$$\langle \tilde{\eta}_1^{B}\tilde{\eta}_2^{B} \rangle = \bar{\eta}^{B^2}(1 + \delta_{\text{beam}}^{\text{BA}})^2(1 + w_{12}^{B}) + \bar{\eta}^{B^2}\delta_{\text{beam}}^{\text{BA}^2}w_{12}^{A}. \tag{A.0.13}$$

Now we consider the one of the cross-terms on the RHS of Eq. (A.0.9), $\langle \tilde{\eta}_1^{A}\tilde{\eta}_2^{B} \rangle$, which we write out as

$$\left\langle \left(\bar{\eta}^{A}(1 + \delta_{\text{beam}}^{\text{AB}}) + \Delta \eta_1^{A}(1 + \delta_{\text{beam}}^{\text{AB}}) + \bar{\eta}^{A}\frac{\alpha^{A}}{s}\Delta \mathcal{S}_1^{B} + \frac{\alpha^{A}}{s}\Delta \eta_1^{A}\Delta \mathcal{S}_1^{B} \right) \times \left(A1 \leftrightarrow B2 \right) \right\rangle. \tag{A.0.14}$$

Expanding, and keeping all non-zero and leading order terms as before we derive

$$\langle \tilde{\eta}_1^{B}\tilde{\eta}_2^{B} \rangle = \bar{\eta}^{A}\bar{\eta}^{B}[(1 + \delta_{\text{beam}}^{\text{AB}})(1 + \delta_{\text{beam}}^{\text{BA}}) + \delta_{\text{beam}}^{\text{AB}}(1 + \delta_{\text{beam}}^{\text{BA}})w_{12}^{B} + \delta_{\text{beam}}^{\text{BA}}(1 + \delta_{\text{beam}}^{\text{AB}})w_{12}^{A}], \tag{A.0.15}$$

which is symmetric in $A \leftrightarrow B$. Putting Eqs. (A.0.12), (A.0.13) and (A.0.15) together, we can write Eq. (A.0.9) as

$$\begin{aligned} \langle (\tilde{\eta}_1^{A} + \tilde{\eta}_1^{B})(\tilde{\eta}_2^{A} + \tilde{\eta}_2^{B}) \rangle = {} & \bar{\eta}^{A^2}(1 + \delta_{\text{beam}}^{\text{AB}})^2(1 + w_{12}^{A}) + \bar{\eta}^{A^2}\delta_{\text{beam}}^{\text{AB}^2}w_{12}^{B} \\ & + \bar{\eta}^{B^2}(1 + \delta_{\text{beam}}^{\text{BA}})^2(1 + w_{12}^{B}) + \bar{\eta}^{B^2}\delta_{\text{beam}}^{\text{BA}^2}w_{12}^{A} \\ & + 2\bar{\eta}^{A}\bar{\eta}^{B}[(1 + \delta_{\text{beam}}^{\text{AB}})(1 + \delta_{\text{beam}}^{\text{BA}}) \\ & + \delta_{\text{beam}}^{\text{AB}}(1 + \delta_{\text{beam}}^{\text{BA}})w_{12}^{B} + \delta_{\text{beam}}^{\text{BA}}(1 + \delta_{\text{beam}}^{\text{AB}})w_{12}^{A}]. \end{aligned} \tag{A.0.16}$$

Rewriting the LHS using Eq. (A.0.21) and cancelling terms this simplifies to

$$\begin{aligned} [\bar{\eta}^{A}(1 + \delta_{\text{beam}}^{\text{AB}}) + \bar{\eta}^{B}(1 + \delta_{\text{beam}}^{\text{BA}})]^2\tilde{w}_{12}^{\text{tot}} = {} & [\bar{\eta}^{A}(1 + \delta_{\text{beam}}^{\text{AB}}) + \bar{\eta}^{B}\delta_{\text{beam}}^{\text{BA}}]^2 w_{12}^{A} \\ & + [\bar{\eta}^{B}(1 + \delta_{\text{beam}}^{\text{BA}}) + \bar{\eta}^{A}\delta_{\text{beam}}^{\text{AB}}]^2 w_{12}^{B}. \end{aligned} \tag{A.0.17}$$

Now we make the simplifying assumptions that $\bar{\eta}^{A} = \bar{\eta}^{B} = \bar{\eta}$ (which implies $\delta_{\text{beam}}^{\text{AB}} = \delta_{\text{beam}}^{\text{BA}} = \delta_{\text{beam}}$), and $w_{12}^{A} = w_{12}^{B} = w_{12}$. In this simplified case we can write Eq. (A.0.17) as

$$4\bar{\eta}^2(1 + \delta_{\text{beam}})^2\tilde{w}_{12}^{\text{tot}} = 2\bar{\eta}^2[(1 + \delta_{\text{beam}}) + \delta_{\text{beam}}]^2 w_{12}, \tag{A.0.18}$$

which implies that

$$\tilde{w}_{12}^{\text{tot}} = w_{12}^{\text{tot}} \left(\frac{1 + 2\delta_{\text{beam}}}{1 + \delta_{\text{beam}}} \right)^2, \qquad (A.0.19)$$

where we have recalled from Eq. (A.0.4) that $w_{12}^{\text{tot}} = w_{12}/2$. Thus in this framework we do derive a blending bias. This result is useful as it shows how faint galaxies in interval A blending with galaxies near the flux limit in B (and vice-versa) induce cross-correlations between the two intervals that boost their combined clustering. It also predicts that this blending bias should increase with the shape of the galaxy counts, α, and the PSF size through $\bar{\mathcal{S}}$. However, it does not quite behave as that observed from our simulation data, in the limit $\delta_{\text{beam}} \to \infty$ the blending bias factor is predicted to behave such that $b_{\text{b}} \to 2$, however we have found larger blending bias factors $b_{\text{b}} \approx 2\sqrt{2}$ (Fig. 4.10), suggesting something is missing from this analytical derivation. Furthering the derivation presented here will form the basis of a future study.

For the sake of completeness we now generalise this to N redshift intervals A,B,C ... etc. This follows the same procedure as before, however, it is somewhat more involved, so the reader may wish to skip ahead to Eq. (A.0.32).

We write down the 'beam perturbed' number density in a redshift slice as

$$\begin{aligned}
\tilde{\eta}_1^{\text{A}}(> s_{\text{lim}}) &= \eta_1^{\text{A}}(> s_{\text{lim}} - \mathcal{S}_1^{\text{A}} - \mathcal{S}_1^{\text{B}} - \mathcal{S}_1^{\text{C}} - ...) \\
&\approx \eta_1^{\text{A}}(> s_{\text{lim}}) - \frac{d\eta^{\text{A}}}{ds}\mathcal{S}_1^{\text{A}} - \frac{d\eta^{\text{A}}}{ds}\mathcal{S}_1^{\text{B}} - \frac{d\eta^{\text{A}}}{ds}\mathcal{S}_1^{\text{C}} - ... \\
&= \eta_1^{\text{A}}\left[1 - \frac{d\eta^{\text{A}}}{ds}\frac{s}{\eta_1^{\text{A}}}\frac{\mathcal{S}_1^{\text{A}}}{s} - \frac{d\eta^{\text{A}}}{ds}\frac{s}{\eta_1^{\text{A}}}\frac{\mathcal{S}_1^{\text{B}}}{s} - \frac{d\eta^{\text{A}}}{ds}\frac{s}{\eta_1^{\text{A}}}\frac{\mathcal{S}_1^{\text{C}}}{s} - ... \right] \\
&= \eta_1^{\text{A}}\left[1 + \alpha^{\text{A}}\frac{\mathcal{S}_1^{\text{A}}}{s} + \alpha^{\text{A}}\frac{\mathcal{S}_1^{\text{B}}}{s} + \alpha^{\text{A}}\frac{\mathcal{S}_1^{\text{C}}}{s} + ... \right] \\
&= \eta_1^{\text{A}}\left[1 + \frac{\alpha^{\text{A}}}{s}\sum_{\beta}\mathcal{S}_1^{\beta} \right]. \qquad (A.0.20)
\end{aligned}$$

Following the same procedure as before, we want to find

$$\langle(\tilde{\eta}_1^{\text{A}} + \tilde{\eta}_1^{\text{B}} + \tilde{\eta}_1^{\text{C}} + ...)(\tilde{\eta}_2^{\text{A}} + \tilde{\eta}_2^{\text{B}} + \tilde{\eta}_2^{\text{C}} + ...)\rangle = (\bar{\tilde{\eta}}^{\text{A}} + \bar{\tilde{\eta}}^{\text{B}} + \bar{\tilde{\eta}}^{\text{C}} + ...)^2(1 + \tilde{w}_{12}^{\text{tot}}) \quad (A.0.21)$$

in terms of w_{12}^{tot}. We being with an auto-term $\langle\tilde{\eta}_1^{\text{A}}\tilde{\eta}_2^{\text{A}}\rangle$. As before we write $\tilde{\eta}_2^{\text{A}}$ as

$$\eta_1^A \left[1 + \frac{\alpha^A}{s} \sum_\beta \boldsymbol{\mathcal{S}}_1^\beta \right] = (\bar\eta^A + \Delta\eta_1^A) \left[1 + \frac{\alpha^A}{s} \sum_\beta \bar{\boldsymbol{\mathcal{S}}}^\beta + \frac{\alpha^A}{s} \sum_\beta \Delta\boldsymbol{\mathcal{S}}_1^\beta \right]$$

$$= \bar\eta^A \left(1 + \frac{\alpha^A}{s} \sum_\beta \bar{\boldsymbol{\mathcal{S}}}^\beta \right) + \bar\eta^A \frac{\alpha^A}{s} \sum_\beta \Delta\boldsymbol{\mathcal{S}}_1^\beta$$

$$+ \Delta\eta_1^A \left(1 + \frac{\alpha^A}{s} \sum_\beta \bar{\boldsymbol{\mathcal{S}}}^\beta \right) + \Delta\eta_1^A \frac{\alpha^A}{s} \sum_\beta \Delta\boldsymbol{\mathcal{S}}_1^\beta.$$

$$(A.0.22)$$

We now multiply out the auto-term $\langle \tilde\eta_1^A \tilde\eta_2^A \rangle$, which, as before, we write as

$$\left\langle \left(\bar\eta^A \left(1 + \frac{\alpha^A}{s} \sum_\beta \bar{\boldsymbol{\mathcal{S}}}^\beta \right) + \bar\eta^A \frac{\alpha^A}{s} \sum_\beta \Delta\boldsymbol{\mathcal{S}}_1^\beta + \Delta\eta_1^A \left(1 + \frac{\alpha^A}{s} \sum_\beta \bar{\boldsymbol{\mathcal{S}}}^\beta \right) + \Delta\eta_1^A \frac{\alpha^A}{s} \sum_\beta \Delta\boldsymbol{\mathcal{S}}_1^\beta \right) \right.$$

$$\left. \times \left(1 \leftrightarrow 2 \right) \right\rangle.$$

$$(A.0.23)$$

Keeping non-zero, leading order terms and removing terms that only contribute at zero-separation we have

$$\langle \tilde\eta_1^A \tilde\eta_2^A \rangle = \bar\eta^{A^2} \left(1 + \frac{\alpha^A}{s} \sum_\beta \bar{\boldsymbol{\mathcal{S}}}^\beta \right)^2$$

$$+ \bar\eta^{A^2} \left(1 + \frac{\alpha^A}{s} \sum_\beta \bar{\boldsymbol{\mathcal{S}}}^\beta \right)^2 w_{12}^A$$

$$+ \bar\eta^{A^2} \left(\frac{\alpha^A}{s} \right)^2 \sum_\beta \bar{\boldsymbol{\mathcal{S}}}^{\beta^2} w_{12}^\beta$$

$$+ 2\bar\eta^{A^2} \left(1 + \frac{\alpha^A}{s} \sum_\beta \bar{\boldsymbol{\mathcal{S}}}^\beta \right) \frac{\alpha^A}{s} \bar{\boldsymbol{\mathcal{S}}}^A w_{12}^A. \qquad (A.0.24)$$

For ease of notation we re-define $\delta_{\text{beam}}^A \equiv (\alpha^A/s) \sum_\beta \bar{\boldsymbol{\mathcal{S}}}^\beta$, so that the above expression can be written as

$$\langle \tilde\eta_1^A \tilde\eta_2^A \rangle = \bar\eta^{A^2} \left[\left(1 + \delta_{\text{beam}}^A \right)^2 (1 + w_{12}^A) + 2(1 + \delta_{\text{beam}}^A) \frac{\alpha^A}{s} \bar{\boldsymbol{\mathcal{S}}}^A w_{12}^A + \left(\frac{\alpha^A}{s} \right)^2 \sum_\beta \bar{\boldsymbol{\mathcal{S}}}^{\beta^2} w_{12}^\beta \right].$$

$$(A.0.25)$$

Now we consider a cross term from Eq. (A.0.21). We write $\langle \tilde{\eta}_1^A \tilde{\eta}_2^B \rangle$ as

$$
\left\langle \left(\bar{\eta}^A \left(1 + \frac{\alpha^A}{s} \sum_\beta \bar{\boldsymbol{s}}^\beta \right) + \bar{\eta}^A \frac{\alpha^A}{s} \sum_\beta \Delta \boldsymbol{s}_1^\beta + \Delta \eta_1^A \left(1 + \frac{\alpha^A}{s} \sum_\beta \bar{\boldsymbol{s}}^\beta \right) + \Delta \eta_1^A \frac{\alpha^A}{s} \sum_\beta \Delta \boldsymbol{s}_1^\beta \right) \right.
$$
$$
\left. \times \left(A1 \leftrightarrow B2 \right) \right\rangle .
$$
(A.0.26)

Multiplying out and keeping only relevant terms as before we obtain

$$
\langle \tilde{\eta}_1^A \tilde{\eta}_2^B \rangle = \bar{\eta}^A \bar{\eta}^B \left[(1 + \delta_{\text{beam}}^A)(1 + \delta_{\text{beam}}^B) + \frac{\alpha^A}{s} \frac{\alpha^B}{s} \sum_\beta \bar{\boldsymbol{s}}^{\beta^2} w_{12}^\beta \right.
$$
$$
\left. + (1 + \delta_{\text{beam}}^B) \frac{\alpha^A}{s} \bar{\boldsymbol{s}}^B w_{12}^B + (1 + \delta_{\text{beam}}^A) \frac{\alpha^B}{s} \bar{\boldsymbol{s}}^A w_{12}^A \right], \quad (A.0.27)
$$

which we note is symmetric in $A \leftrightarrow B$.

So now we can write

$$
\langle (\tilde{\eta}_1^A + \tilde{\eta}_1^B + \tilde{\eta}_1^C + ...)(\tilde{\eta}_2^A + \tilde{\eta}_2^B + \tilde{\eta}_2^C + ...) \rangle = (\bar{\bar{\eta}}^A + \bar{\bar{\eta}}^B + \bar{\bar{\eta}}^C + ...)^2 (1 + \tilde{w}_{12}^{\text{tot}})
$$
$$
= \left[\sum_{\mathcal{A}} \bar{\eta}^{\mathcal{A}} \left(1 + \delta_{\text{beam}}^{\mathcal{A}} \right) \right]^2 (1 + \tilde{w}_{12}^{\text{tot}}),
$$
(A.0.28)

as

$$
\left\langle \left(\sum_{\mathcal{A}} \tilde{\eta}_1^{\mathcal{A}} \right) \left(\sum_{\mathcal{A}'} \tilde{\eta}_2^{\mathcal{A}'} \right) \right\rangle =
$$

$$
\bar{\eta}^{A^2} \left[\left(1 + \delta_{\text{beam}}^A \right)^2 \left(1 + w_{12}^A \right) + 2(1 + \delta_{\text{beam}}^A) \frac{\alpha^A}{s} \bar{\boldsymbol{s}}^A w_{12}^A + \left(\frac{\alpha^A}{s} \right)^2 \sum_\beta \bar{\boldsymbol{s}}^{\beta^2} w_{12}^\beta \right]
$$
$$
+ \bar{\eta}^{B^2} \left[\left(1 + \delta_{\text{beam}}^B \right)^2 \left(1 + w_{12}^B \right) + 2(1 + \delta_{\text{beam}}^B) \frac{\alpha^B}{s} \bar{\boldsymbol{s}}^B w_{12}^B + \left(\frac{\alpha^B}{s} \right)^2 \sum_\beta \bar{\boldsymbol{s}}^{\beta^2} w_{12}^\beta \right]
$$
$$
+ \bar{\eta}^{C^2} \left[\left(1 + \delta_{\text{beam}}^C \right)^2 \left(1 + w_{12}^C \right) + 2(1 + \delta_{\text{beam}}^C) \frac{\alpha^C}{s} \bar{\boldsymbol{s}}^C w_{12}^C + \left(\frac{\alpha^C}{s} \right)^2 \sum_\beta \bar{\boldsymbol{s}}^{\beta^2} w_{12}^\beta \right]
$$
$$
+ ...
$$

$$+2\bar{\eta}^A\bar{\eta}^B\left[(1+\delta^A_{\text{beam}})(1+\delta^B_{\text{beam}})+\frac{\alpha^A}{s}\frac{\alpha^B}{s}\sum_\beta\bar{\boldsymbol{s}}^{\beta^2}w^\beta_{12}\right.$$

$$\left.+(1+\delta^B_{\text{beam}})\frac{\alpha^A}{s}\bar{\boldsymbol{s}}^B w^B_{12}+(1+\delta^A_{\text{beam}})\frac{\alpha^B}{s}\bar{\boldsymbol{s}}^A w^A_{12}\right]$$

$$+2\bar{\eta}^A\bar{\eta}^C\left[(1+\delta^A_{\text{beam}})(1+\delta^C_{\text{beam}})+\frac{\alpha^A}{s}\frac{\alpha^C}{s}\sum_\beta\bar{\boldsymbol{s}}^{\beta^2}w^\beta_{12}\right.$$

$$\left.+(1+\delta^C_{\text{beam}})\frac{\alpha^A}{s}\bar{\boldsymbol{s}}^C w^C_{12}+(1+\delta^A_{\text{beam}})\frac{\alpha^C}{s}\bar{\boldsymbol{s}}^A w^A_{12}\right]$$

$$+\dots$$

$$+2\bar{\eta}^B\bar{\eta}^C\left[(1+\delta^B_{\text{beam}})(1+\delta^C_{\text{beam}})+\frac{\alpha^B}{s}\frac{\alpha^C}{s}\sum_\beta\bar{\boldsymbol{s}}^{\beta^2}w^\beta_{12}\right.$$

$$\left.+(1+\delta^C_{\text{beam}})\frac{\alpha^B}{s}\bar{\boldsymbol{s}}^C w^C_{12}+(1+\delta^B_{\text{beam}})\frac{\alpha^C}{s}\bar{\boldsymbol{s}}^B w^B_{12}\right]$$

$$+\dots.$$

$$(A.0.29)$$

Cancelling terms, this expression simplifies to

$$\left[\sum_{\mathcal{A}}\bar{\eta}^{\mathcal{A}}\left(1+\delta^{\mathcal{A}}_{\text{beam}}\right)\right]^2\tilde{w}^{\text{tot}}_{12}=$$

$$\bar{\eta}^{A^2}\left[\left(1+\delta^A_{\text{beam}}\right)^2 w^A_{12}+2(1+\delta^A_{\text{beam}})\frac{\alpha^A}{s}\bar{\boldsymbol{s}}^A w^A_{12}+\left(\frac{\alpha^A}{s}\right)^2\sum_\beta\bar{\boldsymbol{s}}^{\beta^2}w^\beta_{12}\right]$$

$$+\quad\bar{\eta}^{B^2}\left[\left(1+\delta^B_{\text{beam}}\right)^2 w^B_{12}+2(1+\delta^B_{\text{beam}})\frac{\alpha^B}{s}\bar{\boldsymbol{s}}^B w^B_{12}+\left(\frac{\alpha^B}{s}\right)^2\sum_\beta\bar{\boldsymbol{s}}^{\beta^2}w^\beta_{12}\right]$$

$$+\quad\bar{\eta}^{C^2}\left[\left(1+\delta^C_{\text{beam}}\right)^2 w^C_{12}+2(1+\delta^C_{\text{beam}})\frac{\alpha^C}{s}\bar{\boldsymbol{s}}^C w^C_{12}+\left(\frac{\alpha^C}{s}\right)^2\sum_\beta\bar{\boldsymbol{s}}^{\beta^2}w^\beta_{12}\right]$$

$$+\qquad\qquad\qquad\qquad\dots$$

$$+2\bar{\eta}^A\bar{\eta}^B\left[\frac{\alpha^A}{s}\frac{\alpha^B}{s}\sum_\beta\bar{\boldsymbol{s}}^{\beta^2}w^\beta_{12}+(1+\delta^B_{\text{beam}})\frac{\alpha^A}{s}\bar{\boldsymbol{s}}^B w^B_{12}+(1+\delta^A_{\text{beam}})\frac{\alpha^B}{s}\bar{\boldsymbol{s}}^A w^A_{12}\right]$$

$$+2\bar{\eta}^A\bar{\eta}^C\left[\frac{\alpha^A}{s}\frac{\alpha^C}{s}\sum_\beta\bar{\boldsymbol{s}}^{\beta^2}w^\beta_{12}+(1+\delta^C_{\text{beam}})\frac{\alpha^A}{s}\bar{\boldsymbol{s}}^C w^C_{12}+(1+\delta^A_{\text{beam}})\frac{\alpha^C}{s}\bar{\boldsymbol{s}}^A w^A_{12}\right]$$

$$+\qquad\qquad\qquad\qquad\dots$$

$$+2\bar{\eta}^B\bar{\eta}^C\left[\frac{\alpha^B}{s}\frac{\alpha^C}{s}\sum_\beta\bar{\boldsymbol{s}}^{\beta^2}w^\beta_{12}+(1+\delta^C_{\text{beam}})\frac{\alpha^B}{s}\bar{\boldsymbol{s}}^C w^C_{12}+(1+\delta^B_{\text{beam}})\frac{\alpha^C}{s}\bar{\boldsymbol{s}}^B w^B_{12}\right]$$

$$+\qquad\qquad\qquad\qquad\dots.$$

$$(A.0.30)$$

In order to simplify this, we group all terms containing w_{12}^{A}, which gives

$$[\bar{\eta}^{A}(1 + \delta_{\text{beam}}^{A}) + \delta_{\text{beam}}^{A'}]^{2}, \tag{A.0.31}$$

where we have defined $\delta_{\text{beam}}^{A'} \equiv \bar{\mathcal{S}}^{A} \sum_{\beta} \bar{\eta}^{\beta} \alpha^{\beta}/s$, for ease of notation.

Finally, we can write

$$\left[\sum_{A} \bar{\eta}^{A} \left(1 + \delta_{\text{beam}}^{A}\right) \right]^{2} \tilde{w}_{12}^{\text{tot}} = \sum_{A} \left[\bar{\eta}^{A}(1 + \delta_{\text{beam}}^{A}) + \delta_{\text{beam}}^{A'} \right]^{2} w_{12}^{A}, \tag{A.0.32}$$

where we remind the reader that $\delta_{\text{beam}}^{A} \equiv (\alpha^{A}/s) \sum_{\beta} \bar{\mathcal{S}}^{\beta}$, where $\alpha^{A} \equiv -\mathrm{d}\ln\eta^{A}/\mathrm{d}\ln s$ and $\bar{\mathcal{S}}^{\beta} = \Omega_{\text{beam}} \int_{0}^{s_{\text{split}}} s\,(\mathrm{d}\eta^{\beta}/\mathrm{d}s)\mathrm{d}s$.

In the case without 'beam perturbed' number counts we would have obtained

$$w_{12}^{\text{tot}} = \frac{\sum_{A} \bar{\eta}^{A^{2}} w_{12}^{A}}{\left[\sum_{A} \bar{\eta}^{A} \right]^{2}}. \tag{A.0.33}$$

However, we obtained

$$\tilde{w}_{12}^{\text{tot}} = \frac{\sum_{A} \left[\bar{\eta}^{A}(1 + \delta_{\text{beam}}^{A}) + \delta_{\text{beam}}^{A'} \right]^{2} w_{12}^{A}}{\left[\sum_{A} \bar{\eta}^{A} \left(1 + \delta_{\text{beam}}^{A}\right) \right]^{2}}. \tag{A.0.34}$$

In the case of N intervals, and making the same simplifying assumptions as before (number counts and clustering of objects are the same in each redshift slice i.e. there is no evolution of the population). Then $\delta_{\text{beam}}^{A} = N\bar{\mathcal{S}}\alpha/s \equiv N\delta$, $\delta_{\text{beam}}^{A'} = N\bar{\eta}\bar{\mathcal{S}}\alpha/s = N\bar{\eta}\delta$ and $w_{12}^{\text{tot}} = w_{12}/N$. so we obtain

$$\tilde{w}_{12}^{\text{tot}} = \left(\frac{1 + 2N\delta}{1 + N\delta} \right)^{2} w_{12}^{\text{tot}}, \tag{A.0.35}$$

where $\delta = -(\mathrm{d}\ln\eta/\mathrm{d}\ln s)(\bar{\mathcal{S}}/s)$ and $\bar{\mathcal{S}} = \Omega_{\text{beam}} \int_{0}^{s_{\text{split}}} s\,(\mathrm{d}\eta/\mathrm{d}s)\mathrm{d}s$. Note the similarity of this expression to Eq. (A.0.19).

Appendix B
# The Effect of a Non-universal IMF on Stellar Masses Inferred from SED Fitting

[1]The galaxy formation model that we have used in this thesis incorporates two IMFs, a solar neighbourhood Kennicutt (1983) IMF for quiescent mode star formation, which occurs in the galactic disc, and a top-heavy IMF for burst mode star formation, which is triggered by some dynamical event and occurs in a forming galactic bulge. The top-heavy IMF is described by a slope of $x = 1$ in $dN(m)/d\ln m \propto m^{-x}$ [for reference a Salpeter (1955) IMF has a slope of $x = 1.35$]. Therefore galaxies in the model will contain stellar populations that formed with different IMFs.

Typically, stellar masses are inferred from observations by fitting model SEDs to observed broadband photometry making a number of assumptions [for a discussion see e.g. Mitchell et al. (2013); Pforr et al. (2012)], one of which is that the IMF is universal and has a form similar to that observed for the solar neighbourhood. Here we investigate what corrections, if any, it may be necessary to apply to the stellar masses predicted by the model to account for this assumption when comparing to observational data.

To do this we use the SED fitting code presented in Mitchell et al. (2013). We utilise simulated photometry from the same broadband filters as used in the Ilbert et al. (2010) study that derived the stellar masses for the Béthermin et al. (2015) sample we are comparing our model predictions to in Chap. 5. These comprise 15 bands, the *GALEX* far- and near-UV, Subaru/SuprimeCam *BVgriz*, CFHT/WIRCAM *JHK* and the 4 *Spitzer*/IRAC bands. We also assume the same star formation history grid as used in Ilbert et al. (2010), that is a grid of exponentially decaying star formation histories, $\exp(-t_{age}/\tau)$, where $\tau = 0.1, 1, 2, 3, 5, 10, 15, 30$ Gyr, and t_{age}, the time since the star formation began, is constrained to be less than the age of the Universe. We use the stellar population models of Maraston (2005), which are calculated for a grid of 4 metallicities ($Z = 0.02, 0.5, 1, 2\ Z_\odot$) and 67 ages ranging from 10^3 yr

---

[1]The content of this Appendix is based on Appendix A of the article Cowley et al. 'The far-infrared SEDs of main sequence and starburst galaxies', Monthly Notices of the Royal Astronomical Society, Volume 467, Issue 1, p. 1231–1248, published 20 January 2017. Reproduced with permission. All rights reserved, https://doi.org/10.1093/mnras/stx165.
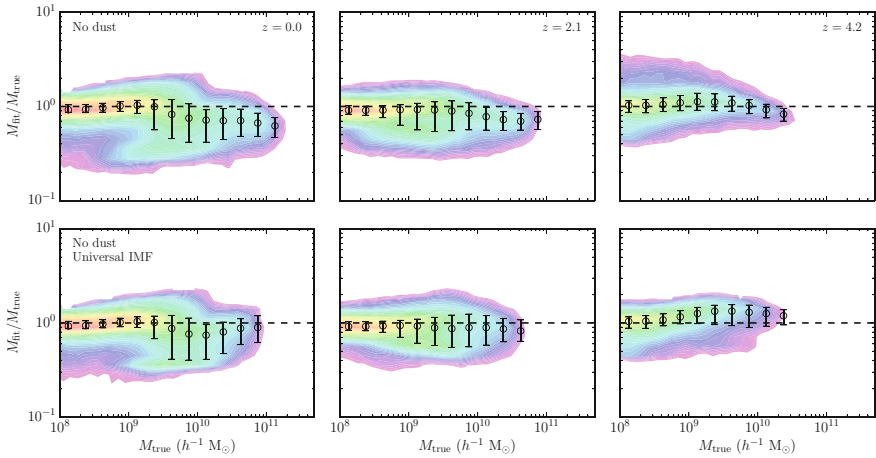
Fig. B.1 The ratios of stellar masses inferred from broadband photometry using the SED fitting code presented in Mitchell et al. (2013), ignoring attenuation by interstellar dust, to the true stellar masses predicted by GALFORM. The *colour scale* indicates the logarithmic density of points from *red* (high density) to *purple* (low density). *Top row:* Fiducial model with a top heavy IMF for burst mode star formation. *Bottom row:* Model with a universal IMF. *Open symbols* and *errorbars* show the median and 16–84 percentiles of the distribution of inferred to true mass ratio at a given true stellar mass. For reference, the *horizontal black dashed line* in each panel indicates unity

to 15 Gyr. In the model SED fitting we always assume a universal Kennicutt (1983) IMF, and for simplicity we ignore the effects of dust attenuation.

We use SED fitting to derive (likelihood weighted) inferred masses for a sample of our model galaxies and show the ratio of inferred stellar mass to true stellar mass as a function of true stellar mass at a range of redshifts in Fig. B.1. We do this for both the fiducial model (top row) and for a model which assumes a universal Kennicutt (1983) IMF[2] (bottom row).

Even in the highly simplified case in which the effects of dust are ignored, there are no errors associated with the input photometry, and the same stellar population models and IMF are used in both the model and SED fitting (bottom row), the ratio of inferred to true stellar masses has a median value that can deviate from unity and shows 16–84 percentile scatter of up to a factor of ∼3. We note that the differences between the top and bottom rows in Fig. B.1 that are caused by having a top-heavy IMF for burst mode star formation in the fiducial model are typically smaller than the amount of scatter seen in both rows and between different redshifts for the same model.

We conclude that any corrections due to having a non-universal IMF are small compared to the uncertainties associated with the SED fitting technique itself, and so would not have a significant effect on the results presented in Chap. 5. Therefore,

---

[2]We do not consider this an acceptable model of galaxy formation as it fails to reproduce the observed number counts of galaxies at 850 μm by more than an order of magnitude.

we make no explicit correction for this in Chap. 5. We caution however, that this may not be the case for some populations of galaxies, depending on the selection criteria, e.g. sub-mm galaxies selected by their 850 µm flux.

Appendix C
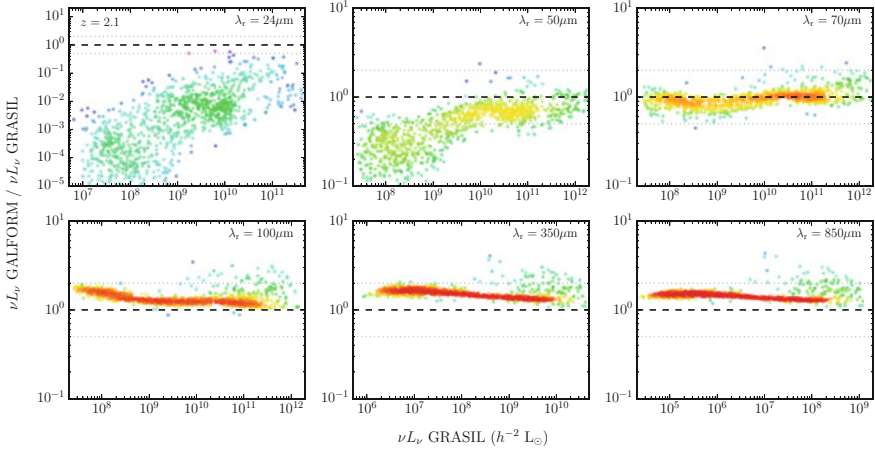# Comparing the Simple Dust Model
with GRASIL

[3]In this Appendix we perform a brief comparison of the predictions made using our simple model for dust absorption and emission (Sect. 2.9) with those of the spectrophotometric radiative transfer code, GRASIL Silva et al. (1998). The simple dust model assumes the same geometry as GRASIL, but GRASIL but treats some of the physics involved in more detail: (i) dust temperature is calculated self-consistently at each location across the galaxy and also according to the size and composition of the dust grains (GRASIL assumes a distribution of grain sizes and two compositions: graphite and astronomical silicate); (ii) temperature fluctuations for small grains due to finite heat capacities and (iii) the inclusion of emission from PAH molecules. Whilst the GRASIL calculation is more physically sophisticated it is too computationally expensive to run for each galaxy in the samples we are considering in this thesis. For this reason, here we restrict ourselves to a random sample of $\sim$1000 star-forming galaxies (as defined by $\mathrm{sSFR}' > \mathrm{sSFR}'_{\mathrm{split}}$, see Chap. 5) at $z = 2.1$.

A crude comparison of the computational cost of GRASIL and GALFORM was made using the galaxy sample generated for this section. GRASIL took, on average, $\sim$160 CPU seconds per galaxy, while GALFORM (including the galaxy formation calculation) took $\sim$$6.2 \times 10^{-3}$ CPU seconds of which approximately 10% was spent computing SEDs. Thus we infer that the GRASIL calculation is $\sim$$2.6 \times 10^5$ longer than the simple dust model used here.

In Fig. C.1 we show the comparison of the luminosities predicted by the GALFORM dust model to those calculated using GRASIL at rest-frame wavelengths of 24, 50, 70, 100, 350 and 850 μm, as indicated in the panels, at $z = 2.1$. We see that for rest-frame wavelengths of $\lambda_{\mathrm{rest}} \gtrsim 70\,\mu$m the simple model can reproduce the results of GRASIL to better than a factor of two (indicated in each panel by the grey dotted lines), with a relatively small amount of scatter. However, at shorter rest-frame wavelengths the

---

[3]The content of this Appendix is based on Appendix B of the article Cowley et al. 'The far-infrared SEDs of main sequence and starburst galaxies', Monthly Notices of the Royal Astronomical Society, Volume 467, Issue 1, p. 1231–1248, published 20 January 2017. Reproduced with permission. All rights reserved, https://doi.org/10.1093/mnras/stx165.

Fig. C.1 Comparison of the predictions of the simple dust model with those from GRASIL (Silva et al. 1998), at a range of rest-frame wavelengths λ_{rest} = 24, 50, 70, 100, 350 and 850 μm, at redshift $z = 2.1$, for a random sample of ∼1000 star-forming galaxies. The *black dashed line* in each panel indicates unity and the *grey dotted lines* indicate a factor of ±0.3 dex from unity. Note that for the $\lambda_{rest} = 24$ μm panel the ordinate axis covers a much larger dynamic range than for the other wavelengths considered. The *colourscale* indicates the logarithmic density of points from *red* (high density) to *purple* (low density)

approximations in the simple model break down, as can be seen by the increased scatter and larger deviation from unity. We therefore are confident in the predictions of our simple dust model (Sect. 2.9) for rest-frame wavelengths longer than 70 μm.

Appendix D
Background ALMA Number Counts

[4]In this Appendix we use the imaging methodology presented in Chap. 3 to investigate the number counts of SMGs found in the backgrounds of ALMA maps, and compare our predictions to the observational results of Simpson et al. (2015). Doing so provides a further test of the model prediction that blended SMGs are physically unassociated, as presented in Chap. 3.

Simpson et al. made use of ALMA follow-up imaging of bright ($S_{850\mu m} \gtrsim 8$ mJy) sub-mm sources identified in the SCUBA-2 Cosmology Legacy Survey (S2CLS e.g. Geach et al. 2013, 2017) in the UKIDS-UDS[5] field. These authors were able to further constrain the bright end of the interferometric-derived sub-mm number counts as they utilised an area $\sim 2\times$ larger earlier follow-up studies (e.g. Karim et al. 2013). Due to their increased sample size they were also able to probe the origin of the SMG source multiplicity discussed in Chap. 3.

Simpson et al. investigated potential physical associations through studying the small-scale clustering of SMGs in their ALMA maps. This involved calculating the surface number density of serendipitous secondary[6] galaxies in their ALMA maps. If the value for this is greater than expected for a blank field then it indicates that the galaxies may be clustered i.e. physically associated. To do this they first identified and removed from their analysis ALMA maps which did not contain a galaxy intrinsically (i.e. with an ALMA flux) brighter than the flux limit of their original single dish survey. These maps were targeted with ALMA as the emission

---

[4]This Appendix summaries the author's contribution to the article Simpson et al. 'The SCUBA-2 Cosmology Legacy Survey: ALMA resolves the bright end of the sub-millimetre number counts', Astrophysical Journal, Volume 807, Issue 2, article id. 128, 13 p, published 7 July 2015. All rights reserved, https://doi.org/10.1088/0004-637X/807/2/128. This Appendix is the author's original work and no text or figures from the Simpson et al. publication have been reproduced here.

[5]United Kingdom Infra-red Telescope (UKIRT) Infra-red Deep Sky Survey—Ultra Deep Survey.

[6]By secondary we mean that they are not the brightest galaxy in their ALMA map.

from secondary galaxies had been blended together by the SCUBA-2 beam to boost the brightest galaxy into the source selection, thus the secondary galaxies are not serendipitous. They then counted the surface number density of secondary galaxies in the remaining ALMA maps. These galaxies were not the reason that their patch of sky had been observed with ALMA and thus they represent true serendipitous galaxies. Finally, they discarded galaxies with $S_{850\mu m} < 2$ mJy, as these galaxies would not be observable over the whole area of the ALMA map due to their Gaussian sensitivity profile. This gave Simpson et al. 11 serendipitous/secondary SMGs with $S_{850\mu m} > 2$ mJy from 11 ALMA maps, resulting in a surface number density of secondary galaxies of $5.5^{+2.2}_{-1.6} \times 10^4$ deg^{-2}. This was a factor of ∼80 times greater than their blank field expectation, which was based on fitting an assumed functional form to their interferometric number counts, and those of Karim et al. (2013).

One might expect such an analysis to be affected by Eddington bias (e.g. Eddington 1913). Galaxies which were intrinsically brighter than the single-dish flux limit, but were pushed below it by negative noise, would never be followed up with ALMA. This is expected to happen preferentially to galaxies just above the flux limit of the single-dish survey with few secondary SMGs within the ALMA primary beam, and less likely to happen to those with many secondary SMGs, as the blended flux contribution of the secondary galaxies make it less likely that a negative noise pixel would be able to 'push' the galaxy out of the single-dish catalogue. Measuring the surface number density of serendipitous secondary ALMA SMGs might then be biased high by such an effect, even if the galaxies themselves were randomly distributed (i.e. not clustered).

In order to test how big an affect this bias might have on such an analysis, in Simpson et al. we used the methodology developed in Chap. 3 to perform a similar analysis on predictions from the Lacey et al. (2016) model. However, the result could also be affected by the predicted clustering of SMGs in the model, which may or may not be representative of the actual clustering of such objects (see Chap. 4). In order to negate this issue, we first randomise the positions of the simulated SMGs prior to creating the simulated imaging, thus all secondary galaxies in our maps would be the result of a chance alignment. We used the same beam size (15 arcsec) and included a similar level of instrument noise (∼1 mJy/beam) as was found in the single-dish maps used by Simpson et al.

The result of this analysis is presented in Fig. D.1. We find that the background number counts of ALMA secondary sources are a factor of ∼1.7 greater than expected for a blank field due to the (negative) Eddington bias mentioned above. We have repeated this for a set of images in which the clustering predicted by the model was retained and have found similar results. This is significantly lower than the factor of ∼80 observed by Simpson et al. At least some of this difference may be due to the different blank field number accounts assumed, as the predicted secondary source number density is only a factor of ∼10 lower than observed by Simpson et al. However, it indicates that for the bright sources ($S_{850\mu m} > 8$ mJy) at least,
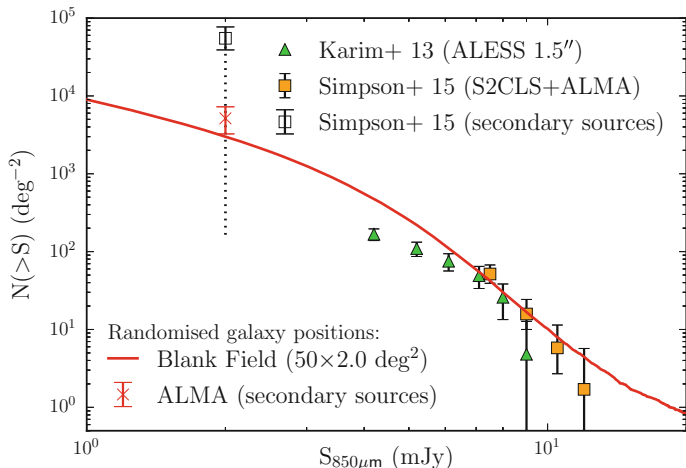
Fig. D.1 Predicted 850 μm background ALMA number counts for a set of 50×2 deg^2 simulated images made from the Lacey et al. (2016) model with the positions of the galaxies randomised prior to creating the images. The *solid line* shows the predicted intrinsic blank field number counts. The *cross* indicates the predicted surface number density of galaxies with $S_{850\mu m} > 2.0$ mJy in ALMA maps targeted at sources with $S_{850\mu m} > 8$ mJy that contain a galaxy with $S_{850\mu m} > 8$ mJy, that are not the brightest galaxy within their ALMA map. The *errorbars* indicate the predicted 16–84 (1σ) percentile field-to-field variation. The *open square* indicates same statistic as the *cross* but derived from the observational data of Simpson et al. (2015). Observational data for blank field interferometric number counts are from Karim et al. (2013, *triangles*) and Simpson et al. (2015, *filled squares*). For reference, the *vertical dotted line* indicates a flux limit of 2 mJy

the source multiplicity observed is potentially inconsistent with the blended galaxies being predominantly physically unassociated, as is predicted by the Lacey et al. (2016) model (Chap. 3). This result is also discussed by Simpson et al. (2015).

Bibliography

Abramson, L. E., Kelson, D. D., Dressler, A., Poggianti, B., Gladders, M. D., Oemler, A, Jr., et al. (2014). *ApJ*, *785*, L36.

Agladze, N. I., Sievers, A. J., Jones, S. A., Burlitch, J. M., & Beckwith, S. V. W. (1996). *ApJ*, *462*, 1026.

Alcock, C., et al. (2000). *ApJ*, *542*, 281.

Almaini, O., Lawrence, A., & Boyle, B. J. (1999). *MNRAS*, *305*, L59.

Almeida, C., Baugh, C. M., Lacey, C. G., Frenk, C. S., Granato, G. L., Silva, L., et al. (2010). *MNRAS*, *402*, 544.

Almeida, C., Baugh, C. M., & Lacey, C. G. (2011). *MNRAS*, *417*, 2057.

Alpher, R. A., Bethe, H., & Gamow, G. (1948). *Phys. Rev.*, *73*, 803.

Amblard, A., et al. (2011). *Nature*, *470*, 510.

Angulo, R. E., Baugh, C. M., Frenk, C. S., & Lacey, C. G. (2008). *MNRAS*, *383*, 755.

Aretxaga, I., Wilson, G. W., Aguilar, E., et al. (2011). *MNRAS*, *415*, 3831.

Arnouts, S., et al. (2005). *ApJ*, *619*, L43.

Baldry, I. K., et al. (2012). *MNRAS*, *421*, 621.

Bardeen, J. M., Bond, J. R., Kaiser, N., & Szalay, A. S. (1986). *ApJ*, *304*, 15.

Barger, A. J., Cowie, L. L., Sanders, D. B., Fulton, E., Taniguchi, Y., Sato, Y., et al. (1998). *Nature*, *394*, 248.

Barnes, J. E. (1998). R. C. Kennicutt, Jr., F. Schweizer, J. E. Barnes, D. Friedli, L. Martinet & D. Pfenniger (Eds.), *Saas-fee advanced course 26: Galaxies: Interactions and induced star formation* (p. 275).

Basilakos, S., Plionis, M., Georgakakis, A., & Georgantopoulos, I. (2005). *MNRAS*, *356*, 183.

Bastian, N., Covey, K. R., & Meyer, M. R. (2010). *ARA&A*, *48*, 339.

Baugh, C. M. (2006). *Reports on Progress in Physics*, *69*, 3101.

Baugh, C. M., Cole, S., Frenk, C. S., & Lacey, C. G. (1998). *ApJ*, *498*, 504.

Baugh, C. M., Lacey, C. G., Frenk, C. S., et al. (2005). *MNRAS*, *356*, 1191.

Behroozi, P. S., Wechsler, R. H., & Conroy, C. (2013). *ApJ*, *770*, 57.

Benson, A. J. (2005). *MNRAS*, *358*, 551.

Benson, A. J. (2010). *Phys. Rep.*, *495*, 33.

Benson, A. J., & Bower, R. (2010). *MNRAS*, *405*, 1573.

Benson, A. J., Bower, R. G., Frenk, C. S., Lacey, C. G., Baugh, C. M., & Cole, S. (2003). *ApJ*, *599*, 38.

Berlind, A. A., & Weinberg, D. H. (2002). *ApJ*, *575*, 587.

Béthermin, M., Le Floc'h, E., Ilbert, O., et al. (2012). *A&A*, *542*, A58.

Béthermin, M., Wang, L., Doré, O., Lagache, G., Sargent, M., Daddi, E., et al. (2013). *A&A*, *557*, A66.

Béthermin, M., et al. (2015). *A&A*, *573*, A113.

Bianchi, S., Ferrara, A., & Giovanardi, C. (1996). *ApJ*, *465*, 127.

Biggs, A. D., Ivison, R. J., Ibar, E., et al. (2011). *MNRAS*, *413*, 2314.

Bigiel F., Leroy A., Walter F., Brinks E., de Blok W. J. G., Madore B., & Thornley M. D. (2008). *AJ*, *136*, 2846.

Bigiel, F., et al. (2011). *ApJ*, *730*, L13.

Binney J., & Tremaine S. (1987). *Galactic dynamics*.

Bisigello L., et al. (2017). (arXiv:1706.05063).

Blain, A. W., & Longair, M. S. (1993). *MNRAS*, *264*, 509.

Blain, A. W., Smail, I., Ivison, R. J., Kneib, J.-P., & Frayer, D. T. (2002). *Physics Report*, *369*, 111.

Blain, A. W., Chapman, S. C., Smail, I., & Ivison, R. (2004). *ApJ*, *611*, 725.

Blaizot, J., Wadadekar, Y., Guiderdoni, B., et al. (2005). *MNRAS*, *360*, 159.

Blake, C., Pope, A., Scott, D., & Mobasher, B. (2006). *MNRAS*, *368*, 732.

Blitz, L., & Rosolowsky, E. (2006). *ApJ*, *650*, 933.

Bond, J. R., Cole, S., Efstathiou, G., & Kaiser, N. (1991). *ApJ*, *379*, 440.

Boudet, N., Mutschke, H., Nayral, C., Jäger, C., Bernard, J.-P., Henning, T., et al. (2005). *ApJ*, *633*, 272.

Bouwens, R. J., et al. (2003). *ApJ*, *595*, 589.

Bouwens, R. J., et al. (2010). *ApJ*, *709*, L133.

Bouwens, R. J., et al. (2015). *ApJ*, *803*, 34.

Bower, R. G., Benson, A. J., Malbon, R., et al. (2006). *MNRAS*, *370*, 645.

Bower, R. G., Vernon, I., Goldstein, M., Benson, A. J., Lacey, C. G., Baugh, C. M., et al. (2010). *MNRAS*, *407*, 2017.

Bowler, R. A. A., et al. (2014). *MNRAS*, *440*, 2810.

Brammer, G. B., van Dokkum, P. G., & Coppi, P. (2008). *ApJ*, *686*, 1503.

Bruzual, G., & Charlot, S. (2003). *MNRAS*, *344*, 1000.

Burgarella, D., et al. (2013). *A&A*, *554*, A70.

Caputi, K. I., Cirasuolo, M., Dunlop, J. S., McLure, R. J., Farrah, D., & Almaini, O. (2011). *MNRAS*, *413*, 162.

Caputi, K. I., et al. (2015). *ApJ*, *810*, 73.

Carniani, S., et al. (2015). *A&A*, *584*, A78.

Casey, C. M., Chen, C.-C., Cowie, L. L., et al. (2013). *MNRAS*, *436*, 1919.

Casey, C. M., Narayanan, D., & Cooray, A. (2014). *Physics Report*, *541*, 45.

Chabrier, G. (2003). *PASP*, *115*, 763.

Chakrabarti, S., Fenner, Y., Cox, T. J., Hernquist, L., & Whitney, B. A. (2008). *ApJ*, *688*, 972.

Chandrasekhar, S. (1943). *ApJ*, *97*, 255.

Chapin, E. L., Chapman, S. C., Coppin, K. E., et al. (2011). *MNRAS*, *411*, 505.

Chapman, S. C., Blain, A. W., Smail, I., & Ivison, R. J. (2005). *ApJ*, *622*, 772.

Chen, C.-C., Cowie, L. L., Barger, A. J., et al. (2013). *ApJ*, *776*, 131.

Chen, C.-C., et al. (2015). *ApJ*, *799*, 194.

Chen, C.-C., et al. (2016). *ApJ*, *820*, 82.

Christodoulou, D. M., Shlosman, I., & Tohline, J. E. (1995). *ApJ*, *443*, 551.

Clements, D. L., et al. (2010). *A&A*, *518*, L8.

Cole, S. (1991). *ApJ*, *367*, 45.

Cole, S., & Lacey, C. (1996). *MNRAS*, *281*, 716.

Cole, S., Aragon-Salamanca, A., Frenk, C. S., Navarro, J. F., & Zepf, S. E. (1994). *MNRAS*, *271*, 781.

Cole, S., Lacey, C. G., Baugh, C. M., & Frenk, C. S. (2000). *MNRAS*, *319*, 168.

Cole, S., et al. (2001). *MNRAS*, *326*, 255.

Cole, S., et al. (2005). *MNRAS*, *362*, 505.

Combes, F. (2000). F. Hammer, T. X. Thuan, V. Cayatte, B. Guiderdoni & J. T. Thanh Van (Eds.), *Building galaxies; from the primordial universe to the present* (p. 413). (arXiv:astro-ph/9904031).

Conroy, C., & van Dokkum, P. G. (2012). *ApJ*, *760*, 71.

Cooray, A., & Sheth, R. (2002). *Physics Reports*, *372*, 1.

Coppin, K., Chapin, E. L., Mortier, A. M. J., et al. (2006). *MNRAS*, *372*, 1621.

Cowley, W. I., Lacey, C. G., Baugh, C. M., & Cole, S. (2015). *MNRAS*, *446*, 1784.

Cowley, W. I., Lacey, C. G., Baugh, C. M., & Cole, S. (2016). *MNRAS*.

Cowley, W., Baugh, C., Cole, S., Frenk, C., & Lacey, C. (2017a). (arXiv:1702.02146).

Cowley, W. I., Béthermin, M., Lagos, C. D. P., Lacey, C. G., Baugh, C. M., & Cole, S. (2017b). *MNRAS*, *467*, 1231.

Cowley, W. I., Lacey, C. G., Baugh, C. M., Cole, S., & Wilkinson, A. (2017c). *MNRAS*, *469*, 3396.

Crain, R. A., et al. (2015). *MNRAS*, *450*, 1937.

Croton, D. J., et al. (2006). *MNRAS*, *365*, 11.

da Cunha, E., Charlot, S., & Elbaz, D. (2008). *MNRAS*, *388*, 1595.

da Cunha, E., et al. (2015). *ApJ*, *806*, 110.

Cyburt, R. H., Fields, B. D., & Olive, K. A. (2008). *J. Cosmology Astropart. Phys.*, *11*, 012.

Danielson, et al. (2017). *ApJ*, *840*, 78.

Davis, M., Efstathiou, G., Frenk, C. S., & White, S. D. M. (1985). *ApJ*, *292*, 371.

Davis, M., Efstathiou, G., Frenk, C. S., & White, S. D. M. (1992). *Nature*, *356*, 489.

Di Matteo, T., Springel, V., & Hernquist, L. (2005). *Nature*, *433*, 604.

Dole, H., et al. (2006). *A&A*, *451*, 417.

Dolley, T., et al. (2014). *ApJ*, *797*, 125.

Draine, B. T., & Lee, H. M. (1984). *ApJ*, *285*, 89.

Draine, B. T., & Li, A. (2007). *ApJ*, *657*, 810.

Driver, S. P., et al. (2012). *MNRAS*, *427*, 3244.

Dunkley, J., et al. (2009). *ApJS*, *180*, 306.

Eddington, A. S. (1913). *MNRAS*, *73*, 359.

Efstathiou, G., Lake, G., & Negroponte, J. (1982). *MNRAS*, *199*, 1069.

Efstathiou, G., Sutherland, W. J., & Maddox, S. J. (1990). *Nature*, *348*, 705.

Efstathiou, G., Bernstein, G., Tyson, J. A., Katz, N., & Guhathakurta, P. (1991). *ApJ*, *380*, L47.

Eisenstein, D. J., et al. (2005). *ApJ*, *633*, 560.

Eke V. R., Cole S., & Frenk C. S. (1996). *MNRAS*, *282*.

Elbaz, D., et al. (2007). *A&A*, *468*, 33.

Fakhouri, O., Ma, C.-P., & Boylan-Kolchin, M. (2010). *MNRAS*, *406*, 2267.

Fall, S. M., & Efstathiou, G. (1980). *MNRAS*, *193*, 189.

Farrah, D., et al. (2006). *ApJ*, *643*, L139.

Ferrara, A., Bianchi, S., Cimatti, A., & Giovanardi, C. (1999). *ApJS*, *123*, 437.

Finkelstein, S. L., et al. (2015). *ApJ*, *810*, 71.

Fioc, M., & Rocca-Volmerange, B. (1997). *A&A*, *326*, 950.

Fixsen, D. J., Dwek, E., Mather, J. C., Bennett, C. L., & Shafer, R. A. (1998). *ApJ*, *508*, 123.

Font, A. S., et al. (2011). *MNRAS*, *417*, 1260.

Frenk, C. S. (1986). *Philosophical Transactions of the Royal Society of London Series A*, *320*, 517.

Gardner, J. P., et al. (2006). *Space Science Reviews*, *123*, 485.

Gautier III, T. N., Boulanger, F., Perault, M., & Puget, J. L. (1992). *AJ*, *103*, 1313.

Geach, J. E., et al. (2013). *MNRAS*, *432*, 53.

Geach, J. E., et al. (2017). *MNRAS*, *465*, 1789.

Gonzalez-Perez, V., Baugh, C. M., Lacey, C. G., & Kim, J.-W. (2011). *MNRAS*, *417*, 517.

Gonzalez-Perez, V., Lacey, C. G., Baugh, C. M., Frenk, C. S., & Wilkins, S. M. (2013). *MNRAS*, *429*, 1609.

Gonzalez-Perez, V., Lacey, C. G., Baugh, C. M., et al. (2014). *MNRAS*, *439*, 264.

González, J. E., Lacey, C. G., Baugh, C. M., & Frenk, C. S. (2011). *MNRAS*, *413*, 749.

Granato, G. L., & Danese, L. (1994). *MNRAS*, *268*, 235.

Granato, G. L., Danese, L., & Franceschini, A. (1997). *ApJ*, *486*, 147.

Granato, G. L., Lacey, C. G., Silva, L., et al. (2000). *ApJ*, *542*, 710.

Griffin, M. J., Abergel, A., Abreu, A., et al. (2010). *A&A*, *518*, L3.

Groth, E. J., & Peebles, P. J. E. (1977). *ApJ*, *217*, 385.

Gruppioni, C., et al. (2013). *MNRAS*, *432*, 23.

Gunawardhana, M. L. P., et al. (2011). *MNRAS*, *415*, 1647.

Gunawardhana, M. L. P., et al. (2013). *MNRAS*, *433*, 2764.

Gunn, J. E., & Gott, J. R, I. I. I. (1972). *ApJ*, *176*, 1.

Guo, Q., White, S., Li, C., & Boylan-Kolchin, M. (2010). *MNRAS*, *404*, 1111.

Guo, Q., White, S., Angulo, R. E., et al. (2013). *MNRAS*, *428*, 1351.

Guo, Q., et al. (2016). *MNRAS*, *461*, 3457.

Guth, A. H. (1981). *Physical Review Letters D*, *23*, 347.

Hainline, L. J., Blain, A. W., Smail, I., Alexander, D. M., Armus, L., Chapman, S. C., et al. (2011). *ApJ*, *740*, 96.

Harrison, E. R. (1970). *Physical Review Letters D*, *1*, 2726.

Hatsukade, B., Kohno, K., Aretxaga, I., et al. (2011). *MNRAS*, *411*, 102.

Hatsukade, B., Ohta, K., Seko, A., Yabe, K., & Akiyama, M. (2013). *ApJ*, *769*, L27.

Hauser, M. G., & Dwek, E. (2001). *ARA&A*, *39*, 249.

Hayward, C. C., Kereš, D., Jonsson, P., et al. (2011). *ApJ*, *743*, 159.

Hayward, C. C., Behroozi, P. S., Somerville, R. S., et al. (2013). *MNRAS*, *434*, 2572.

Helly, J. C., Cole, S., Frenk, C. S., et al. (2003). *MNRAS*, *338*, 903.

Helou, G., Soifer, B. T., & Rowan-Robinson, M. (1985). *ApJ*, *298*, L7.

Henriques, B. M. B., White, S. D. M., Thomas, P. A., Angulo, R. E., Guo, Q., Lemson, G., et al. (2013). *MNRAS*, *431*, 3373.

Herschel, W. (1800a). *Philosophical Transactions of the Royal Society of London*, *90*, 255.

Herschel, W. (1800b). *Philosophical Transactions of the Royal Society of London*, *90*, 284.

Herschel, W. (1800c). *Philosophical Transactions of the Royal Society of London*, *90*, 293.

Herschel, W. (1800d). *Philosophical Transactions of the Royal Society of London*, *90*, 437.

Hickox, R. C., et al. (2012). *MNRAS*, *421*, 284.

Hodge, J. A., Karim, A., Smail, I., et al. (2013). *ApJ*, *768*, 91.

Hogg, D. W. (2001). *AJ*, *121*, 1207.

Holland, W. S., et al. (2013). *MNRAS*, *430*, 2513.

Hopkins, P. F., Cox, T. J., Younger, J. D., & Hernquist, L. (2009). *ApJ*, *691*, 1168.

Hopkins, P. F., Cox, T. J., Hernquist, L., Narayanan, D., Hayward, C. C., & Murray, N. (2013). *MNRAS*, *430*, 1901.

Hou, J., Frenk, C. S., Lacey, C. G., & Bose, S. (2016). *MNRAS*

Hubble, E. P. (1925). *Popular Astronomy*, *33*

Hughes, D. H., Serjeant, S., Dunlop, J., et al. (1998). *Nature*, *394*, 241.

Ilbert, O., et al. (2010). *ApJ*, *709*, 644.

Ilbert, O., et al. (2013). *A&A*, *556*, A55.

Ilbert, O., et al. (2015). *A&A*, *579*, A2.

Infante, L., et al. (2015). *ApJ*, *815*, 18.

Ivison, R. J., et al. (2002). *MNRAS*, *337*, 1.

Jiang, C. Y., Jing, Y. P., Faltenbacher, A., Lin, W. P., & Li, C. (2008). *ApJ*, *675*, 1095.

Jiang, L., Helly, J. C., Cole, S., & Frenk, C. S. (2014). *MNRAS*, *440*, 2115.

de Jong, T., Klein, U., Wielebinski, R., & Wunderlich, E. (1985). *A&A*, *147*, L6.

Kaiser, N. (1986). *MNRAS*, *222*, 323.

Kalnajs, A. J. (1972). *ApJ*, *175*, 63.

van Kampen, E., et al. (2005). *MNRAS*, *359*, 469.

Karim, A., et al. (2011). *ApJ*, *730*, 61.

Karim, A., Swinbank, A. M., Hodge, J. A., et al. (2013). *MNRAS*, *432*, 2.

Kennicutt, R. C, Jr. (1983). *ApJ*, *272*, 54.

Kennicutt, R. C, Jr. (1998). *ARA&A*, *36*, 189.

Kessler, M. F., et al. (1996). *A&A*, *315*, L27.

Kim, H.-S., Lacey, C. G., Cole, S., Baugh, C. M., Frenk, C. S., & Efstathiou, G. (2012). *MNRAS*, *425*, 2674.

Klypin, A. A., Trujillo-Gomez, S., & Primack, J. (2011). *ApJ*, *740*, 102.

Knudsen, K. K., van der Werf, P. P., & Kneib, J.-P. (2008). *MNRAS*, *384*, 1611.

Kochanek, C. S., et al. (2001). *ApJ*, *560*, 566.

Komatsu, E., Smith, K. M., Dunkley, J., et al. (2011). *ApJS*, *192*, 18.

Kroupa, P. (2002). *Science*, *295*, 82.

Labbé, I., et al. (2005). *ApJ*, *624*, L81.

Lacey, C., & Cole, S. (1993). *MNRAS*, *262*, 627.

Lacey, C., & Silk, J. (1991). *ApJ*, *381*, 14.

Lacey, C. G., Baugh, C. M., Frenk, C. S., Silva, L., Granato, G. L., & Bressan, A. (2008). *MNRAS*, *385*, 1155.

Lacey, C. G., Baugh, C. M., Frenk, C. S., & Benson, A. J. (2011). *MNRAS*, *412*, 1828.

Lacey, C. G., et al. (2016). *MNRAS*, *462*, 3854.

Lagache, G., & Puget, J. L. (2000). *A&A*, *355*, 17.

Lagos, C. D. P., Cora, S. A., & Padilla, N. D. (2008). *MNRAS*, *388*, 587.

Lagos, C. D. P., Lacey, C. G., Baugh, C. M., Bower, R. G., & Benson, A. J. (2011). *MNRAS*, *416*, 1566.

Lagos, C. D. P., Bayet, E., Baugh, C. M., Lacey, C. G., Bell, T. A., Fanidakis, N., et al. (2012). *MNRAS*, *426*, 2142.

Lagos, C. D. P., Lacey, C. G., & Baugh, C. M. (2013). *MNRAS*, *436*, 1787.

Lagos, C. D. P., Davis, T. A., Lacey, C. G., Zwaan, M. A., Baugh, C. M., Gonzalez-Perez, V., et al. (2014). *MNRAS*, *443*, 1002.

Landy, S. D., & Szalay, A. S. (1993). *ApJ*, *412*, 64.

Larson, R. B. (1974). *MNRAS*, *169*, 229.

Larson, R. B. (2005). *MNRAS*, *359*, 211.

Laurent, G. T., Aguirre, J. E., Glenn, J., et al. (2005). *ApJ*, *623*, 742.

Leroy, A. K., Walter, F., Brinks, E., Bigiel, F., de Blok, W. J. G., Madore, B., & Thornley, M. D. (2008). *AJ*, *136*, 2782.

Lewis, A. (2008). *Physics Review D*, *78*, 023002.

Lilly, S. J., Eales, S. A., Gear, W. K. P., Hammer, F., Le Fèvre, O., Crampton, D., et al. (1999). *ApJ*, *518*, 641.

Limber, D. N. (1953). *ApJ*, *117*, 134.

Linde, A. D. (1986). *Physics Letters B*, *175*, 395.

Linsky, J. L., et al. (2006). *ApJ*, *647*, 1106.

Magdis, G. E., et al. (2012). *ApJ*, *760*, 6.

Magnelli, B., et al. (2014). *A&A*, *561*, A86.

Magorrian J., et al. (1998). *AJ*, *115*, 2285.

Malbon, R. K., Baugh, C. M., Frenk, C. S., & Lacey, C. G. (2007). *MNRAS*, *382*, 1394.

Mannucci, F., Cresci, G., Maiolino, R., Marconi, A., & Gnerucci, A. (2010). *MNRAS*, *408*, 2115.

Maraston, C. (2005). *MNRAS*, *362*, 799.

Marigo, P., Bressan, A., & Chiosi, C. (1996). *A&A*, *313*, 545.

Massey, R., et al. (2007). *ApJS*, *172*, 239.

McCullagh, N., Norberg, P., Cole, S., Gonzalez-Perez, V., Baugh, C., & Helly, J. (2017). (arXiv:1705.01988).

McKee, C. F., & Ostriker, E. C. (2007). *ARA&A*, *45*, 565.

Meiksin, A. (2005). *MNRAS*, *356*, 596.

Menéndez-Delmestre, K., Blain, A. W., Swinbank, M., Smail, I., Ivison, R. J., Chapman, S. C., et al. (2013). *ApJ*, *767*, 151.

Merson, A. I., Baugh, C. M., Helly, J. C., et al. (2013). *MNRAS*, *429*, 556.

Messier, C. (1781). *Technical report, Catalogue des Nébuleuses & des amas d'Étoiles (Catalog of Nebulae and Star Clusters)*.

Meszaros, P. (1974). *A&A*, *37*, 225.

Michałowski, M., Hjorth, J., & Watson, D. (2010). *A&A*, *514*, A67.

Michałowski, M. J., Dunlop, J. S., Ivison, R. J., et al. (2012a). *MNRAS*, *426*, 1845.

Michałowski, M. J., Dunlop, J. S., Cirasuolo, M., Hjorth, J., Hayward, C. C., & Watson, D. (2012b). *A&A*, *541*, A85.

Mihos, J. C., & Hernquist, L. (1994). *ApJ*, *425*, L13.

Mihos, J. C., & Hernquist, L. (1996). *ApJ*, *464*, 641.

Miller, T. B., Hayward, C. C., Chapman, S. C., & Behroozi, P. S. (2015). *MNRAS*, *452*, 878.

Mitchell, P. D., Lacey, C. G., Baugh, C. M., & Cole, S. (2013). *MNRAS*, *435*, 87.

Mitchell, P. D., Lacey, C. G., Cole, S., & Baugh, C. M. (2014). *MNRAS*, *444*, 2637.

Mo, H. J., & Fukugita, M. (1996). *ApJ*, *467*, L9.

Mo, H. J., Mao, S., & White, S. D. M. (1998). *MNRAS*, *295*, 319.

Mo, H. J., Mao, S., & White, S. D. M. (1999). *MNRAS*, *304*, 175.

Moreno, J., Torrey, P., Ellison, S. L., Patton, D. R., Bluck, A. F. L., Bansal, G., et al. (2015). *MNRAS*, *448*, 1107.

Muñoz, Arancibia, A. M., Navarrete, F. P., Padilla, N. D., Cora, S. A., Gawiser, E., Kurczynski, P., & Ruiz, A. N., (2015). *MNRAS*, *446*, 2291.

Nagashima, M., Lacey, C. G., Baugh, C. M., Frenk, C. S., & Cole, S. (2005). *MNRAS*, *358*, 1247.

Narayanan, D., Hayward, C. C., Cox, T. J., Hernquist, L., Jonsson, P., Younger, J. D., et al. (2010). *MNRAS*, *401*, 1613.

Navarro, J. F., Frenk, C. S., & White, S. D. M. (1997). *ApJ*, *490*, 493.

Negrello, M., et al. (2010). *Science*, *330*, 800.

Neugebauer, G., et al. (1984). *ApJ*, *278*, L1.

Nguyen, H. T., et al. (2010). *A&A*, *518*, L5.

Norberg, P., et al. (2002). *MNRAS*, *336*, 907.

Norberg, P., Baugh, C. M., Gaztañaga, E., & Croton, D. J. (2009). *MNRAS*, *396*, 19.

Oesch, P. A., et al. (2012). *ApJ*, *759*, 135.

Oesch, P. A., et al. (2014). *ApJ*, *786*, 108.

Okamoto, T., Gao, L., & Theuns, T. (2008). *MNRAS*, *390*, 920.

Oke, J. B. (1974). *ApJS*, *27*, 21.

Oke, J. B., & Sandage, A. (1968). *ApJ*, *154*, 21.

Oliver, S. J., et al. (2010). *A&A*, *518*, L21.

Ono, Y., et al. (2013). *ApJ*, *777*, 155.

Oort, J. H. (1932). *Bulletin of the Astronomical Institutes of the Netherlands*, *6*, 249.

Osterbrock, D. E. (1974). *Astrophysics of gaseous nebulae*. Freeman and Co: W. H.

Ostriker, J. P., & Peebles, P. J. E. (1973). *ApJ*, *186*, 467.

Panuzzo, P., Bressan, A., Granato, G. L., Silva, L., & Danese, L. (2003). *A&A*, *409*, 99.

Parkinson, H., Cole, S., & Helly, J. (2008). *MNRAS*, *383*, 557.

Peacock, J. A., et al. (2000). *MNRAS*, *318*, 535.

Peebles, P. J. E. (1980). *The large-scale structure of the universe*. Princeton, NJ: Princeton Univ. Press.

Peng, C. Y., Ho, L. C., Impey, C. D., & Rix, H.-W. (2002). *AJ*, *124*, 266.

Penzias, A. A., & Wilson, R. W. (1965). *ApJ*, *142*, 419.

Perlmutter, S., et al. (1999). *ApJ*, *517*, 565.

Pforr, J., Maraston, C., & Tonini, C. (2012). *MNRAS*, *422*, 3285.

Pilbratt, G. L., Riedinger, J. R., Passvogel, T., et al. (2010). *A&A*, *518*, L1.

Collaboration, Planck, et al. (2011). *A&A*, *536*, A18.

Collaboration, Planck, et al. (2014). *A&A*, *571*, A30.

Collaboration, Planck, et al. (2016). *A&A*, *594*, A13.

Portinari, L., Chiosi, C., & Bressan, A. (1998). *A&A*, *334*, 505.

Press, W. H., & Schechter, P. (1974). *ApJ*, *187*, 425.

Puget, J.-L., Abergel, A., Bernard, J.-P., et al. (1996). *A&A*, *308*, L5.

Reddy, N. A., & Steidel, C. C. (2009). *ApJ*, *692*, 778.

Rieke, G. H., Alonso-Herrero, A., Weiner, B. J., Pérez-González, P. G., Blaylock, M., Donley, J. L., et al. (2009). *ApJ*, *692*, 556.

Riess, A. G., et al. (1998). *AJ*, *116*, 1009.

Roche, N., & Eales, S. A. (1999). *MNRAS*, *307*, 703.

Rodighiero, G., et al. (2011). *ApJ*, *739*, L40.

Rodrigues, L. F. S., Vernon, I., & Bower, R. G. (2017). *MNRAS*, *466*, 2418.

Rozo, E., et al. (2010). *ApJ*, *708*, 645.

Rubin, V. C., Ford, W. K. J., & Thonnard, N. (1980). *ApJ*, *238*, 471.

Rujopakarn, W., Rieke, G. H., Weiner, B. J., Pérez-González, P., Rex, M., Walth, G. L., et al. (2013). *ApJ*, *767*, 73.

Rybicki, G. B., & Lightman, A. P. (1979). *Radiative processes in astrophysics*.

Salpeter, E. E. (1955). *ApJ*, *121*, 161.

Sanders, D. B., & Mirabel, I. F. (1996). *ARA&A*, *34*, 749.

Santini, P., et al. (2012). *A&A*, *538*, A33.

Santini, P., et al. (2014). *A&A*, *562*, A30.

Savage, B. D., & Mathis, J. S. (1979). *ARA&A*, *17*, 73.

Sawala, T., Frenk, C. S., Crain, R. A., Jenkins, A., Schaye, J., Theuns, T., et al. (2013). *MNRAS*, *431*, 1366.

Sawicki, M., & Thompson, D. (2006). *ApJ*, *642*, 653.

Schaye, J., et al. (2015). *MNRAS*, *446*, 521.

Schenker, M. A., et al. (2013). *ApJ*, *768*, 196.

Schmidt, M. (1959). *ApJ*, *129*, 243.

Schreiber, C., et al. (2015). *A&A*, *575*, A74.

Schreiber, C., Elbaz, D., Pannella, M., Ciesla, L., Wang, T., Koekemoer, A., et al. (2016). *A&A*, *589*, A35.

Scott, S. E., Dunlop, J. S., & Serjeant, S. (2006). *MNRAS*, *370*, 1057.

Scott, K. S., Wilson, G. W., Aretxaga, I., et al. (2012). *MNRAS*, *423*, 575.

Shang, C., Haiman, Z., Knox, L., & Oh, S. P. (2012). *MNRAS*, *421*, 2832.

Sheth, R. K., Mo, H. J., & Tormen, G. (2001). *MNRAS*, *323*, 1.

Shibuya, T., Ouchi, M., & Harikane, Y. (2015). *ApJS*, *219*, 15.

Silk, J., & Rees, M. J. (1998). *A&A*, *331*, L1.

Silva, L., Granato, G. L., Bressan, A., & Danese, L. (1998). *ApJ*, *509*, 103.

Silva, L., Maiolino, R., & Granato, G. L. (2004). *MNRAS*, *355*, 973.

Silva, L., et al. (2011). *MNRAS*, *410*, 2043.

Silva, L., Fontanot, F., & Granato, G. L. (2012). *MNRAS*, *423*, 746.

Simha V., & Cole S. (2016). (arXiv:1609.09520).

Simpson, J. M., Swinbank, A. M., Smail, I., et al. (2014). *ApJ*, *788*, 125.

Simpson, J. M., et al. (2015). *ApJ*, *807*, 128.

Smail, I., Ivison, R. J., & Blain, A. W. (1997). *ApJ*, *490*, L5.

Smail, I., Ivison, R. J., Blain, A. W., & Kneib, J.-P. (2002). *MNRAS*, *331*, 495.

Smit, R., et al. (2015). *ApJ*, *801*, 122.

Smolčić, V., Aravena, M., Navarrete, F., et al. (2012). *A&A*, *548*, A4.

Smoot, G. F., et al. (1992). *ApJ*, *396*, L1.

Springel, V., White, S. D. M., Tormen, G., & Kauffmann, G. (2001). *MNRAS*, *328*, 726.

Springel, V., White, S. D. M., Jenkins, A., et al. (2005). *Nature*, *435*, 629.

Stanway, E. R., Bunker, A. J., & McMahon, R. G. (2003). *MNRAS*, *342*, 439.

Steidel, C. C., & Hamilton, D. (1993). *AJ*, *105*, 2017.

Steidel, C. C., Giavalisco, M., Pettini, M., Dickinson, M., & Adelberger, K. L. (1996). *ApJ*, *462*, L17.

Steigman, G. (2007). *Annual Review of Nuclear and Particle Science*, *57*, 463.

Stetson, P. B. (1987). *PASP*, *99*, 191.

Sutherland, R. S., & Dopita, M. A. (1993). *ApJS*, *88*, 253.

Swinbank, A. M., Chapman, S. C., Smail, I., Lindner, C., Borys, C., Blain, A. W., et al. (2006). *MNRAS*, *371*, 465.

Swinbank, A. M., Lacey, C. G., Smail, I., et al. (2008). *MNRAS*, *391*, 420.

Swinbank, A. M., et al. (2011). *ApJ*, *742*, 11.

Swinbank, A. M., et al. (2014). *MNRAS*, *438*, 1267.

Tacconi, L. J., et al. (2008). *ApJ*, *680*, 246.

Tegmark, M., & Efstathiou, G. (1996). *MNRAS*, *281*, 1297.

Tinsley, B. M. (1972). *A&A*, *20*, 383.

Toft, S., et al. (2014). *ApJ*, *782*, 68.

Toomre, A. (1964). *ApJ*, *139*, 1217.

Vega, O., Silva, L., Panuzzo, P., Bressan, A., Granato, G. L., & Chavez, M. (2005). *MNRAS*, *364*, 1286.

Vieira, J. D., Crawford, T. M., Switzer, E. R., et al. (2010). *ApJ*, *719*, 763.

Vieira, J. D., Marrone, D. P., Chapman, S. C., et al. (2013). *Nature*, *495*, 344.

Viero, M. P., et al. (2009). *ApJ*, *707*, 1766.

Viero, M. P., et al. (2013). *ApJ*, *772*, 77.

Vikhlinin, A., & Forman, W. (1995). *ApJ*, *455*, L109.

Vikhlinin, A., et al. (2009). *ApJ*, *692*, 1060.

Vogelsberger, M., et al. (2014). *MNRAS*, *444*, 1518.

Wagoner, R. V. (1973). *ApJ*, *179*, 343.

Wang, W.-H., Cowie, L. L., Barger, A. J., & Williams, J. P. (2011). *ApJ*, *726*, L18.

Wardlow, J. L., Smail, I., Coppin, K. E. K., et al. (2011). *MNRAS*, *415*, 1479.

Weiß, A., Kovács, A., Coppin, K., et al. (2009). *ApJ*, *707*, 1201.

Werner, M. W., et al. (2004). *ApJS*, *154*, 1.

White, S. D. M., & Frenk, C. S. (1991). *ApJ*, *379*, 52.

White, S. D. M., & Rees, M. J. (1978). *MNRAS*, *183*, 341.

Wilkins, S. M., Bunker, A. J., Ellis, R. S., Stark, D., Stanway, E. R., Chiu, K., et al. (2010). *MNRAS*, *403*, 938.

Wilkinson, A., et al. (2017). *MNRAS*, *464*, 1380.

Woosley, S. E., & Weaver, T. A. (1995). *ApJS*, *101*, 181.

Zavala, J. A., et al. (2015). *MNRAS*, *452*, 1140.

Zeldovich, Y. B. (1972). *MNRAS*, *160*, 1P.

Zemcov, M., Blain, A., Halpern, M., & Levenson, L. (2010). *ApJ*, *721*, 424.

Zwicky, F. (1933). *Helvetica Physica Acta*, *6*, 110.